Structural Response and Wake Vortex Dynamics of Cylindrical Structures Undergoing VIV with Elliptic Trajectories

by

Erik Marble

A thesis
presented to the University of Waterloo
in fulfillment of the
thesis requirement for the degree of
Master of Applied Science
in
Mechanical and Mechatronics Engineering

Waterloo, Ontario, Canada, 2018

I hereby declare that I am the sole author of this thesis. This is a true copy of the thesis, including any required final revisions, as accepted by my examiners.

I understand that my thesis may be made electronically available to the public.

Abstract

Vortex Induced Vibrations (VIV) of a pivoted circular cylinder were examined through experiments conducted in a water tunnel facility at the University of Calgary. The structural response and wake dynamics of the system were evaluated with the goal of quantitatively describing the attendant fluid-structure interaction. Experiments were performed at a fixed Reynolds number of 3100, a mass ratio of 10.8, and a range of reduced velocities, $4.42 \leq U^* \leq 9.05$. Laser based displacement sensors and time-resolved, two-component particle image velocimetry (PIV) measurements were used to quantify the structural response and flow development, respectively. The results provide new insight into the fluid-structure interaction for pivoted cylinders, which is of practical engineering interest as this phenomenon is encountered in various civil structures and mechanical devices.

For the investigated conditions, the cylinder traces elliptic trajectories, with the experimental conditions producing three out of four possible combinations of orbiting direction and primary axis alignment relative to the incoming flow. The study focuses on the quantitative analysis of wake topology and its relation to this type of structural response. The planar phase-averaged wake topology generally agrees with the Morse and Williamson [1] shedding map for one-degree-of-freedom vortex induced vibrations, with 2S, $2P_0$, and 2P shedding patterns observed within the range of reduced velocities studied here. A new Eulerian vortex identification, tracking, and strength quantification methodology is developed and applied to analyze the vortex shedding process. In the case of 2S vortex shedding, vortices are shed when the cylinder is approaching the maximum transverse displacement and reaches the streamwise equilibrium. 2P vortices are shed approximately half a period earlier in the cylinder's elliptic trajectory. Leading vortices shed immediately after the peak in transverse oscillation and trailing vortices shed near the equilibrium of transverse oscillation. The orientation and direction of the cylinder's elliptic trajectory are shown to influence the timing of vortex shedding, inducing changes in the 2P wake topology.

Three dimensional reconstructions of the phase averaged wake velocity measurements reveal 2S shedding along the span of a stationary cylinder and hybrid shedding for the VIV cases at $U^* = 5.48$ and 7.08, with planar wake topology transitioning from 2S to P+S to 2S, and 2S to P+S, respectively. The observed wake topologies show significant deviation from predictions based on the Morse and Williamson [1] shedding map. Examination of the time averaged wake characteristics shows the formation length, wake half-width, and maximum velocity deficit exhibit spanwise trends that support the observed region of wake transition between different shedding regimes. Spectral analysis of the wake velocity indicates cycle-to-cycle variations of the spanwise location of wake topology transition as well as transience in the frequency of vortex shedding.

Acknowledgements

I owe my deepest gratitude to my supervisors, Professor Serhiy Yarusevych and Professor Christopher Morton, for their guidance, encouragement and patience during my studies. Your dedication and approach to research provide the foundation for academic success and professional development.

It has been a pleasure working with the members of the FMRL group at the University of Waterloo. Ajith Airody, Jonathan Deng, Amit Dutta, Laura Haya, Winston Hu, Mark Istvan, John Kurelek, Jeff McClure, Supun Pieris, Ben Pocock, Yash Shah, Burak Tuna, Dallyn Wynnychuk, and Caddie Zhang, thank you for the insightful conversations and your enthusiasm in lending a helping hand. Special thanks is owed to John and Jeff, who were always eager to answer my MATLAB and PIV related questions, Ben and Caddie, who readily offered their help during coursework, and Mark, who pulled me away from my desk for the occasional spin or swim.

I would like to show my gratitude to the LTRAC group at the University of Calgary, where I completed my experimental campaigns. Conrad Bingham, Robert Crane, Sina Daneshvar, Eric Limacher, and Graham Riches, thank you for welcoming me into your facility and taking the time to help me conduct experiments. Without your knowledge, I would surely still be sitting in that basement flicking the lights on and off.

I am grateful for the unwavering love and support from my family and friends. To my parents, Robert and Carolyn, your infallible encouragement and financial support throughout my academic endeavours has allowed me to achieve a higher education. To my sister, Elyse, you reminded me to maintain balance and helped me to keep a lighthearted approach in my studies. To the rest of my family and friends, the many conversations and adventures over the past two years go further than you may think and have kept me motivated and optimistic in the pursuit of my goals. Finally I want to thank Alyssa Janssen, your encouragement and support kept me grounded as I worked on this thesis.

I would like to thank the Natural Sciences and Engineering Research Council of Canada (NSERC) and the University of Waterloo for funding this work.

Table of Contents

List of Tables

List of Figures

Nomenclature

Dimensionless Quantities

Symbol	Description	Definition
AR	aspect ratio	$\frac{L}{D}$
A_x^*	normalized amplitude of streamwise vibration	$\frac{A_x}{D}$
A_y^*	normalized amplitude of transverse vibration	$\frac{A_y}{D}$
f_x^*	normalized streamwise frequency	$\frac{f_x}{f_n}$
f_y^*	normalized transverse frequency	$\frac{f_y}{f_n}$
I^*	moment of inertia ratio	$\frac{I}{I_d}$
$I^*\zeta$	moment of inertia-damping parameter	$\frac{I\zeta}{I_d}$
m^*	mass ratio	$\frac{m}{m_d}$
$m^*\zeta$	mass-damping parameter	$\frac{m\zeta}{m_d}$
Re	Reynolds number	$\frac{U_0 D}{\nu}$

t^*	normalized time for vibrations in quiescent water	tf_n
U_c^*	coupling-frequency based reduced velocity	$\frac{U}{f_c D}$
U^*	reduced velocity	$\frac{U_0}{f_n D}$

Roman Symbols

Symbol	Description	Units
A_x	amplitude of streamwise vibrations	m
A_y	amplitude of transverse vibrations	m
a_i	temporal POD coefficients	–
B_1, B_2	coefficients in Eqs. (2.23) and (2.24), defined in Eqs. (2.25) and (2.26)	–
b	distance between the springs and the pivot point of the cylinder	m
C_A	added mass coefficient	–
C_D	amplitude of drag coefficient fluctuations of a stationary circular cylinder	–
C_L	amplitude of lift coefficient fluctuations of a stationary circular cylinder	–
$C_x(z)$	local amplitude of drag coefficient fluctuations of a vibrating circular cylinder	–
$C_y(z)$	local amplitude of lift coefficient fluctuations of a vibrating circular cylinder	–
CCW	counter-clockwise	–
CW	clockwise	–
c	damping coefficient	$\mathrm{kg\,s^{-1}}$
D	cylinder diameter	m
d_{wake}	wake half-width ($u_d/u_{d\ max} = 0.5$)	m
$d_1 - d_4$	coefficients in Eqs. (2.23) and (2.24), defined in Eqs. (2.27)–(2.30)	–
d_{98}	half-wake width ($U/U_0 = 0.98$)	m

F_s	sample rate	Hz
F_x	fluid force per unit length in the streamwise direction	$\mathrm{N\,m^{-1}}$
F_y	fluid force per unit length in the transverse direction	$\mathrm{N\,m^{-1}}$
f_a	natural frequency in air	Hz
f_c	coupling frequency	Hz
f_n	natural frequency in quiescent water	Hz
f_r	non-dimensional coefficient in Eqs. (2.18) and (2.19), $f_r = (f_a/f_n)I^*/(I^* + C_A)$	–
f_s	vortex shedding frequency of a stationary cylinder	Hz
f_u	frequency of the streamwise velocity signal	Hz
f_v	frequency of the transverse velocity signal	Hz
f_x	frequency of streamwise vibrations	Hz
f_y	frequency of transverse vibrations	Hz
g	acceleration due to gravity	$\mathrm{m\,s^{-2}}$
H	the Hilbert transform	–
I	moment of inertia of the cylinder about the pivot point	$\mathrm{kg\,m^2}$
I_A	added moment of inertia	$\mathrm{kg\,m^2}$
I_d	moment of inertia of the displaced fluid about the pivot point	$\mathrm{kg\,m^2}$
$\hat{i}$	component of vector x	–
$\hat{j}$	component of vector y	–
k	spring stiffness coefficient	$\mathrm{N\,m^{-1}}$

$\hat{k}$	component of vector z	–
k_e	effective stiffness of the springs	$\mathrm{N\,m^{-1}}$
k_c	cross-stiffness	$\mathrm{N\,m^{-1}}$
L	length of the cylinder	m
L_f	formation length	m
L_0	wetted length of the cylinder	m
M_x	fluid moment in the streamwise direction	$\mathrm{N\,m}$
M_y	fluid moment in the transverse direction	$\mathrm{N\,m}$
m	mass of the cylinder	kg
m_d	mass of the displaced fluid	kg
$p_{\vec{x}}$	probability distribution	–
PSD	power spectrum density	dB
R_x	ratio of the amplitude of streamwise vibrations associated with f_n and that associated with $2f_n$	–
R_y	ratio of the amplitude of transverse vibrations associated with f_n and that associated with $2f_n$	–
t	time	s
$\vec{U}$	mean velocity field	$\mathrm{m\,s^{-1}}$
U_e	velocity at the transverse extent of wake measurements	$\mathrm{m\,s^{-1}}$
U_r	non-dimensional coefficient in Eqs. (2.18) and (2.19), $(U^*/U_c^*)^2 I^*/(I^* + C_A)$	–
U_0	free stream velocity	$\mathrm{m\,s^{-1}}$
$\vec{u}$	velocity field, $\vec{u} = u\hat{i} + v\hat{j} + w\hat{k}$	$\mathrm{m\,s^{-1}}$
$\vec{u}'$	fluctuating coherent periodic component of the velocity field	$\mathrm{m\,s^{-1}}$

$\vec{u}''$	fluctuating incoherent turbulence of the velocity field	$\mathrm{m\,s^{-1}}$
u_d	local velocity deficit	$\mathrm{m\,s^{-1}}$
x	streamwise direction	$-$
x_{ss}	steady state cylinder displacement in the streamwise direction	m
y	transverse direction	$-$
y_{ss}	steady state cylinder displacement in the transverse direction	m
z	spanwise direction	$-$

Greek Symbols

Symbol	Description	Units
α	measured quanitity	–
β	desired quanitity	–
Γ	circulation	$\mathrm{m^2\,s^{-1}}$
γ_{ik}	GMM responsibility of subpopulation k towards point x_i	–
Δt	PIV frame separation	µs
$\Delta\theta$	phase bin size	rad
δ	maximum deflection angle of the structure	rad
ϵ_β	uncertainty estimate of β	–
ζ	damping ratio	–
θ	phase angle	degrees (°)
κ	logarithmic decrement	–
λ_i	POD mode energy	–
$\vec{\mu}_i$	GMM subpopulation mean	m
ν	kinematic viscosity	$\mathrm{m\,s^{-2}}$
π_i	GMM subpopulation weight	–
ρ	water density	$\mathrm{kg\,m^{-3}}$
Σ_i	GMM subpopulation covariance	–
$\vec{\phi}_i$	spatial POD modes, $\vec{\phi}_i = \phi_{ix}\hat{i} + \phi_{iy}\hat{j}$	–
ψ	phase angle between streamwise and transverse cylinder motion	rad
ψ_{force}	phase angle between the fluid force in the streamwise and transverse directions	rad

$\vec{\omega}$	vorticity, $\vec{\omega} = \omega_x \hat{i} + \omega_y \hat{j} + \omega_z \hat{k}$	s^{-1}
ω_n	angular natural frequency of the structure, $2\pi f_n$	Hz

Chapter 1

Introduction

Cross-flow over a cylinder is of fundamental importance to the fluid mechanics community: it is ubiquitous to engineering applications, such as buildings, bridges, heat exchangers, offshore structures and pipelines [2–6]. Over the past several decades, numerous studies have examined the flow around cylindrical structures due to their widespread application [6–12]. The majority of interest has been focused on an intermediate Reynolds number range where the phenomenon of vortex shedding occurs in the wake [4]. The flow development over a circular cylinder is depicted by the conceptual diagram in Fig. 1.1 and begins with the approaching fluid diverting around the upper and lower halves of the cylinder. Boundary layers form at the solid surface due to the no slip-condition and grow towards the aft of the cylinder as a result of the dominant viscous forces near the surface. Subject to a sufficient adverse pressure gradient, the boundary layers detach from the surface to form separated shear layers. For $Re \gtrsim 49$ [4], the separated shear layers roll up to develop vortices that are shed periodically from both sides of the cylinder to form a continuous pattern in the wake, known as the vortex street [13]. The circular cylinder provides the foundations to study vortex shedding, which is prevalent in various forms for all bluff bodies.

Vortex shedding in the near wake causes fluctuating structural forces that can excite the structure to undergo vibrations [14]. This phenomenon is known as Vortex Induced Vibrations (VIV) and results in a significant response if the frequency of periodically shed vortices approaches the natural frequency of the structure [15–19]. The repetitive structural motion can cause substantial acoustic noise [20] and may impede system operation, with the extreme being fatigue failure [21, 22]. Knowledge of the fluid-structure interaction is essential to understand how energy is transferred from the fluid to the structure and how it can be mitigated from a safety and reliability standpoint. Conversely, the energy may

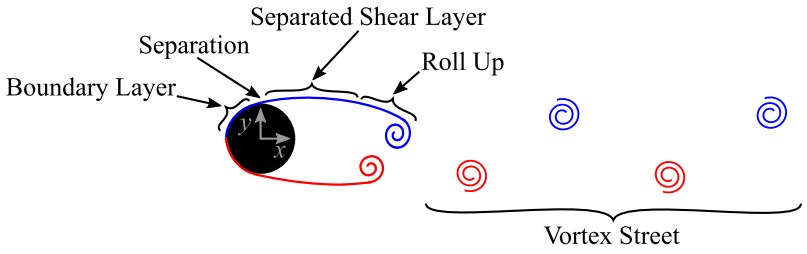

Figure 1.1: Diagram of flow development over a circular cylinder.

be harvested as a renewable source by allowing the vibrations to occur [23, 24]. Mitigation or enhancement of VIV can be achieved through passive or active structural modifications [5, 25].

The majority of early studies concerning VIV of cylinders constrain the oscillatory motion in the transverse direction to the flow because the fluid-structure forcing induced by vortex shedding is primarily transverse to the flow [18, 26–28]. Studies permitting the cylinder to oscillate in both the transverse and streamwise directions offer a more realistic representation of practical engineering applications. In most of these two degree-of-freedom (2DOF) studies, the structures were elastically mounted to produce uniform amplitudes of vibration along the cylinder span [29–35]. However, practical engineering structures undergoing VIV often oscillate with an amplitude that varies along the span [36, 37]. A flexible cantilever [38–40] or flexible cable [41–44] offers the best approximation since their design can incorporate structural properties that represent a scaled version of a specific structure. The pivoted cylinder [45–50] is a simplification of the flexible structure and represents a body having a linear variation of amplitude along its span. Its local flow features are expected to be generic to other cases of spanwise amplitude variation without being system specific. The present study focuses on the VIV of a pivoted cylinder.

The structural response for 2DOF VIV of cylinders exhibits two types of trajectories: figure-eight and elliptic, both of which have been reported to occur naturally [51–53]. The figure-eight trajectory is described by the frequency of streamwise oscillations being twice that of the transverse oscillations ($f_x = 2f_y$), whereas the frequencies are equal for the elliptic trajectory ($f_x = f_y$). Structures with uniform spanwise amplitude solely exhibit the figure-eight response [29, 34, 35], while those with spanwise variation of amplitude have been observed to exhibit both figure-eight [46–48] and elliptic [40, 45, 49] trajectories. Kheirkhah *et al.* [45] argue that the structural coupling between the streamwise and transverse motion governs the occurrence of either figure-eight or elliptic trajectories.

Effects of the reduced velocity and the amplitude of structural oscillations on the wake topology are well documented in a shedding map for cylinders forced to oscillate with

1DOF transverse to the flow [1, 54]. Williamson and Roshko [54] describe the vortex formation process in relation to the transverse structural motion for the various shedding regimes observed. While the shedding map agrees with flow visualizations for 1DOF VIV in the transverse direction [18, 36], the additional streamwise motion in 2DOF VIV studies has been shown to cause the observed wake topology to deviate from predictions [34, 47–49]. Extensive research for the figure-eight trajectory has found the vortex street exhibits unique patterns in the case of massive amplitudes of oscillation [34, 47]. Furthermore, Flemming and Williamson [47] observed hybrid vortex shedding in the wake of a pivoted cylinder undergoing a figure-eight trajectory as a result of the spanwise variation of amplitude. On the other hand, there are limited studies focused on the elliptic trajectory [40, 45, 49]. Kheirkhah *et al.* [45] used cylinder displacement measurements to investigate the structural response and focused on identifying the cause for either a figure-eight or elliptic trajectory. Oviedo-Tolentino *et al.* [40] and Kheirkhah *et al.* [49] used qualitative flow visualization techniques to examine the wake topology in limited planes along the span. While Kheirkhah *et al.* [49] identified hybrid shedding in the wake and discuss wake development, the vortex dynamics at the transition between shedding patterns is unclear. Furthermore, the influence of the structure's elliptic trajectory on the vortex formation process remains to be investigated and would extend observations of the timing of vortex shedding for 1DOF cases [54–56] to 2DOF cases, thus providing valuable insight into the effect of an additional degree of freedom on the fluid-structure interaction.

1.1 Study Objectives

VIV studies of pivoted cylinders undergoing an elliptic trajectory have investigated structural response and have used flow visualization to provide qualitative description of the attendant wake topology. However, assessment of the elliptic trajectory effects on the wake development and the vortex dynamics associated with hybrid shedding is presently lacking. The purpose for this investigation is to provide a quantitative assessment of the flow development and vortex dynamics for a wide range of elliptic structural responses. The specific research objectives of this thesis are as follows:

1. Investigate the influence of an elliptic trajectory on the wake topology, in order to
   (a) provide a quantitative time-resolved description of the wake development for a range of reduced velocities to confirm previous qualitative observations, and
   (b) identify the timing of vortex shedding and its relation to the structural response.
2. Examine the effect of a structural response with spanwise variation of amplitude on the coherent structures in the wake for a stationary cylinder and two cases of VIV at $U^* = 5.48$ and 7.08 by

(a) reconstructing the three-dimensional wake topology from time-resolved wake velocity measurements, and
(b) identifying and characterizing the vortex interactions associated with spanwise transition between vortex shedding modes.

1.2 Thesis Overview

The thesis is organized as follows: Chapter 2 provides an overview of the relevant literature on VIV of cylinders and related geometries. The experimental methodology employed and experimental configuration are described in Chapter 3. An analysis of the results is given in Chapters 4 and 5, followed by concluding remarks and recommendations in Chapters 6 and 7, respectively.

Chapter 2

Background

This chapter serves as a comprehensive, but not exhaustive, review of literature pertaining to flow over a circular cylinder and its related geometries. The focus is to review the flow development and vortex dynamics in the wake, which are largely governed by vortex shedding from the cylinder. Following this, a review of the structural response of an elastically mounted cylinder and the associated fluid-structure interaction is completed for various flow and structural conditions. The attendant fluid-structure interaction is essential for understanding how the energy transfer from the fluid to the structure can be detrimental to performance, requiring mitigation [5, 25], or how it can be utilized for the purposes of energy extraction [23]. The review first discusses the stationary circular cylinder in Section 2.1, which instructively provides the fundamentals of flow development. The following Sections 2.2 and 2.3 present research on cylinders permitted to oscillate with a uniform spanwise variation of amplitude in either one or two-degrees of freedom. Sections 2.4 and 2.5 then expand this review with the investigations of cylinders permitted to oscillate with a spanwise variation of amplitude.

2.1 Flow over a stationary circular cylinder

Flow around a stationary uniform circular cylinder involves the development of a boundary layer, separated shear layer, and wake region [3, 4]. Numerous studies have examined this flow due to its widespread application [4–7, 9–12, 15, 57]. A review of the flow development by Williamson [4] discusses the distinct flow regimes which can be identified based on the Reynolds number (Re_D). For all regimes, the boundary layer forms at the solid surface of the cylinder, due to the no-slip condition, and grows towards the aft of the cylinder due to the dominant viscous forces near the surface. Subject to a sufficient adverse pressure

gradient, the boundary layers detach from the cylinder to form separated shear layers. For $Re_D \lesssim 49$ the flow is laminar and consists of two symmetric recirculating regions surrounded by separated shear layers that merge at a confluence point downstream of the cylinder. These regions elongate downstream as the Reynolds number increases until the flow transitions from the steady laminar regime to unsteady laminar vortex shedding [58]. In the laminar vortex shedding regime ($49 \lesssim Re_D \lesssim 190$) the separated shear layers roll up to develop vortices that shed periodically at the dimensionless shedding frequency $f_s = St_D U/D$. The flow in this regime is considered two-dimensional since vortex shedding is spanwise invariant with vortices shed parallel to the cylinder. The flow may become three-dimensional unless laboratory conditions are controlled [13, 59, 60]. As the Reynolds number is further increased, the inception of secondary streamwise vortex structures causes the flow to become three-dimensional with transition to turbulence occurring in the far wake. This wake transition regime exists for $190 \lesssim Re_D \lesssim 1000$. Within the range $190 \lesssim Re_D \lesssim 260$, mode A and B instabilities cause two discontinuous changes in the wake [61]. The first occurs near $Re_D \approx 180 - 194$; a the secondary mode A instability develops and is characterized by paired streamwise vortices separated by a spanwise wavelength of approximately 3-4 diameters [4]. The second discontinuity occurs over the range $230 \lesssim Re_D \lesssim 250$ as energy is gradually transferred from mode A to mode B [4]. Mode B is characterized by finer scale streamwise vortices with a smaller spanwise wavelength of approximately one diameter [4]. As the Reynolds number is increased to 1000, the fine scale three dimensionalities become increasingly disordered, the length of the formation region increases, and the transition to turbulence moves upstream towards the near wake. At $Re_D \approx 1000$, the laminar shear layers undergo turbulent transition due to a Kelvin-Helmholtz instability in the free shear layer [62, 63]. Within the regime $1000 \lesssim Re_D \lesssim 2 \times 10^5$, the point of turbulent transition moves upstream with increasing Reynolds number, but remains in the separated shear layer [64]. This shear layer transition regime has a Reynolds number range that is applicable to many practical engineering applications and is the focus of the present study. Within the critical regime, $2 \times 10^5 \lesssim Re_D \lesssim 6 \times 10^6$, turbulent transition remains in the separated shear layers; however, it may cause the separated shear layers to reattach on one or both sides of the cylinder [5]. The formed separation-reattachment bubble regions greatly narrow the wake and reduce the drag on the cylinder. Beyond $Re_D \approx 6 \times 10^6$, transition occurs in the boundary layer prior to separation and prevents the formation of separation bubbles [4].

The dynamics of vortex shedding can be divided into three distinct stages: formation, saturation, and downstream advection [65]. Formation begins with the generation of vorticity at the surface of the cylinder due to the tangential pressure gradient along this boundary [66]. This is the sole vorticity source for the shed vortices since vorticity can only

be generated at the boundaries of a homogeneous fluid [66]. The vorticity is supplied at a nearly constant rate to the near wake by the viscous boundary layers and separated shear layers. As the separated shear layers roll up, the circulation concentrates and increases until saturation is achieved and the vortex sheds [55]. Upon saturation, only a portion of the vorticity generated at the surface of the cylinder is carried away by the rolled-up vortices [7]. This is attributed to the cross annihilation of opposite signed vorticity as it is entrained across the wake from the shear layers [66–68]. The ratio of circulation advected via the shed vortices to that generated in the same signed boundary layer at the cylinder surface is termed the deficit ratio. Experimental investigations have directly measured this ratio to vary between 0.4 and 0.7 [2, 7, 69], depending on the Reynolds number and turbulence intensity. The ratio varies from cycle to cycle because the strength of shed vortices is not consistent [70].

Vortex dynamics in the wake of a circular cylinder can be complex. Compared to the vortices shed in the laminar regime, the presence of streamwise and spanwise structures in the wake of transitional and turbulent regimes can lead to intricate vortex connections. These interactions are not without physical constraints, the most fundamental being the Helmholtz's vortex theorems for irrotational flow [71]:

> Theorem 1: Vortex lines move at the velocity of the fluid.
> Theorem 2: The strength of a vortex tube (its circulation) is constant along its length.
> Theorem 3: A vortex tube cannot end within a fluid. It must either end at a boundary or form a closed loop.
> Theorem 4: The strength of a vortex tube remains constant in time.

Although these theorems do not hold for viscous flows, they provide valuable insight and utility in the analysis of vortex behaviour and dynamics in the wake region for flow around complex geometries [72–74]. In particular, the viscous diffusion of vorticity causes the strength of vortices to dissipate in time, thus violating the fourth theorem. Furthermore, the dissipation rate depends on the gradient of the velocity field and may vary along the length of the vortex tube, thus violating the second theorem.

2.2 One DOF uniform amplitude VIV

Vortex Induced Vibration (VIV) of circular cylinders is a classic fluid-structure interaction problem and is of relevance to numerous engineering applications [1, 15]. Periodic vortex shedding that takes place in the near wake induces unsteady structural forcing [14] with significant response occuring in the lock-in region [15]. Within the lock-in region, the

cylinder motion is coupled to the vortex shedding, collapsing the frequencies of structural oscillation and vortex shedding into a single frequency close to the natural frequency of the structure [15–18]. The structural response transverse to the free stream is dominant compared to that in the streamwise direction because the induced fluid forces resulting from the vortex dynamics are primarily in this direction [75]. Therefore, numerous studies have investigated the VIV of a cylinder constrained to 1DOF in the transverse direction [18, 26–28] and are summarized in reviews pertaining to VIV [11, 16, 17].

The amplitude of response is defined as half of the peak to peak amplitude of steady state structural oscillations [45]. The magnitude of oscillations depends primarily upon the reduced velocity, U^*, mass ratio, m^*, damping ratio, ζ, and Reynolds number, Re, as determined through a dimensional analysis carried out by Sarpkaya [15]. Other forms of non-dimensional terms have been derived [76] and are consistent with the analysis by Sarpkaya [15]. The investigation into VIV of high mass ratio cylinders, $m^* = 320$, with 1DOF in the transverse direction by Feng [26] demonstrated that the resonance of a body occurs over a lock-in region defined by the reduced velocity range $5 \leq U^* \leq 8$. Khalak and Williamson [18] investigated the effects of U^* on the structural response at low and moderate mass ratios of $m^* = 2.4$ and $m^* = 10.3, 20.6$, respectively. They found a lower mass ratio to correlate with a wider lock-in region, specifically, the lock-in regions of reduced velocity for the three cases investigated ($m^* = 2.4, 10.3$, and 20.6) were $2.5 \leq U^* \leq 13$, $3.5 \leq U^* \leq 12$, and $4 \leq U^* \leq 10.5$, respectively. The peak amplitudes are controlled principally by the combined mass-damping ratio, $m^*\zeta$. Despite the criticisms of Sarpkaya [15, 16] stating that the two parameters should not be combined into one, it has largely become common practice [18, 27, 29, 46, 77] with compelling reasoning provided by Klamo [76] in their investigation of damping effects on VIV.

Feng [26] and Khalak and Williamson [18] observed distinct branches in the amplitude response, the number of which depends on the combined mass-damping ratio [18]. Systems with a high mass-damping parameter exhibit an initial branch, corresponding to the highest amplitudes reached, and a lower branch in the lock-in region. The transition between these two branches is hysteretic. In contrast, low mass-damping systems show the existence of an additional upper response branch situated between the initial and lower branches, and therefore two mode transitions. The transition between the initial and upper branch is hysteretic, while the transition between the upper and lower branch is not hysteretic and instead involves intermittent switching between branches.

Williamson and Roshko [54] studied a cylinder forced to oscillate with a single degree of freedom (1DOF) transverse to the flow and used flow visualization to create a map of wake vortex shedding regimes over a range of reduced velocities and oscillation amplitudes, see Fig. 2.1a. Morse and Williamson [1] created an updated map with higher parameter

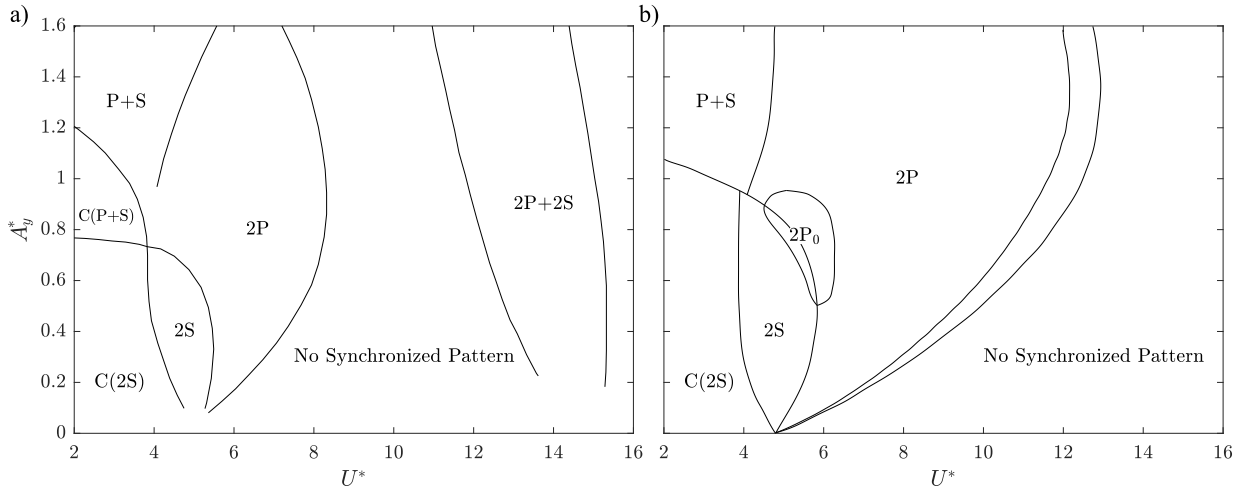

Figure 2.1: Map of vortex shedding regimes adapted by (a) Williamson and Roshko [54] and (b) Morse and Williamson [1].

resolution using Particle Image Velocimetry (PIV), see Fig. 2.1b. The shedding regimes identified in the lock-in region include 2S, 2P, P+S and $2P_0$. The 2S regime involves shedding of two oppositely signed vortices within each oscillation period, see Fig. 2.2a; whereas, the 2P regime is defined by two pairs of counter rotating vortices shed in each period, see Fig. 2.2c. A combination of 2S and 2P patterns involving a vortex pair and a single vortex shed each period constitutes the P+S regime, see Fig. 2.2b. The $2P_0$ regime, defined by Morse and Williamson [1], is similar to 2P except the second vortex shed in each pair is substantially weaker than the first, see Fig. 2.2d. Morse and Williamson [1] and Williamson and Roshko [54] observed a regime at higher reduced velocities where the vortex shedding is not synchronized with the cylinder motion. Despite the desynchronized shedding, a substantial component of fluid forcing at the frequency of oscillation gives rise to free cylinder vibrations.

Khalak and Williamson [18] and Brika and Laneville [36] employed flow visualization techniques in the investigation of high mass-damping systems undergoing VIV with 1DOF to show that the transition from the initial branch to the lower branch corresponds with a vortex shedding regime change from 2S to 2P. Their observation agrees with the experiments of Hover *et al.* [78] and the map developed by Williamson and Roshko [54]. Govardhan and Williamson [27] examined the wake of a low mass-damping system using PIV and determined the transition between initial and upper response branches corresponds with switching between 2S and 2P vortex shedding, respectively, while there is no change in the vortex shedding regime with transition between the upper and lower response

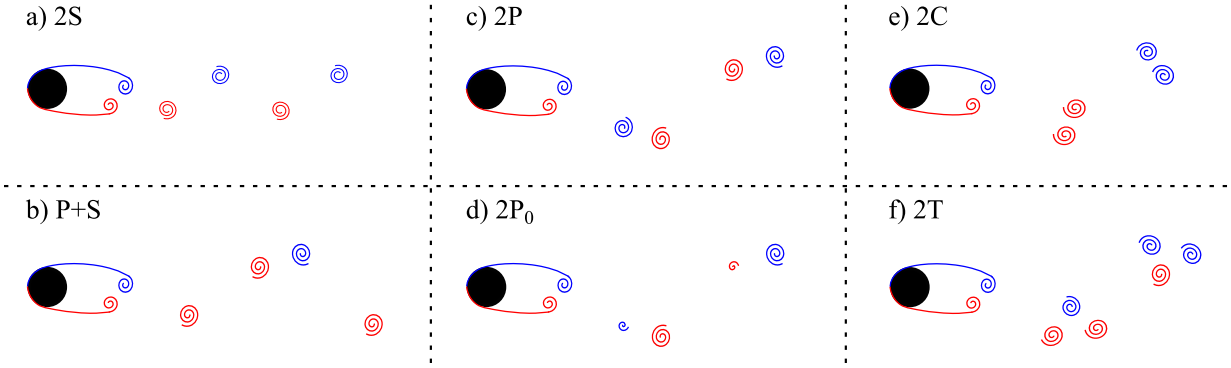

Figure 2.2: Diagram of vortex shedding patterns observed in the wake of a cylinder undergoing VIV with one or two degrees-of-freedom. Flow is from left to right.

branches since both are associated with the 2P regime.

Govardhan and Williamson [27] further investigated the branch transitions by employing two distinct formulations for the equations of motion. The traditional equation of motion is given in Equation 2.1, where m is the mass of the cylinder, c is the structural damping, k is the total spring stiffness, $y = Asin(\omega t)$ is the cylinder motion in the transverse direction, F_{total} is the total fluid force, $\omega = 2\pi f$; f is the frequency of oscillation, and ϕ_{total} is the phase angle between the fluid force and the cylinder displacement. This equation offers a good approximation of the total force when the frequency of cylinder oscillation is synchronized with the periodic vortex wake [27]. Lighthill [79] showed that the total force, F_{total}, acting on the body can be separated into the potential force, $F_{potential}$, and the vortex force, F_{vortex}, as shown in Equation 2.2. In this approach, the potential force contains the entirety of the added mass effect and is given by $F_{potential} = -C_a m_d y''$, where C_a is the ideal added mass coefficient ($C_a \approxeq 1.0$ for a circular cylinder [17]) and m_d is the mass of the displaced fluid. The vortex force consists of all shed vorticity minus the thin boundary vortex sheet to maintain slip associated with the potential flow assumption involved in this decomposition. Substituting the force decomposition, Equation 2.2, into Equation 2.1 provides the equation of motion in terms of the vortex force, see Equation 2.3, where m_a is the added mass and ϕ_{vortex} is the phase angle between the vortex induced force on the structure and the cylinder displacement.

$$my'' + cy' + ky = F_{total} sin(\omega t + \phi_{total}) \tag{2.1}$$

$$F_{total} = F_{potential} + F_{vortex} \tag{2.2}$$

$$(m + m_a)y'' + cy' + ky = F_{vortex}sin(\omega t + \phi_{vortex}) \tag{2.3}$$

High mass-damping systems exhibit a transition between the initial and lower response branches that results in a simultaneous jump in both the total phase and vortex phase [27]. In the case of low mass-damping systems, the first transition between the initial and upper branches involves an insignificant change in the total phase and a large jump in the vortex phase. This is associated with the change between 2S and 2P vortex shedding and accounts for the switch in the timing of vortex shedding. The second transition between the upper and lower branches corresponds with a large jump in the total phase and insignificant change in the vortex phase, since both branches are associated with 2P shedding. This jump in total phase is not reflective of a switch in the timing of vortex shedding.

The lock-in phenomenon is classically defined as the synchronization of the vortex formation frequency, f_v, and the structural oscillation frequency, f, with the natural frequency of the system, f_n, such that the nondimensionalized frequency, $f^* = f/f_n$, is close to unity over a range of reduced velocities [80, 81]. This scenario is valid for high mass ratio systems [11, 26]; however, significant departure from unity has been observed experimentally for low mass ratio systems [18, 28, 30, 82]. For example, Khalak and Williamson [28] observed $f^* \approx 1.4$ throughout the synchronization region for a system with $m^* = 2.4$. This result is in agreement with the discussion of Bearman [11] and the work on the added mass coefficient by Sarpkaya [83]. Therefore, lock-in cannot be defined as the region within which the shedding frequency is close to the structural natural frequency. Instead, Khalak and Williamson [18] suggest that lock-in be defined as the matching of the frequency of the periodic wake vortex mode with the structural oscillation frequency.

The structural response frequency may be derived from the fundamental equation of motion, Eq. 2.1, following the procedure of Khalak and Williamson [18],

$$f^* = \sqrt{\frac{m^* + C_a}{m^* + C_{ea}}} \tag{2.4}$$

where C_{ea} is an effective added mass coefficient that includes an apparent effect due to the total transverse fluid force in phase with the structure's acceleration. Results of Khalak and Williamson [18] show that a decrease in the mass ratio results in an increase in the frequency of structural oscillations, in agreement with Eq. 2.4. Govardhan and Williamson [27] further investigate this relationship and show that there exists a critical mass ratio, $m^*_{critical} = 0.54 \pm 0.02$, below which the response frequency and lock-in regime extend to infinity. The critical mass ratio was obtained by collapsing a large data set of lower branch frequencies, f^*_{lower}, at numerous mass ratios onto a single curve fit based on Eq. 2.4, see

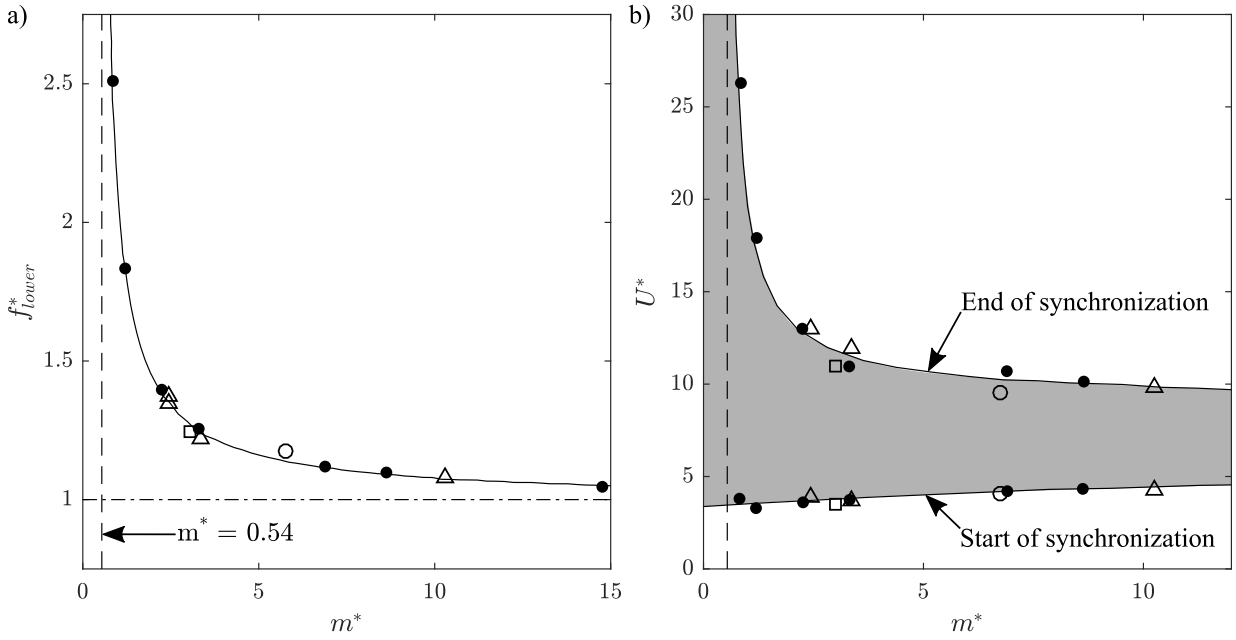

Figure 2.3: Extent of the lock-in region for 1DOF-transverse VIV [27]: (a) variation of the lower branch frequency (f^*_{lower}) as a function of the mass ratio, m^*; (b) the lock-in region extends to infinity as the mass ratio approaches the critical value of $m^*_{critical} = 0.54$. Symbols are: •, Govardhan and Williamson [27]; △, Khalak and Williamson [18]; ∘, Anand and Torum [84]; □, Hover *et al.* [78].

Fig. 2.3a:

$$f^*_{lower} = \sqrt{\frac{m^* + 1}{m^* - 0.54}} \tag{2.5}$$

The lower response branch for systems below the critical mass ratio can never be reached for finite reduced velocities and ceases to exist; hence, the upper branch continues indefinitely and the lock-in region extends to infinity. For systems above the critical mass ratio, Govardhan and Williamson [27] develop Eq. 2.6 to predict the extent of the lock-in region by collapsing data from the end of the lower branch in a manner similar to the above analysis. The expression quantifies the upper boundary of the shaded lock-in region depicted in Fig. 2.3b.

$$U^*_{end\ of\ synchronization} = 9.25\sqrt{\frac{m^* + 1}{m^* - 0.54}} \tag{2.6}$$

2.3 Two DOF uniform amplitude VIV

Although numerous papers dedicated to the transverse only VIV of a cylinder provide insight into the fluid-structure interaction, allowing the cylinder to oscillate streamwise as well as transverse to the flow offers a more realistic representation of practical engineering applications. Several investigations have examined cylinders undergoing 2DOF VIV [29–35]. This section reviews the literature pertinent to 2DOF uniform amplitude VIV and compares the findings with the 1DOF VIV studies discussed in Section 2.2.

Early investigations of 2DOF VIV, performed by Moe and Wu [30] and Sarpkaya [31], employed structures with different mass ratios in the streamwise and transverse directions, and either constant [30] or variable [31] natural frequencies. Sarpkaya [31] found that for equivalent natural frequencies in the streamwise and transverse directions, $f_{nx} = f_{ny}$, the additional degree of freedom produced a 19% increase in amplitude and a shift to higher reduced velocities for the peak transverse response, when compared to their 1DOF transverse case. Neither Moe and Wu [30] nor Sarpkaya [31] observed evidence of distinct response branches.

Jeon and Gharib [33] investigated the addition of streamwise motion by forcing a cylinder to move in the streamwise and transverse directions. The prescribed motion, Eqs. (2.7) and (2.8), was given phase angles $\psi = 0$ and $7\pi/4$ and amplitudes $A_x = 0.1D$ and $A_y = 0.5D$ to produce a figure-eight trajectory, since they suggest nature prefers this motion. Figure 2.4 depicts the possible figure-eight trajectories for various phase angles. Two cases of reduced velocity were examined, corresponding to predicted 2S and 2P vortex shedding based on the Williamson and Roshko [54] shedding map. Jeon and Gharib [33] observed that the additional streamwise motion increased phase coherence for 2S shedding and inhibited formation of the second vortex within 2P pairs. It is interesting that such small streamwise motion can significantly impact wake development. The selected phase and amplitude from the large set comprising the four parameters A_x, A_y, ψ and f_y/f_x influence the resulting conclusions since free vibration studies have observed notably different figure-eight motion at comparable conditions [34, 35].

$$x(t) = A_x sin(2\omega_n t + \psi) \tag{2.7}$$

$$y(t) = A_y sin(\omega_n t) \tag{2.8}$$

Jauvtis and Williamson [34] examined the 2DOF VIV of a cylinder with equivalent mass ratios and natural frequencies in both directions. For $m^* > 6$, the transverse response exhibited initial, upper and lower branches unlike the continuous response observed in the

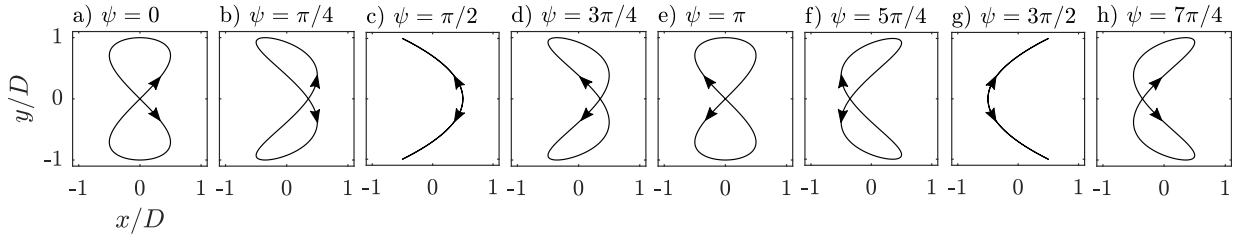

Figure 2.4: Figure-eight cylinder trajectories based on Eqs. (2.7) and (2.8) for various phase angles, ψ, and $A_y/A_x = 2$. Flow is from left to right with the motion of the cylinder in the direction as indicated.

investigations of Moe and Wu [30] and Sarpkaya [31]. A 2S, 2P and 2P vortex shedding pattern in the wake was observed for the initial, upper and lower branches, respectively. The response branches, peak amplitudes, induced forces and vortex shedding patterns are similar to those obtained for 1DOF transverse VIV. Therefore, they conclude that results from 1DOF VIV can be used to predict the structural response for systems undergoing 2DOF VIV with $m^* > 6$. A dramatic change in the fluid-structure interaction occurs for $m^* < 6$, where the additional streamwise motion significantly impacts the amplitude response in the transverse direction [34, 35]. Of the branches observed for $m^* > 6$, the upper branch is replaced by a "super-upper" branch [34], yielding large amplitudes of oscillation, $A_y^* \approx 1.5$, that are much greater than the $A_y^* \approx 1.0$ observed for 1DOF VIV [27]. Cylinder displacement in the super-upper branch is temporally stable with hysteretic switching between the super-upper and lower branches. Jauvtis and Williamson [34] propose that the massive amplitudes of vibration are attributed to the observed 2T vortex shedding pattern in the super-upper branch, where two triplets of vortices are shed each period of cylinder oscillation, see Fig. 2.2f. The initial and lower branches exhibit 2S and 2P vortex shedding patterns, respectively, similar to the 1DOF study of Govardhan and Williamson [27].

The amplitude of vibration in the streamwise and transverse directions is a function of both the damping ratio and the mass ratio [35]. Jauvtis and Williamson [34] and Blevins and Coughran [35] indicate that a lower mass ratio correlates with a wider lock-in region, in agreement with the 1DOF study of Khalak and Williamson [18]. Specifically, for $m^* = 2.6$, 5.01, and 17.1 the reduced velocities defining the lock-in region were $2.4 \leq U^* \leq 12.6$, $3.2 \leq U^* \leq 9.8$, and $4.0 \leq U^* \leq 7.9$, respectively. Srinil and Zanganeh [85] numerically modeled 2DOF VIV of a circular cylinder based on double Duffing-van der Pol oscillators with cubic nonlinearities to capture the coupling of streamwise and transverse motion. They conducted a parametric analysis, which captures the lock-in region and hysteretic branch transition for a figure-eight trajectory. The predicted amplitudes agree well with

the experimental results of Jauvtis and Williamson [34] and Blevins and Coughran [35] for various combinations of mass ratio and damping ratio.

For the frequency response in 2DOF VIV, both the reduced velocity and mass ratio affect the lock-in frequency of vortex shedding and cylinder oscillation [29, 34, 35] in a similar manner to transverse 1DOF VIV. For systems with a moderate to high mass ratio, the nondimensionalized frequency of structural oscillation, $f^* = f/f_n$, is close to unity throughout the lock-in region [35], while there is significant departure from unity for low mass ratio systems [34, 35]. Following the methodology of Govardhan and Williamson [27] for the transverse 1DOF case, Jauvtis and Williamson [34] developed Eq. 2.9 from an extensive set of experiments conducted at different mass ratios. The critical mass ratio, $m^*_{critical} = 0.52$, is similar to the 1DOF critical mass ratio, $m^*_{critical} = 0.54$. This is expected since the response in the lower branch is primarily in the transverse direction with little streamwise oscillation affecting the vortex formation [34].

$$f^*_{lower} = \sqrt{\frac{m^* + 1}{m^* - 0.52}} \tag{2.9}$$

Published investigations of a cylinder undergoing 2DOF VIV with uniform amplitude along the span indicate a structural response where the frequency of streamwise oscillations is approximately twice that of the transverse oscillations, $f_x = 2f_y$, for the range of mass ratios and reduced velocities investigated [29, 31–35]. As such, the motion of the cylinder traces a figure-eight orbit, where the direction and skew are dictated by the phase difference between the streamwise and transverse motion [34], see Fig. 2.4.

2.4 One DOF variable amplitude VIV

In addition to the freedom to move in both streamwise and transverse directions, practical engineering structures undergoing VIV often oscillate with an amplitude that varies along the span [36, 41]. A flexible cantilever or flexible cable offers the best approximation since their design can incorporate structural properties that represent a scaled version of a specific structure. The pivoted cylinder is a simplification of the flexible structure and represents a body having a linear variation of amplitude along its span. Its local flow features are expected to be generic to other cases of spanwise amplitude variation without being system specific. The present study focuses on the VIV of a pivoted cylinder. As with the uniform amplitude case, it is instructive to first discuss the experimental [36, 37, 77, 86] and analytical [75] studies investigating the 1DOF VIV of a cylinder with variable amplitude along its span.

In the case of a flexible cylinder [36, 75, 86], there are two response branches, initial and lower, with a hysteretic jump from one to the other. There is no discontinuity in the initial branch to provide evidence of the third upper branch, unlike the three branches for uniform spanwise amplitude VIV for comparable mass and damping. Flow visualizations performed by Brika and Laneville [36] have shown that, 2S and 2P vortex shedding occur in the initial and lower branches, respectively, coinciding with the suggested map of Williamson and Roshko [54]. Fujarra *et al.* [86] hypothesize that the 2S and 2P shedding modes may exist simultaneously along the span. Splitting of the vortex tubes would occur in a manner similar to the hybrid mode found by Techet *et al.* [87] for an oscillating tapered cylinder. Within the lock-in region, the frequency response of cylinder oscillation and vortex shedding is greater than the natural frequency of the structure [36, 86], which is characteristic of the low mass ratio systems undergoing uniform amplitude VIV [18, 28, 82]. Outside of synchronization, the cylinder oscillation and vortex shedding frequency match the Strouhal frequency of a stationary cylinder.

Compared to the flexible case, the response characteristics of a pivoted cylinder are similar [37, 77]. Specifically, initial and lower response branches for the low mass ratio structure examined by Voorhees *et al.* [77] are observed within the reduced velocity ranges $3.8 \leq U^* \leq 7.0$ and $7.0 \leq U^* \leq 9.2$, respectively. The frequency response is similar to systems undergoing uniform amplitude VIV [18, 28, 82], where the cylinder oscillation and vortex shedding lock onto a frequency slightly above the natural frequency in the lower response branch. Voorhees *et al.* [77] made an interesting observation of axial flows oriented towards the free surface and in excess of 25% of the free stream velocity. They attribute this flow to the effect of linearly increasing oscillation amplitude along the cylinder span and argue that increased vortex strength and increased amplitude create an axial pressure gradient that pumps fluid towards the surface. In combination with the free surface and pivoted structure, the axial flow results in a three dimensional curvature of the vortices.

2.5 Two DOF variable amplitude VIV

Permitting the cylinder to oscillate streamwise as well as transverse to the flow offers a more realistic representation of practical engineering applications. Numerous investigations have examined flexible cantilevers, [38–40], flexible cables [41–44], and pivoted cylinders [45–50] undergoing 2DOF VIV. This section reviews literature concerning the VIV of cylinders with 2DOF and variable amplitude along their span, and emphasizes the findings for pivoted cylinders, since this structure is the focus of the present study.

2.5.1 Amplitude Response

Flemming and Williamson [47] studied a pivoted cylinder mounted as a pendulum, set up such that its moment of inertia ratio, I^*, and mass ratio, m^*, were equivalent. Their results indicate that the amplitude response depends on the mass ratio in a similar manner to that of uniform amplitude studies, where the size of the lock-in region decreases with increasing mass ratio. Specifically, lock-in exists within the reduced velocity ranges $2.5 \leq U^* \leq 19.7$, $3.4 \leq U^* \leq 14.1$, and $3.8 \leq U^* \leq 11.5$ for mass ratios $m^* = 1.03$, 2.68, and 7.69, respectively. A comparison with the results of Kheirkhah *et al.* [45] and Marble *et al.* [50] confirms the mass ratio has a similar effect on lock-in range for a pivoted cylinder mounted as an inverted pendulum. It should be noted that Flemming and Williamson [47] varied the reduced velocity by adjusting the free stream velocity, whereas Kheirkhah *et al.* [45] and Marble *et al.* [50] did so by adjusting the natural frequency of the structure, while maintaining a constant Reynolds number. If the cylinder is instead mounted as a flexible cantilever or flexible cable, the lock-in region becomes notably smaller at comparable structural parameters. Oviedo-Tolentino *et al.* [40] show that for a mass ratio of $m^* = 8.13$, the lock-in region of a flexible cantilever occurs within $4.1 \leq U^* \leq 8.5$. Similarly, the results of Huera-Huarte and Bearman [41], who studied a flexible cable with a mass ratio of $m^* = 1.8$ at various tensions, show that the size of the lock-in region is approximately half that for a pivoted cylinder at a comparable mass ratio [47].

The response branches observed for pivoted cylinders are analogous to 1DOF and 2DOF uniform amplitude studies. For a moderate mass ratio, the structural response exhibits initial and lower branches [45, 47, 50]; however, it is unknown whether the transition is hysteretic or intermittent. The low mass ratio system examined by Flemming and Williamson [47] features an additional upper branch with hysteretic transition between the initial and upper branches and intermittent switching between the upper and lower branches. Amplitudes of these branches are similar to that for 2DOF uniform amplitude VIV studied by Jauvtis and Williamson [34]. For flexible cylinders, the relatively smooth amplitude response exhibits initial, upper and lower branches for both low and moderate mass ratio systems [40, 41].

Following the critical mass ratio analysis of 1DOF VIV in the transverse direction found in Govardhan and Williamson [27], Flemming and Williamson [47] experimentally predicted there exists a critical inertia ratio of $I^*_{critical} = m^*_{critical} \approx 0.5$, below which the structural response exhibits an infinitely wide lock-in region. Their analysis indicates that for any positive $I^* < I^*_{critical}$, both the transverse and streamwise motion will persist to infinite reduced velocity. Leong and Wei [46] confirm that for a mass ratio of $m^* = 0.45$, the lower branch ceases to exist and the upper branch extends well beyond the maximum reduced velocity tested. As a result of the lower mass-damping ratio, the maximum amplitude

in the transverse direction, $A_y^* \approxeq 2.0$, is slightly larger than the $A_y^* \approxeq 1.5$ observed by Flemming and Williamson [47], while the maximum streamwise response, $A_x^* \approxeq 2.5$, is much greater than the $A_x^* \approxeq 0.4$.

2.5.2 Frequency Response

Regarding the frequency response, the effect of reduced velocity and mass ratio on the lock-in frequency is largely similar to 1DOF and 2DOF VIV with uniform amplitude. At reduced velocities below the lock-in region, the frequency of structural oscillation locks onto the vortex shedding frequency of a stationary cylinder. Within the lock-in region, both pivoted and flexible systems with a moderate to high mass ratio [40, 45, 50] exhibit a nondimensionalized frequency, $f^* = f/f_n$, that is close to unity. Whereas, that of pivoted systems with a low mass ratio is greater and departs from unity [46, 47]. Flemming and Williamson [47] show this departure increases with increasing reduced velocity, unlike the constant lock-in frequency observed by Jauvtis and Williamson [34] for 2DOF uniform amplitude VIV.

Two types of trajectories have been observed for VIV of cylinders with spanwise amplitude variation: figure-eight [46–48] and elliptic [40, 45, 49], both of which have been reported to occur naturally [51–53, 88]. The figure-eight response is the same as that observed in VIV of cylinders with uniform spanwise amplitude [29, 34, 35] and is described by the frequency of streamwise oscillations being twice that of the transverse oscillations ($f_x = 2f_y$). The figure-eight trajectory, based on Eqs. (2.7) and (2.8), is shown in Fig. 2.4 for various phase angles. The elliptic trajectory is distinguished by a frequency response that is equal in the streamwise and transverse directions ($f_x = f_y$). Figure 2.5 depicts the trajectory, based on Eqs. (2.10) and (2.11), for various phase angles.

$$x(t) = A_x sin(\omega_n t + \psi) \tag{2.10}$$

$$y(t) = A_y sin(\omega_n t) \tag{2.11}$$

Kheirkhah *et al.* [45] argue that the structural coupling between streamwise and transverse motion governs the occurrence of either figure-eight or elliptic trajectories. Their investigation extends a simplified mathematical model based on the conservation of angu-

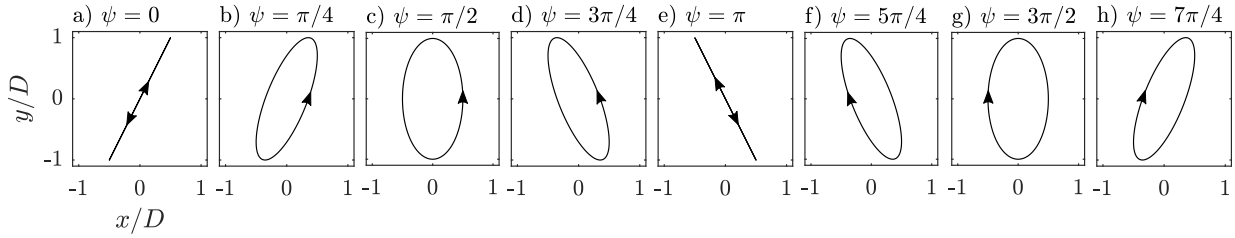

Figure 2.5: Elliptical cylinder trajectories based on Eqs. (2.10) and (2.11) for various phase angles, ψ, and $A_y/A_x = 2$. Flow is from left to right with the motion of the cylinder in the direction as indicated.

lar momentum, proposed by Flemming and Williamson [47], to incorporate the coupling:

$$I\frac{d^2}{dt^2}\left(\frac{x}{L}\right) + cb^2\frac{d}{dt}\left(\frac{x}{L}\right) + (k_e b^2 - mg(L/2) + m_d b^2(L_0/2))\left(\frac{x}{L}\right) + k_c b^2\left(\frac{y}{L}\right) = M_x(t) \tag{2.12}$$

$$I\frac{d^2}{dt^2}\left(\frac{y}{L}\right) + cb^2\frac{d}{dt}\left(\frac{y}{L}\right) + (k_e b^2 - mg(L/2) + m_d b^2(L_0/2))\left(\frac{y}{L}\right) + k_c b^2\left(\frac{x}{L}\right) = M_y(t) \tag{2.13}$$

The origin of the coordinate system for this model is located at the top of the pivoted cylinder when at rest. The left hand side of Eqs. (2.12) and (2.13) considers (i) inertial, (ii) damping, (iii) restoring (spring, gravity, and buoyancy), and (iv) cross-stiffness structural moments. The aerodynamic forces are neglected because they are much smaller than the hydrodynamic forces for a substantial water depth, L_0. Equivalent in both streamwise, x, and transverse, y, directions, the structural stiffness is modeled using linear springs with an effective stiffness of k_e and structural damping is modeled using linear viscous dampers with a damping coefficient of c. The springs and dampers are located at $z = L - b$, where L is the cylinder length and b is the vertical distance from the water tunnel floor to the springs. Following the methodology of Wardlaw *et al.* [89], system coupling is modeled using a cross stiffness term, k_c. Kheirkhah *et al.* [45] and Flemming and Williamson [47] decompose the fluid moment exerted on the structure ($M_x(t)$ and $M_y(t)$) into the total instantaneous fluid forcing moment and the fluid inertia moment:

$$M_x(t) = \int_{L-L_0}^{L} F_x(z,t)(L-z)dz - I_A\frac{d^2(x/L)}{dt^2} \tag{2.14}$$

$$M_y(t) = \int_{L-L_0}^{L} F_y(z,t)(L-z)dz - I_A\frac{d^2(y/L)}{dt^2} \tag{2.15}$$

where I_A is the added moment of inertia. The terms $F_x(z,t)$ and $F_y(z,t)$, defined in Eqs. (2.16) and (2.17), respectively, are the instantaneous local forces per unit length the fluid exerts on the structure, where the force coefficients are $C_x(z) = C_D(L-z)/L_0$ and $C_y(z) = C_L(L-z)/L_0$.

$$F_x(z,t) = 0.5\rho U_0^2 D C_x(z) sin(2\omega_n t + \psi_{force}) \tag{2.16}$$
$$F_y(z,t) = 0.5\rho U_0^2 D C_y(z) sin(2\omega_n t) \tag{2.17}$$

The non-dimensionalized form of Eqs. (2.12) and (2.13) is:

$$\frac{d^2}{dt^{*2}}\left(\frac{x}{D}\right) + 4\pi\zeta f_r \frac{d}{dt^*}\left(\frac{x}{D}\right) + 4\pi^2\left(\frac{x}{D}\right) + 4\pi^2 U_r\left(\frac{y}{D}\right) = C_D \frac{2L}{\pi L_0}\frac{U^{*2}}{I^* + C_A} sin(4\pi t^* + \psi_{force}) \tag{2.18}$$

$$\frac{d^2}{dt^{*2}}\left(\frac{y}{D}\right) + 4\pi\zeta f_r \frac{d}{dt^*}\left(\frac{y}{D}\right) + 4\pi^2\left(\frac{y}{D}\right) + 4\pi^2 U_r\left(\frac{x}{D}\right) = C_L \frac{2L}{\pi L_0}\frac{U^{*2}}{I^* + C_A} sin(2\pi t^*) \tag{2.19}$$

where C_A is the added mass coefficient, $t^* = t f_n$ is the non-dimensionalized time, and f_n, f_r, and U_r, are given in Eqs. (2.20)–(2.22), respectively.

$$f_n = \frac{1}{2\pi}\sqrt{\frac{k_e b^2 - mgL/2 + m_d g L_0/2}{I + I_A}} \tag{2.20}$$

$$f_r = \frac{f_a}{f_n}\frac{I^*}{I^* + C_A} \tag{2.21}$$

$$U_r = \left(\frac{U^*}{U_c^*}\right)^2 \frac{I^*}{I^* + C_A};\ U_c^* = \frac{U}{f_c D} \tag{2.22}$$

For systems with very low damping, $\zeta \ll 1$, and a coupling frequency that is less than the structure's natural frequency, $f_c/f_n < 1$, the steady state solution of Eqs. (2.18) and (2.19) is given by Eqs. (2.23) and (2.24), respectively, with a detailed solution discussed

by Kheirkhah [90]:

$$\frac{x_{SS}(t^*)}{D} = \frac{B_1}{U_r}\left[d_3 sin(4\pi t^*) + d_4 cos(4\pi t^*)\right] + B_2\left(\frac{U^*}{U_c^*}\right)^2 sin(2\pi t^*) \tag{2.23}$$

$$\frac{y_{SS}(t^*)}{D} = B_1\left[d_1 sin(4\pi t^*) + d_2 cos(4\pi t^*)\right] + B_2\left(2\zeta\frac{f_a}{f_n}\right) cos(2\pi t^*) \tag{2.24}$$

where the constants $B_1,\ B_2,\ d_1,\ d_2,\ d_3$, and d_4 are provided by Eqs. (2.25)–(2.30), respectively.

$$B_1 = \frac{U_r C_D (L/L_0) U^{*2}}{2\pi^3 (I^* + C_A)\left[16\zeta^2 f_r^2 + (U_r - 3)^2\right]\left[16\zeta^2 f_r^2 + (U_r + 3)^2\right]} \tag{2.25}$$

$$B_2 = \frac{C_L (L/L_0) U^{*2}}{2\pi^3 (I^* + C_A)\left[4\zeta^2 (f_c/f_a)^2 + (U^*/U_c^*)^4\right]} \tag{2.26}$$

$$d_1 = (U_r^2 - 9 + 16\zeta^2 f_r^2) cos(\psi_{force}) + 24\zeta f_r sin(\psi_{force}) \tag{2.27}$$

$$d_2 = -24\zeta f_r cos(\psi_{force}) + (U_r^2 - 9 + 16\zeta^2 f_r^2) sin(\psi_{force}) \tag{2.28}$$

$$d_3 = 4\zeta f_r\left[6U_r + 16\zeta^2 f_r^2 + (U_r - 3)^2\right] sin(\psi_{force}) + 3\left[U_r^2 - 9 - 16\zeta^2 f_r^2\right] cos(\psi_{force}) \tag{2.29}$$

$$d_4 = 3\left[U_r^2 - 9 - 16\zeta^2 f_r^2\right] sin(\psi) - 4\zeta f_r\left[6U_r + 16\zeta^2 f_r^2 + (U_r - 3)^2\right] cos(\psi_{force}) \tag{2.30}$$

Kheirkhah *et al.* [45] used this mathematical model to analyze trends in the frequency response. Specifically they determined the dominant frequency of streamwise and transverse vibrations by calculating the ratio of the respective amplitude associated with f_n to that associated with $2f_n$. These ratios, R_x and R_y, are given in Eqs. (2.31) and (2.32), respectively.

$$R_x = \frac{B_2}{B_1}\frac{(U^*/U_c^*)^2}{\sqrt{d_3^2 + d_4^2}} U_r \tag{2.31}$$

$$R_y = \frac{B_2}{B_1}\frac{2\zeta(f_a/f_n)}{\sqrt{d_1^2 + d_2^2}} \tag{2.32}$$

Through means of a parametric analysis, bounded by feasibility in practical applications, Kheirkhah *et al.* [45] determined that R_x and R_y depend primarily on U_c^* and ζ within the lock-in region. Figure 2.6 depicts the contours of R_x and R_y computed from Eqs. (2.31) and (2.32), respectively, using the experimental parameters at $U^* = 6.5$ in the

investigation of Kheirkhah *et al.* [45]. There are two distinct regions in the streamwise amplitude ratio, (1) $R_x > 1$ and (2) $R_x < 1$, for which the transverse ratio $R_y > 1$. The model predicts that structures with strong structural coupling, *i.e.*, lower U_c^*, will occur within the first region and will exhibit an elliptic trajectory where streamwise vibrations lock onto the natural frequency of the structure, $f_x = f_n$. On the other hand, weakly coupled structures, *i.e.*, high U_c^*, are predicted to exhibit a response in the second region where streamwise vibrations occur at $f_x = 2f_n$, thus producing a figure-eight trajectory. Kheirkhah [90] experimentally verified the predicted response in both regions, where the dashed box in Fig. 2.6 indicates the region of observed elliptic trajectory response. Furthermore, Leong and Wei [46] and Flemming and Williamson [47] reported figure-eight trajectories in their VIV studies. Their systems were weakly coupled, *i.e.*massive coupling frequency based reduced velocity, $U_c^* \to \infty$, since the cylinder was mounted as a pendulum from a flexible pin. As such, their observations agree well with the model prediction.

There exist four distinct types of elliptical trajectories, depicted in Figs. 2.5b, 2.5d, 2.5f, and 2.5h, where the general direction and tilt of the orbit correspond to a range of phase angles, ψ, between the streamwise and transverse vibrations. Kheirkhah *et al.* [45] show that the type of elliptic trajectory is governed by the structural coupling, with approximate ranges of the coupling frequency based reduced velocity, U_c^*, corresponding to each of the identified trajectory types. Specifically the ranges $U_c^* < 18.0$, $18.0 < U_c^* < 26.0$, $26.0 < U_c^* < 35.7$, and $35.7 < U_c^*$ correspond to the phase angle ranges $0 < \psi < \pi/2$, $\pi < \psi < 3\pi/2$, $\pi/2 < \psi < \pi$, and $3\pi/2 < \psi < 2\pi$, respectively.

2.5.3 Vortex Shedding

Similar to the study of the elastically mounted cylinder by Jauvtis and Williamson [34], Flemming and Williamson [47] observe shedding regimes of a pivoted cylinder undergoing VIV with small streamwise motion generally agree with the Williamson and Roshko [54] shedding map. However, low mass ratio systems require the streamwise amplitude as a third dimension on the shedding map to distinguish response branches. The large transverse and streamwise motion of the upper branch indicates existence in quite a different parameter space, where 2C vortex shedding is observed and is characterized by two pairs of co-rotating vortices shed each period of oscillation, see Fig. 2.2e. The effect of large amplitude of oscillation on the predicted shedding regime is further exemplified by the study of Leong and Wei [46], who used flow visualization to study the wake of a cylinder below critical mass ratio. They observed P+S shedding in the upper branch around the maximum amplitude response, which is uncharacteristic of the Morse and Williamson [1] map. However, unlike Flemming and Williamson [47], Leong and Wei [46] did not confirm

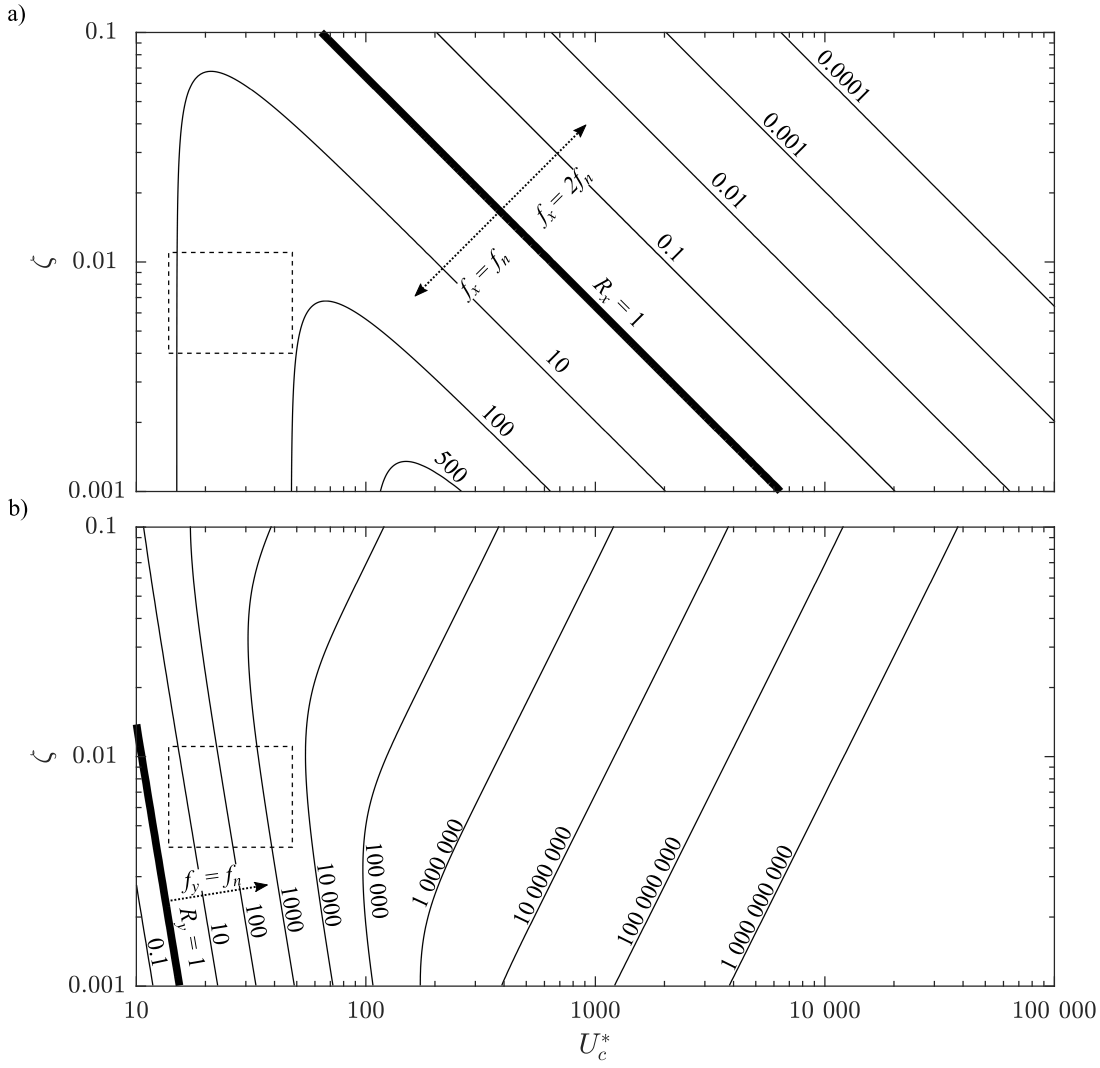

Figure 2.6: Contours of (a) R_x and (b) R_y computed from Eqs. (2.31) and (2.32), respectively, for the parameters at $U^* = 6.5$ in the investigation of Kheirkhah *et al.* [45]. The dashed box indicates the experimental conditions for their study of a cylinder undergoing VIV with elliptic trajectories.

existence of the 2C shedding mode. This may be due to the location of their measurement plane since spanwise variation of oscillation amplitude can cause multiple shedding regimes to coexist along the cylinder span, resulting in a more complex and hybrid type response.

Hybrid shedding features vortex dislocations at the boundaries between different shedding modes, where the vortices split into two parts [13, 60, 72]. Flemming and Williamson [47], Kheirkhah *et al.* [49], and Techet *et al.* [87] examined hybrid vortex shedding in the wake of a cylinder. Techet *et al.* [87] used lead precipitation and PIV techniques to examine the flow past a linearly tapered cylinder forced to oscillate in the transverse direction at various selected amplitudes and Reynolds numbers Re = 400, 800, and 1500. Flemming and Williamson [47] and Kheirkhah *et al.* [49] used PIV and planar laser induced fluorescence, respectively, to investigate changes in shedding regimes from the base to the tip of a pivoted cylinder. Figure 2.7 depicts the results of the aforementioned investigations overlaid on the Morse and Williamson [1] vortex shedding map. Each pair of data points connected by a dashed line corresponds to one tested experimental condition, where the data points mark the extremes of the spanwise survey. The map predicts that, for the results of a tapered cylinder at $Re = 800$ [87], changes in the local response will result in a transition between 2S and 2P vortex shedding patterns with an intermediary $2P_0$ pattern. This prediction agrees well with the flow visualizations for the two lower amplitude cases, while the case with the largest amplitude was found to exhibit 2P shedding along the entire cylinder span. Predicted vortex shedding based on results for the pivoted cylinder study by Flemming and Williamson [47] agrees well with the observed wake topology for $U^* = 3.99$, 5.67, and 8.30. However, in contrast to the map's predictions at $U^* = 6.15$ in the upper response branch, Flemming and Williamson [47] observe a transition from 2C to 2S along the cylinder span.

For a pivoted cylinder with a moderate mass ratio, Kheirkhah *et al.* [49] qualitatively investigated vortex shedding near the boundary between 2P and non-synchronized regimes. Specifically, Kheirkhah *et al.* [49] investigated the wake topology at two different planes along the span for two of the four distinct types of elliptical trajectories identified by Kheirkhah *et al.* [45]. The direction of cylinder motion in both cases is CW, while the phase angle between the streamwise and transverse motion for the first and second cases is $\psi \approx 135°$ and 17°, respectively. For both cases, they observed the formation of 2S and 2P vortices at the planes closest to and furthest from the pivot point, respectively. However, in the first case, adjacent 2P vortices of the positive sign merged within four diameters of the cylinder, thus forming a P+S pattern in the wake. Compared to the predicted hybrid modes in Fig. 2.7, the flow visualizations of Kheirkhah *et al.* [49] indicate that wake topologies for 2DOF VIV with spanwise variation of amplitude can deviate significantly from those predicted by the Williamson and Roshko [54] or Morse and Williamson [1]

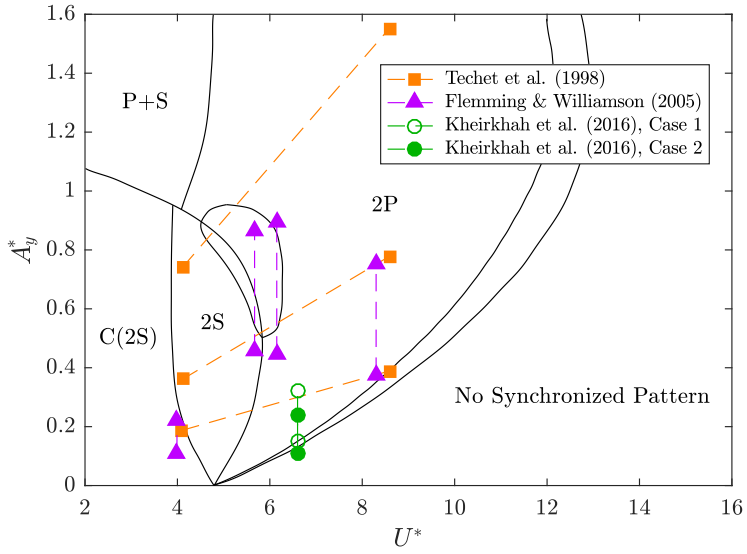

Figure 2.7: Structural response results of hybrid wake investigations overlaid on the Morse and Williamson [1] vortex shedding map.

shedding maps.

Cagney and Balabani [48] studied the effect of transverse motion by comparing wake dynamics and structural response for 2DOF VIV of a pivoted cylinder with those from their streamwise 1DOF VIV study [91]. Both studies exhibit a response containing two branches that are separated by a region of low amplitude response. They show that vortex shedding can switch intermittently between symmetric and alternate shedding modes for both 1DOF and 2DOF VIV; however, the switching does not cause any change in the streamwise or transverse amplitude of oscillation. This can be explained if the wake is three-dimensional, since the wake shedding modes may destructively interfere and cause a reduction in the fluid forcing and amplitude of oscillation [92]. They also argue that the additional degree of freedom affects the overall fluid-structure dynamics and simplifies the system by reducing the possible states the cylinder can occupy and thereby the possible shedding modes.

Chapter 3

Experimental Methodology

In this study, the flow around a cylinder with linear variation in amplitude is examined experimentally, with a focus on the influence of cylinder trajectory on wake development and the associated vortex dynamics. Experiments were conducted in the recirculating water tunnel facility at the University of Calgary [93–96]. The model was adapted from a system previously examined experimentally by Kheirkhah *et al.* [45, 49, 97]. The mathematical model by Kheirkhah *et al.* [45] was used to select the mass, moment of inertia and aspect ratios in order to obtain significant VIV response within the facility's operating conditions. Based on these criteria, the diameter based Reynolds number for the majority of the investigation was $Re_D = 3027$. Experimental techniques used in the analysis include laser based displacement sensors and time-resolved two-component PIV measurements to provide the means for a comprehensive description of the structural response and flow development.

This chapter describes the experimental setup of the model in the tunnel, measurement techniques, and methods for data analysis. Details for the equipment calibration and uncertainty calculations mentioned in this chapter are included in Appendices A and B, respectively.

3.1 Experimental Setup

3.1.1 Water Tunnel

Experiments were conducted in the free-surface closed-loop water tunnel facility, shown in Fig. 3.1, at the University of Calgary. Water is pumped into the main plenum and through a

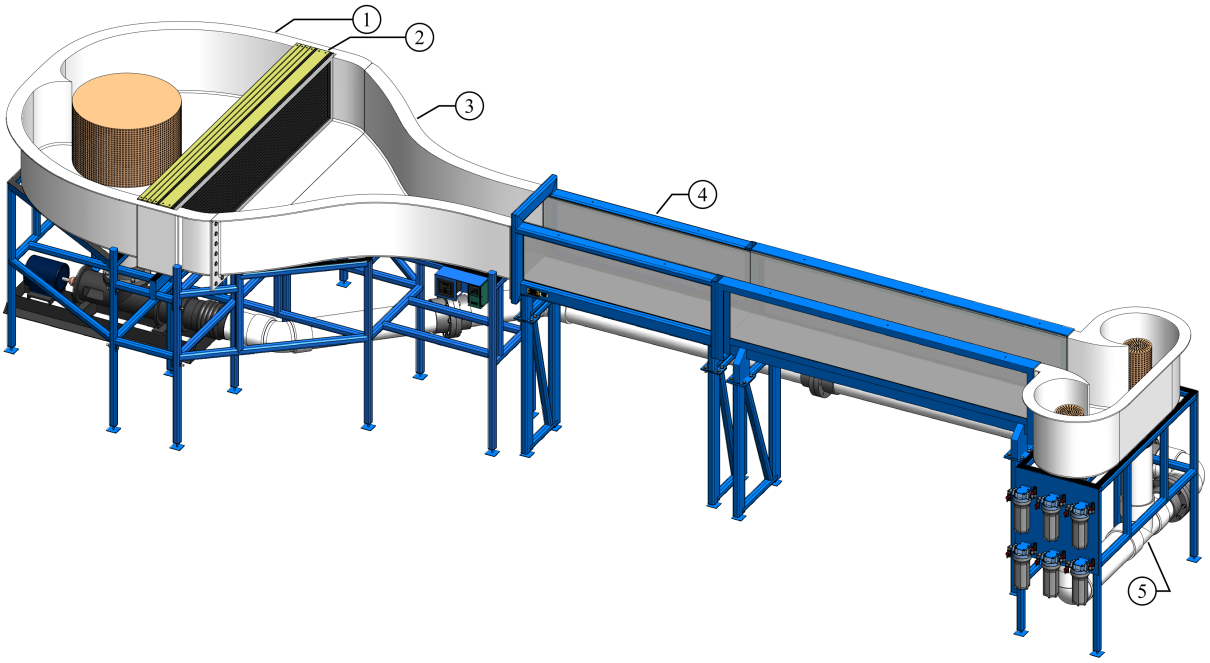

Figure 3.1: University of Calgary closed-loop water tunnel facility. ① Settling chamber; ② flow conditioning; ③ contraction; ④ test section; ⑤ recirculation.

series of flow conditioning elements to improve uniformity and reduce turbulence intensity. The conditioning unit consists of one honeycomb flow straightener and three fine screens. A contraction with a six-to-one ratio accelerates the flow into the first of two test sections. The reservoir at the end of the second test section facilitates water recirculation back to the plenum through an axial pump controlled with a variable frequency drive. Both the walls and the floor of the test sections are made of glass for optical access. The test sections have a total length of 4 m with a cross-section that is approximately 450 mm in height and 385 mm in width. Experiments were conducted in the first test section with the water level maintained at 430 mm, resulting in a uniform free stream velocity of 0.161 m/s and turbulence intensity less than 1.5% of the free stream velocity.

3.1.2 Cylinder Model

Experiments were performed using a vertically mounted pivoted cylinder model with a tapered base to reduce friction at the pivot point. A diagram of the model within the test section is provided in Fig. 3.2, where the origin of the coordinate system is located

at the base of the cylinder. The x, y, and z-coordinates are in the streamwise, transverse, and spanwise directions, respectively. The cylinder has a diameter $D = 19.4$mm, length $L = 1250$mm, mass ratio $m^* = 10.8$, and a moment of inertia ratio about the pivot point, I^*, varying from 87.0 to 109.5.

The model was supported by four springs with stiffness, k, of 24.5 N/m mounted as pairs in the streamwise and transverse directions (Fig. 3.2). The springs were attached to a mounting frame and a collar around the cylinder. Adjusting the position of the springs along the vertical axis varied the natural frequency, f_n, of the structure, as determined from spectral analysis of free vibration tests in quiescent water. This provided a range of reduced velocities (listed in Table 3.1) while maintaining a constant diameter based Reynolds number, Re. Table 3.1 summarizes essential experimental conditions for both campaigns. The first campaign examines the wake in a single plane for a wide range of reduced velocities, while the second campaign focuses on reconstructing the wake for two specific reduced velocities.

Free vibration tests in air were used to determine the structural characteristics of the

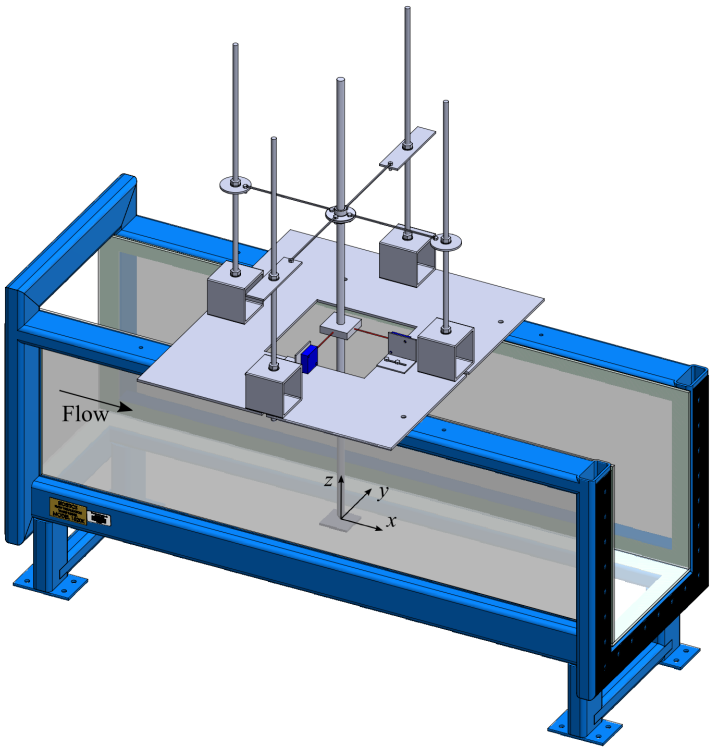

Figure 3.2: Experimental model setup in the first test section of the water tunnel facility.

Table 3.1: Experimental Conditions

Campaign	Re	m^*	f_n	U^*	I^*	ζ ($\times 10^{-3}$)
1	3027	10.8	0.96 - 1.89	4.38 - 8.67	87.0 - 115.5	1.6 - 2.9
2	3027	10.8	1.17 & 1.51	5.48 & 7.08	91.2 & 100.4	3.4 & 4.1

system. Figures 3.3a and 3.3b depict the streamwise and transverse response of the cylinder tip, respectively, when released from rest at $(y/D, x/D) = (1, 0)$. The observed motion is oscillatory with decaying amplitude. Time is normalized ($t^* = tf_a$) with respect to the natural frequency of the structure in air, f_a, which was obtained from spectral analysis of the measured oscillations and is equivalent in both the streamwise and transverse directions for all cases examined. The presence of streamwise oscillation indicates structural coupling is present since the system was initially excited in the transverse direction. This coupling is periodic with a frequency, f_c, that pertains to the time between the nodes in the streamwise component of oscillation ($t^* = 0,\ t^* \approx 140,$ and $t^* \approx 280$ in Fig. 3.3a). Damping is assessed with the assumption of logarithmic decay for the underdamped system. The damping coefficient, ζ, is calculated by computing the mean of the first ten coefficients, as outlined in Eq. 3.1, where κ is the logarithmic decrement.

$$\zeta_i = \frac{\kappa_i}{2\pi}$$

$$\kappa_i = ln\frac{y(t^* = i-1)}{y(t^* = i)}$$

$$\zeta = \sum_{i=1}^{N=10} \frac{1}{2\pi} ln\left[\frac{y(t^* = i-1)}{D} \Big/ \frac{y(t^* = i)}{D}\right] \Big/ N \tag{3.1}$$

3.2 Measurement Techniques

3.2.1 Cylinder Displacement

Streamwise and transverse cylinder position were measured using two Hoskin CP24MHT80 laser-based displacement sensors secured to the mounting frame. The sensors have a measuring range of 120 mm, equivalent to ± 6.19 cylinder diameters, and a resolution of 20 µm. The calibration of the sensor was verified using a Velmex BiSlide traverse, with details of

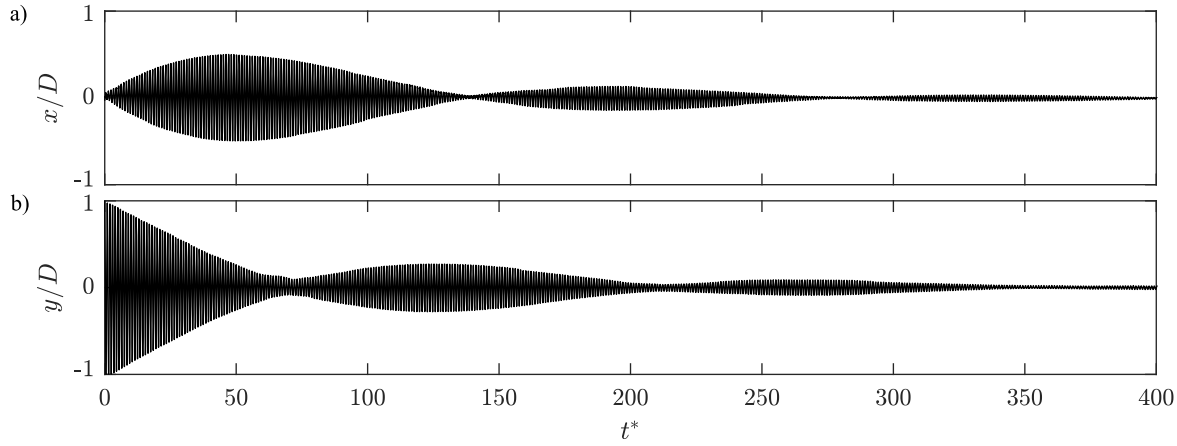

Figure 3.3: Structural response in the (a) streamwise (b) transverse directions for free vibrations in quiescent air with respect to the normalized time, tf_n.

the verification outlined in Appendix A. Uncertainty associated with model displacement measurements is estimated to be within $\pm 0.026D$ and $\pm 0.004D$ for the streamwise and transverse directions, respectively, with details provided in Appendix B.

In the first campaign, the analog signals from the displacement sensors were acquired using a SainSmart Mega 2560 arduino. The sampling was nonuniform with a mean frequency of 702 Hz. Once acquired, the data was resampled to a uniform 500 Hz and a 0.03% timing correction was applied to correct for the arduino's internal clock lag of 26 seconds over a 24 hour period. In the second campaign, the analog signals were acquired using a NI USB-6212 board at a sampling frequency of 10 000 Hz. Given the measuring rate of the displacement sensors is 1500 Hz, the oversampled data was resampled to 100 Hz to eliminate any repeated data. The final sampling frequency for both campaigns is at least 50 times greater than the largest natural frequency of the structure in the present study and is sufficient to resolve temporal variation in the cylinder displacement.

3.2.2 Particle Image Velocimetry

Two-component Time-Resolved Particle Image Velocimetry (TR-PIV) measurements were used to estimate the planar velocity in the horizontal, $x-y$, and vertical, $x-z$, planes. The system configurations for the two planes are depicted in Figs. 3.4a and 3.4b, respectively. A detailed outline of the operating principles and recommendations for performing 2D PIV measurements is given by Willert and Gharib [98], Westerweel [99], Scarano and Riethmuller [100], and Raffel *et al.* [101]. Here, the procedure and selected parameters

pertinent to the present study are discussed.

The flow was seeded with nearly neutrally buoyant hollow glass spheres with a mean diameter of 10 µm and specific gravity of approximately 1.05. A 2 mm thick planar laser sheet was produced by passing a laser source (Photonics DM30 high-repetition pulsed laser) through a series of spherical and cylindrical lenses. The laser sheet could be arranged in a vertical $(x-z)$ or horizontal $(x-y)$ configuration to illuminate the tracer particles, which approximate the fluid motion. Particle images were captured with Phantom Miro Lab 340 high speed cameras synchronized with the laser via a LaVision timing unit controlled with LaVision's DaVis 8 software. During PIV acquisition, the simultaneous measurement of the controller's Q-switch and the cylinder displacement allowed for temporal alignment of the laser displacement and PIV measurements.

For the horizontal plane configuration (Fig. 3.4a), the laser beam was conditioned into a sheet using two 90° turning mirrors and a −10 mm focal length cylindrical lens. A single high speed camera, fitted with a Nikon 35 mm fixed focal length lens, was placed beneath the tunnel on mounting rails approximately three diameters downstream of the cylinder. In the first experimental campaign, the camera's sensors were cropped to 1728 × 1080 pixels and images were acquired in single frame mode at a sampling frequency, F_s, of 125 Hz to provide a particle displacement of 12 pixels in the wake's outer flow region. In the second experimental campaign, the camera's sensors were cropped to 2048 × 1280 pixels. Images were acquired in double frame mode at a sampling frequency of 20 Hz with a selected

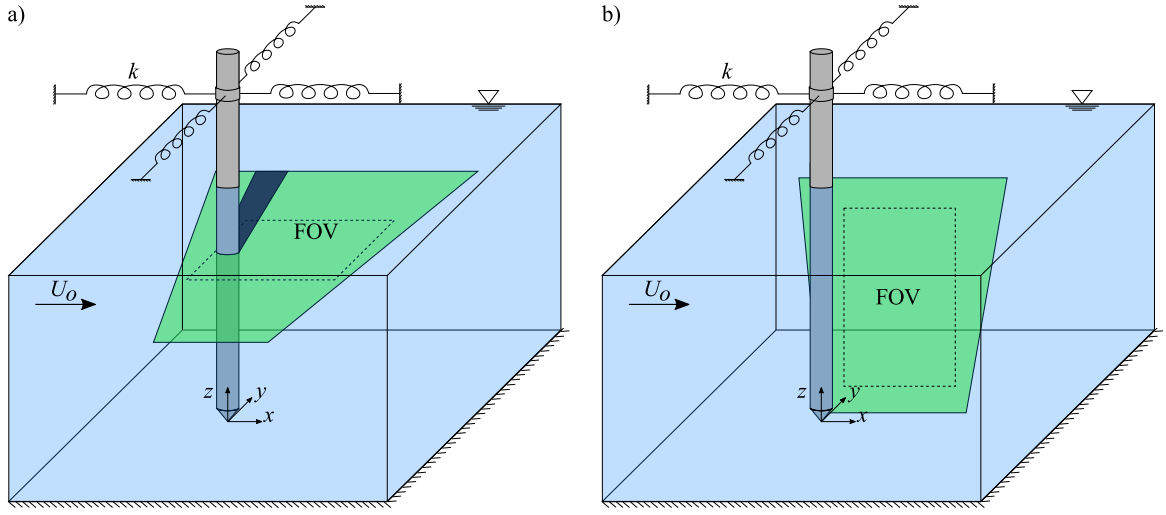

Figure 3.4: Experimental configuration for PIV measurements in the (a) $x-y$ and (b) $x-z$ planes.

frame separation time of 3000 µs to provide a particle displacement of 5 to 6 pixels in the wake's outer flow region. Double frame acquisition allows for a smaller pixel shift, reducing the chance that particles will move out of plane. Both the laser optics and camera were mounted on a Velmex BiSlide MN10 traverse, with a displacement resolution of 5 µm. The traverse is operated by a stepper motor to precisely control the vertical location of the measurement plane, with repeatability of 5.1 µm for short term usage.

For the vertical plane configuration (Fig. 3.4b), the laser beam was conditioned into a sheet using three 90° turning mirrors followed by two cylindrical lenses with focal lengths of −50 mm and −100 mm, for an effective focal length of −33 mm. The two high speed cameras, fitted with Nikon 60 mm fixed focal length lenses, were placed on mounting rails to the side of the water tunnel in spanwise succession. The full sensor resolution, 2560 × 1600 pixels, was used for both cameras and the fields of view were overlapped by approximately 10%. Images were acquired in double frame mode at a sampling rate of 20 Hz with a frame separation time of 3000 µs. The separation time was selected to provide a particle displacement of 6 pixels in the wake's outer flow region.

Particle image acquisition and processing was done with LaVision's DaVis 8 software. For both PIV configurations, the camera focus was adjusted to produce particles of approximately 3 pixels in diameter. Calibration was achieved by imaging a calibration target, consisting of 2 mm filled circular marks in a 10 × 10 mm grid, positioned in plane with the laser sheet. Third order polynomial functions were fit to the target images for the horizontal PIV planes, whereas a pinhole calibration method was applied to the vertical PIV planes. The particle images were pre-processed using a spatial sliding minimum subtraction and intensity normalization. Particle displacements were calculated using an iterative multi-grid cross-correlation algorithm with window deformation. A final interrogation window size of 24 × 24 pixels was employed with a 75% overlap, resulting in the vector pitches outlined in Table 3.2. The results were post-processed using universal outlier detection with vector removal and replacement [102]. If more than one camera was used, the mean velocity fields for each camera were cross-correlated to orient the two FOVs. The vector fields were interpolated onto a common coordinate system and stitched together using a cosine weighted blending function in the overlap region. Once the results were calculated, the random errors in the instantaneous velocity fields were evaluated using the correlation statistics method [103]. The mean uncertainty in the wake region is estimated to be less than 14.2% and 5.1% of the free stream velocity within 95% confidence for the horizontal and vertical PIV configurations, respectively. Appendix B provides detailed methodology and discussion of PIV uncertainty and Table 3.2 provides a summary of the pertinent PIV parameters.

Table 3.2: PIV acquisition parameters

	Campaign1	Campaign2		Unit
Plane	Horizontal	Horizontal	Vertical	-
Lens focal length	35	35	60	mm
Sensor resolution	1728 × 1080	2048 × 1280	2560 × 1600	px
Total field of view	$9.3D \times 5.8D$	$8.5D \times 5.3D$ to $10.5D \times 6.6D$	$6.0D \times 18.2D$	-
PIV mode	Single frame	Double frame	Double frame	-
Sample rate, F_s	125	20	20	Hz
Frame separation, Δt	-	3000	3000	µs
Outer flow displacement	12	5 to 6	6	px
Window size	24 × 24	24 × 24	24 × 24	px
	2.50 × 2.50	1.95 × 1.95 to 2.41 × 2.41	1.77 × 1.77	mm
Vector pitch	0.624	0.489 to 0.603	0.444	mm
	$0.032D$	$0.025D$ to $0.031D$	$0.023D$	-

3.3 Techniques for Data Analysis

3.3.1 Proper Orthogonal Decomposition

The velocity field for turbulent bluff body flow consists of time-averaged and time-dependent components, where the latter is a combination of quasi periodic coherent structures and incoherent turbulence. As such, the triple decomposition of the instantaneous flow field is expressed in Eq. 3.2 [104, 105]; where $\vec{U}(\vec{x})$ is the mean flow field, $\vec{u}'(\vec{x},t)$ is the component due to coherent motions, and $\vec{u}''(\vec{x},t)$ is the incoherent component.

$$\vec{u}(\vec{x},t) = \vec{U}(\vec{x}) + \vec{u}'(\vec{x},t) + \vec{u}''(\vec{x},t) \tag{3.2}$$

Lumley [106] introduced Proper Orthogonal Decomposition (POD) to the fluid mechanics community as a method of studying the coherent structures in turbulent flow. It has since been applied extensively in the analysis of bluff body flows [107–109], with methodology outlined in detail by Berkooz *et al.* [110]. In general, POD is an energy based decomposition of the velocity field, where the fluctuating field, $\vec{u}'(\vec{x},t)+\vec{u}''(\vec{x},t)$, is decomposed into a set of spatial modes, $\vec{\phi}_i$, and temporal coefficients, a_i, Eq. 3.3. The present study employs the POD snapshot method [111], which reduces the computational effort

by solving the eigenvalue problem for the velocity autocorrelation operator [112]. The obtained eigenfunctions are the spatial modes and their corresponding eigenvalues are the relative energy content of each spatial mode, λ_i. Temporal coefficients are obtained from the projection of the quasi periodic velocity field onto the i^{th} spatial mode. The obtained set of N modes is ordered according to its descending relative energy content, where the relative energy content is indicative of the planar turbulent kinetic energy since the POD is computed on the 2D velocity fluctuations.

$$\vec{u}'(\vec{x},t) + \vec{u}''(\vec{x},t) = \sum_{i=1}^{N} a_i(t)\vec{\phi}_i(\vec{x}) \tag{3.3}$$

Given a data set that is statistically large enough to distinguish coherent motions from turbulence, the quasi periodic component, $\vec{u}'(\vec{x},t)$, of the flow is approximated as the finite sum of the spatial modes multiplied with their corresponding temporal coefficients. Such a low order model can be calculated from time resolved data and is useful in resolving the coherent structures in the flow. For strongly periodic flows, the dominant structures can be approximated by the first pair of POD modes combined with the mean flow [107–109]:

$$\vec{u}_{LOM}(\vec{x},t) = \vec{U}(\vec{x}) + a_1(t)\vec{\phi_1}(\vec{x}) + a_2(t)\vec{\phi_2}(\vec{x}) \tag{3.4}$$

3.3.2 Phase Averaging

Phase averaging is a common method of investigating coherent structures whereby data is conditionally averaged based on a reference signal. This signal is selected such that its phase is representative of the dominant periodic component of the flow. In the present study, the flow periodicity is governed by vortex shedding. In doing so, the incoherent motions in phase averaged fields are eliminated. The present study employs both the first pair of POD temporal coefficients and the cylinder displacement in the transverse direction as reference signals. The former must be used for stationary cylinders and is arguably more indicative of the flow since its periodicity is associated with the advection of the dominant structures in the wake. The latter was shown to provide similar phase averaged results and is advantageous when reconstructing a 3D velocity field from multiple two-dimensional fields as it provides a common reference point between planes. To illustrate the two methods, the case of 2P shedding at $U^* = 7.08$ is considered.

As mentioned in Section 3.3.1, studies have shown that, for strongly periodic flows, the first two POD modes form a pair associated with the shedding of dominant vortical structures [107–109]. Depicted in Fig. 3.6a, this pair exhibits strong periodicity with a

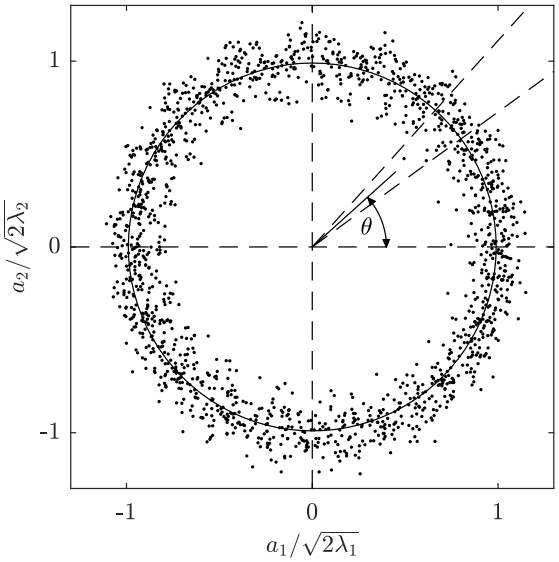

Figure 3.5: Normalized cross plot of POD temporal coefficients a_1 and a_2 computed from PIV data acquired in the horizontal, $x-y$, plane at $z/D = 12.4$ for 2P shedding at $U^* = 7.08$.

$\pi/2$ phase shift. Their normalized cross plot in Fig. 3.5 confirms the periodicity, where each data point corresponds to a single planar PIV snapshot. The phase angle of vortex shedding, θ, estimated by Eq. 3.5 and depicted in Fig. 3.6c, can be used to phase average PIV results, where instantaneous velocity fields are separated into discrete phase bins of size $\Delta\theta = \pi/15$, exaggerated by the dashed lines in Fig. 3.5. If the phase resolution of PIV data exceeds $\Delta\theta$, multiple fields may fall into a single phase angle bin for a given oscillation cycle. Thus, to ensure equal weighting between different cycles and minimize phase smearing, only a single velocity field closest to the midpoint of the bin was selected from any given cycle for phase averaging.

$$\theta = arctan\left(\sqrt{\frac{\lambda_1}{\lambda_2}}\frac{a_2}{a_1}\right) \tag{3.5}$$

The cylinder displacement in the transverse direction is depicted in Fig. 3.6b. The Hilbert transform of the signal, outlined in Eq. 3.6, is used to extract its phase, which is depicted in Fig. 3.6c. In both methods, the phase angle is shifted such that zero phase ($\theta = 0$) occurs when the cylinder crosses the transverse equilibrium ($y/D = 0$) in the positive y-direction. The resultant phases from both methods are nearly identical (Fig. 3.6c),

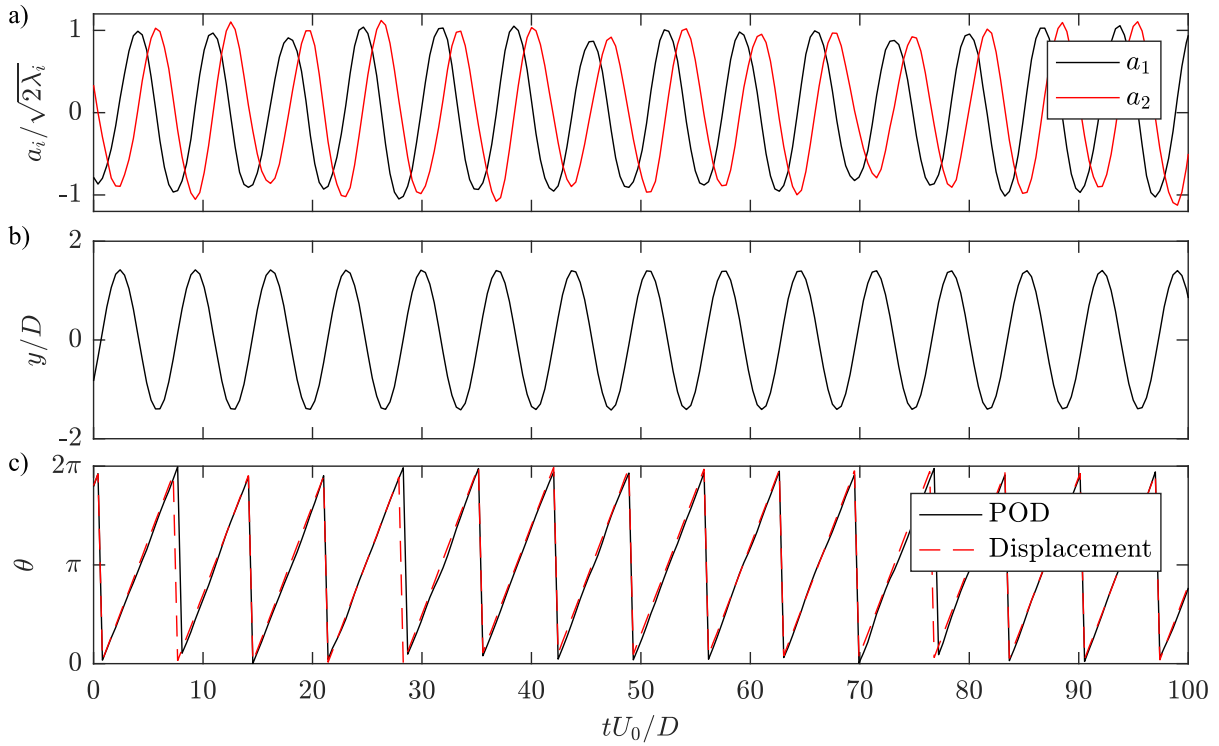

Figure 3.6: Reference signals and their computed phase; (a) POD temporal coefficients a_1 and a_2, (b) non-dimensionalized cylinder displacement in the transverse direction, and (c) computed phase of each reference signal.

indicating that phase averaging yields similar results, whether the first pair of POD temporal coefficients or cylinder displacement in the transverse direction is used as a reference signal.

$$H(t) = \frac{1}{\pi}\int_{-\infty}^{\infty}\frac{y(t)}{t-s}dt$$
$$\theta(t) = arctan\left(\frac{H_{imag}(t)}{H_{real}(t)}\right) \tag{3.6}$$

3.3.3 Statistical Vortex Identification

In the present work, vortex strengths and trajectories are characterized for different shedding regimes. Such an analysis requires vortex identification, for which numerous methods

have been developed over the last several decades. Inherently, the simplest identification methods are based on vorticity [113, 114] or streamlines [115]. However, the former approach does not allow differentiation between rotational and shear dominated regions in the flow [116], while the latter methodology is reference frame dependent [115]. This has led to several Galilean invariant Eulerian methods, none of which is universally accepted as optimal. These methods include the Δ-criterion [117], Q-criterion [118], λ_2-criterion [116] and λ_{ci}^2-criterion [119], all based on the velocity gradient tensor as well as the Γ_1 & Γ_2-criterion [120], based on the topology of the velocity field. Furthermore, Green *et al.* [121] identified Lagrangian coherent structures (LCS) from direct Lyapunov exponents (DLE) to improve upon the disadvantages of Eulerian methods, specifically the subjectivity involved with vortex boundary thresholding and the time-dependent rotation variance.

The present study employs the Q-criterion due to its relatively easy implementation and widespread use in vortex dominated flows [65, 118, 119]. Phase-averaged contours of positive Q-criterion and the corresponding vorticity contours are shown in Figs. 3.7a and 3.7b, respectively. It can be seen that a 2S shedding pattern is produced in the wake for this case, with general vortex identification being rather straightforward for Figs. 3.7a and 3.7b. However, as typical for turbulent wake flows, robust identification of vortex boundaries and vortex cores is not trivial due to the presence of smaller scale structures. In the present study, this is accomplished using a statistical method based on the distribution of Q-criterion. The utilization of such a statistical approach improves consistency and reduces subjectivity associated with defining vortex boundaries, especially in the near wake. Regions identified as vortex cores are grouped by fitting a Gaussian mixture model (GMM) to the Q-criterion using an iterative expectation-maximization algorithm (EM). This probabilistic model is often used in machine learning to cluster subpopulations within an overall population [122, 123].

In terms of the present study, a subpopulation is a region of positive Q-criterion, which corresponds to a single vortex. The overall GMM probability distribution, $p(\vec{x})$, of the Q-criterion in the wake is the weighted sum of each subpopulation probability distribution, Eq. 3.7: where $\vec{\mu}_i$, Σ_i, and π_i are the mean, covariance, and weight of each subpopulation, respectively. The multi-dimensional probability distribution for each subpopulation

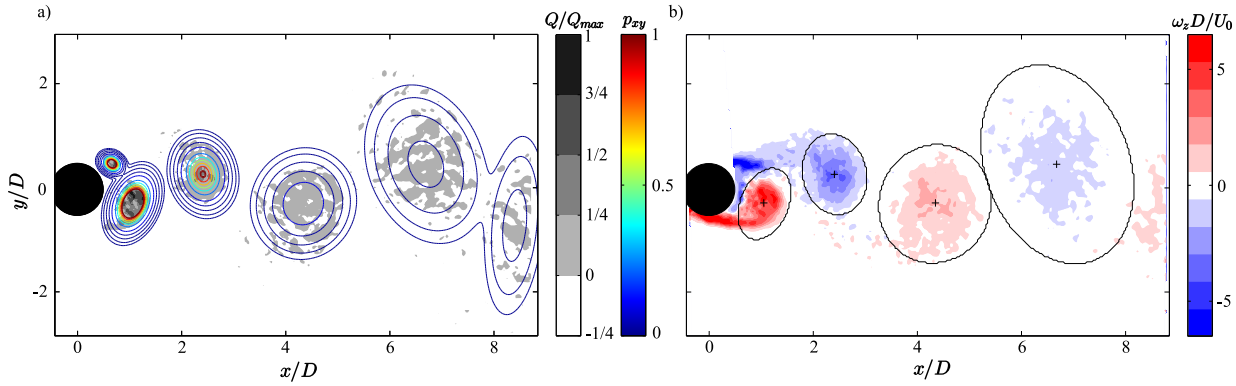

Figure 3.7: 2S vortex shedding at $U^* = 5.28$ with contours of (a) the GMM based probability distribution, $p_{\vec{x}}$, overlaid on the Q-criterion, greyscale colourbar indicates the fraction of global maximum, Q/Q_{max}, and (b) the non-dimensionalized phase-averaged vorticity field with vortex centroids and boundaries indicated by plus symbols and surrounding ellipses. Note, flow is from left to right and the cylinder is represented by the black circle at $(x/D, y/D) \approx (0, 0)$.

is calculated using Eq. 3.8 with the cumulative subpopulation weight being unity (Eq. 3.9).

$$p(\vec{x}) = \sum_{i=1}^{K} \pi_i \mathcal{N}(\vec{x} \mid \vec{\mu}_i, \Sigma_i) \tag{3.7}$$

$$\mathcal{N}(\vec{x} \mid \vec{\mu}_i, \Sigma_i) = \frac{1}{\sqrt{(2\pi)^K |\Sigma_i|}} \exp\left(-\frac{1}{2}(\vec{x} - \vec{\mu}_i)^{\mathrm{T}} {\Sigma_i}^{-1} (\vec{x} - \vec{\mu}_i)\right) \tag{3.8}$$

$$\sum_{i=1}^{K} \pi_i = 1 \tag{3.9}$$

The EM algorithm is an iterative numerical technique for maximizing the likelihood that the GMM represents the subpopulations. It is initialized by estimating the mean and covariance for each of the K-specified subpopulations from the Q-criterion field and by assuming their weight is equally distributed, $\pi_k = 1/K$. Each iteration begins with the expectation step, which determines the responsibility (probability), γ_{ik}, that a point in space, x_i, is generated by the subpopulation k, for each of the N points in space and K subpopulations, Eq. 3.10. The maximization step then refines the weight, mean, and covariance given the newfound responsibilities for each of the subpopulations as per Eqs. (3.11)–(3.13), respectively. The algorithm refines the model until convergence is reached at 0.0001% of

the log-likelihood of the overall probability distribution.

$$\gamma_{ik} = \frac{\pi_k \mathcal{N}(\vec{x}_i \mid \vec{\mu}_k, \Sigma_k)}{\sum_{j=1}^{K} \pi_j \mathcal{N}(\vec{x}_i \mid \vec{\mu}_j, \Sigma_j)} \tag{3.10}$$

$$\pi_k = \sum_{i=1}^{N} \frac{\gamma_{ik}}{N} \tag{3.11}$$

$$\vec{\mu}_k = \frac{\sum_{i=1}^{N} \gamma_{ik} \vec{x}_i}{\sum_{i=1}^{N} \gamma_{ik}} \tag{3.12}$$

$$\Sigma_k = \frac{\sum_{i=1}^{N} \gamma_{ik} (\vec{x}_i - \vec{\mu}_k)^{\mathrm{T}} (\vec{x}_i - \vec{\mu}_k)}{\sum_{i=1}^{N} \gamma_{ik}} \tag{3.13}$$

The results from the refined GMM are processed to remove any subpopulations with an aspect ratio greater than two. In doing so, regions of shear vorticity in the two shear layers that the Q-criterion identified as rotational vorticity are eliminated from consideration. Figure 3.7a depicts an example of the resultant GMM probability distribution, which clusters regions of positive Q-criterion. Vortex centroids are located by the spatial mean of each subpopulation and their area by the region encompassed within three standard deviations around the centroid to statistically account for 99.7% of the vortex core for the assumed Gaussian distribution. The results obtained for the data in Fig. 3.7a are presented on top of the vorticity contours in Fig. 3.7b. Vortex identification and characterization were confined to the region that is one diameter downstream of the cylinder and one diameter upstream of the edge of the FOV, so as to reduce the adverse influence of velocity measurement boundaries on the results. The results in Fig. 3.7b illustrate that the method correctly identifies vortices, distinguishing rotational from shear regions, and captures their skewed shape. It should be noted that the outlined statistical approach was verified to produce comparable results using the λ_2-criterion, see Appendix G for details.

It is important to note that application of the model assumes a Gaussian distribution of the data within each of the subpopulations. Given that the spatial distribution of vorticity within a vortex is Gaussian [124–126], it follows that the distribution of the vortex identification Q-criterion should also be Gaussian since it represents the local balance between shear strain rate and vorticity magnitude [116], which is greatest at the vortex center with outward radial decay. This assumption has been verified to be reasonable through the analysis of quantile-quantile plots of subpopulations. Figure 3.8 depicts quantile-quantile plots of the Q-criterion distribution for the vortex at $x/D \approx 4.3$ in Fig. 3.7. In general the distributions in the streamwise and transverse directions are very close to the standard normal, especially within half a diameter from the vortex center. Slight deviation from the

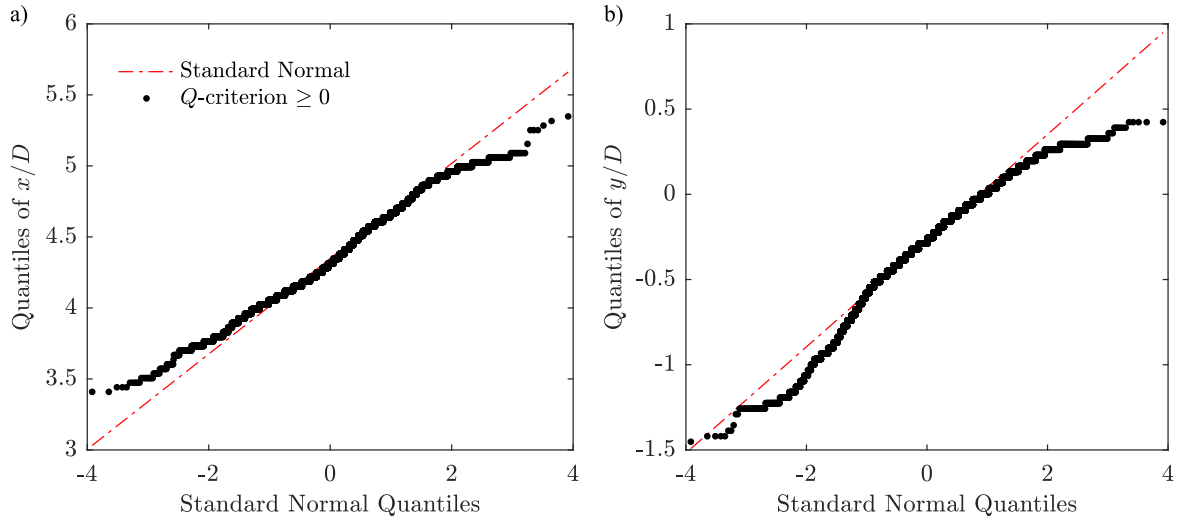

Figure 3.8: Quantile-quantile plots for the spatial distribution of the vortex identification Q-criterion in the (a) streamwise and (b) transverse direction for the positively signed vortex at $x/D \approx 4.3$ in Fig. 3.7.

standard normal towards the extremities of the vortex indicates that there is less variance than expected and that the distribution is slightly skewed in the negative transverse direction. This discrepancy agrees with the results of Bray [125], who observed increasing error in the spatial distribution of vorticity outwards from the vortex center.

This iterative GMM refinement employed in this study requires an initial estimate of the mean, covariance and weight for each of the subpopulations. The mean, $\vec{\mu}_k$, is manually input as the approximate cluster center based on the positive Q-criterion for each of the K subpopulations. The initial covariance, Σ_k, of each subpopulation is automatically computed from the Q-criterion surrounding the estimated mean and each subpopulation is initially weighted equally. The EM algorithm then iteratively refines the mean, covariance and weighting proportion until convergence is reached. Sensitivity tests have shown that the covariance computed from data within $0.1D$ to $5.0D$ of the initial mean produced identical refined probability distributions. Furthermore, it was verified that initializing the spatial mean of each subpopulation to within approximately $1.0D$ of the true converged mean consistently produced identically refined probability distributions. As such, the model is most sensitive to the specified number of subpopulations where more complex models typically better represent the data. This brings to light that the model suffers from overfitting, which was addressed in the present study by applying user input to ascertain how many subpopulations best located the vortices in the wake. An objective method for

evaluating the quality of the statistical fit and improving the automated identification is proposed in Chapter 7.

Chapter 4

Vortex Dynamics in the Wake[1]

In this chapter, the vortex induced vibrations of a pivoted cylinder are investigated experimentally at a fixed Reynolds number of 3100 and a range of reduced velocities, $4.4 \leq U^* \leq 9.1$. The study focuses on a quantitative analysis of the planar wake topology and its relation to the structural response. Vortex identification and tracking are used to analyze the shedding process based on the vortex strength and its core acceleration.

4.1 Amplitude Response

The amplitude response of a pivoted cylinder is characterized using the peak deflection angle, $\delta = tan^{-1}(A/L)$, where A is the amplitude of the high-pass filtered structural oscillations in either the streamwise or transverse directions. Given the relatively small deflection angles in the $y-z$ and $x-z$ planes, the following approximations can be used $\delta_{yz} \approx A_y/L = A_y^*/AR$ and $\delta_{xz} \approx A_x/L = A_x^*/AR$. Figure 4.1 depicts variation of the peak deflection angles with reduced velocity. Substantial response within $4.7 \leq U^* \leq 9.0$ indicates a lock-in region with two response branches: an initial branch ($4.7 \leq U^* \leq 5.9$) and a lower branch ($5.9 \leq U^* \leq 9.0$). As will be discussed in more detail in the following sections, shedding patterns observed from phase-averaged vorticity fields agree with previously documented 2S and 2P regimes in the initial and lower branches, respectively [18, 26]. Figure 4.1a shows some variation in amplitude response and length of

[1]This is an Accepted Manuscript of an article published by Springer Berlin Heidelberg in Experiments in Fluids on April 12, 2018, available online: 10.1007/s00348-018-2530-3. E. Marble, C. Morton, and S. Yarusevych, "Vortex dynamics in the wake of a pivoted cylinder undergoing vortex-induced vibrations with elliptic trajectories."

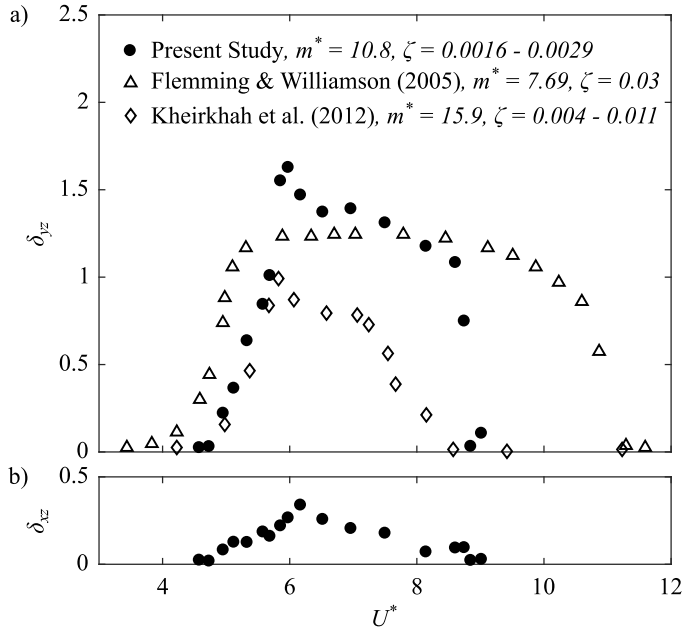

Figure 4.1: Variation of peak deflection angle in the (a) $y - z$ and (b) $x - z$ planes with the reduced velocity. Deflection angle is measured in degrees.

lock-in region between the results from different studies performed on pivoted cylinders at comparable structural parameters and Reynolds numbers. The larger maximum amplitude and intermediate length of lock-in region seen in the present data are primarily due to the lower damping coefficient and moderate mass ratio [85].

4.2 Frequency Response

Variation of the normalized frequency of streamwise and transverse vibrations with the reduced velocity is shown in Fig. 4.2a. The dominant frequencies were obtained from spectral analysis of displacement signals, with representative spectra of streamwise and transverse displacements depicted in Figs. 4.2b and 4.2c, respectively. Pronounced peaks in the spectra at the system's natural frequency and harmonics within $4.85 \leq U^* \leq 8.55$ indicate the lock-in region. The dominant peaks of both streamwise and transverse spectra occur at the natural frequency, indicating the system follows an elliptic trajectory. Energy content of these peaks is greater and more concentrated in the transverse spectra, implying a trajectory with larger amplitude of oscillation in the transverse direction. Evidence of elevated spectral energy content associated with the vortex shedding frequency of a

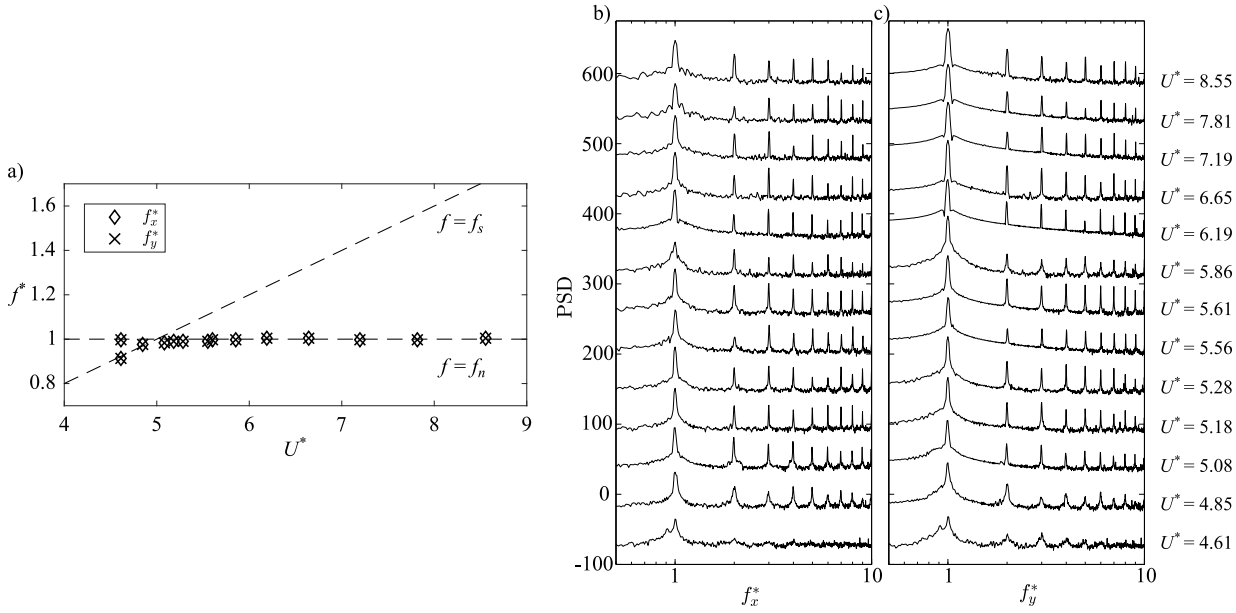

Figure 4.2: (a) Normalized frequency of streamwise and transverse vibrations; (b) spectra of streamwise vibrations, (c) spectra of transverse vibrations. Note, spectra are plotted with a consistent amplitude offset for clarity.

stationary cylinder is observed only at $U^* = 4.61$ in the transverse spectra at $f_y^* = 0.87$. Compared with the other cases, the spectral peak at the natural frequency for $U^* = 4.61$ is less pronounced which is attributed to the fact that this condition is near the onset of lock-in. A comparison of spectra for the fluctuating wake velocity and cylinder displacement confirmed that vortices shed at the Strouhal frequency for $U^* = 4.61$, while shedding frequency locked onto the structure's natural frequency for the remaining reduced velocities examined in Fig. 4.2.

Phase-averaged cylinder trajectories at the PIV laser height for three representative reduced velocities are depicted in Fig. 4.3, with associated uncertainty in the phase-averaged results shown in grey based on a 99% confidence interval. The results show that cylinder trajectories are elliptic with the majority of motion in the transverse direction, similar to the cases investigated by Kheirkhah *et al.* [45] and Oviedo-Tolentino *et al.* [40]. Kheirkhah *et al.* [45] outline four possible regimes for VIV with cylindrical trajectories based on the orientation of the ellipse with respect to the y-axis and orbiting direction. Three of these regimes are observed for the range of parameters investigated in the present study (Figs. 4.3a–c). The fourth regime was not observed because the structural coupling of the system did not permit for the necessary reduced coupling velocity range as suggested

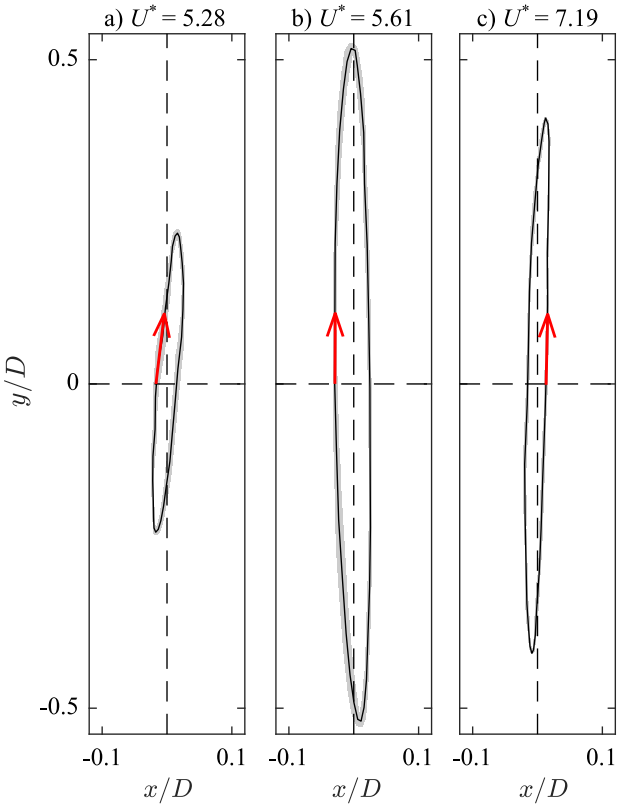

Figure 4.3: Cylinder trajectories at PIV measurement plane $z/D = 18$ for (a) $U^* = 5.28$, (b) $U^* = 5.61$, and (c) $U^* = 7.19$. A red arrow in each image denotes the orbiting direction. Grey contours correspond to uncertainty in the phase-averaged results based on a 99% confidence interval.

by Kheirkhah *et al.* [45]. For each case of reduced velocity, the direction of orbit and orientation of the ellipse remain constant during multiple experiments.

4.3 Wake Topology

The results of the present investigation are overlaid on the Morse and Williamson [1] shedding map, developed from forced 1DOF-transverse vibrations of a cylinder, in Fig. 4.4a. Purple, green and orange markers correspond to 2S, $2P_o$ and 2P shedding regimes, respectively, as determined based on analysis of phase-averaged vorticity fields. Representative phase-averaged vorticity fields are depicted in Figs. 4.4b–d at the same phase angle of

cylinder motion. The results suggest that the observed vortex shedding regimes, at the investigated spanwise plane, agree with the Morse and Williamson [1] shedding map except for the 2P pattern observed at $U^* = 8.55$, in the zone of predicted desynchronized shedding. This is close to the region where Kheirkhah *et al.* [49] noticed significant departure from the predicted shedding regimes for 2DOF variable amplitude VIV. Further deviations form the vortex shedding map observed by Leong and Wei [46] and Flemming and Williamson [47] were attributed to the additional streamwise DOF as well as the highly three dimensional wake, which is caused by the structure's spanwise variable amplitude. The authors of the present study have verified hybrid vortex shedding in the wake exists near the regime transitions on the Morse and Williamson [1] shedding map; however, the analysis presented here focuses on the wake dynamics captured at a single spanwise plane. At the boundary between 2S and 2P regimes, there is a shift in the phase of vortex shedding with respect to cylinder motion. Figure 4.4b displays a positive vortex attached to the lower shear layer, while it has separated in Fig. 4.4c and is located considerably far downstream in Fig. 4.4d. This shift has been shown to coincide with the transition from 2S to 2P shedding as the structural response changes between initial and lower branches [1, 27].

The $2P_o$ regime is distinguishable by the weaker second vortex in each vortex pair, as exemplified by the weak negative vortex at $x/D \approx 1.8$ in Fig. 4.4c. Morse and Williamson [1] observed intermittent switching of the wake within the $2P_o$ regime. This shedding regime occurs at $U^* = 5.86$ in the present study. Corresponding peaks in the spectra of the streamwise and transverse vibrations in Figs. 4.2b and 4.2c are notably more broadband than those at neighbouring reduced velocities pertaining to either 2S or 2P regimes. This indicates temporal variability in the fluid structure interaction that may be attributed to intermittent switching of the wake between 2S, $2P_o$, and 2P vortex shedding at these conditions, as observed by Morse and Williamson [1]. However, unlike the spectral analysis, examination of the cylinder displacement signals showed that amplitude fluctuations are insignificant throughout time and are not indicative of such intermittent switching.

The shedding of vortical structures in the wake in relation to the elliptical motion of the cylinder is illustrated using phase-averaged vorticity field sequences in Fig. 4.5. Figures 4.5a–e display the wake of 2S shedding at $U^* = 5.28$. At the peak of the trajectory in the transverse direction (Fig. 4.5a), positive vortex A has recently shed, with a weak region of vorticity between the vortex and the shear layer still identifiable in the image, and vortex B is in the process of rolling up from the negative shear layer. As the cylinder moves along its clockwise (CW) trajectory, vortex A advects downstream allowing positive vortex C to start rolling up (Fig. 4.5b). Near the bottom of the cylinder trajectory (Fig. 4.5e), vortex C has moved far enough across the wake to impinge upon the negative shear layer, cutting off the supply of negative vorticity and causing vortex B to shed. This process

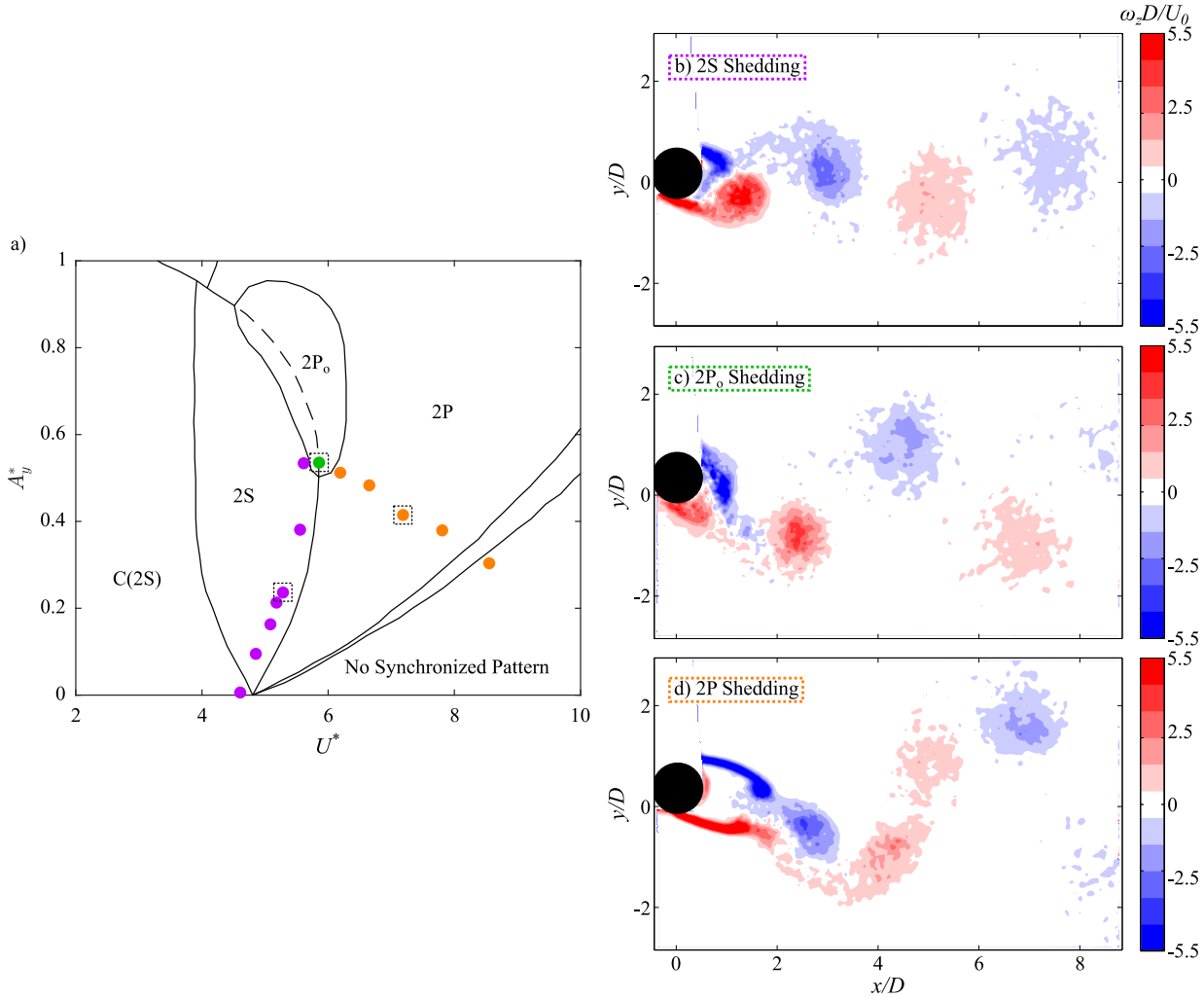

Figure 4.4: (a) Amplitude response at the PIV measurement plane $z/D = 18$ overlaid on the Morse and Williamson [1] shedding map. Red, green and blue markers indicate 2S, 2P$_o$ and 2P shedding regimes, respectively, and were determined from phase-averaged vorticity fields. Representative normalized phase-averaged vorticity contours are shown for (b) $U^* = 5.28$, (c) $U^* = 5.86$, and (d) $U^* = 7.19$.

repeats itself as the cylinder completes the second half of its oscillatory motion.

Vorticity contours of 2P shedding at $U^* = 6.65$ are displayed in Figs. 4.5f–j for half a period. The orientation and direction of elliptic cylinder trajectory are similar to the 2S case; however, the transverse amplitude is approximately twice that found for 2S and the shear layers extend further beyond the cylinder prior to vortex formation. The pairs of shed counter-rotating vortices, which are characteristic of $2P_o$ and 2P shedding, consist of a leading and trailing vortex, where the leading vortex sheds first and is followed by the trailing vortex. At the peak of the trajectory in the transverse direction (Fig. 4.5f), A1 and A2 are vortices having originated from a negative vortex A that split at an earlier phase in the cylinder trajectory. Trailing vortex A1 is advecting downstream and vortices A2 and B are in the process of rolling up. Vortex B moves across the wake as the cylinder continues CW along its trajectory in Fig. 4.5g, cutting off the supply of vorticity to A2 and causing it to shed in a similar manner to 2S shedding. Immediately afterwards, vortex C forms at the end of the negative shear layer and then vortex B splits to form B1 and B2 (Fig. 4.5h). Govardhan and Williamson [27] speculate the vortex splitting is due to strain caused by the significant relative velocity between the cylinder and vortex B as well as the velocity induced by vortex A2. Positive leading vortex A2 and negative trailing vortex B1 then form a counter rotating pair, see Fig. 4.5i. As the cylinder approaches the bottom of its trajectory in the tranverse direction, the newly formed vortex pair advects downstream as vortices B2 and C continue to roll up (Fig. 4.5j). This process repeats itself as the cylinder completes the second half of its motion period.

The observed 2S and 2P shedding modes generally agree with those reported for the 1DOF-transverse VIV study by Govardhan and Williamson [27] and the 2DOF VIV studies by Jauvtis and Williamson [34] and Flemming and Williamson [47], at comparable reduced velocities. There are, however, notable differences in the timing of vortex shedding with comparison to 1DOF studies. Figures 4.5a–e indicate 2S vortices are shed near the peaks of transverse motion; whereas, it can be deduced from the studies of Jeon and Gharib [55] and Hsieh *et al.* [56] that shedding occurs approximately $\pi/4$ prior to the transverse peaks, while that of Williamson and Roshko [54] indicates shedding occurs approximately $\pi/2$ after the peaks. As for the 2P mode, the observed vortex shedding timing agrees with the results of Williamson and Roshko [54]; whereas, the study of Jeon and Gharib [55] indicates that shedding occurs approximately $\pi/4$ later in the transverse motion. Such variability in vortex timings from previous investigations may in part be attributed to the semi-qualitative identification of this important aspect of wake dynamics.

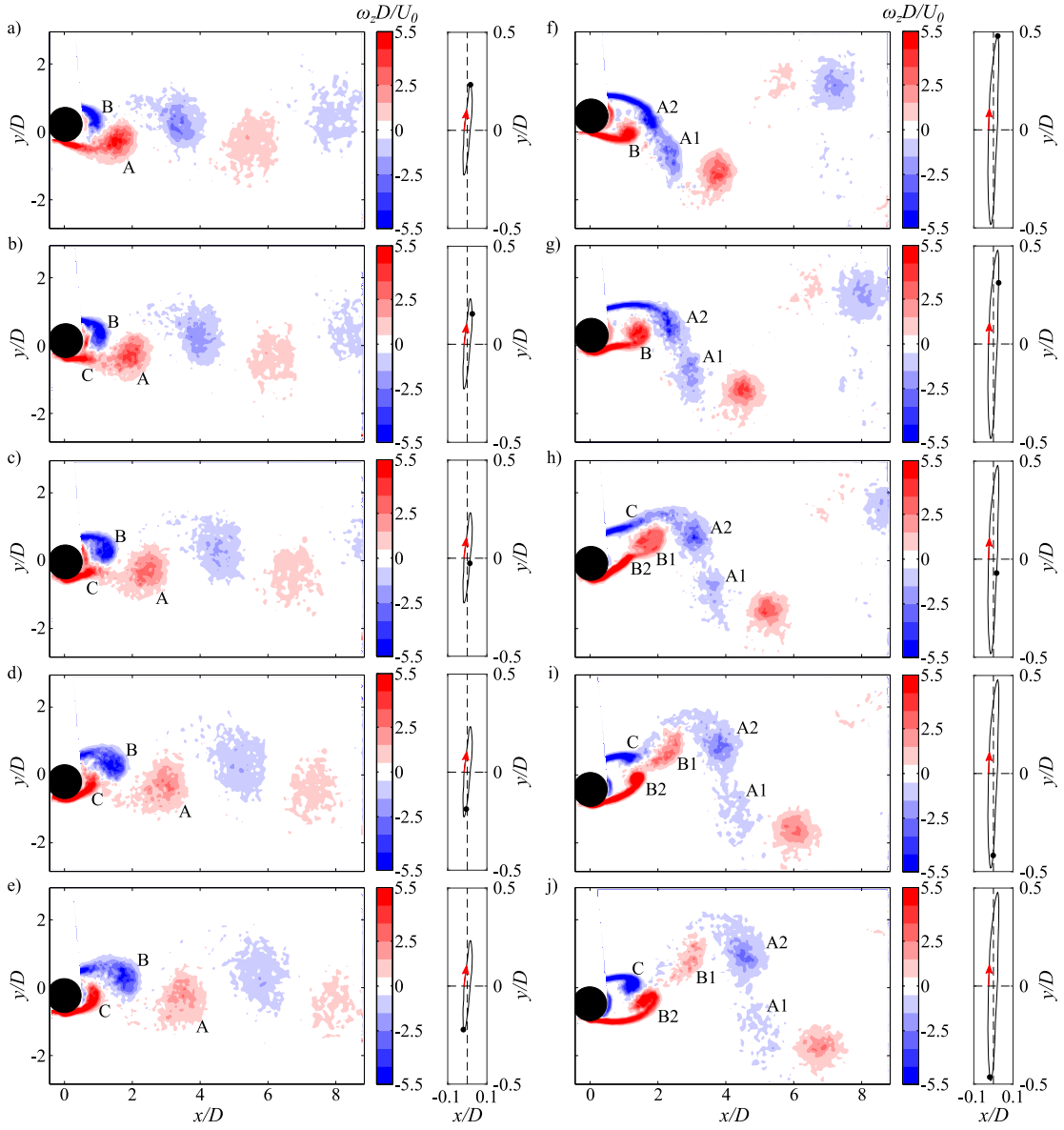

Figure 4.5: Phase-averaged vorticity fields illustrating shedding for half a period ($\theta = 8\pi/15, 12\pi/15, 16\pi/15, 20\pi/15$, and $24\pi/15$); (a-e) 2S shedding at $U^* = 5.28$ and (f-j) 2P shedding at $U^* = 6.65$. Zero phase ($\theta = 0$) is when the cylinder crosses the transverse equilibrium ($y/D = 0$) in the positive y-direction. Location of the cylinder along its elliptic trajectory is shown for each flow field.

4.4 Vortex Shedding Characteristics

The discussion in the previous subsection provides a general overview of vortex shedding regimes attendant in VIV with elliptic trajectories. Here, additional quantitative analysis is carried out to study the shedding dynamics. As described in the experimental methodology, vortices were identified using a statistical method based on the spatial distribution of vortex identification Q-criterion. The approach fits a GMM to the Q-criterion, calculated from the phase-averaged velocity fields, and iteratively refines the probability distribution using an EM algorithm. Vortex centroids were determined from the spatial mean of each subpopulation and their area by the region encompassed within three standard deviations around the centroid. The algorithm was verified to produce area estimates that reflect vorticity diffusion, i.e., vortex areas increase as vortices advect in the wake. Based on this analysis, the position and kinematics of vortex cores, as well as strength of vortices in terms of circulation (Γ), were characterized. The absolute vortex trajectories are depicted in Fig. 4.6 for 2S (Fig. 4.6a) and 2P (Figs. 4.6b and 4.6c) regimes. For the 2P regime, the effect of the cylinder orbiting direction is illustrated, as the two possible directions produce distinctly different vortex trajectories and thereby have different effects on the vortex dynamics in the wake. In contrast, for the 2S regime, the direction of orbiting did not have any appreciable effect on wake shedding characteristics and is thus not considered here for brevity. For the 2S regime (Fig. 4.6a), the positive and negative vortices follow a similar absolute trajectory in the near wake, remaining close to the wake centerline as they advect downstream. There is a slight advection towards the wake centerline in the region $1.0 \leq x/D \leq 3.5$, followed by an outward deviation from the centerline. The streamwise 1DOF VIV study by Cagney and Balabani [127], where vortex trajectory was determined from the swirling strength parameter defined by Wu and Christensen [128], also observed a “slight transverse rebound" for this shedding regime.

The absolute vortex trajectories for 2P shedding are shown in Figs. 4.6b and 4.6c for CW and CCW orbiting, respectively. During and shortly after formation, trailing vortices cross the wake centerline, while leading vortices remain on one side of the wake. Once shed, both leading and trailing vortices advect outward from the wake centerline as they travel downstream. Trailing vortices diffuse faster than their leading counterparts due to significant cross annihilation of vorticity [66], making their identification difficult relatively early downstream in comparison to the leading vortices. They follow a similar absolute path for the CW case (Fig. 4.6b); however, for the CCW case, the negative trailing vortex remains closer to the transverse equilibrium ($y/D = 0$) in the near wake than the positive trailing vortex (Fig. 4.6c). The absolute trajectory of leading vortices is initially similar to the trailing vortices until the positive and negative leading vortices begin to deviate at

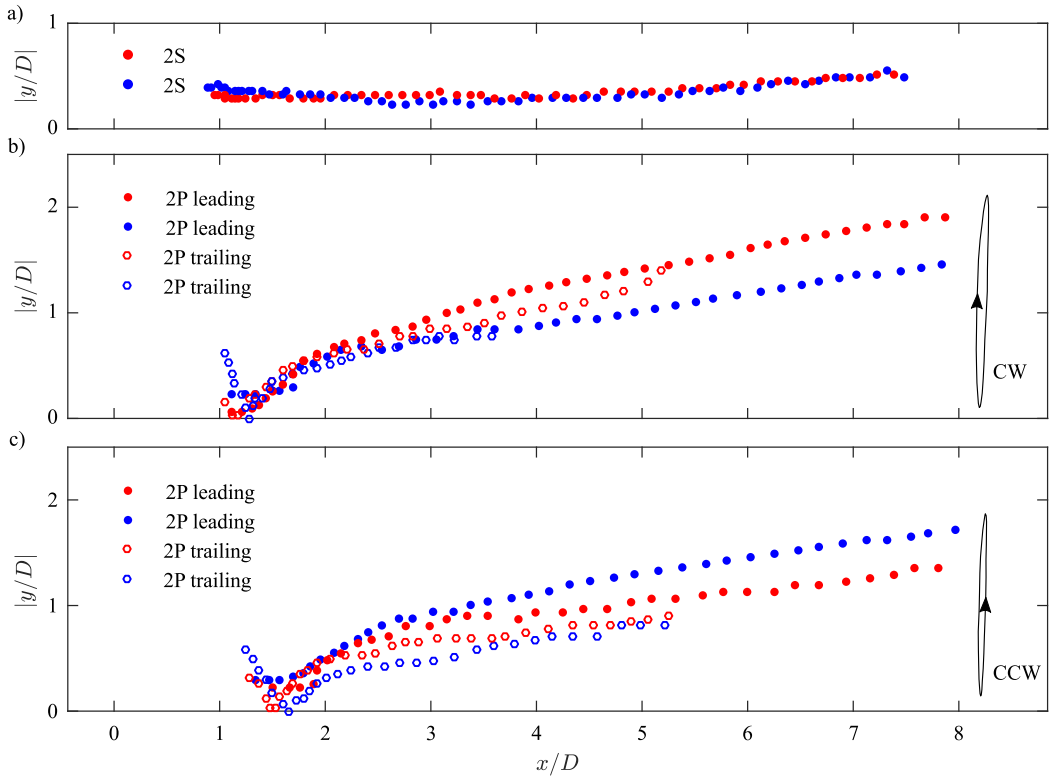

Figure 4.6: Vortex trajectories obtained based on phase-averaged results for (a) 2S shedding at $U^* = 5.28$ and 2P shedding at (b) $U^* = 6.65$ and (c) $U^* = 7.19$. The two selected 2P cases correspond to different direction of orbiting. Red and blue markers indicate positively and negatively signed vortices, respectively.

$x/D \approx 2.5$. For the CW case (Fig. 4.6b), the deviation increases until $x/D \approx 4$, at which point the positive leading vortex remains about $0.5D$ further from the wake centerline than the negative leading vortex. In contrast, the negative leading vortex remains about $0.4D$ further from the wake centerline than the positive leading vortex for the CCW case (Fig. 4.6c).

Variation of vortex position, acceleration, and circulation with phase of cylinder motion is presented in Figs. 4.7 and 4.8 for 2S and 2P regimes, respectively, in order to elucidate the shedding process. The acceleration of vortices is estimated based on numerical differentiation of the streamwise position data, using first order forward and backward difference schemes at the beginning and end of each data set and a second order central difference scheme for all inner points. The circulation is computed by integrating the vorticity within the area defined by GMM vortex identification, with error bars showing the methodologi-

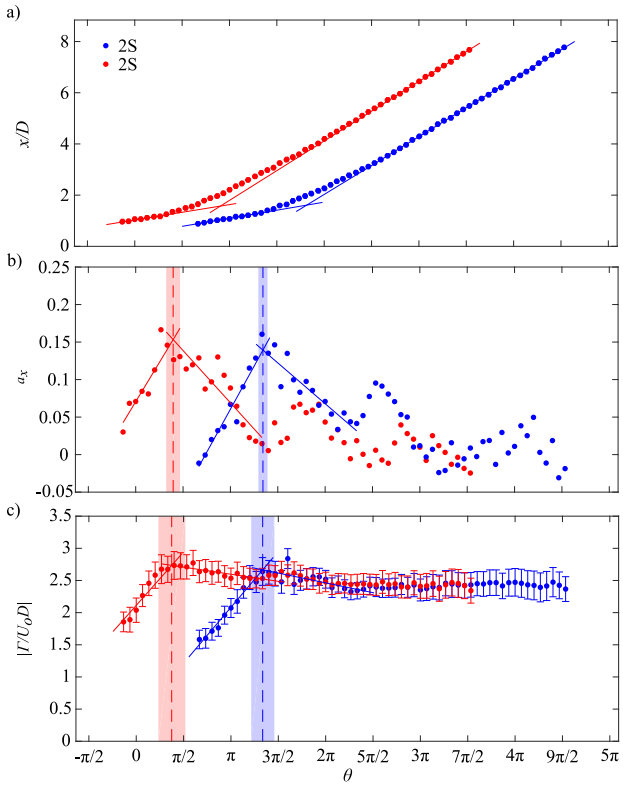

Figure 4.7: Variation of (a) streamwise vortex core position, (b) streamwise vortex core acceleration, and (c) vortex strength with respect to phase angle of cylinder motion for 2S shedding at $U^* = 5.28$. Dashed lines indicate the estimated timing of vortex shedding, with shaded regions representing methodological uncertainty.

cal uncertainty associated with phase averaging based on a 99% confidence interval. The phase angle is defined as zero when the cylinder crosses the wake centerline in the positive y-direction. The phase-averaged vorticity fields in Figs. 4.5a–e and Figs. 4.5f–j depict the 2S and 2P shedding processes, respectively, at $\theta = 8\pi/15, 12\pi/15, 16\pi/15, 20\pi/15$, and $24\pi/15$.

Similar to the wake development of a stationary cylinder described in Rockwood *et al.* [65], the vortex shedding process in the wake of a cylinder undergoing VIV can be divided into three distinct stages: formation, saturation, and downstream advection. For 2S and 2P shedding regimes, each shedding process stage is associated with distinct trends in data presented in Figs. 4.7 and 4.8. The initial stage, vortex formation, occurs as the separated shear layer rolls up into a vortex. For instance, the formation of the negative

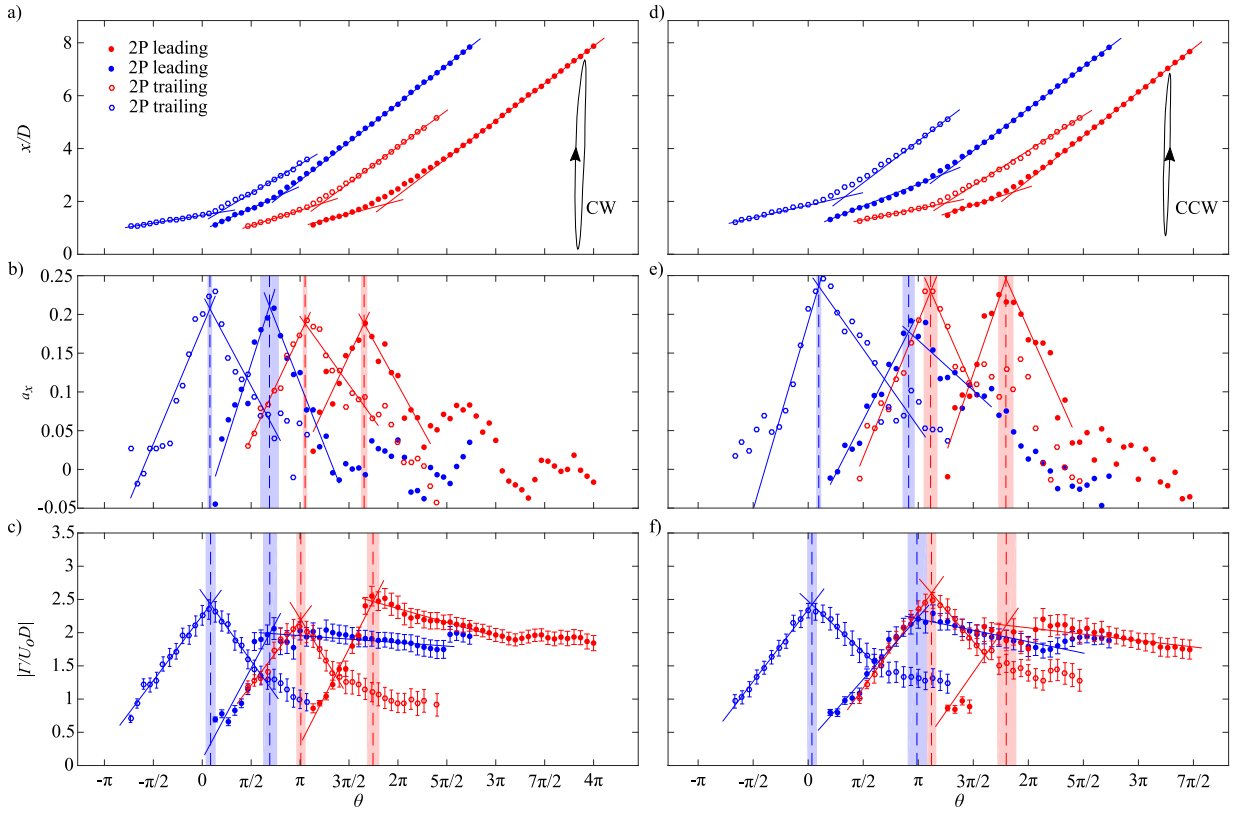

Figure 4.8: Variation of (a & d) streamwise vortex core position, (b & e) streamwise vortex core acceleration, and (c & f) vortex strength with respect to phase angle of cylinder motion for 2P shedding at (a-c) $U^* = 6.65$ and (d-f) $U^* = 7.19$. Dashed lines indicate the estimated timing of vortex shedding, with shaded regions representing methodological uncertainty.

2S vortex labeled as B occurs from $8\pi/15 \leq \theta \leq 20\pi/15$ in Figs. 4.5a–c. During this stage, the vortex core experiences relatively small downstream displacements in the vortex formation region due to a gradual shear layer elongation, with a linear increase in acceleration (Figs. 4.7b, 4.8b, and 4.8e). The continuous flux of vorticity supplied by the shear layer contributes to a nearly linear increase in circulation (Figs. 4.7c, 4.8c, and 4.8f), which agrees with observations from Jeon and Gharib [55] and Konstantinidis *et al.* [129]. The increase in circulation eventually saturates and the vortex sheds [55]. Thus the cylinder phase angle at which shedding occurs can be identified based on the phase at which maximum circulation is attained [55, 56, 129, 130]. An alternative method for shedding identification based on the kinematics of vortex cores is explored here, with

shedding expected to coincide with maximum vortex core acceleration. Peak circulation and acceleration are estimated from the intersection of two linear fits to the data before and after the expected instant of shedding. The line prior to shedding is automatically fit using the first five data points, then extended by iteratively adding points one by one as long as their deviation from the linear fit is less than two standard deviation of the error between each of the points and the corresponding fit. The line subsequent to shedding is similarly generated starting with the point excluded from the first linear fit based on the aforementioned procedure. Linear fits were implemented because they approximate well the changes in vortex growth and acceleration during formation and downstream advection immediately subsequent to shedding, while not introducing much added complexity to the method. The corresponding phase angles of intersection are marked by vertical dashed lines, with methodological uncertainty limits identified by shaded regions. It can be seen that the phase angles corresponding to maximum circulation and peak acceleration agree to within experimental uncertainty for all the cases, marking the instant of shedding of the corresponding vortices for each shedding regime. Note that the estimates of shedding timing from vortex circulation are not affected appreciably if vortex area is defined based on two or three standard deviations from the centroids in GMM. Comparing streamwise vortex core position with the estimated vortex shedding phase angles suggests that shedding is marked by the onset of vortex core position departure from the initial linear trend in vortex position (Figs. 4.7a, 4.8a, and 4.8d). This is substantiated by the approach employed by Huang and Green [131] and Rockwood *et al.* [65], who inferred shedding phase angle from the changes in the position of the Lagrangian saddle point. Once shed, the vortex advects downstream, its circulation decaying due to viscous diffusion and cross annihilation of vorticity [66], and eventually reaches a nearly-constant advection velocity. It can be seen from a comparison of Figs. 4.7 and 4.8 that the formation and saturation stages of the shedding process occur more rapidly for 2P than 2S shedding because two additional vortices are shed within each cylinder oscillation period. Compared to 2S shedding, the shorter period of formation and greater amplitude of cylinder oscillation for 2P shedding results in the vortices experiencing greater acceleration at saturation and attaining lower strength throughout the shedding process.

The results in Figs. 4.7b and 4.7c indicate that positive and negative 2S vortices are shed approximately $\Delta\theta = \pi$ apart, agreeing with 1DOF VIV results from Williamson and Roshko [54], and have similar accelerations and absolute strengths throughout the shedding process. The location of the cylinder along its elliptic trajectory and the corresponding phase-averaged vorticity fields at the identified instances of shedding for the 2S regime are depicted in Fig. 4.9. It can be seen that 2S vortices are shed as the cylinder passes the streamwise equilibrium ($x/D = 0$), with positive and negative vortices shed during the

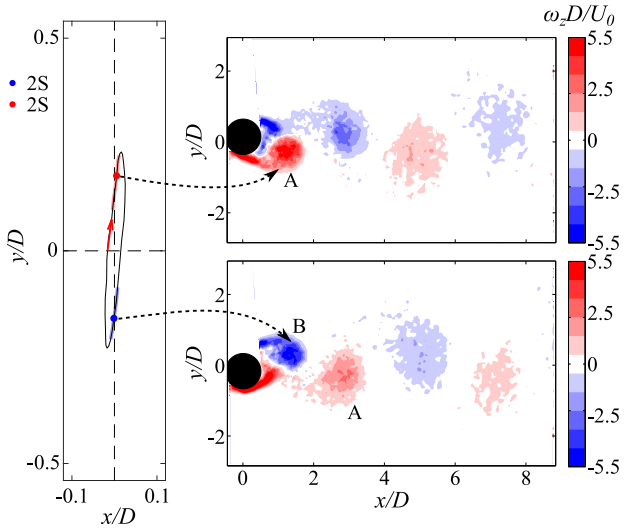

Figure 4.9: Phase-averaged vorticity fields corresponding to the identified instances of vortex shedding for the 2S regime at $U^* = 5.28$.

upward and downward transverse motion of the cylinder, respectively.

The flow fields corresponding to the shedding phases for the 2P regimes are shown in Fig. 4.10. For the case of CW cylinder trajectory (Fig. 4.10a), leading vortices (A2 and B2) shed immediately after the cylinder reaches its transverse peak of oscillation and trailing vortices (A1 and B1) shed near the transverse equilibrium. For the CCW orbiting trajectory (Fig. 4.10b), these vortices are shed at phase angles occurring later in the cylinder's trajectory as a result of the higher reduced velocity. In both CW and CCW cases, the leading and trailing vortices of a pair shed within less than one quarter of a period and experience similar accelerations, Figs. 4.8b and 4.8e. The cumulative negatively and positively signed circulation generated in each cycle of 2P vortex shedding are similar for both cases; however, for the CW case, the pair with a leading positive vortex and negative trailing vortex is stronger upon shedding than the other pair (Fig. 4.8c). In contrast, this is the weaker pair for the CCW case (Fig. 4.8f). The observed differences in vortex strength between the two cases are attributed to the differences in vorticity production associated with trailing and leading vortices. In particular, stronger vortex pairs (B2 and A1 in Fig. 4.10a, and A2 and B1 in Fig. 4.10b) form when the cylinder moves in the direction opposite of that of the incoming flow, leading to a higher rate of vorticity production during this part of the oscillation. On the other hand, the weaker vortex pairs form when the situation is reversed. Compared to the classical description developed for 1DOF-transverse VIV [27], the additional streamwise freedom of motion

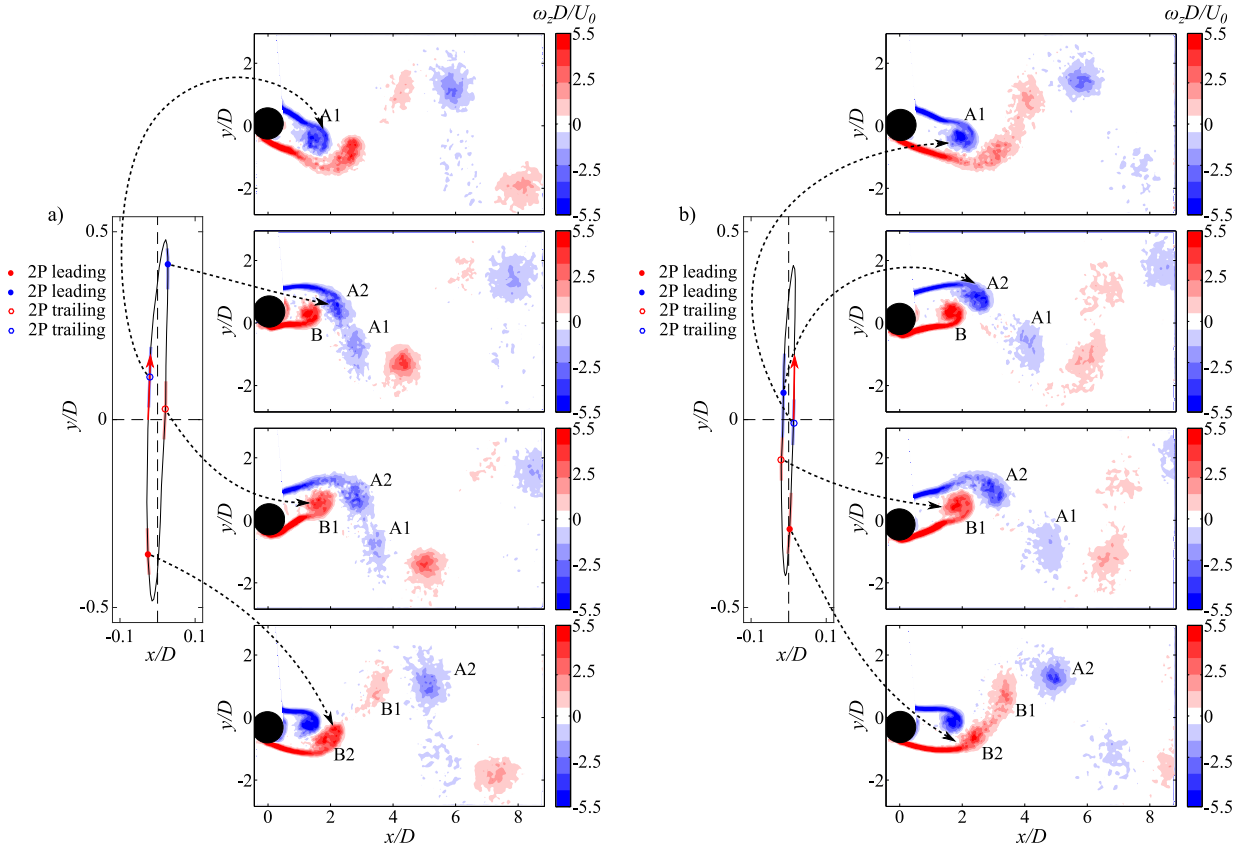

Figure 4.10: Phase-averaged vorticity fields corresponding to the identified instances of vortex shedding for the 2P regime at (a) $U^* = 6.65$ and (b) $U^* = 7.19$.

in 2DOF VIV impacts the 2P vortex formation process if the cylinder follows an elliptic orbit. For both cases of orbiting direction, upon saturation, the decay in circulation for the trailing vortices is faster than that for the leading vortices, which is ascribed to significant cross annihilation of vorticity as the trailing vortex passes between its leading counterpart and the oppositely signed shear layer (see Figs. 4.5f–j: B1 passes between A2 and C with rapid reduction in its local vorticity concentration).

The variation in the cylinder oscillation phase at vortex shedding with reduced velocity is presented in Fig. 4.11a for all the cases investigated. Zero phase angle ($\theta = 0$) corresponds to the instant when the cylinder crosses the transverse equilibrium ($y/D = 0$) in the positive direction, and error bars represent methodological uncertainty with a 95% confidence interval. 2S shedding occurs within the range $4.61 \leq U^* \leq 5.61$ with significant cylinder oscillations starting at $U^* = 4.85$. Closed and open markers in the range

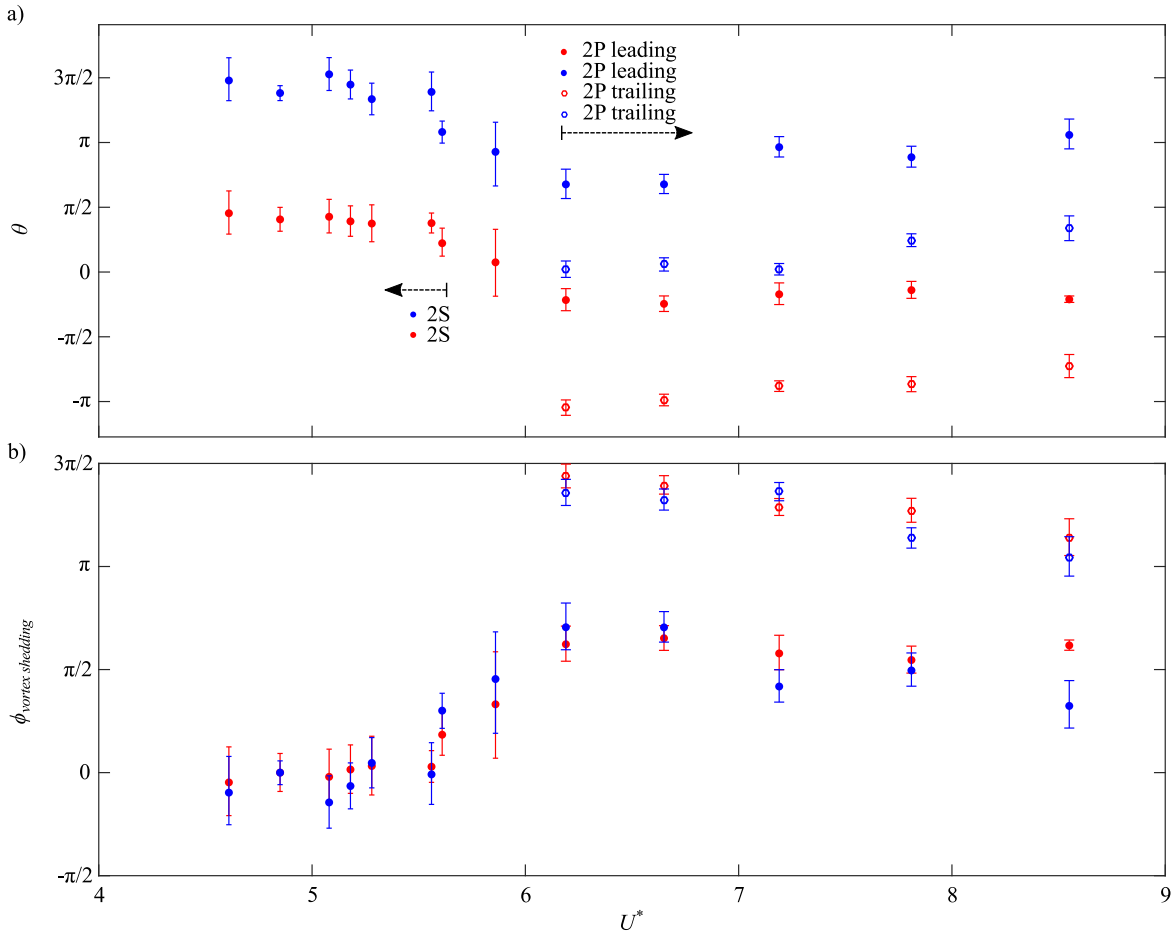

Figure 4.11: Variation in characteristic phase of vortex shedding with U^*: (a) phase angle of cylinder oscillation at the moment of shedding and (b) relative phase angle between vortex shedding and cylinder oscillations. Red and blue correspond to positively and negatively signed vortices, respectively.

$6.19 \leq U^* \leq 8.55$ indicate leading and trailing 2P vortices, respectively. Only the leading $2P_o$ vortices at $U^* = 5.86$ are shown since the weak nature of trailing $2P_o$ vortices prevented reliable determination of their shedding phase. It can be seen that the timing of vortex shedding changes notably as the shedding regime changes from 2S to 2P, where 2P vortices are shed earlier in the elliptic cylinder orbit than 2S vortices of the same sign.

It is also of interest to consider the relative phase angle between vortex shedding and cylinder oscillation, $\phi_{vortex\ shedding}$. The results are presented in Fig. 4.11b, with the origin set such that the relative shedding phase is zero at $U^* = 4.85$, which is in line with the re-

sults of Govardhan and Williamson [27] and Morse and Williamson [1] for a similar reduced velocity. It can be seen that the relative phase angle does not vary significantly throughout the 2S regime. It begins to increase as the shedding mode switches to $2P_o$ ($U^* = 5.86$), and a sharp increase is seen at the onset of the 2P regime ($U^* = 6.19$). Approximating the shedding phase of the 2P regime as the average of the relative phase angles of same-signed leading and trailing vortices, the phase jump from 2S to 2P is approximately π. As such, 2P vortices shed approximately half a period earlier in the cylinder trajectory than 2S vortices. This phase jump agrees with the results from the high mass damping case by Govardhan and Williamson [27] who found it to coincide with a slight increase in the frequency of cylinder oscillation. As the reduced velocity increases within the 2P regime, the relative vortex phase is seen to gradually decrease, in agreement with the 1DOF-transverse forced vibration study of Morse and Williamson [1].

It has been shown that the timing of 2P vortex shedding relative to the cylinder motion in the streamwise direction influences the vortex dynamics during formation, specifically, the vortex strength at shedding. As such, the wake topology shows notable deviations from the classic 2P shedding observed by Govardhan and Williamson [27] in their 1DOF-transverse VIV study. Associated changes in the wake topology are elucidated in Figs. 4.12a and 4.12b for $U^* = 6.65$ and $U^* = 7.19$, respectively. Phase-averaged vorticity fields are shown at the peaks of transverse cylinder motion with dashed lines indicating the streamwise location of leading vortices in the wake. For the case of CW orbiting in Fig. 4.12a, the leading vortices in the wake are separated by $x/D \approx 3.5$ when the cylinder is at the top of its trajectory, whereas they are only separated by $x/D \approx 2.0$ at the bottom. This streamwise staggering is a result of the vortex pair B2 and A1 shedding upstream of the streamwise equilibrium of cylinder oscillation ($x/D = 0$) while the other pair, A2 and B1, sheds downstream (Fig. 4.10a). Similar uneven streamwise spacing between vortex pairs is seen in Fig. 4.12b when the cylinder orbiting direction is CCW, with smaller and larger streamwise spacing between vortex pairs occurring at opposite cylinder positions. This indicates that streamwise motion of the cylinder and its phase difference relative to the transverse motion cause vortex staggering in the wake since both the direction of orbiting as well as the tilt of elliptical trajectories have a notable influence on wake vortex dynamics. The observed streamwise staggering leads to changes in induced velocities in the wake, and is thus contributing to the differences seen between the trajectories of the leading positive and negative vortices in Figs. 4.6b and 4.6c. Considering the CW case (Fig. 4.12a) when the cylinder is at the top of its trajectory, the distance between the positive leading vortex at $x/D \approx 3.7$ and the downstream pair is increased; whereas, at the bottom of the trajectory, the negative leading vortex at $x/D \approx 4.3$ is relatively close to the downstream pair. Consequently, the leading positive and negative vortices experience

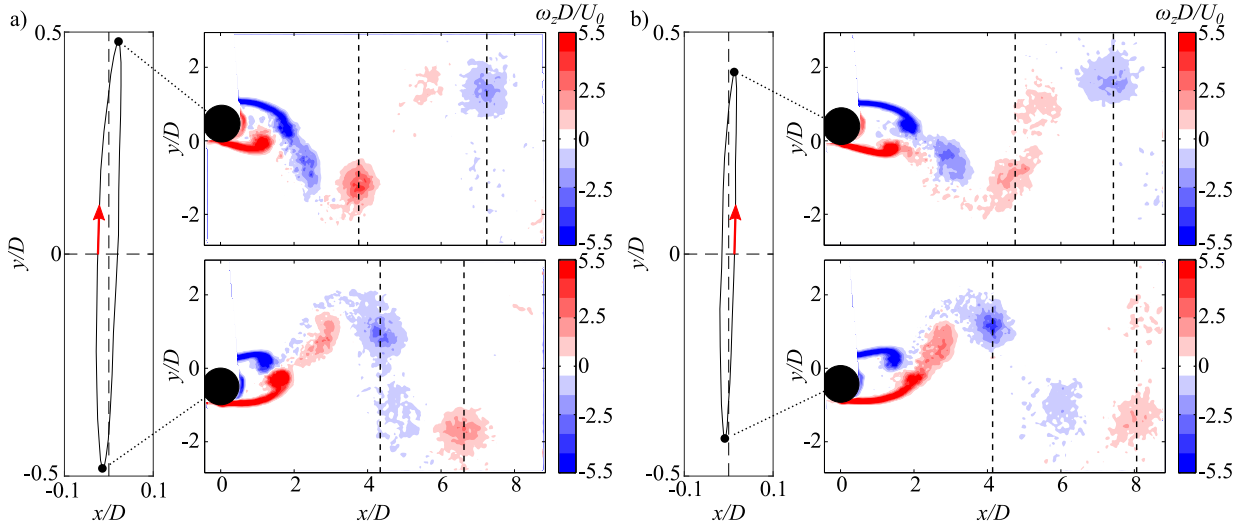

Figure 4.12: Difference in wake topology for the 2P regime for different orbiting directions assessed based on phase-averaged vorticity fields presented for the same phase of cylinder oscillations: (a) CW orbiting at $U^* = 6.65$ and (b) CCW orbiting at $U^* = 7.19$.

different induced velocity from the surrounding structures, leading to the differences seen in their trajectories in Figs. 4.6b and 4.6c. As expected from Figs. 4.12a and 4.12b, the trajectories of the leading positive and negative vortices in Figs. 4.6b and 4.6c are reversed since the orientation of orbiting changes between the two cases.

Several classical definitions of the vortex formation length for a stationary circular cylinder exist. These include the minimum of the mean pressure on the wake centerline [2, 9], the maximum of the wake streamwise and transverse velocity fluctuations on the wake centerline [132, 133], the streamwise extent of the recirculation region [134], and the location of minimal transverse spacing of the maximum in the streamwise velocity fluctuations [135]. Figure 4.13 compares the streamwise location of vortex shedding determined from the GMM based circulation analysis with the formation length as per $v_{RMS\ Max}$, $u_{RMS\ Max}$, and the streamwise extent of the recirculation region. The results are compared for a stationary cylinder at $U^* = 0$ and all VIV cases investigated in the this chapter, with error bars representing methodological uncertainty for a 95% confidence interval. Examination of the stationary case shows good agreement amongst the methods, although the peak v_{RMS} is slightly further downstream. For the VIV cases, the circulation based location of vortex shedding is similar for the positively and negatively signed 2S vortices. For 2P shedding, the leading vortices are shed further downstream than the trailing vortices and there is a notable difference in the shedding location of positively and negatively signed

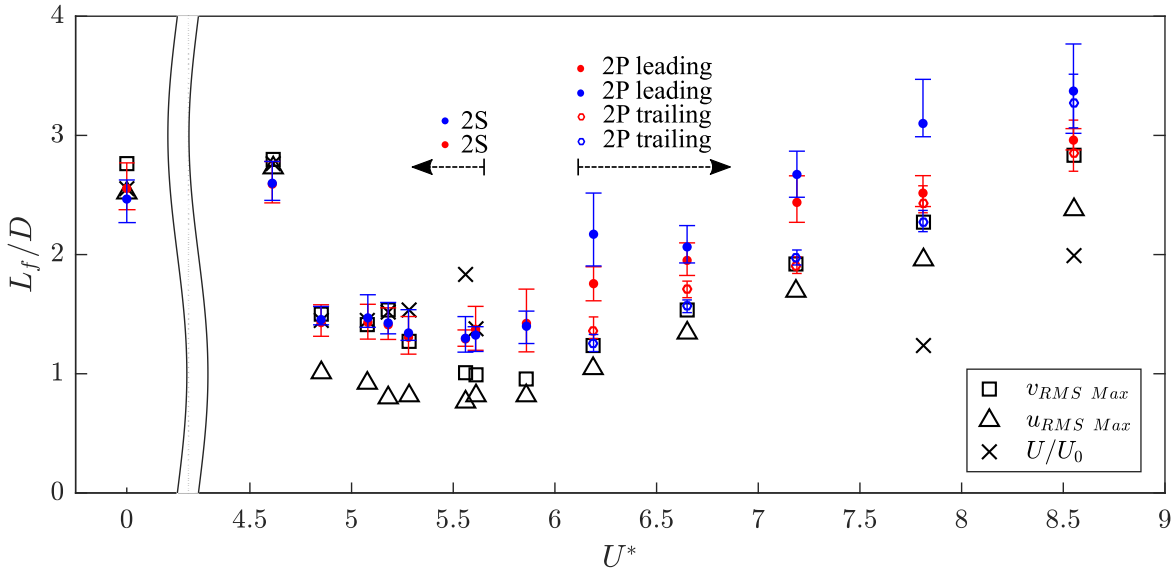

Figure 4.13: Variation of the formation length with U^*. Filled and empty circles correspond to the streamwise location of vortex shedding determined from the GMM based circulation analysis. Squares and triangles indicate the streamwise location along the wake centerline to the peak in the v_{RMS} and u_{RMS} fields, respectively. Crosses indicate the streamwise extent of the recirculation region ($U/U_0 < 0$). Red and blue correspond to positively and negatively signed vortices, respectively.

leading vortices. As previously discussed, these differences are attributed the timing of 2P vortex shedding relative to the cylinder motion. Compared to the classical definitions of the vortex formation length, there is good agreement between the location of $v_{RMS\ Max}$ along the wake centerline and the shedding of 2S vortices as well as 2P trailing vortices, except near the transition between the initial and lower branches in the region $5.5 \lesssim U^* \lesssim 6$. The streamwise extent of the recirculation region agrees with these methods at low reduced velocities, but deviates significantly and ceases to exist as the amplitude of cylinder oscillations increases and the recirculation region becomes indiscernible in the mean streamwise velocity field. The locations of peak u_{RMS} along the wake centerline are generally further upstream than the other methods, except at the lowest reduced velocity.

The findings from this results Chapter indicate that streamwise motion of the cylinder can significantly impact the vortex dynamics in the wake for 2P shedding. Specifically, the strength of vortices depends upon whether the cylinder is moving upstream or downstream during the vortex formation process. Furthermore, the trajectory of leading vortices and

the streamwise staggering of 2P pairs depends upon vortex shedding timing relative to the streamwise equilibrium ($x/D = 0$) of cylinder oscillations in the streamwise direction. These findings appear to be inherent to the elliptic trajectory-type response. In contrast, Jauvtis and Williamson [34] and Flemming and Williamson [47] observed that the additional streamwise motion of the cylinder affects the shedding pattern in the cylinder wake if the mass ratio is relatively low, $m^* < 6$. However, for moderate mass ratios, they found the application of 1DOF-transverse data reasonably predicts the classically defined wake modes.

Chapter 5

Spanwise Wake Development

In this chapter, the spanwise wake development is investigated experimentally at a fixed Reynolds number of 3100 for a stationary cylinder and two cases of vortex induced vibrations of a pivoted cylinder with reduced velocities $U^* = 5.48$ and 7.08. Time-resolved planar PIV measurements in the horizontal and vertical planes in the wake are combined with the measured structural response to form a comprehensive description of the spanwise vortical structures. The discussion is divided into six sections: (i) structural response, (ii) an overview of the flow development, (iii) time averaged velocity fields, (iv) vortex shedding characteristics, (v) reconstruction of the 3D wake topology, and (vi) analysis of the wake using Proper Orthogonal Decomposition.

5.1 Structural Response

Low pass filtered instantaneous trajectories of the cylinder tip are depicted in Figs. 5.1a and 5.1b for the VIV cases $U^* = 5.48$ and 7.08, respectively. Both cases exhibit an elliptic trajectory with dominant motion in the transverse direction having oscillations with amplitudes that are approximately $10\times$ that of the streamwise direction. Both orbits exhibit CW rotation; however, their tilt with respect to the y-axis is different and corresponds to two of the four possible elliptic orientations [45]. Calculated using the Hilbert transform of the displacement signal, the phase difference between the streamwise and transverse motion is $\psi = 1.69\pi$ and 1.33π for $U^* = 5.48$ and 7.08, respectively. Similar to the results presented in Section 4.2, spectral analysis of the displacement signals showed pronounced energy content near the natural frequency of the structure and its harmonics, with natural frequencies $f_n = 1.51$Hz and 1.17Hz for $U^* = 5.48$ and 7.08, respectively.

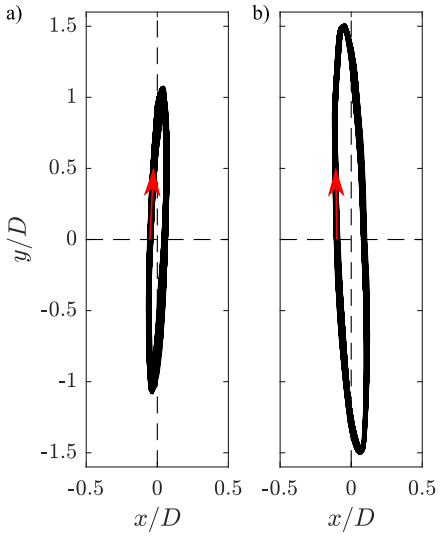

Figure 5.1: Cylinder tip trajectories for (a) $U^* = 5.48$ and (b) $U^* = 7.08$. A red arrow in each image denotes the orbiting direction.

The structural response for both cases is overlaid on the Morse and Williamson [1] shedding map, developed from forced 1DOF-transverse vibrations of a cylinder, in Fig. 5.2b. Each pair of data points connected by a line corresponds to one tested experimental condition, where the data points mark the extremes of the spanwise survey using 2D PIV in the horizontal, $x - y$, plane. The investigated spanwise range for each case was selected to encompass the predicted hybrid shedding. Specifically, the range for $U^* = 5.48$ was selected because, unlike the spanwise transition from 2S near the base to 2P near the midspan, which has previously been observed [47, 49, 87], the anticipated base to midspan wake transition from 2P to 2S has not yet been reported. The hybrid wake with 2P and 2S shedding in spanwise regions with relatively small and large structural oscillations, respectively, is of interest since VIV investigations [27, 34] typically show 2P shedding to occur at greater amplitudes of oscillation than 2S shedding. The range for $U^* = 7.08$ was selected to focus on the vortex dislocations at the boundary between the desynchronized regime and 2P shedding. This is of interest because the 2P vortices shed in synchronization with the structural motion are expected to interact and form connections with vortices in a desynchronized wake topology lower along the span. Furthermore, the quantitative investigation of the wake in this region of the map is intended to address significant departures from the predicted wake topology observed at $U^* = 8.55$ in Section 4.3 and at $U^* = 6.6$ by Kheirkhah *et al.* [49] for VIV of a pivoted cylinder.

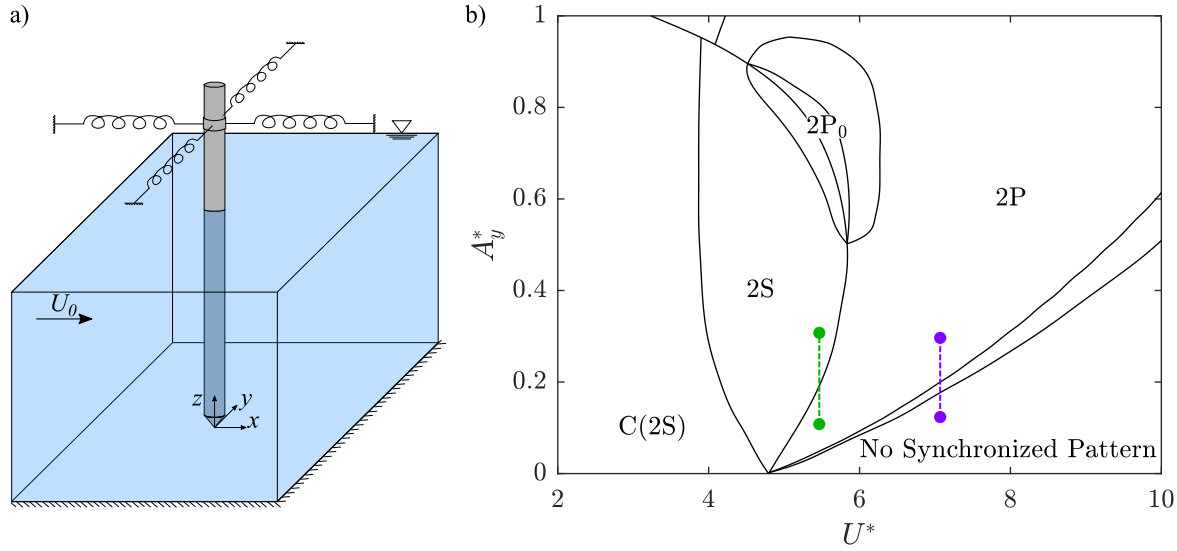

Figure 5.2: (a) Experimental geometry and (b) structural response overlaid on the Morse and Williamson [1] vortex shedding map for the hybrid wake investigations at $U^* = 5.48$ and $U^* = 7.08$. Data points, connected by a line, mark the extremes of the spanwise survey.

5.2 Instantaneous Flow Development

Instantaneous snapshots of the streamwise velocity obtained from PIV measurements in the vertical, $x - z$, plane are depicted in Figs. 5.3a–c for the stationary, $U^* = 5.48$, and $U^* = 7.08$ cases, respectively. The plane is positioned at $y/D = 1.25$ to pass through the dominant spanwise coherent structures forming on one side of the wake, which are identifiable by the bands of high and low streamwise velocity, while avoiding measurement of the separated shear layer. The flow in Fig. 5.3 is from left to right and the black dashed lines indicate the extent of the spanwise investigation in the horizontal $x - y$ plane.

For the stationary case, the spanwise vortices in Fig. 5.3a are nearly uniform along the span and, from visual inspection, have a streamwise wavelength of approximately $2D$. This is expected for a uniform flow; however, the free stream characterization in Appendix C shows that the streamwise velocity is slower than the free stream in the region $z/D \lesssim 8$. The result is cellular shedding, which was confirmed through observation of sequential instantaneous streamwise velocity fields and is further analyzed in Appendix F. It is important to note that the cellular shedding occurs below the spanwise region where measurements were performed in multiple $x - y$ planes, $8.5 \lesssim z/D \lesssim 16$.

For the VIV cases, the velocity magnitudes induced by vortical structures are notably

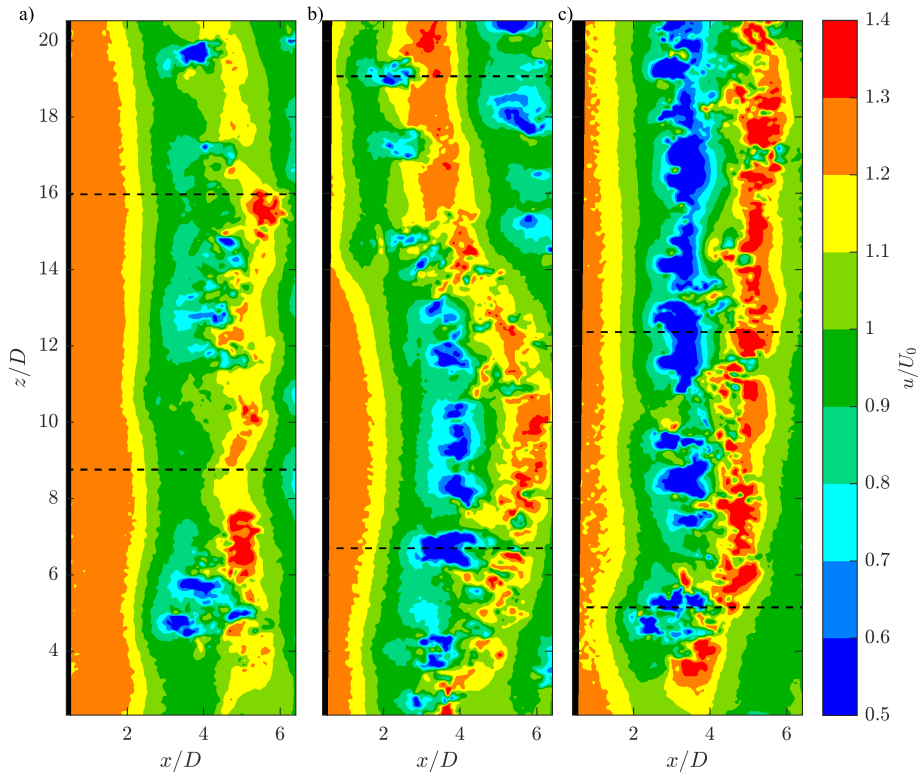

Figure 5.3: Instantaneous streamwise velocity fields in the $x-z$ plane for (a) stationary cylinder, (b) $U^* = 5.48$, and (c) $U^* = 7.08$. Black dashed lines indicate the extent of measurements in multiple $x-y$ planes. The flow is from left to right.

stronger than in the stationary case, but have approximately the same streamwise wavelength. The contrast between bands is most evident for the case $U^* = 7.08$ and is attributed to where the plane crosses the vortices as well as the vortex pattern in the wake. Unlike the nearly spanwise uniform structures in the stationary case, the vortices are curved for $U^* = 5.48$ in Fig. 5.3b and tilted downstream for $U^* = 7.08$ in Fig. 5.3c. This deformation is indicative of spanwise changes in vortex shedding and a transition in the wake topology.

Instantaneous snapshots of the vorticity derived from PIV measurements in the horizontal, $x-y$, plane are depicted in Fig. 5.4 at select heights for the stationary, $U^* = 5.48$, and $U^* = 7.08$ cases. These snapshots are representative of the typical vortex shedding patterns, despite some variations from cycle-to-cycle. The vorticity fields show that separated shear layers in the near wake roll up to form vortices that are shed periodically to form an alternating wake pattern. The streamwise location of vortex formation is relatively

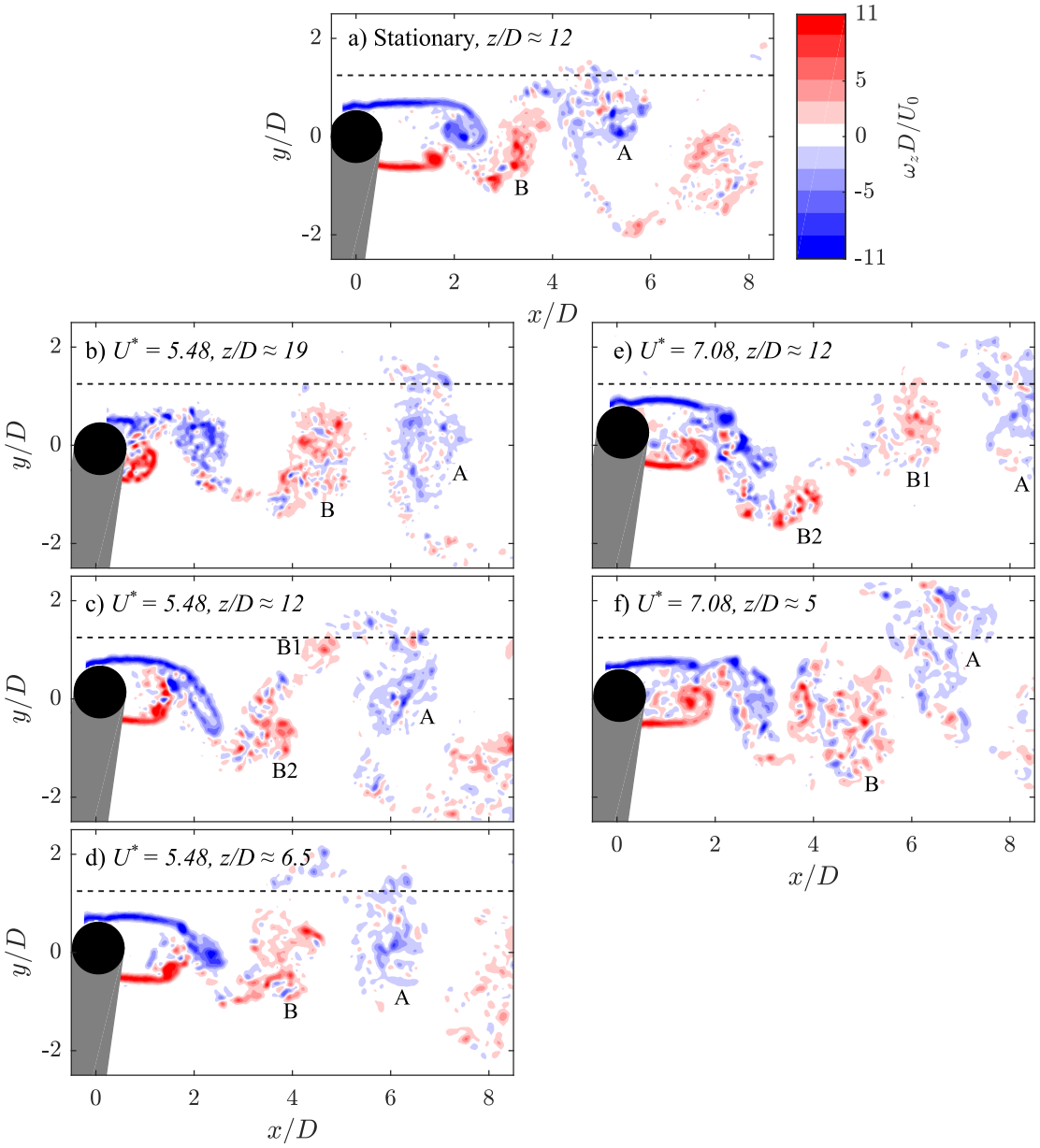

Figure 5.4: Instantaneous vorticity fields in the $x-y$ plane for (a) stationary cylinder at $z/D \approx 12$, (b, c & d) $U^* = 5.48$ at $z/D \approx 19$, 12 & 6.5, respectively, and (e & f) $U^* = 7.08$ at $z/D \approx 12$ & 5, respectively. The black dashed line indicates the location of the vertical $x-z$ measurement plane.

consistent along the span for the stationary cylinder and the VIV case at $U^* = 7.08$; however, it moves upstream with increasing z/D at $U^* = 5.48$. This upstream shift agrees with the curvature of the vortex structures in the instantaneous streamwise velocity snapshots in the $x - z$ plane (Fig. 5.3b) and causes reorientation of the vorticity in the dominant structures. Since the curvature is relatively small, nearly all the vorticity of the structure is accounted for when derived from $x - y$ planar wake measurements.

Inspection of the instantaneous vorticity fields shows that wake topology is consistently 2S along the span for the stationary cylinder, whereas the VIV cases exhibit hybrid shedding. For $U^* = 5.48$, the wake topology transitions along the span from 2S to P+S to 2S. The lower and upper planes (Figs. 5.4d and 5.4f, respectively) exhibit 2S shedding, whereby the two oppositely signed vortices, A and B, are shed within one oscillation period. Positive vortex B splits to form B1 and B2 in the middle plane (Fig. 5.4c), resulting in a P+S pattern involving a vortex pair, A and B1, and a single vortex, B2, shed each oscillation period. For the VIV case at $U^* = 7.08$, the wake topology transitions from 2S to P+S. The transition similarly occurs because positive vortex B in the lower plane (Fig. 5.4f) splits into two vortices, B1 and B2, in the upper plane (Fig. 5.4e) to form the P+S shedding pattern. Analysis of the wake development and changes along the span are outlined in more detail in the following sections.

5.3 Time Averaged Flow Field Characteristics

Previous analysis of the instantaneous fields indicates the presence of spanwise changes in the wake topology. The discussion in this section aims to present some of the trends relating to these spanwise changes through investigation of the time averaged wake characteristics. Figures 5.5–5.7 present the normalized mean and RMS contours of the streamwise and transverse velocity components for the stationary, $U^* = 5.48$, and $U^* = 7.08$ cases, respectively. For clarity, the figures show results in every third plane within the investigated region.

In general, the VIV cases have a greater impact on the wake than the stationary case. The wakes for $U^* = 5.48$ and $U^* = 7.08$ are wider and have stronger velocity fluctuations than the wake for the stationary case. This is revealed by the transverse extent of the contours in the mean streamwise velocity fields and the magnitude of the peaks in the RMS fields. Examination of the mean streamwise velocity fields shows the wake is symmetric about the wake centerline, $y/D = 0$, for the stationary case and asymmetric for the VIV cases, where the mean streamwise velocity is lower on the negative transverse side of the wake centerline, $y/D < 0$. This is a result of the vortex dynamics during the shedding

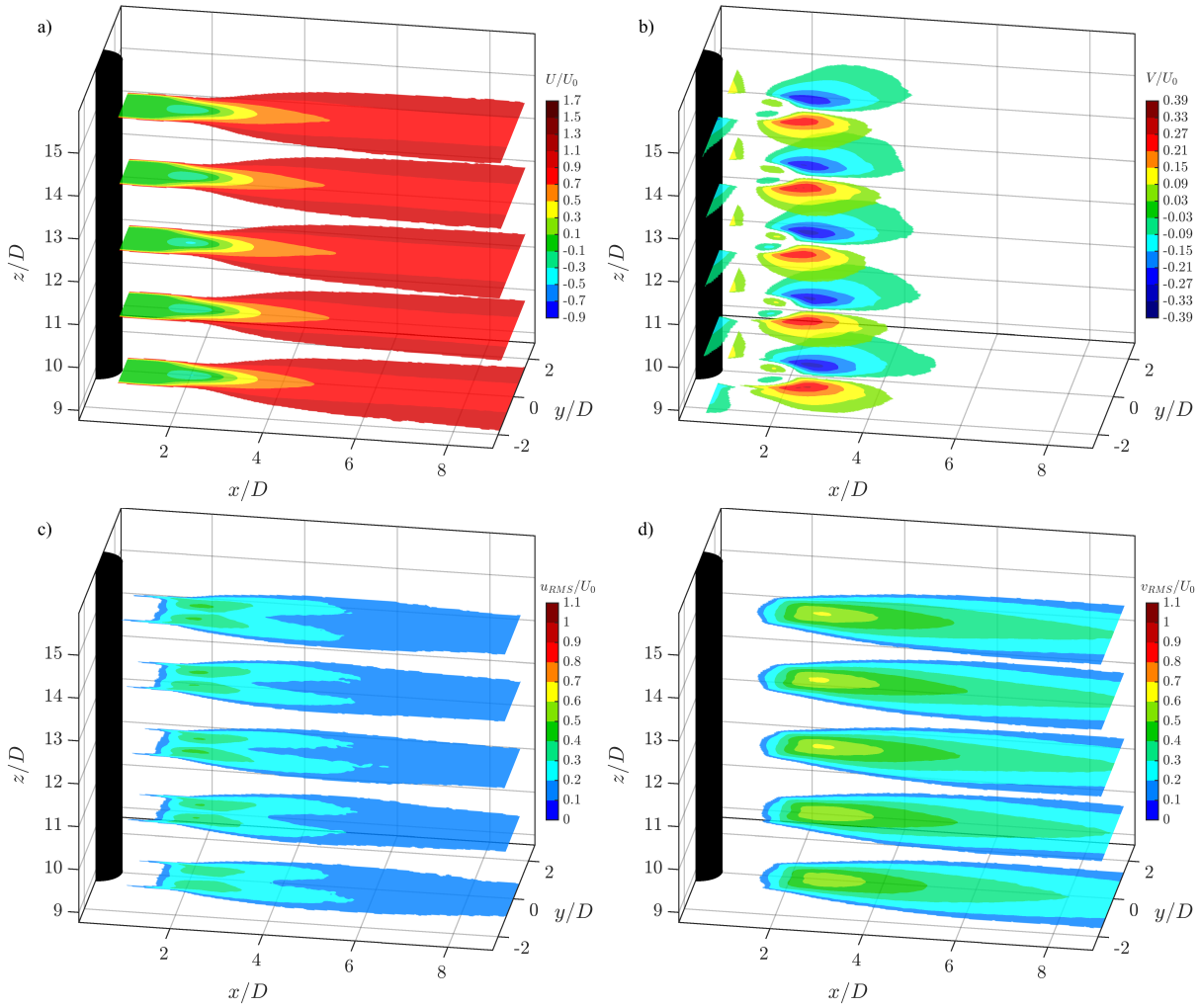

Figure 5.5: Mean and RMS contours of the streamwise, (a) and (c), respectively, and transverse, (b) and (d), respectively, velocity for the stationary cylinder case. Note, every third plane is shown for clarity.

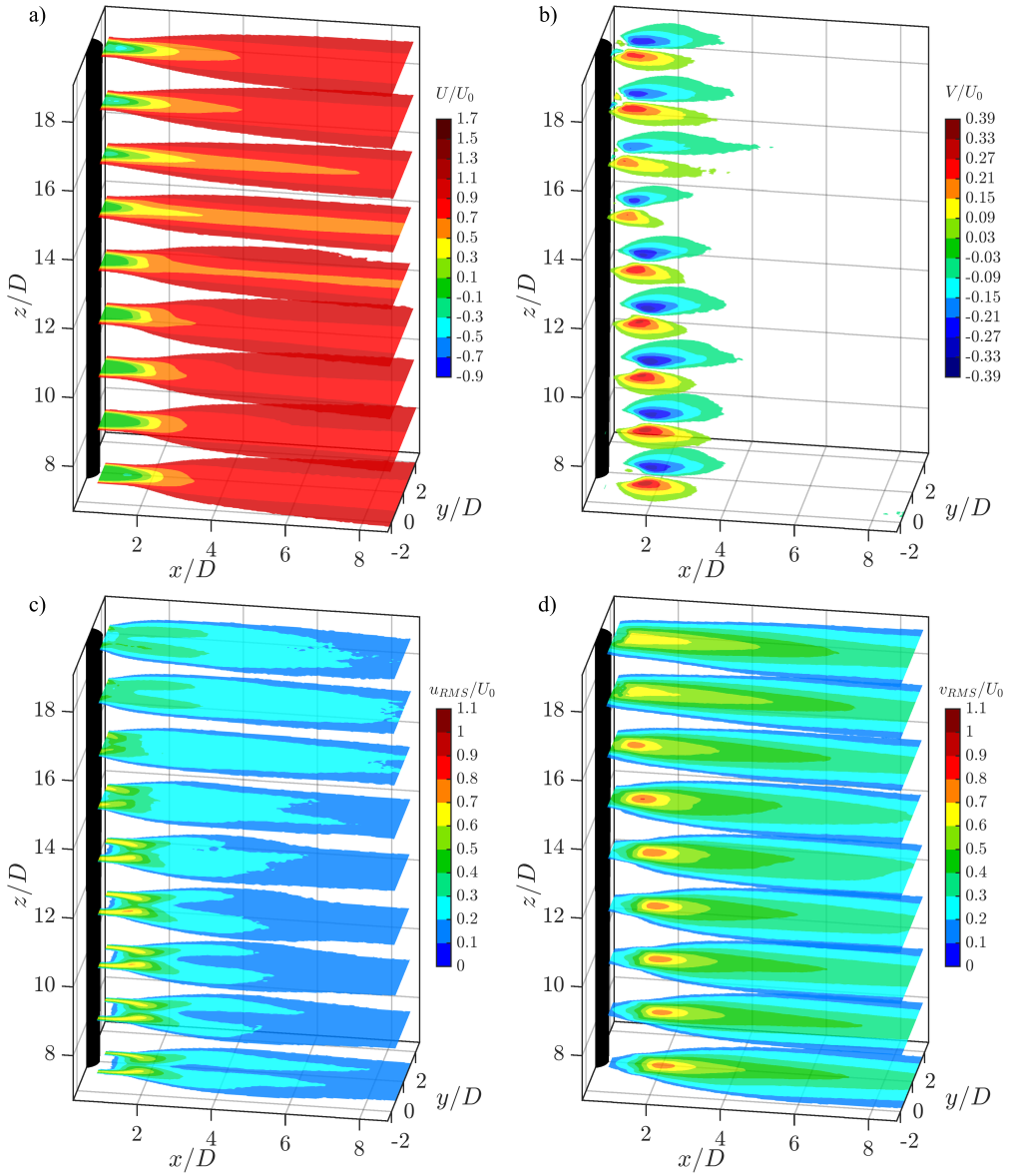

Figure 5.6: Mean and RMS contours of the streamwise, (a) and (c), respectively, and transverse, (b) and (d), respectively, velocity for $U^* = 5.48$. Note, every third plane is shown for clarity.

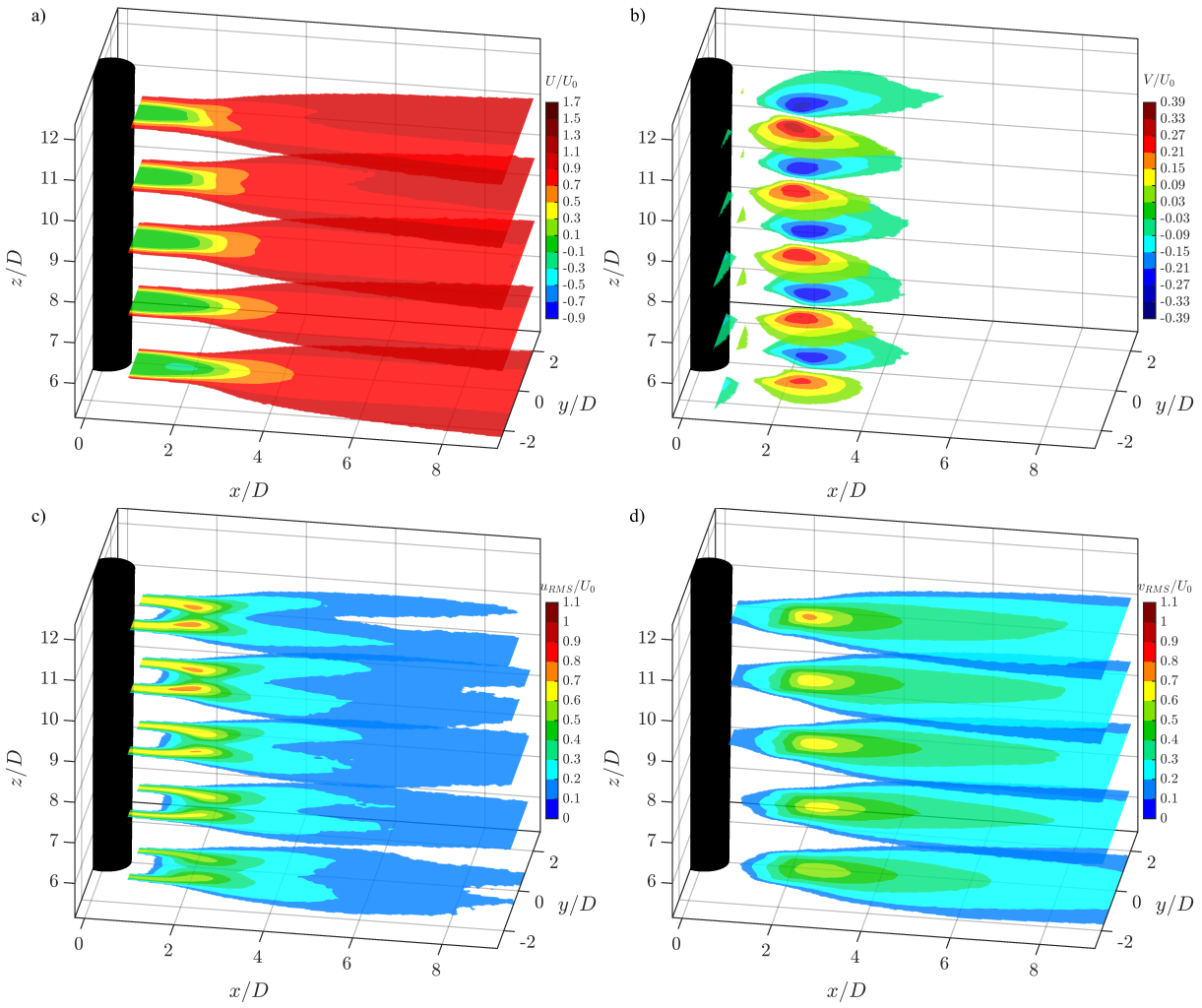

Figure 5.7: Mean and RMS contours of the streamwise, (a) and (c), respectively, and transverse, (b) and (d), respectively, velocity for $U^* = 7.08$. Note, every third plane is shown for clarity.

process as discussed in Section 4.4, and is linked to the direction of elliptic trajectory. Further analysis of the wake half-width in this section provides quantitative assessment of the asymmetry.

In all cases, the recirculation region is indicated by the zone downstream of the cylinder with negative mean streamwise velocity values. It is largest for the stationary case and becomes smaller as the amplitude of oscillation increases for the VIV cases. It was verified in Section 4.4 that this region becomes indiscernible higher along the span for cases with large amplitudes of oscillation. The location of vortex roll up occurs near the downstream extent of the recirculation region where the velocity fluctuations are greatest. Various definitions exist for the vortex formation length [133–135]; however, the findings from Section 4.4 indicate the streamwise location of the maximum v_{RMS} along the wake centerline provides a formation length estimate that agrees with estimates based on vortex identification for both the stationary case and the investigated VIV cases. Qualitative observation of v_{RMS} peaks in Figs. 5.5d and 5.7d indicates the formation length is relatively consistent along the span for the stationary and $U^* = 7.08$ cases, whereas they shift upstream with increasing z/D for $U^* = 5.48$ in Fig. 5.6d.

In addition to the vortex formation length, other parameters used to quantitatively characterize the mean streamwise flow development are defined in Fig. 5.8. The following discussion uses $u_d(x, y)$ and $u_{d\ Max}$ to denote the local velocity deficit and the maximum velocity deficit in the wake, respectively. The velocity deficit is determined as the difference between the streamwise velocity at the transverse extent of the wake measurements and the local streamwise velocity, $u_d = U_e - U$. The wake half-width, d_{wake}, is the transverse distance from the wake centerline to the point where the velocity deficit is $0.5u_{d\ Max}$. Since the wake can be transversely asymmetric, it is necessary to specify the half-width corresponding to the positive and negative sides of the wake as d^+_{wake} and d^-_{wake}, respectively.

Spanwise variation of the formation length, wake half-width at the location of maximum v_{RMS}, and maximum velocity deficit with respect to z/D is depicted in Fig. 5.9. Dashed lines are linear fits to the data using a least squares technique. For the stationary case, the wake characteristics show good spanwise uniformity. For the VIV case at $U^* = 5.48$, there are three regions, approximately separated at $z/D \approx 13.5$ and 16. In the lower region ($z/D \lesssim 13.5$), the wake is wider, has a shorter formation length, and incurs a smaller maximum velocity deficit than in the upper region ($z/D \gtrsim 16$). Furthermore, distinct spanwise trends in the wake characteristics distinguish these regions. In the lower region, the formation length and maximum velocity deficit show a marginal decrease along the span, whereas they are nearly uniform in the upper region. The wake half-width increases considerably along the span in the lower region and decreases in the upper region. Such

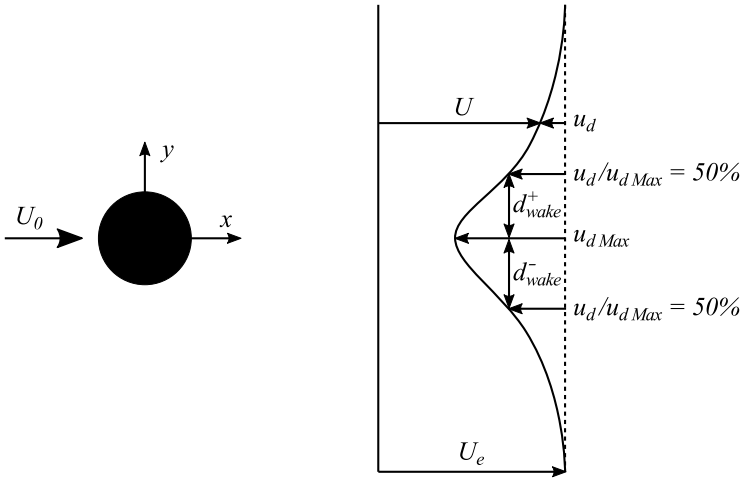

Figure 5.8: Wake half-width and velocity deficit nomenclature.

changes in the wake characteristics between the lower and upper regions are consistent with the transition from P+S to 2S shedding outlined in the instantaneous vorticity snapshots (Figs. 5.4b and 5.4c). The 2S vortices higher along the span form further upstream than the P+S vortices near the midspan. Furthermore, the wake width for 2S shedding is smaller than P+S shedding because 2S vortices do not advect as far from the wake centerline as P+S vortices [17, 54]. Changes in the wake characteristics between the lower and upper regions occur over the intermediate region ($13.5 \lesssim z/D \lesssim 16$) instead of one specific height because of cycle-to-cycle variations in vortex shedding, where the spanwise location of the connection between P+S and 2S vortices may vary. The transient nature of this vortex dislocation is further examined in Section 5.5 since the results in Fig. 5.9 are time averaged. For the VIV case at $U^* = 7.08$, the spanwise changes in formation length, wake half-width, and maximum velocity deficit are relatively consistent with little deviation from the linear fits. Since the spanwise extent of investigation for this case stops below the transitional range observed for $U^* = 5.48$, it is not possible to use the acquired data to determine whether the wake characteristics will exhibit similar changes. However, such changes in the wake characteristics higher along the span are not predicted to occur for $U^* = 7.08$ because the Morse and Williamson [1] shedding map (Fig. 5.2b) does not indicate a wake transition to 2S vortex shedding over this spanwise range.

A comparison between cases shows that the freedom to oscillate generally causes a shorter formation length and a wider wake with a smaller velocity deficit. However, above $z/D \approx 16$ for the VIV case at $U^* = 5.48$, the wake width and maximum velocity deficit are comparable to the stationary case even though the cylinder is oscillating with a transverse

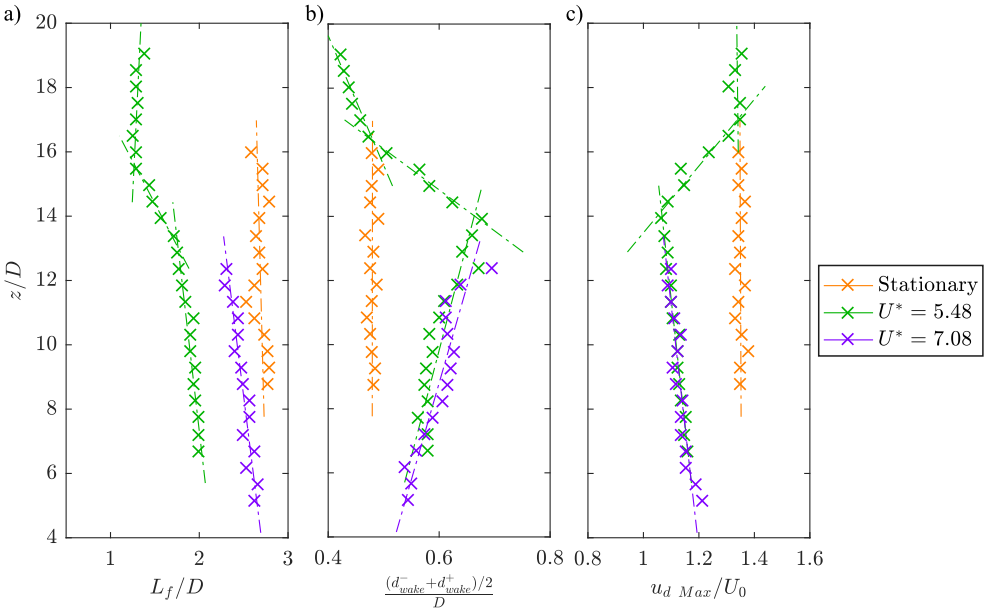

Figure 5.9: Spanwise variation of (a) formation length as per the location of maximum v_{RMS}, (b) wake half-width at the streamwise location of maximum v_{RMS}, and (c) maximum velocity deficit. Dashed lines are least square fits to data segments.

amplitude of $A_y \approx 0.3D$. Such a similarity may be attributed to the wake topology as opposed to the structural motion since both cases exhibit 2S vortex shedding in this spanwise region. Below $z/D \approx 13.5$, trends in the wake width and maximum velocity deficit of both VIV cases are comparable, which may be attributed to both cases exhibiting a transition from 2S to P+S shedding in this region, as indicated by the instantaneous vorticity snapshots (Fig. 5.4).

Figure 5.10 depicts spanwise changes of the wake half-width calculated at the location of maximum v_{RMS} in each horizontal plane. The half-width is approximately equal on the positive and negative sides of the wake centerline for the stationary case, whereas, for the VIV cases, the half-width is larger on the negative side, $y/D < 0$. The observed asymmetry agrees with the findings of Section 4.4, which employs the kinematics and dynamics of vortices to conclude that asymmetry is governed by the direction of elliptical orbit due to its impact on wake vortex dynamics. For the case of $U^* = 5.48$, the asymmetry is significant below $z/D \approx 14$ where P+S shedding is observed; whereas, the wake becomes mostly symmetric higher along the span where 2S shedding is observed. Such observations from the time averaged wake characteristics agree with the results of Chapter 4, which found symmetry and asymmetry in the wakes of 2S and 2P shedding, respectively. On

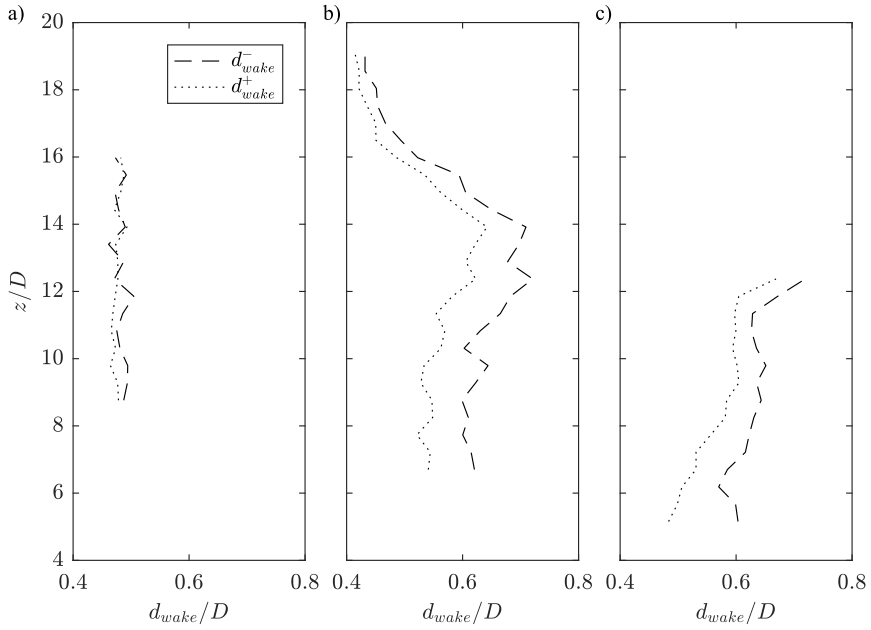

Figure 5.10: Spanwise variation of wake half-width at the streamwise location of maximum v_{RMS} for (a) stationary cylinder, (b) $U^* = 5.48$, and (c) $U^* = 7.08$.

the other hand, these results disagree lower along the span where the half-width indicates an asymmetric wake for both VIV cases despite the instantaneous vorticity snapshots depicting 2S shedding. The cause for this wake asymmetry was not resolved in the present study, but is speculated to result from the the vortex connections at the transition from 2S to P+S shedding higher along the span.

Streamwise variation of the wake half-width downstream of the formation length is depicted in Fig. 5.11. The half-width at a given streamwise location is relatively consistent along the cylinder span for the stationary case (Fig. 5.11a). In the streamwise direction, the half-width increases by approximately $0.4D$ within the first two diameters downstream of the vortex formation region, $x = L_f$, and remains nearly constant thereafter. Extrapolation of these measurements agrees well with the investigations by Hussain and Hayakawa [136], Ferré and Giralt [137], and Zhou *et al.* [138], who observed wake half-widths of $d_{wake} = 0.80$, 0.90, and 0.79, respectively, at $x/D = 10$ in the wake of a stationary cylinder. Similarly, for the VIV case at $U^* = 5.48$ in Fig. 5.11b, the half-width closer to the pivot point, e.g. at planes $z/D \approx 6.5$ and 9, initially increases by approximately $0.6D$ then remains nearly constant. Near the downstream extent of measurement, the half-width becomes smaller midway along the span, then increases higher along span. Such changes are surprising because the P+S vortices observed near the midspan in Fig. 5.4c advect further from the

wake centerline and are expected to cause a wider wake. It is speculated that the thinner wake results from the asymmetric wake for P+S shedding. For the VIV case at $U^* = 7.08$, the streamwise variation of half-width generally increases with increasing z because of the spanwise linear variation of amplitude and the wake topology transition from 2S to P+S shedding. The wake half-width near the streamwise extent of measurement is the largest for this case because it is characterized by the larger amplitude of structural oscillation.

Bishop and Yarusevych [139] and Okamoto and Takeuchi [140] examine the half-wake width of a stationary cylinder in the near wake for various blockage ratios. They define the half-wake width, d_{98}, as the transverse distance between the wake centerline and the location where the mean streamwise velocity is 98% of the free stream ($U/U_0 = 0.98$). This definition is different from the previously discussed wake half-width, d_{wake}, which is based on the velocity deficit. Streamwise variation of d_{98} for a stationary cylinder is depicted in Fig. 5.12 for the present study as well as the studies of Bishop and Yarusevych [139] and Okamoto and Takeuchi [140] for a blockage ratio of 5%. While d_{98} similarly increases with downstream progression and exhibits spanwise consistency when compared to d_{wake} in Fig. 5.11a, the value of d_{98} is larger than d_{wake} at all streamwise locations due to their different definitions. The half-wake width is substantially different from the results of Bishop and Yarusevych [139] and Okamoto and Takeuchi [140] because each study was performed at a different Reynolds number. Bishop and Yarusevych [139] and Okamoto and Takeuchi [140] investigated the wake at Re = 57000 and 32200, respectively, whereas Re = 3100 in the present investigation. Consequently, since the length of the formation region depends upon the Reynolds number [4], the half-wake width at any given streamwise location is different between studies. However, there is good agreement between the three studies if d_{98} is shifted over x/D such that the formation lengths coincide.

5.4 Vortex Shedding Frequency

The previous section assessed spanwise changes in the time-averaged wake characteristics. The results suggest that distinct changes in the discussed characteristics are associated with the spanwise transition of wake topology and amplitude variation along the span. This section employs a frequency analysis of the velocity field to analyze the vortex shedding process and investigate the transient nature of the wake topology along the span.

Figures 5.13a–c present spectra of the transverse velocity signal at the location of maximum v_{RMS} for each horizontal, $x - y$, plane in the spanwise PIV investigation of the stationary, $U^* = 5.48$, and $U^* = 7.08$ cases, respectively. All spectra exhibit a dominant peak at the vortex shedding frequency. For the stationary case, vortices are shed

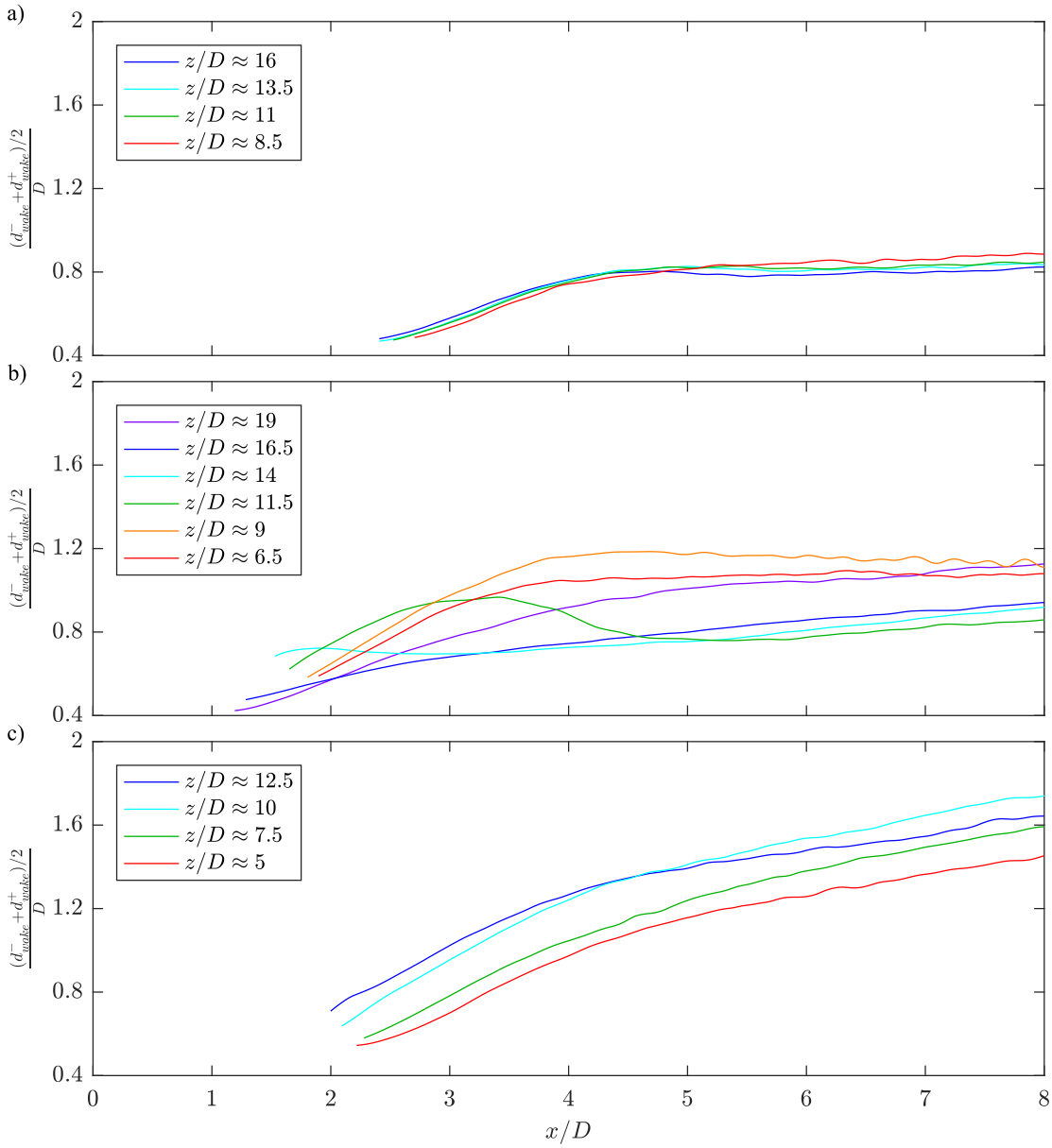

Figure 5.11: Streamwise variation of wake half-width downstream of the formation length for (a) stationary cylinder, (b) $U^* = 5.48$, and (c) $U^* = 7.08$.

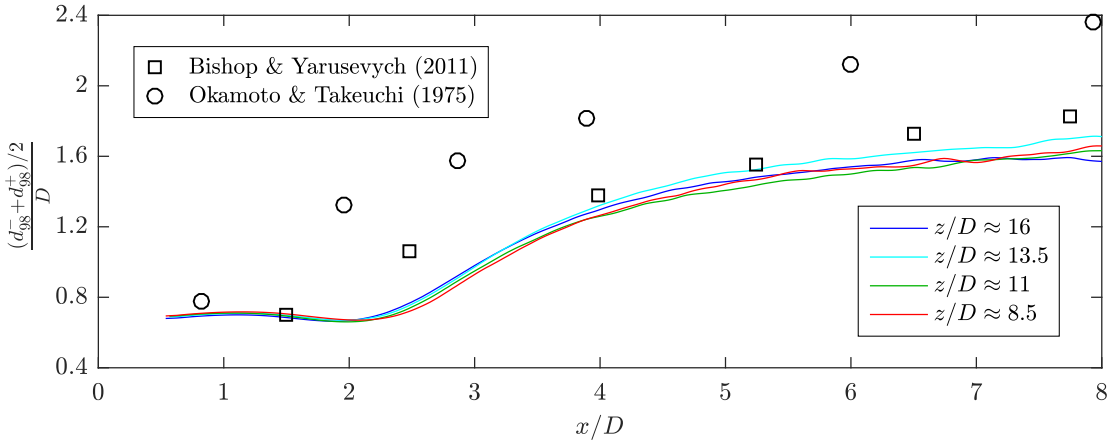

Figure 5.12: Streamwise variation of half-wake width, defined as the transverse distance between the wake centerline and the location where $U/U_0 = 0.98$, for a stationary cylinder. The data for Bishop and Yarusevych [139] and Okamoto and Takeuchi [140] pertain to Re = 57000 and 32200, respectively, and a blockage ratio of 5%.

at $fD/U_0 \approx 0.205$, which agrees with the results of Norberg [141] for a similar Reynolds number. The peak power bands in the spectra for the VIV cases are more concentrated than the stationary case and are shifted to the non-dimensionalized natural frequency, $f_nD/U_0 = 0.182$ and 0.141 for $U^* = 5.48$ and 7.08, respectively, because vortex shedding locks onto the structural oscillations. For the case at $U^* = 5.48$, the peak power is less concentrated in the region $13.5 \lesssim z/D \lesssim 17$ where the wake topology transitions from P+S to 2S. This is likely caused by cycle to cycle variation in the spanwise location of the vortex dislocations and is discussed in more detail in Section 5.5. For the VIV case at $U^* = 7.08$, there is notable energy content near the vortex shedding frequency of a stationary cylinder, $f_sD/U_0 \approx 0.205$, within $5 \leq z/D \leq 8$. This suggests that vortex shedding occurs at two frequencies and may switch from cycle-to-cycle. A peak at f_sD/U_0 is not observed in the other VIV case because of the limited spanwise extent of investigation.

Spectrogram analysis is used to examine temporal variation in the frequency of the dominant energy content in the wake. Figures 5.14a–c depict spectrograms of the transverse velocity signal sampled in the plane $z/D \approx 12$ at the location of maximum v_{RMS} for the stationary, $U^* = 5.48$, and $U^* = 7.08$ cases, respectively. Windows used for each Fourier transform contain data capturing approximately seven vortex shedding cycles and were overlapped by 75% to show the temporal evolution of spectral energy content. Similar to the spectra in Fig. 5.13, the dominant shedding frequency, indicated by the peak energy content, is near f_s for the stationary case and f_n for the VIV cases. The frequency of the

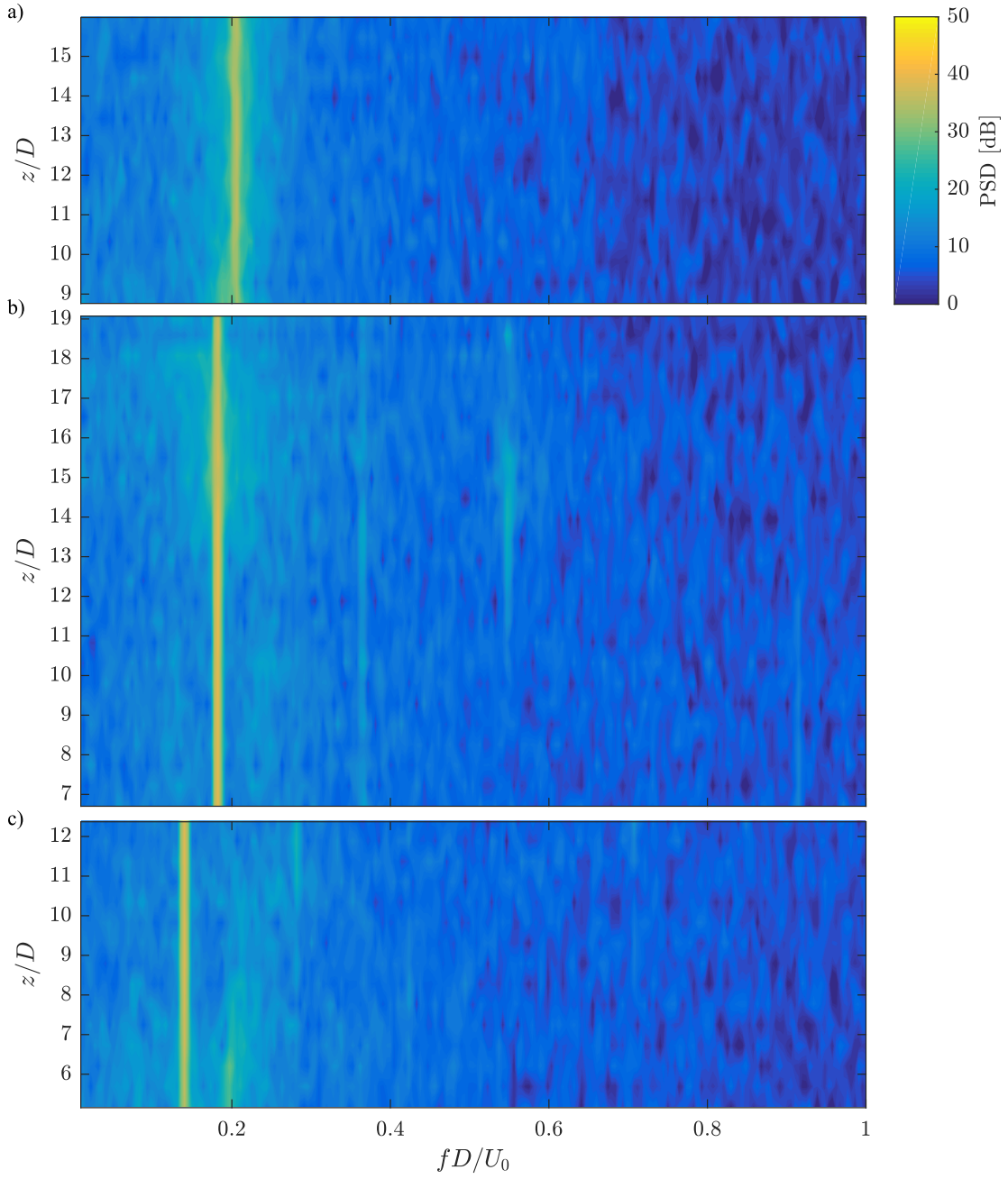

Figure 5.13: Spectra of the transverse velocity signal at the location of maximum v_{RMS} in each $x-y$ plane for (a) stationary cylinder, (b) $U^* = 5.48$, and (c) $U^* = 7.08$.

dominant energy content fluctuates throughout time for the stationary case, whereas, for the VIV cases, the frequency remains nearly constant. Temporal consistency along with a greater peak energy content for the VIV cases are a result of vortex shedding locking onto the structural oscillations. Figure 5.14d depicts the spectrogram lower along the span at $z/D \approx 5$ for $U^* = 7.08$. The peak energy content is weaker and intermittently switches between f_n and f_s. Evidence of vortex shedding at f_s is attributed desynchronization of the wake development with respect to the cylinder motion, as per predictions from the Morse and Williamson [1] shedding map. The observed intermittency is likely caused by cycle-to-cycle variations in the spanwise location of connection between vortical structures shedding at the f_n and f_s.

Spectral peaks at higher harmonics are indiscernible in the spectra for the stationary case (Fig. 5.13a), but are identifiable in the spectra for the VIV cases (Figs. 5.13b and 5.13c). Such results from frequency analysis of the transverse velocity signal depend upon the location at which the signal is sampled. Figures 5.15–5.17 depict spatial contours of the spectral energy content for the stationary, $U^* = 5.48$, and $U^* = 7.08$ cases, respectively, where the spectral energy of the transverse velocity signal is integrated over the bandwidths $0.9f_s < f < 1.1f_s$ (Fig. 5.15a) and $1.9f_s < f < 2.1f_s$ (Fig. 5.15b) for the stationary case, and $0.9f_n < f < 1.1f_n$ (Figs. 5.16a and 5.17a), $1.9f_n < f < 2.1f_n$ (Figs. 5.16b and 5.17b), and $0.9f_s < f < 1.1f_s$ (Fig. 5.17c) for the VIV cases. Regions of high energy associated with the dominant vortex shedding frequency are located on the wake centerline near the vortex roll up region; whereas, fluctuations at the second harmonic are concentrated approximately $0.5D$ off the wake centerline. Consequently, spectra of the transverse velocity signal along the wake centerline do not exhibit strong peaks at the harmonics, as evidenced in Fig. 5.13, where the signal is sampled at the maximum v_{RMS} along the wake centerline. Examination of spectra for the stationary case reveals that the second harmonic contains notably less energy than the dominant vortex shedding frequency, f_s, whereas the VIV cases exhibit significant spectral energy at the second harmonic as a result of the structural motion. For the VIV case at $U^* = 7.08$, spectral energy is largely associated with fluctuations at the natural frequency and its second harmonic higher along the cylinder's span (Figs. 5.17a and 5.17b). Near the bottom of the spanwise region of investigation, some of the energy shifts to the frequency of vortex shedding from a stationary cylinder (Fig. 5.17c) in agreement with the spectral peaks in Fig. 5.13c and the spectrogram analysis in Fig. 5.14d. It is predicted that this trend will persist to the base of the cylinder, whereupon the energy content associated with f_s will be the greatest, thus becoming the dominant vortex shedding frequency.

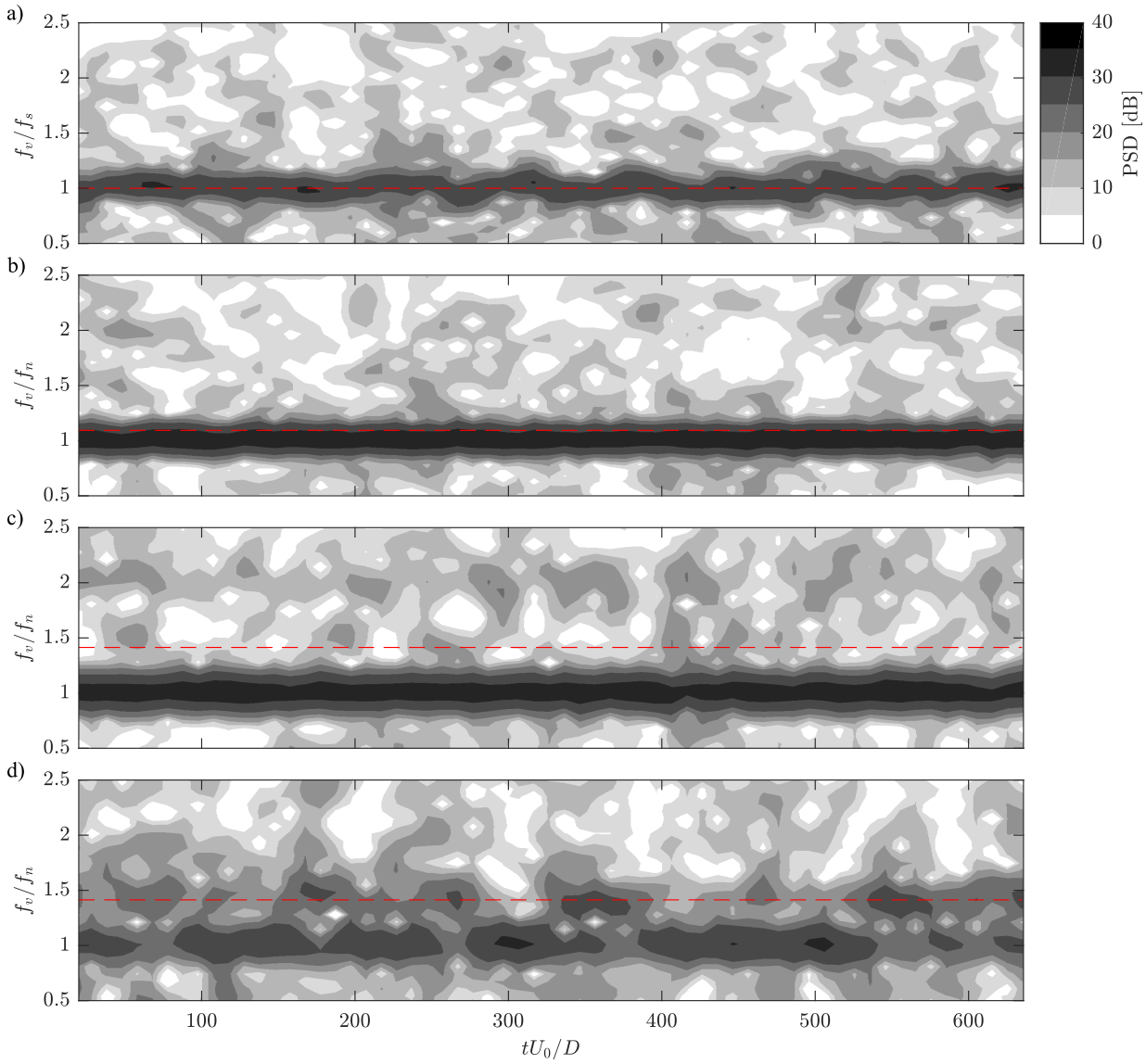

Figure 5.14: Spectrogram of the transverse velocity signal at the location of maximum v_{RMS} in the plane $z/D \approx 12$ for (a) stationary cylinder, (b) $U^* = 5.48$, and (c) $U^* = 7.08$, and the plane $z/D \approx 5$ for (d) $U^* = 7.08$. The red dashed line indicates the vortex shedding frequency of a stationary cylinder, f_s.

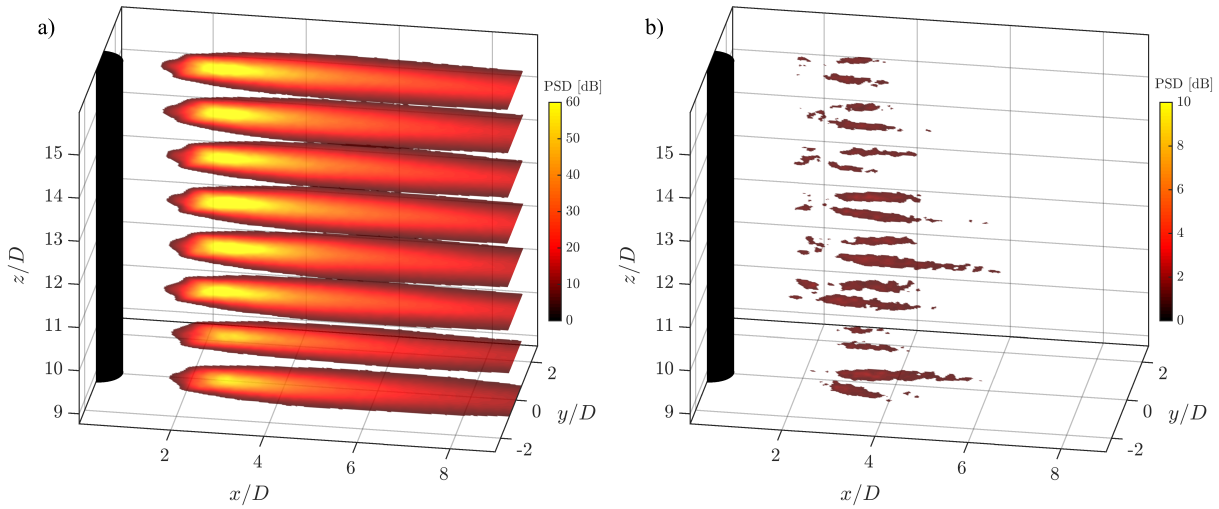

Figure 5.15: Spectral energy of the transverse velocity signal for the stationary cylinder integrated over the bandwidths (a) $0.9f_s < f < 1.1f_s$ and (b) $1.9f_s < f < 2.1f_s$. Note, every second plane is shown for clarity.

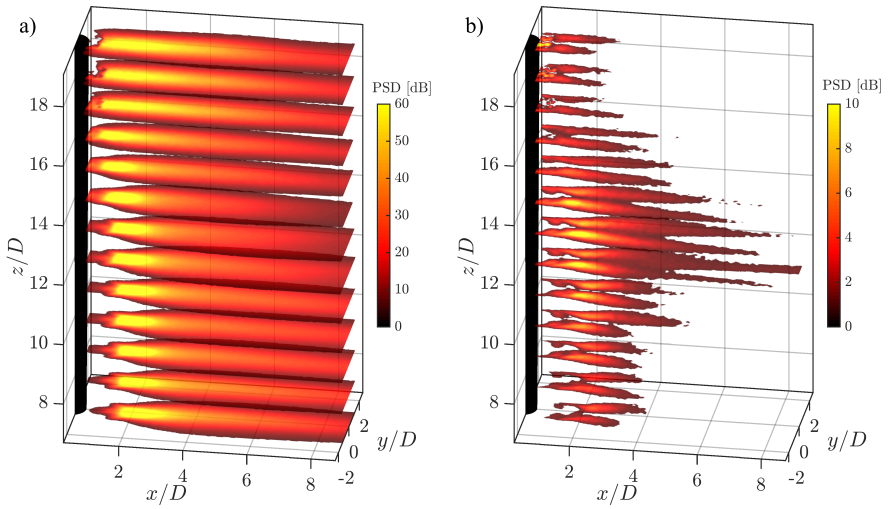

Figure 5.16: Spectral energy of the transverse velocity signal at $U^* = 5.48$ integrated over the bandwidths (a) $0.9f_n < f < 1.1f_n$ and (b) $1.9f_n < f < 2.1f_n$. Note, every second plane is shown for clarity.

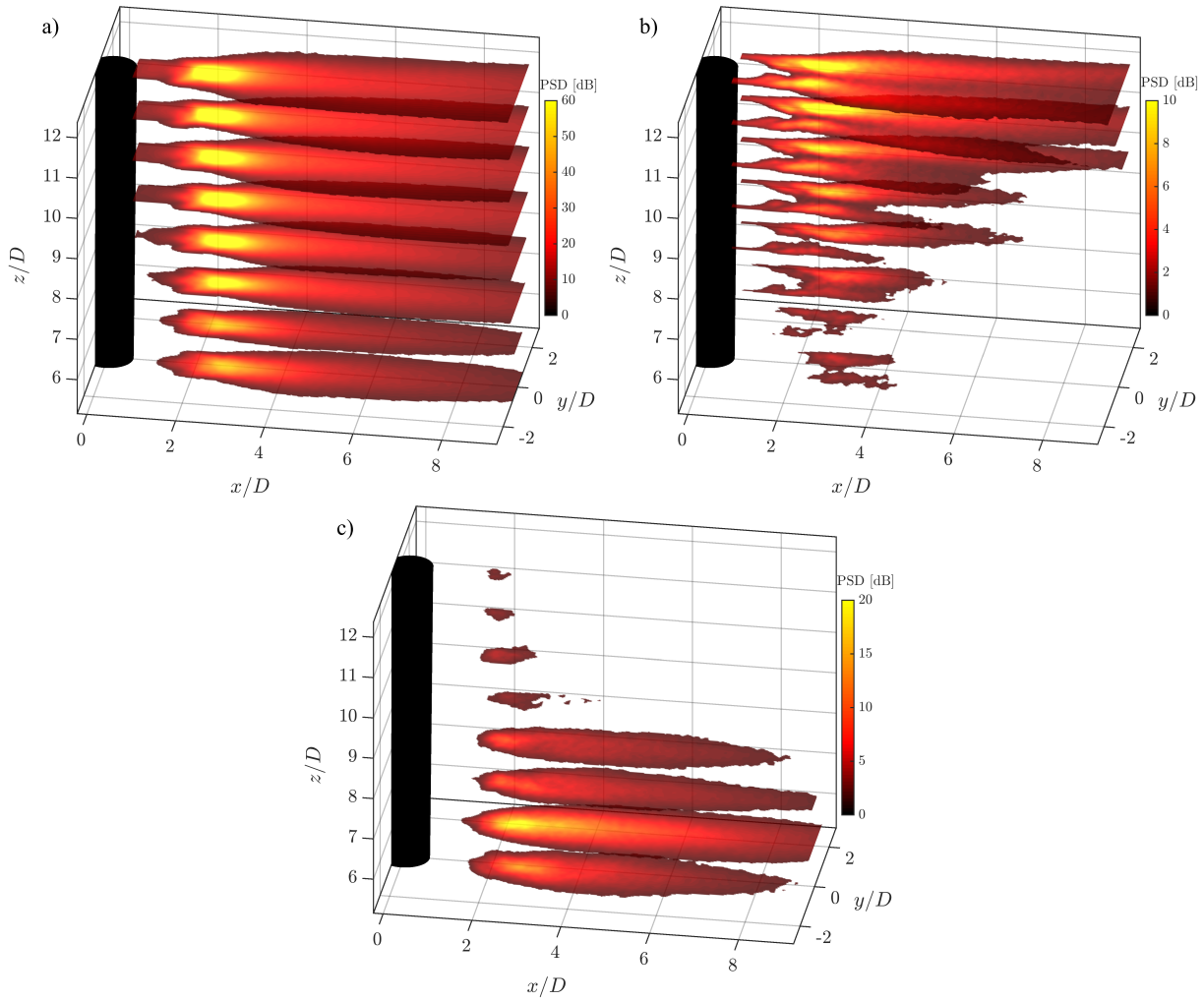

Figure 5.17: Spectral energy of the transverse velocity signal at $U^* = 7.08$ integrated over the bandwidths (a) $0.9f_n < f < 1.1f_n$, (b) $1.9f_n < f < 2.1f_n$, and (c) $0.9f_s < f < 1.1f_s$. Note, every second plane is shown for clarity.

5.5 Wake Reconstruction

This section investigates the spanwise changes in vortex shedding by reconstructing the 3D wake topology from phase averaged planar PIV measurements. The focus is to both qualitatively and quantitatively describe the dominant structures in the wake through analysis of vortex circulation and examination of the reconstructed fields.

The wake topology for the stationary cylinder was reconstructed from POD-based phase averaged velocity fields. The horizontal planes were aligned based on the vertical plane measurements by shifting the phase of each horizontal plane to maximize the cross correlation of streamwise phase averaged velocity signals at the intersection of the two planes. Figures 5.18a and 5.18b depict every second planar vorticity contour and the Q-criterion isosurfaces of $Q = 0.001Q_{max}$ coloured by the sign of spanwise vorticity, respectively. Figures 5.18c and 5.18d depict these fields half a period later in the vortex shedding cycle. For the VIV cases, the phase of each displacement based phase averaged velocity field in the horizontal plane was aligned using the cylinder position obtained from displacement measurements. The phase $\theta = 0$ was set as the instance when the cylinder crosses the transverse equilibrium, $y/D = 0$, in the positive transverse direction. Figures 5.19a and 5.19b depict the planar vorticity contours and Q-criterion isosurfaces, respectively, at the positive transverse peak of the cylinder trajectory for $U^* = 5.48$. The vorticity and Q-criterion fields are also depicted at the negative transverse peak in Figs. 5.19c and 5.19d. For the VIV case at $U^* = 7.08$, Fig. 5.20 similarly depicts the vorticity and Q-criterion fields at the positive and negative transverse peaks of cylinder motion.

The wake reconstruction for the stationary case in Fig. 5.18 clearly depicts a consistent 2S topology along the span, in agreement with observation of the instantaneous snapshots. Examination of the vorticity contours shows the vortex tube sheds from the cylinder at an earlier phase higher along the span, where the positive vortex at $x/D \approx 3.5$ in Fig. 5.18a is shed in the plane $z/D \approx 16$ while remaining connected to the shear layer at $z/D \approx 9$. Consequently, the vortex tubes are slightly curved within the investigated region. The curvature is caused by the wall effects at the base of the water tunnel, which are analyzed and discussed in Appendix C.

The wake for the VIV case at $U^* = 5.48$ is depicted in Fig. 5.19 and exhibits hybrid shedding with three distinct regions: 2S below $z/D \approx 7.5$, P+S within $7.5 \lesssim z/D \lesssim 13.5$, and 2S above $z/D \approx 13.5$. These regions agree with the instantaneous snapshots, but contradict the Morse and Williamson [1] shedding map, which predicts an overall transition from 2P to 2S along the span. Examination of the Q-criterion field in Fig. 5.19b shows that the positively signed vortex tube at $x/D \approx 3$ splits near $z/D \approx 7.5$ to form a leading and trailing vortex tube. The leading vortex tube, upstream of the split, persists along

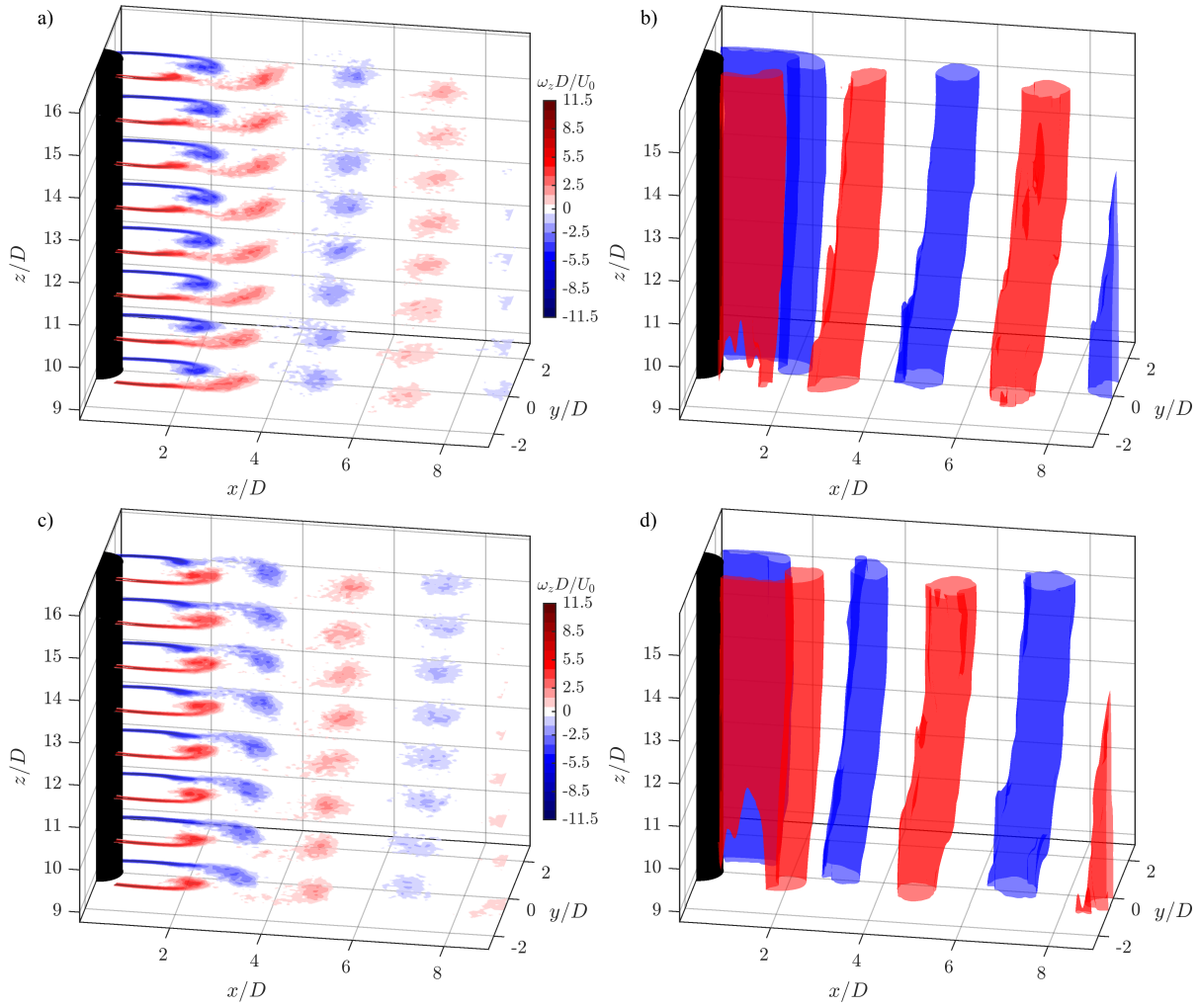

Figure 5.18: POD based phase averaged (a & c) planar vorticity contours and (b & d) Q-criterion isosurfaces of $Q = 0.001Q_{max}$ coloured by the spanwise vorticity in the wake of a stationary cylinder. There is a phase difference of π between (a & b) and (c & d). Note that every second vorticity plane is shown for clarity.

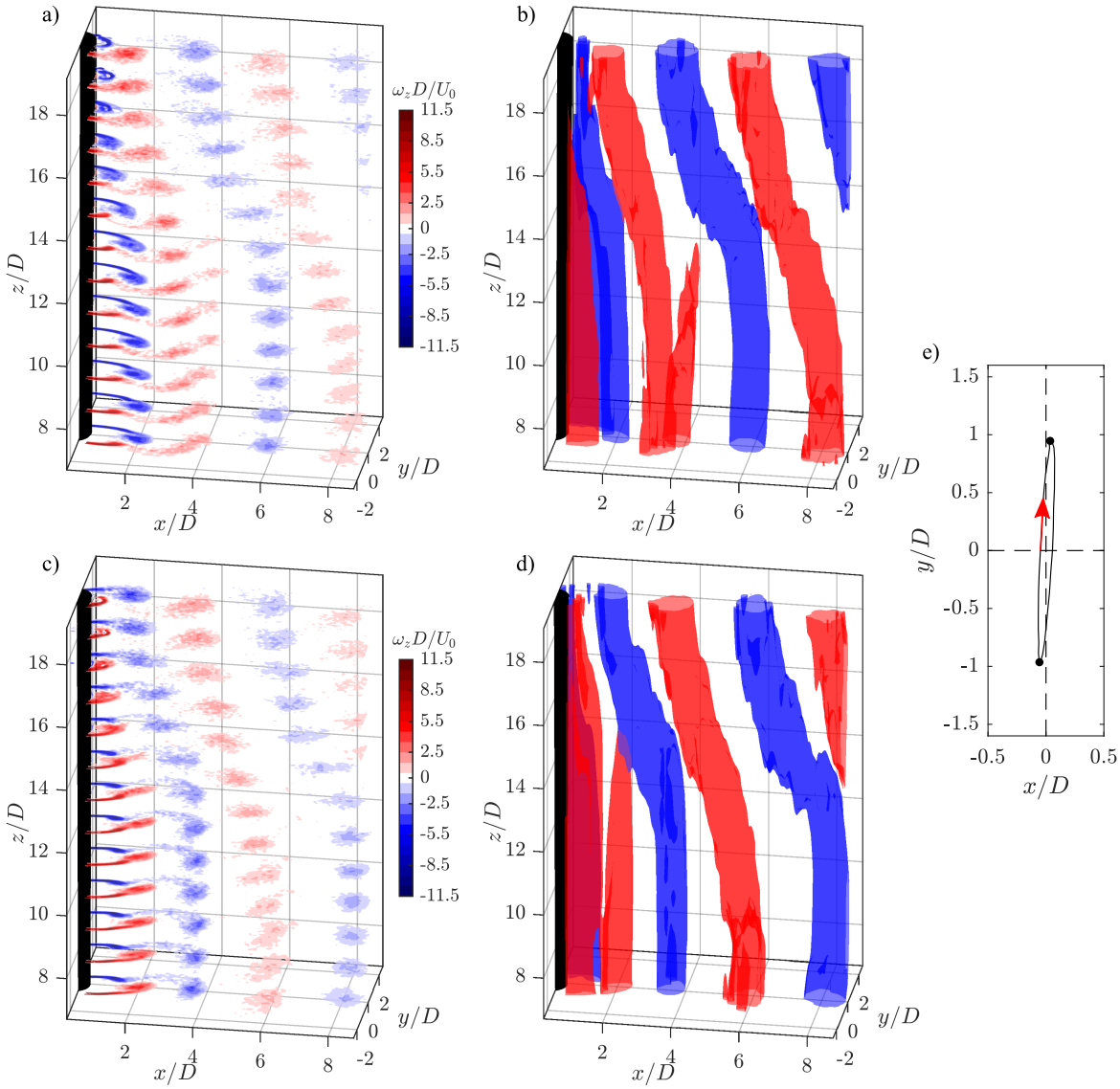

Figure 5.19: Displacement based phase averaged (a & c) planar vorticity contours and (b & d) Q-criterion isosurfaces of $Q = 0.001Q_{max}$ coloured by the spanwise vorticity for $U^* = 5.48$. The cylinder tip is located at the (a & b) positive and (c & d) negative transverse peaks of the (e) phase averaged cylinder tip trajectory ($\theta = \pi/2$ and $3\pi/2$, respectively). Note that every second vorticity plane is shown for clarity.

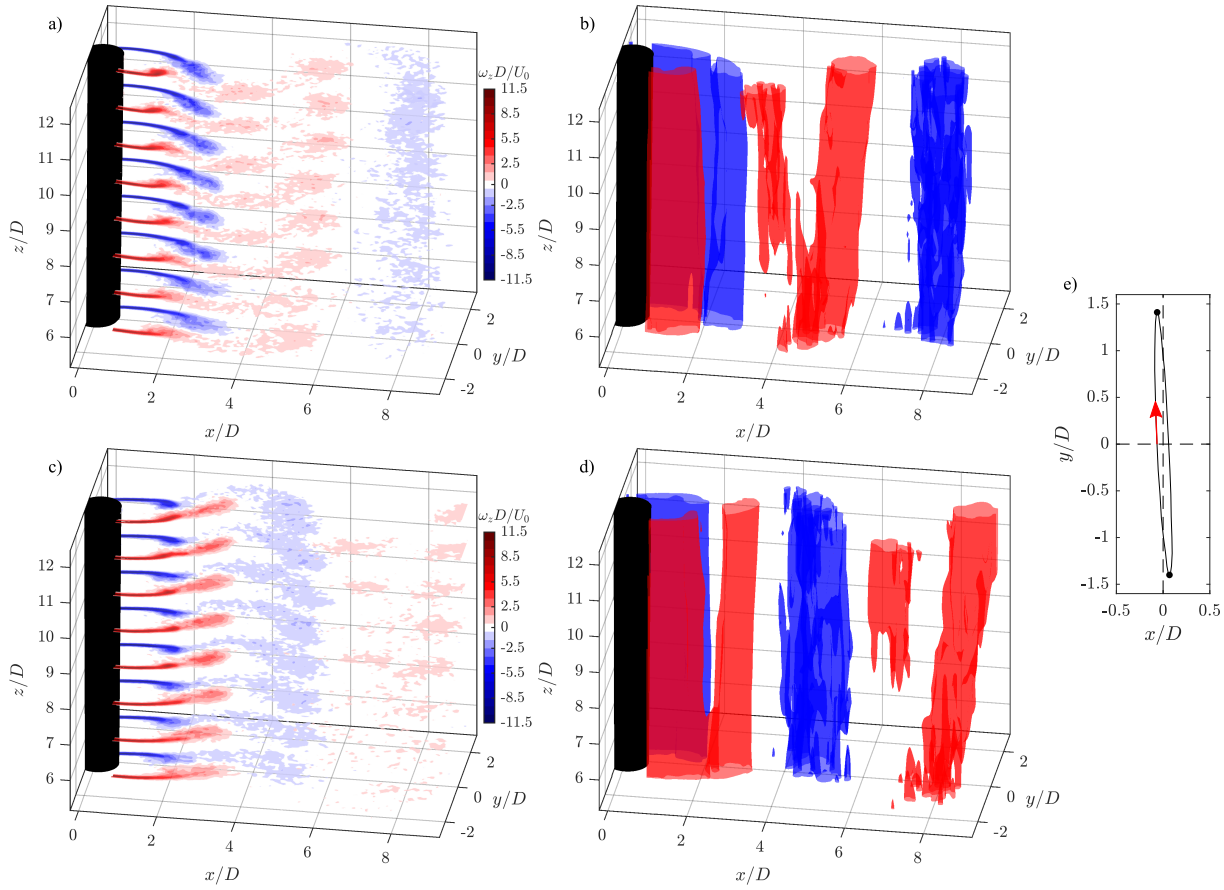

Figure 5.20: Displacement based phase averaged (a & c) planar vorticity contours and (b & d) Q-criterion isosurfaces of $Q = 0.001Q_{max}$ coloured by the spanwise vorticity for $U^* = 7.08$. The cylinder tip is located at the (a & b) positive and (c & d) negative transverse peaks of the (e) phase averaged cylinder tip trajectory ($\theta = \pi/2$ and $3\pi/2$, respectively). Note that every second vorticity plane is shown for clarity.

the span while the trailing vortex tube, downstream of the split, appears to dissipate as it approaches its leading counterpart, the negatively signed vortex tube. The observed decay of vorticity may be a consequence of either the cross annihilation of vorticity [66] and/or its reorientation from the spanwise direction into the streamwise and transverse directions, which cannot be quantified from 2D PIV in the $x-y$ plane. Section 5.5.1 focuses on the vortex dynamics in this region along the span. Throughout its advection downstream, the trailing positive vortex becomes weaker until the vorticity contours and Q-criterion in Figs. 5.19c and 5.19d, respectively, cannot resolve the trailing vortex splitting from the positive vortex at $x/D \approx 6$. The negatively signed vortex tube at $x/D \approx 3.5$ in Figs. 5.19c and 5.19d does not split as it extends along the investigated span. It does exhibit notable reorientation in the region $13 \lesssim z/D \lesssim 16$, along with the positive leading vortex tube, both of which result from a phase jump in vortex shedding along the span. This phase jump is associated with the hybrid wake transition, where P+S vortices are shed earlier in the elliptic cylinder orbit than the 2S vortices of the same sign higher along the span. Similar reorientation due to a phase shift lower along the span near the wake transitions from 2S to P+S is evidenced by the curved band in the instantaneous streamwise velocity snapshot, see Fig. 5.3b. However, the reconstructed wake does not exhibit such a reorientation because the investigated spanwise region does not extend low enough towards the pivot point.

Examination of the reconstructed wake for the VIV case at $U^* = 7.08$, depicted in Fig. 5.20, indicates hybrid shedding, where a 2S mode at the bottom of the investigated region transitions to a P+S mode at the top. This transition agrees with the instantaneous snapshots and occurs where the positive vortex tube at $x/D \approx 5$ in Fig. 5.20b splits into leading and trailing vortex tubes. Unlike the case of VIV at $U^* = 5.48$, the positive trailing vortex tube persists along the span and none of the vortex tubes exhibit significant reorientation attributed to a phase jump because the P+S topology does not revert back to 2S higher along the span. Compared to the case at $U^* = 5.48$, the wake reconstruction for $U^* = 7.08$ is relatively noisy and does not resolve the split in the positive vortex tube. This is attributed to cycle-to-cycle variations in vortex shedding, where the phase averaged reconstruction incorporates the intermittent vortical structures shed at f_s near the base of the cylinder.

To more clearly visualize vortex dislocations within the region where the wake transitions from 2S to P+S shedding, the instances of transient vortex shedding at f_s should not be used for reconstructing the wake. A spectrogram analysis of the wake velocity identifies such transient segments. Figure 5.21a depicts the spectrogram of the transverse velocity signal at the location of maximum v_{RMS} in the plane $z/D \approx 6$. Windows used for each Fourier transform contain data capturing approximately six vortex shedding cycles and were overlapped by 75% to show the temporal evolution of spectral energy content.

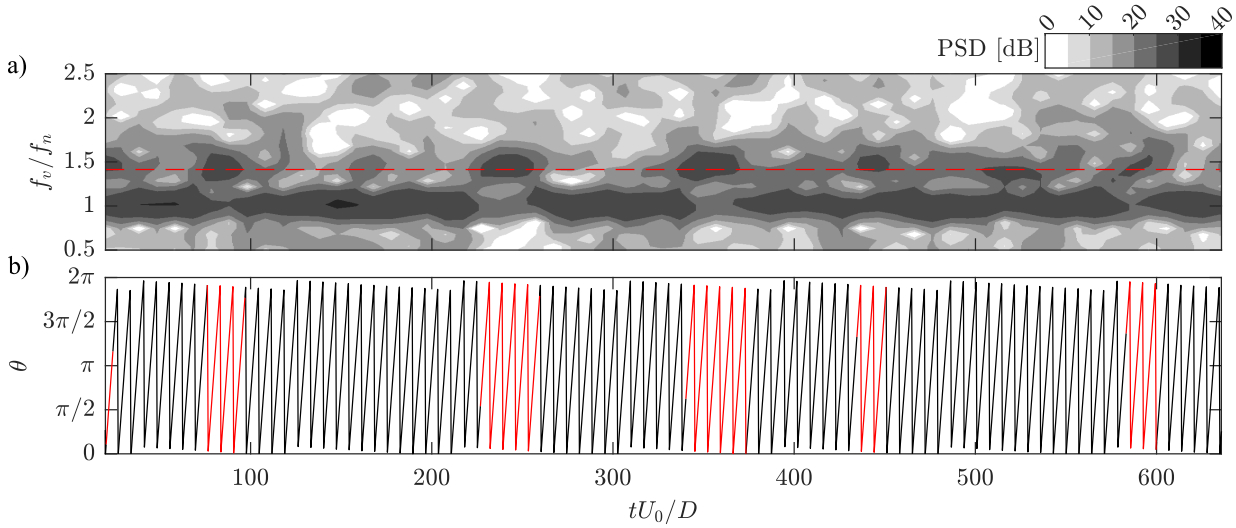

Figure 5.21: (a) Spectrogram of the transverse velocity signal at the location of maximum v_{RMS} in the plane $z/D \approx 6$ for $U^* = 7.08$. The red dashed line indicates vortex shedding at f_s. (b) Phase angle of transverse cylinder displacement. Sections highlighted in red indicate transient segments of vortex shedding at f_s.

PIV data is excluded from phase averaging if the dominant energy content in the wake is associated with the frequency of vortex shedding from a stationary cylinder, f_s, indicated by the red dashed line. The result is illustrated in Fig. 5.21b, which depicts the phase of cylinder displacement in the transverse direction. Sections highlighted in red are discarded from the data prior to phase averaging.

Figure 5.22 presents the vorticity contours and Q-criterion isosurfaces of a displacement-based phase-averaged low order model (LOM) constructed from the first ten POD modes and the mean field. In addition to removing transient segments of vortex shedding at f_s prior to phase-averaging, a LOM is used to clearly visualize the dominant vortical structures by filtering out the smaller, less energetic structures. Analysis of the POD results is discussed in Section 5.6 and Appendix F. Examination of the Q-criterion in Figs. 5.22b and 5.22d elucidates the hybrid shedding, where a 2S mode near the base of the cylinder transitions to a P+S mode at higher z/D. While the negatively signed vortex tube is consistent along the span, the transition is evidenced by a split in the positive vortex tube. Figure 5.22b indicates the single positive tube at $x/D \approx 5$ splits at approximately $z/D \approx 7$ to form leading and trailing vortex tubes.

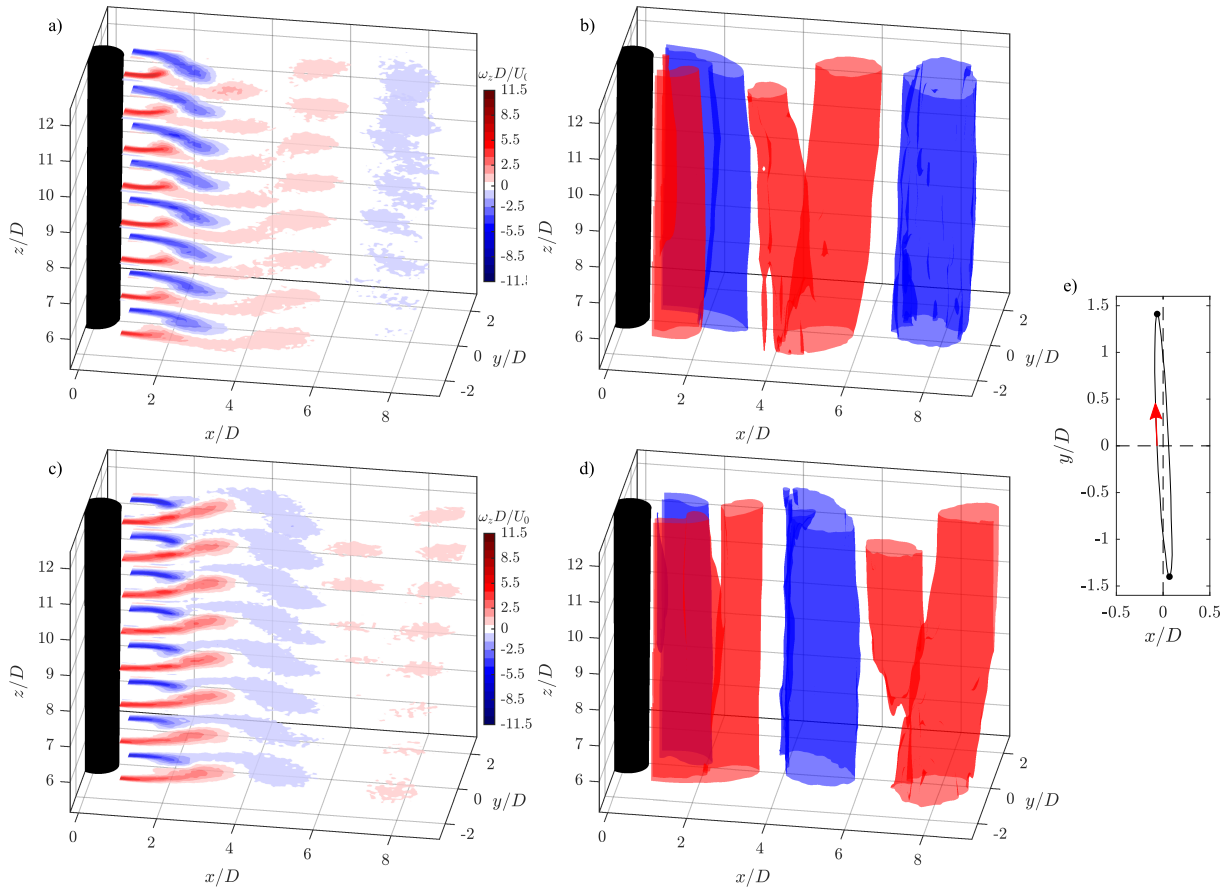

Figure 5.22: Displacement based phase averaged low order model using the first ten POD modes for $U^* = 7.08$; (a & c) planar vorticity contours and (b & d) Q-criterion isosurfaces of $Q = 0.001Q_{max}$ coloured by the spanwise vorticity. The cylinder tip is located at the (a & b) positive and (c & d) negative transverse peaks of the (e) phase averaged cylinder tip trajectory ($\theta = \pi/2$ and $3\pi/2$, respectively). Note that every second vorticity plane is shown for clarity.

5.5.1 Vortex Dynamics

In order to form a comprehensive description of the wake topology, it is necessary to analyze the vortex dynamics along the cylinder span. The GMM based vortex identification algorithm was used to identify vortices in the planar phase averaged fields and to calculate their strength. For the stationary cylinder, Figs. 5.23a–c present vortex position, circulation, and size, respectively, in each of the investigated horizontal planes. The results are presented for fully shed positive and negative vortex tubes for two phases with a separation of π. Examination of the vortex position in Fig. 5.23a shows the positive and negative vortex tubes are at nearly identical streamwise locations in the wake, and that both tubes exhibit a slight curve, which was observed in the wake reconstruction and is a result of the wall effects of the tunnel. The strength of the vortices is similar and is relatively uniform along the span with error bars showing the methodological uncertainty associated with phase averaging based on a 99% confidence interval. Examination of the circulation at later phases verified that advection of the vortices further into the wake incurs decay as

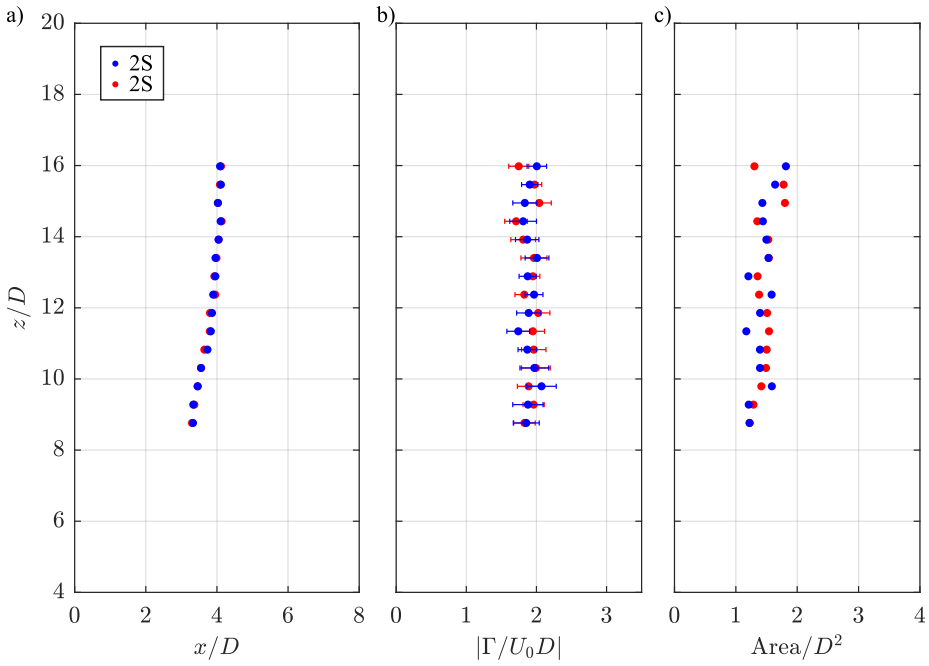

Figure 5.23: Spanwise variation of vortex (a) streamwise position, (b) circulation, and (c) area computed using the GMM based vortex identification algorithm for the stationary case. Red and blue markers indicate positively and negatively signed vortices, respectively, with a phase separation of π.

a result of viscous diffusion and cross annihilation of vorticity [66]. The cross sectional area in the $x-y$ plane of both vortex tubes is approximately the same and is relatively consistent along the span.

Figure 5.24 depicts vortex position, circulation, and cumulative like-signed circulation for the VIV case at $U^* = 5.48$. The results are presented for two phases with a separation of π, in which all identified vortex tubes are fully formed and shed from the cylinder. Based on the location of the wake transition in the vorticity contours of the wake reconstruction, the GMM algorithm was applied with the assumption of P+S shedding in the range $7.5 \lesssim z/D \lesssim 13.5$ and 2S shedding outside this range. The wake reconstruction reveals that 2S vortices and leading P+S vortices of the same sign form a continuous connection. Closer examination of the 2S shedding regions reveals that the two vortex tubes are at nearly identical streamwise locations and have comparable circulation along the span, similar to the observations for the stationary case. However, in the region of P+S shedding, the negative vortex is located between the positive vortices since the trailing vortex is shed prior to the leading vortex. Examination of the circulation in Fig. 5.24b reveals that the

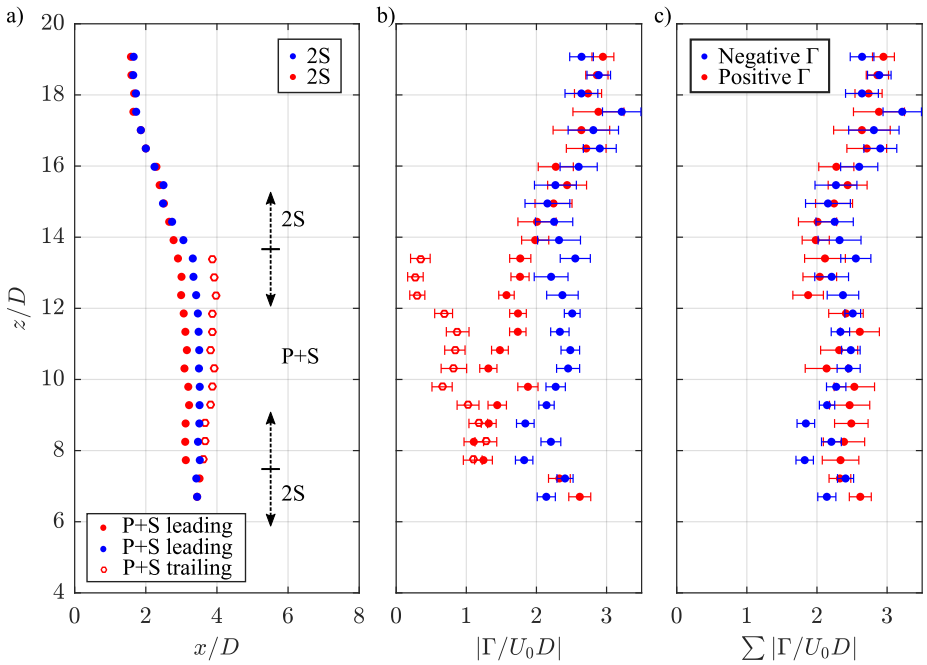

Figure 5.24: Spanwise variation of vortex (a) streamwise position, (b) circulation, and (c) cumulative like-signed circulation computed using the GMM based vortex identification algorithm for the VIV case at $U^* = 5.48$. Red and blue markers indicate positively and negatively signed vortices at the phases $\theta = \pi/2$ and $3\pi/2$, respectively.

positive leading vortex is weaker than the negative leading vortex because some component of the positive vorticity flux generated at the cylinder surface is supplied to the positive trailing vortex. Considered in terms of the cumulative negatively and positively signed circulation generated in each cycle of shedding the strengths agree within the methodological uncertainty over the investigated span, similar to the stationary case.

The wake reconstruction in Fig. 5.19b indicates that the trailing positive vortex ends within the fluid. This violates the theorem stipulating that all vortices must either connect with each other or terminate at a boundary [71]. Although Helmholtz's vortex theorems do not strictly hold for real flows due to the effect of viscosity, they are used to predict the vortex dislocations at the wake transition. Following the third theorem that a vortex tube cannot end within a fluid, it is postulated that the positive trailing vortex tube bends significantly, looping back upstream, to form a connection with the positively signed leading vortex tube. The postulated vortex connections are illustrated in Fig. 5.25. Such a bend occurs at approximately $z/D \approx 14$ and is not captured in the 3D wake reconstruction due to the limitations of 2D PIV but is evidenced in the spanwise circulation. The strength of the positive trailing vortex is weaker at higher z/D. This is partly attributed to the viscous cross annihilation of vorticity [66] with the negatively signed vortex downstream and partly a result of the spanwise vorticity reorienting into the streamwise direction as a connection is formed between the positive trailing and leading vortex tubes. Furthermore, the positive leading and trailing vortices must reconnect since the cumulative negative and positive circulation is similar along the span. It should be noted that since the 2D wake measurements do not provide the spanwise component of velocity for calculation of vorticity in the streamwise and transverse directions, interpretation of the vortex connections requires some degree of prediction.

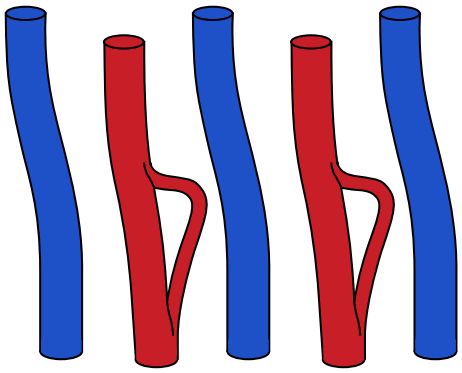

Figure 5.25: Conceptual diagram of the vortex dislocations in the hybrid wake for $U^* = 5.48$.

Figure 5.26 depicts vortex position, circulation, and cumulative like-signed circulation for the VIV case at $U^* = 7.08$. The results are based on GMM-based vortex identification and characterization of the LOM constructed from the first 10 POD modes and are presented for two phases with a separation of π, in which all identified vortex tubes are entirely shed from the cylinder. Vortices in the region of 2S shedding are located at similar streamwise locations, whereas their position is notably different in the P+S region because an additional vortex is shed each period. The P+S pattern results from a split in the positive vortex tube to form trailing and leading vortices with similar strengths. Considered in terms of the cumulative negatively and positively signed circulation generated in each cycle of shedding the strengths agree within the methodological uncertainty over the investigated span, similar to the stationary case.

For the stationary cylinder, the strength of vortices is relatively uniform along the span; whereas, for the VIV cases, vortices have a greater circulation at higher spanwise locations. This is a consequence of the spanwise variation of amplitude, where larger structural os-

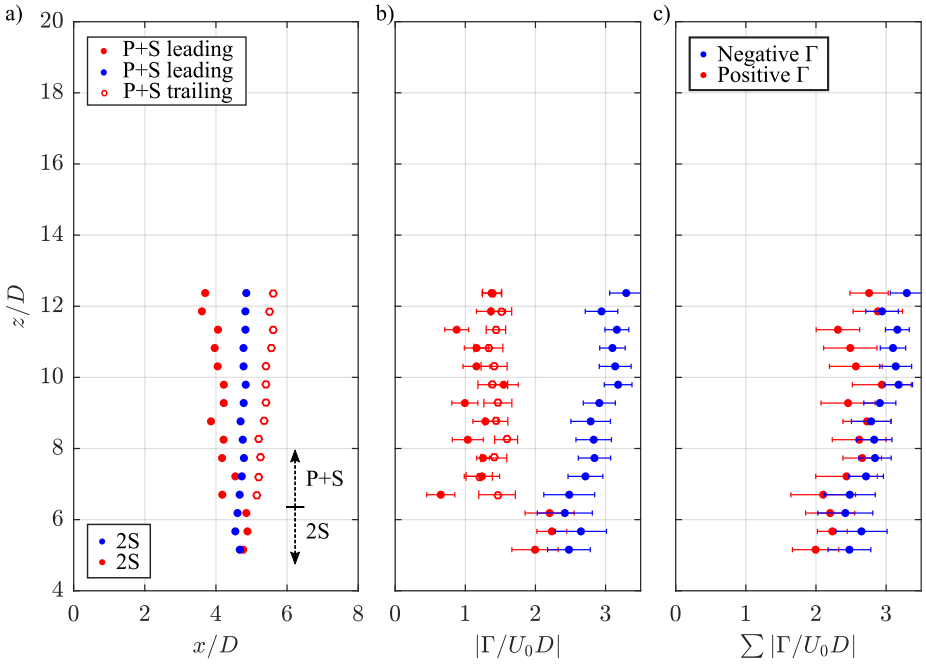

Figure 5.26: Spanwise variation of vortex (a) streamwise position, (b) circulation, and (c) cumulative like-signed circulation computed using the GMM based vortex identification algorithm for the VIV case at $U^* = 7.08$. Red and blue markers indicate positively and negatively signed vortices at the phases $\theta = \pi/2$ and $3\pi/2$, respectively.

cillations generate more vorticity in the boundary layers [66], which then advects via the separated shear layers and rolls up to form stronger vortices. Such a spanwise variation in circulation has previously been observed by Flemming and Williamson [47] and Techet *et al.* [87]. Conservation of circulation along the length of the vortex tube would necessitate small vortex filaments that branch off from the main vortex tube. These are not evidenced in the wake reconstruction because there is likely a high degree of cycle to cycle variation in their spatial location, which causes the structure to be smeared in the phase averaging process.

5.6 Proper Orthogonal Decomposition Analysis

A Proper Orthogonal Decomposition (POD) analysis was performed on the vertical and horizontal planes for the three cases. The POD analysis extracts the dynamics of the most energetic coherent structures for use in producing phase averaged and low order model reconstructions of the wake. The goal is to identify the dominant coherent structures and expound on their spanwise deformation with emphasis on elucidating the transition between vortex shedding patterns and frequencies for a hybrid wake. Appendix F shows the temporal coefficients and corresponding spatial modes at select planes for the three investigated cases.

5.6.1 Modal Energy

For the first ten modes, the relative energy of each POD mode is shown in Figs. 5.27a, 5.27c, and 5.27e, and the cumulative energy is shown in Figs. 5.27b, 5.27d, and 5.27f for the stationary, $U^* = 5.48$, and $U^* = 7.08$ cases, respectively. Periodic coherent structures advected in the fluid are generally represented by a pair of POD modes since a single mode cannot describe their advection [142]. This mode pairing is evident for the first two modes in all three cases, which capture 44-76% of the total fluctuating energy content and exhibit nearly equivalent relative energies. Inspection of their temporal coefficients and spatial modes in Appendix F reveals similar temporal signals and spatial mode topologies that are offset by a phase shift of approximately $\pi/2$. In the regions of P+S shedding, the VIV cases exhibit pairing of modes 3 and 4. This second pair corresponds to the shedding of weaker trailing vortices in the P+S pairs. A comparison with the results of a POD analysis on 2P vortex shedding in Appendix F.4 indicates that energy content of the second pair is greater for 2P shedding than for P+S shedding, which is likely attributed to the additional trailing vortex in the 2P pattern. Higher modes are associated with turbulent motion and contain notably less energy than the first few modes for all cases.

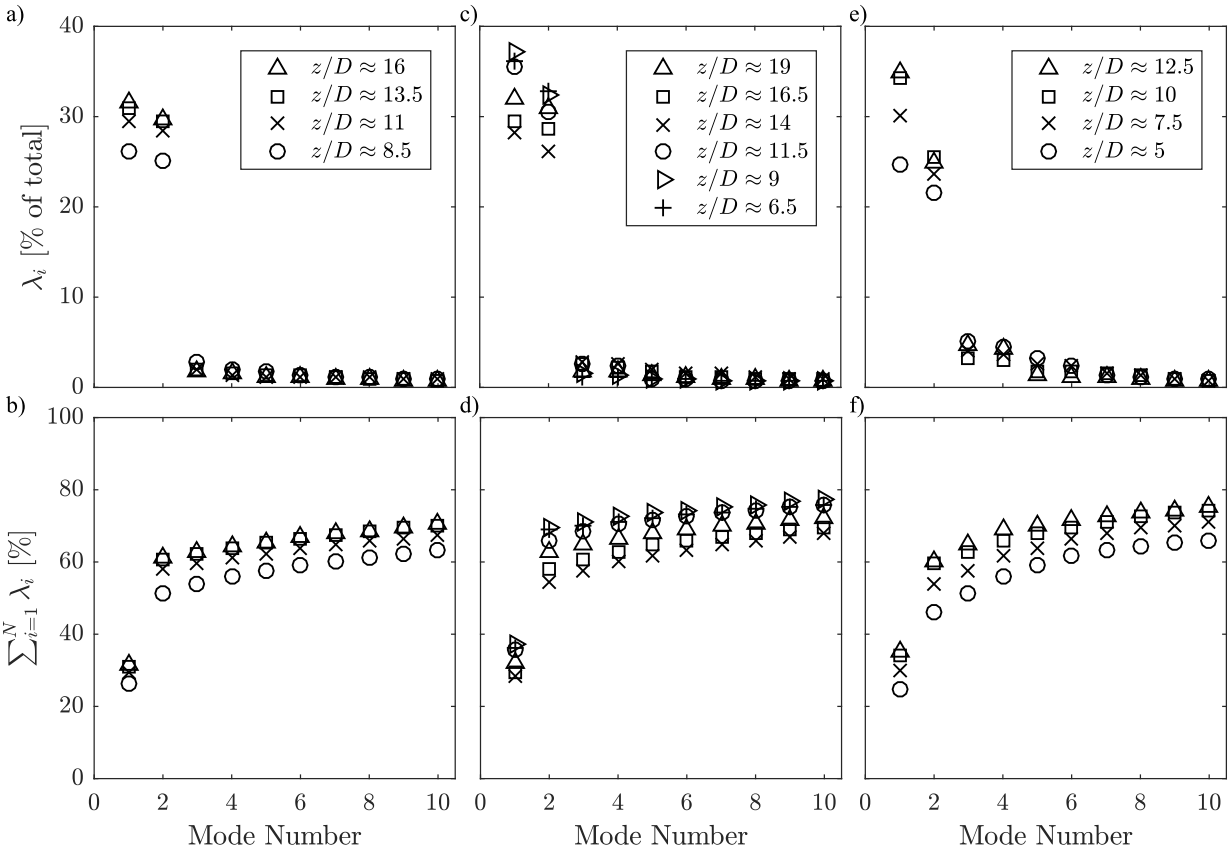

Figure 5.27: Relative turbulent kinetic energy for (a & b) stationary cylinder, (c & d) $U^* = 5.48$, and (e & f) $U^* = 7.08$; (a, c, e) energy distribution over POD modes and (b, d, f) cumulative mode energy.

Spanwise variation of the cumulative relative turbulent kinetic energy for modes 1 and 2, and modes 1 to 4 is depicted in Figs. 5.28a and 5.28b, respectively. Inspection of the stationary case reveals the energy is distributed over a wider range of modes towards the base of the cylinder, where the first two modes capture less of the total energy. This is a result of the turbulence intensity in the tunnel, since the flow is more turbulent towards the floor of the tunnel, Appendix C. The cumulative energy of the first four modes for the VIV case at $U^* = 7.08$ exhibits a similar decrease towards the base of the cylinder; however, the difference in energy between the highest and lowest planes is more significant compared to that for the stationary cylinder. The energy content of the first four modes is greater at higher z/D because the structure's spanwise linear variation of amplitude causes greater velocity fluctuations in the dominant coherent structures at higher z/D.

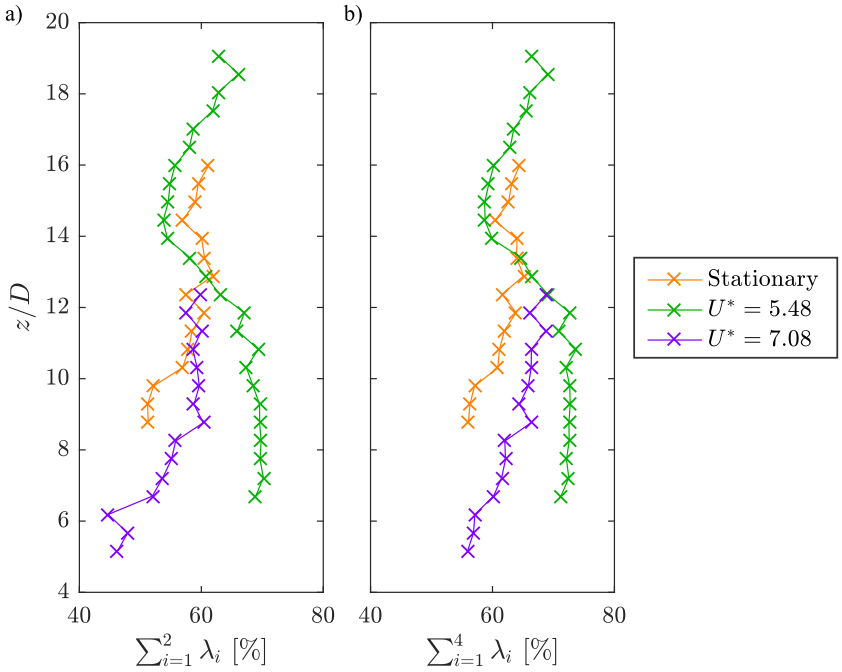

Figure 5.28: Cumulative relative turbulent kinetic energy of (a) POD modes 1 and 2, and (b) POD modes 1 to 4, for each of the investigated horizontal planes.

The VIV case at $U^* = 5.48$ does not exhibit the same decrease in cumulative energy of the first four modes towards the base of the cylinder. Instead, the energy content is relatively constant below $z/D \approx 12$, decreases along the span in the region $12 \lesssim z/D \lesssim 15$, and increases above $z/D \approx 15$. These regions coincide with the wake transition from P+S to 2S observed at $z/D \approx 13.5$, whereby the wake velocity fluctuations associated with the coherent structures in P+S shedding are generally more energetic than 2S shedding because of the additional trailing vortex shed each cycle of cylinder oscillation. Similar to the spanwise analysis of the time averaged wake characteristics, the decrease in cumulative energy between shedding modes occurs over a range instead of one specific height. The gradual decrease in energy is a result of variations in vortex shedding from cycle-to-cycle, which causes the spanwise location of the connection between P+S and 2S vortices to fluctuate. Above $z/D \approx 15$, the energy content increases with higher z/D, similar to the other VIV case.

5.6.2 Temporal Coefficients

Figure 5.29 shows spectra of the temporal coefficients for the four most energetic modes. Spectra are shown for every second horizontal plane in the investigated spanwise region and are offset by 20 dB for clarity. For the stationary case, pairing of the first two modes is further evidenced by the similar spectra in Fig. 5.29a, which exhibit a dominant peak near f_s. Spectra of the third and fourth temporal coefficients in Fig. 5.29b are different and do not indicate mode pairing. Spectra of a_4 exhibits a broad peak centered near f_s, while the spectral energy for a_3 is more concentrated at a lower frequency. A 3D cross plot of the first three temporal coefficients in Fig. 5.30c reveals that fluctuations of a_3 are correlated with the amplitudes of a_1 and a_2. The third POD mode is the "slow drift mode" [143] and represents the base-flow variations for the stationary cylinder [144–146].

Spectra of the first two temporal coefficients for the VIV case at $U^* = 5.48$ exhibit a dominant peak at the natural frequency of the structure, f_n, (Fig. 5.29c). Compared to the stationary case, the spectral energy associated with the dominant peak is more concentrated because vortex shedding is locked onto the structural oscillations. Examination of Fig. 5.29d reveals that the spectra of a_3 and a_4 are similar below $z/D \approx 13.5$ and form a second mode pair with a dominant peak at $2f_n$. This mode pair captures the energy associated with the shedding of P+S pairs in this spanwise region. Above the wake transition from P+S to 2S ($z/D \approx 13.5$), spectral energy shifts from the dominant peak at $2f_n$ to the more broadband peak at f_n. The shift in spectral energy is gradual because of the cycle-to-cycle variations of the spanwise location of the P+S to 2S vortex dislocation, similar to the gradual decrease in cumulative modal energy content of the first four POD modes in Fig. 5.28b.

Vortex shedding at both f_n and f_s for the VIV case at $U^* = 7.08$ was observed in the frequency analysis of the wake velocity in Section 5.4 and is further exemplified by spectral analysis of the POD temporal coefficients. Spectra of a_1 and a_2 in Fig. 5.29e exhibit a dominant peak at the natural frequency and smaller peaks at its harmonics at higher z/D. In the same spanwise region, the dominant spectral peak for a_3 and a_4 in Fig. 5.29f occurs at $2f_n$, which is expected for the P+S shedding observed in this region. Towards the base of the cylinder, shedding of coherent structures at f_s produces spectral peaks marked by the dashed line for both mode pairs. Spectral energy at this frequency increases and becomes more concentrated towards the base of the cylinder. At the lowest plane of investigation $z/D \approx 5$, both mode pairs exhibit a peak at f_n and f_s, associated with their intermittent switching. It is speculated that below $z/D \approx 5$, vortex shedding primarily occurs at f_s since the cylinder is nearly stationary. The dominant spectral peak in the first pair of modes would shift to the f_s, while that of the second pair would shift to f_n.

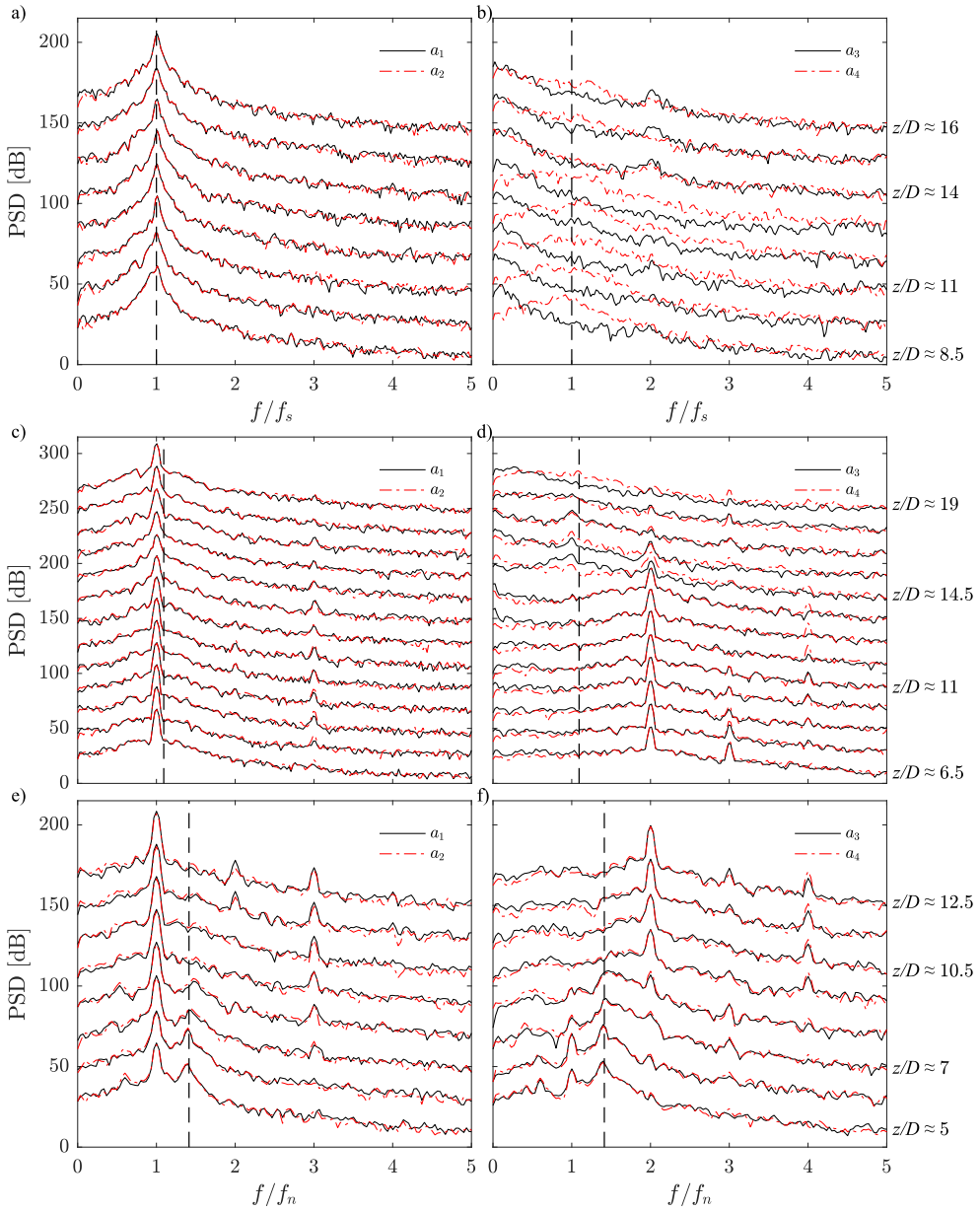

Figure 5.29: Power spectral density of the temporal coefficients for (a & b) stationary cylinder, (c & d) $U^* = 5.48$, and (e & f) $U^* = 7.08$. The dashed black line corresponds to the vortex shedding frequency of a stationary cylinder, f_s. Note that spectra are offset by 20 dB and every second plane is shown for clarity.

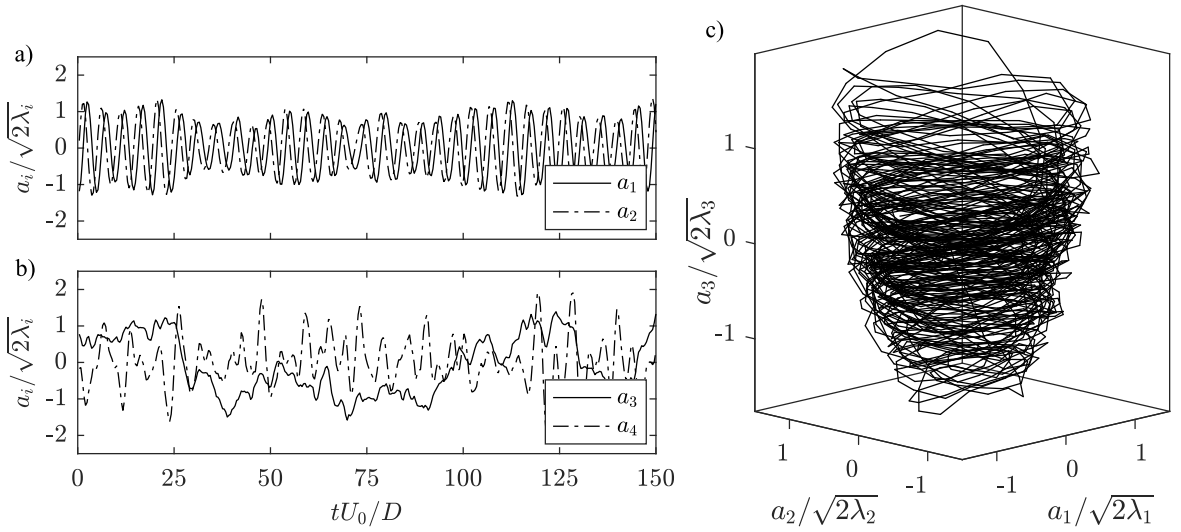

Figure 5.30: Temporal coefficients (a) a_1 and a_2, and (b) a_3 and a_4 from the POD analysis of the flow around a stationary cylinder at $z/D \approx 10$. A three dimensional cross plot is shown for the first three temporal coefficients.

The findings from this results Chapter indicate that linear amplitude variation along the span of a cylinder undergoing VIV can significantly impact the wake development, causing hybrid vortex shedding. Specifically, this Chapter investigates two VIV cases at $U^* = 5.48$ and 7.08, which were found to exhibit vortex shedding transitions from 2S to P+S to 2S, and 2S to P+S, respectively. The transitions occur over a spanwise range because the location of the vortex dislocation between the shedding patterns varies from cycle-to-cycle. In general, the observed wake topology does not agree with the predictions from the Morse and Williamson [1] shedding map, developed from forced 1DOF-transverse vibrations of an elastically mounted cylinder. However, the observed 2S to P+S transition near the boundary between 2P shedding and the desynchronized regime agrees with the observations of Kheirkhah *et al.* [49] and the analysis elucidates the vortex dislocation between these shedding patterns.

Chapter 6

Conclusions

Vortex Induced Vibrations (VIV) of a pivoted cylinder with a moderate mass ratio were investigated experimentally at a fixed Reynolds number of 3100 using simultaneous cylinder displacement measurements and time-resolved PIV. The study is focused on investigating the development of spanwise coherent structures and characterizing the wake dynamics and attendant fluid-structure interaction for VIV with elliptic cylinder trajectories. In addition, a method is developed to identify and characterize vortices in the wake.

6.1 Structural Response and the Associated Vortex Dynamics

The structural response and associated wake topology in the horizontal plane positioned near the cylinder mid-span were examined for a reduced velocity range of $4.42 \leq U^* \leq 9.05$. Within the lock-in region, the cylinder traces an elliptic trajectory with the frequency of both streamwise and transverse oscillations locking onto the structure's natural frequency. Three of the four possible elliptic orientations reported by Kheirkhah *et al.* [45] were observed and are distinguishable based on orbiting direction and tilt with respect to the cross-flow direction. Phase-averaged wake velocity measurements show that vortex shedding conforms to 2S, $2P_0$, and 2P shedding patterns. The relation between these shedding regimes and the branches of amplitude response agree with the map of Morse and Williamson [1] for 1DOF forced VIV, except for 2P shedding observed in the zone of predicted desynchronization.

Quantitative analysis of wake velocity measurements was performed to enable a statistics-based vortex identification and characterization of both vortex kinematics and circulation.

It is shown that the moment of vortex shedding can be identified based on the peak circulation or maximum acceleration of the vortex core. For 2S shedding, the vortices are shed near the cylinder's streamwise equilibrium of oscillation. For 2P shedding, leading vortices shed immediately after the transverse peak and trailing vortices shed near the transverse equilibrium. Thus, the shift from the 2S to 2P shedding between the initial and lower response branches is associated with a phase jump in vortex shedding of approximately π.

The direction of cylinder orbiting is found to have no substantial effect on the wake topology for the 2S regime. In contrast, distinct differences in vortex shedding timing occur for different orbiting directions in the 2P regime. Consequently, the subsequent arrangement and relative strength of the shed vortices is affected. The uneven streamwise spacing between the two vortex pairs shed in each cycle, referred to as streamwise staggering, leads to significant deviation in the absolute trajectory of the leading vortices in the wake. For the case of clockwise cylinder motion, the positive leading vortex advects further from the wake centerline than the negative leading vortex, with the reversed trend seen when the orbiting direction is switched. Such deviations from the classically defined 2P shedding mode are a consequence of the differences in the streamwise motion of the cylinder undergoing elliptic orbiting, which cannot be predicted by 1DOF-transverse studies. Furthermore, this also gives rise to vortex staggering in the wake that has not been observed for the cases of figure-eight trajectory VIV.

6.2 Spanwise Wake Development

The wake development for a stationary cylinder and VIV cases at $U^* = 5.48$ and 7.08 was investigated experimentally. The cylinder trajectory for the VIV cases exhibits two different elliptic orientations, both with a clockwise rotation. Time-resolved, planar, two-component PIV measurements were performed in two different configurations to analyze both the streamwise and spanwise flow development. Three dimensional reconstructions of the phase averaged wake velocity measurements reveal 2S shedding along the span of the stationary cylinder and hybrid shedding for the VIV cases. Within the spanwise region of investigation, the wake topology transitions from 2S to P+S to 2S, and 2S to P+S for the VIV cases at $U^* = 5.48$ and 7.08, respectively. In both cases, the positively signed vortex tube splits to form the vortex pair associated with P+S shedding. The observed wake topology for 2DOF VIV with variable amplitude shows significant deviation from predictions based on the Morse and Williamson [1] shedding map for 1DOF forced VIV. In addition to introducing the streamwise amplitude as a third dimension [47], a separate map should be generated for each type of elliptic orientation since the direction and tilt can impact the wake topology.

Examination of the time averaged wake characteristics shows the recirculation region, formation length, wake half-width, and maximum velocity deficit are relatively consistent along the span for the stationary cylinder. Linear variation of amplitude for the VIV cases causes a gradual reduction along the span in the formation length and maximum velocity deficit, and increase in the wake width. For the VIV case at $U^* = 5.48$, there is a shift in the wake characteristics in the region near hybrid transition from P+S to 2S vortex shedding. The 2S pattern is associated with a thinner wake with a higher maximum velocity deficit than the P+S pattern. A comparison amongst cases reveals similar spanwise trends in wake half-width and maximum velocity deficit for spanwise regions with the same shedding patterns.

Proper Orthogonal Decomposition (POD) is shown to have utility to identify the dominant shedding modes. The first two POD modes capture the dominant coherent structures in the wake for the 2S regime. However, for the P+S regime, four POD modes are required to describe the salient features of the dominant structures. For all cases, the modes required to capture the dominant structures are paired, as indicated by the similar relative modal energy content, dominant frequency of temporal coefficients, and the spatial modes offset by approximately $\pi/2$. Analysis of the spanwise variation of modal energy shows a marginal decrease in the cumulative energy of the modes capturing the dominant structures lower along the span, consistent with the greater turbulence intensity observed near the floor of the tunnel. Furthermore, the first four modes for the VIV case at $U^* = 5.48$ capture less of the total turbulent kinetic energy near the wake transition from P+S to 2S because of the complex vortex dislocations between shedding patterns.

Spectral analysis of the temporal coefficients and the wake velocity reveal cycle-to-cycle variations of the vortex shedding frequency near the floor of the water tunnel for the VIV case at $U^* = 7.08$ and the wake topology near the P+S to 2S hybrid transition for the VIV case at $U^* = 5.48$. Spectra for the stationary case did not indicate any cycle-to-cycle variations in vortex shedding. For the VIV case at $U^* = 5.48$, variation of the spanwise location of hybrid transition from P+S to 2S is evidenced by the gradual shift of the the dominant peak in the spectra of the temporal coefficients as well as their transient amplitude fluctuations. For the VIV case at $U^* = 7.08$, the frequency of vortex shedding closer to the pivot point intermittently switches between the natural frequency of the structure and the frequency of shedding from a stationary cylinder. Towards the base of the cylinder, vortex shedding at the frequency of shedding from a stationary cylinder becomes increasingly pervasive because of the small amplitude of oscillation.

Chapter 7

Recommendations

From the results of the present work and experience gathered throughout the course of this study, the following recommendations for continued research are made:

1. Raise the pivot point of the cylinder above the tunnel floor. In the present study, the cylinder pivots on the tunnel floor due to the limited water depth in the experimental facility. Wall effects of the water tunnel floor result in a lower free stream velocity near the floor and consequently affect the frequency of vortex shedding from the cylinder in this region. Allowing the cylinder to pivot on an elevated end plate would improve the free stream uniformity in the spanwise region of investigation.
2. The mechanism for adjusting the natural frequency of the structure should be improved. The apparatus in the present study uses individual components to connect each spring to a threaded rod. The present study ensured repeatability between tests through careful positioning and monitoring of these four components. Replacing these components with a single plate would improve consistency between tests.
3. A low mass ratio pivoted cylinder undergoing VIV with elliptic trajectories should be investigated. The VIV studies with figure-eight trajectories by Jauvtis and Williamson [34] and Flemming and Williamson [47] observed massive amplitudes of oscillation in the upper response branch of a low mass ratio systems as a result of the 2T and 2C shedding patterns, respectively. The structural response and wake topology in the upper branch remain to be investigated for VIV with elliptic trajectories.
4. The GMM based vortex identification algorithm should be improved. The present study requires the user to define the number of subpopulations and to provide an estimate of their spatial mean to initialize the iterative GMM refinement. Automation and objectivity can be improved by using an additional algorithm to select the

initial means, such as the *k-means++* algorithm, and an evaluation criteria to assess the relative quality of the refined statistical model, such as the Akaike information criterion (AIC) or Bayesian information criterion (BIC). Application of the evaluation criteria would treat the trade-off between goodness of fit and complexity of the model, thus providing an objective solution to the drawback of the GMM algorithm where the model suffers from overfitting.

5. The GMM based vortex identification algorithm should be revised to treat vortices that are partially cut off by the field of view. The present study avoids the identification of such vortices by confining the algorithm to a limited region in the field of view. Automation of this feature would generalize the algorithm to all flows.
6. The Morse and Williamson [1] shedding map should be updated to a multidimensional map to account for the effect of the second degree of freedom in the streamwise direction. Not all shedding patterns observed in the present study and other 2DOF studies [34, 47, 49] coincide with predictions from the map for 1DOF cylindrical structures.
7. The present study reveals the presence of highly three dimensional structures in the wake, especially at the transition between shedding patterns in a hybrid wake. Insight into the vortex dynamics at these transitions would benefit greatly from three-dimensional measurements. The planar measurements of the current investigation are insightful but measurements with stereo or tomographic PIV would enable for complete characterization of the hybrid wake topology.
8. Fluid induced structural loading along the span of a cylinder with linear variation of amplitude remains to be investigated. Methods discussed by Rival and Oudheusden [147] can be employed to extract the overall force on the structure from the velocity fields to describe the fluid-structure interaction throughout the cylinder's trajectory for each of the four common types of elliptical orientation [45].

References

[1] T. Morse and C. Williamson. Fluid forcing, wake modes, and transitions for a cylinder undergoing controlled oscillations. *Journal of Fluids and Structures*, 25(4):697–712, 2009. DOI. ↩

[2] A. Roshko. On the Wake and Drag of Bluff Bodies. *Journal of the Aeronautical Sciences*, 22(2):124–132, 1955. DOI. ↩

[3] P. W. Bearman. On vortex street wakes. *Journal of Fluid Mechanics*, 28(04):625–641, 1967. DOI. ↩

[4] C. H. K. Williamson. Vortex Dynamics in the Cylinder Wake. *Annual Review of Fluid Mechanics*, 28(1):477–539, 1996. DOI. ↩

[5] M. Zdravkovich. Review and classification of various aerodynamic and hydrodynamic means for suppressing vortex shedding. *Journal of Wind Engineering and Industrial Aerodynamics*, 7(2):145–189, 1981. DOI. ↩

[6] A. Roshko. Perspectives on bluff body aerodynamics. *Journal of Wind Engineering and Industrial Aerodynamics*, 49(1-3):79–100, 1993. DOI. ↩

[7] E. Berger and R. Wille. Periodic Flow Phenomena. *Annual Review of Fluid Mechanics*, 4(1):313–340, 1972. DOI. ↩

[8] J. H. Gerrard. The Wakes of Cylindrical Bluff Bodies at Low Reynolds Number. *Philosophical Transactions of the Royal Society A: Mathematical, Physical and Engineering Sciences*, 288(1354):351–382, 1978. DOI. ↩

[9] A. Roshko. On the development of turbulent wakes from vortex streets. Technical report, 1954. URL. ↩

[10] J. T. Lin and Y. H. Pao. Wakes in Stratified Fluids. *Annual Review of Fluid Mechanics*, 11(1):317–338, 1979. DOI. ↩

[11] P. W. Bearman. Vortex Shedding from Oscillating Bluff Bodies. *Annual Review of Fluid Mechanics*, 16(1):195–222, 1984. DOI. ↩

[12] H. Oertel. Wakes Behind Blunt Bodies. *Annual Review of Fluid Mechanics*, 22(1):539–562, 1990. DOI. ↩

[13] C. H. K. Williamson. Oblique and parallel modes of vortex shedding in the wake of a circular cylinder at low Reynolds numbers. *Journal of Fluid Mechanics*, 206(-1):579–627, 1989. DOI. ↩

[14] R. E. D. Bishop and A. Y. Hassan. The Lift and Drag Forces on a Circular Cylinder Oscillating in a Flowing Fluid. *Proceedings of the Royal Society A: Mathematical, Physical and Engineering Sciences*, 277(1368):51–75, 1964. DOI. ↩

[15] T. Sarpkaya. A critical review of the intrinsic nature of vortex-induced vibrations. *Journal of Fluids and Structures*, 19(4):389–447, 2004. DOI. ↩

[16] T. Sarpkaya. Vortex-Induced Oscillations: A Selective Review. *Journal of Applied Mechanics*, 46(2):241, 1979. DOI. ↩

[17] C. Williamson and R. Govardhan. Vortex-induced vibrations. *Annual Review of Fluid Mechanics*, 36(1):413–455, 2004. DOI. ↩

[18] A. Khalak and C. Williamson. Motions, forces and mode transitions in vortex-induced vibrations at low mass-damping. *Journal of Fluids and Structures*, 13(7-8):813–851, 1999. DOI. ↩

[19] P. Bearman. Circular cylinder wakes and vortex-induced vibrations. *Journal of Fluids and Structures*, 27(5):648–658, 2011. DOI. ↩

[20] R. Blevins. Review of sound induced by vortex shedding from cylinders. *Journal of Sound and Vibration*, 92(4):455–470, 1984. DOI. ↩

[21] E. Huse, G. Kleiven, and F. Nielsen. Large Scale Model Testing Of Deep Sea Risers. In *Offshore Technology Conference*, pages 1–9. Offshore Technology Conference, April 1998. DOI. ↩

[22] J. E. Dailey, J. B. Weidler, S. Y. Hanna, M. F. Zedan, and J. Y. Yeung. Pile Fatigue Failures. 3: Motions in Seas. *Journal of Waterway, Port, Coastal, and Ocean Engineering*, 113(3):233–250, 1987. URL. ↩

[23] M. M. Bernitsas, K. Raghavan, Y. Ben-Simon, and E. M. H. Garcia. VIVACE (Vortex Induced Vibration Aquatic Clean Energy): A New Concept in Generation of Clean and Renewable Energy From Fluid Flow. *Journal of Offshore Mechanics and Arctic Engineering*, 130(4):041101, 2008. DOI. ↩

[24] N. Stephen. On energy harvesting from ambient vibration. *Journal of Sound and Vibration*, 293(1-2):409–425, 2006. DOI. ↩

[25] M. Every, R. King, and D. Weaver. Vortex-excited vibrations of cylinders and cables and their suppression. *Ocean Engineering*, 9(2):135–157, 1982. DOI. ↩

[26] C. C. Feng. *The measurement of vortex induced effects in flow past stationary and oscillating circular and D-section cylinders*. Masters in applied science thesis, University of British Columbia, 1968. URL. ↩

[27] R. Govardhan and C. H. K. Williamson. Modes of vortex formation and frequency response of a freely vibrating cylinder. *Journal of Fluid Mechanics*, 420:85–130, October 2000. DOI. ↩

[28] A. Khalak and C. Williamson. Fluid forces and dynamics of a hydroelastic structure with very low mass and damping. *Journal of Fluids and Structures*, 11(8):973–982, 1997. DOI. ↩

[29] A. Sanchis, G. Sælevik, and J. Grue. Two-degree-of-freedom vortex-induced vibrations of a spring-mounted rigid cylinder with low mass ratio. *Journal of Fluids and Structures*, 24(6):907–919, 2008. DOI. ↩

[30] G. Moe and Z. Wu. The Lift Force on a Cylinder Vibrating in a Current. *Journal of Offshore Mechanics and Arctic Engineering*, 112(4):297, 1990. DOI. ↩

[31] T. Sarpkaya. Hydrodynamic Damping, Flow-Induced Oscillations, and Biharmonic Response. *Journal of Offshore Mechanics and Arctic Engineering*, 117(4):232, 1995. DOI. ↩

[32] M. R. Gharib. *Vortex-Induced Vibration, Absence of Lock-in and Fluid Force Deduction*. PhD, California Institute of Technology, 1999. URL. ↩

[33] D. Jeon and M. Gharib. On circular cylinders undergoing two-degree-of-freedom forced motions. *Journal of Fluids and Structures*, 15(3-4):533–541, 2001. DOI. ↩

[34] N. Jauvtis and C. H. K. Williamson. The effect of two degrees of freedom on vortex-induced vibration at low mass and damping. *Journal of Fluid Mechanics*, 509:23–62, June 2004. DOI. ↩

[35] R. D. Blevins and C. S. Coughran. Experimental Investigation of Vortex-Induced Vibration in One and Two Dimensions With Variable Mass, Damping, and Reynolds Number. *Journal of Fluids Engineering*, 131(10):101202, 2009. DOI. ↩

[36] D. Brika and A. Laneville. Vortex-induced vibrations of a long flexible circular cylinder. *Journal of Fluid Mechanics*, 250:481–508, May 1993. DOI. ↩

[37] T. Kitagawa, Y. Fujino, and K. Kimura. Effects of free-end condition on end-cell-induced vibration. *Journal of Fluids and Structures*, 13(4):499–518, 1999. DOI. ↩

[38] B. Vickery and R. Watkins. Flow-induced vibrations of cylindrical structures. In *Hydraulics and Fluid Mechanics*, pages 213–241. Elsevier, 1964. DOI. ↩

[39] R. King. *Vortex Excited Structural Oscillations of a Circular Cylinder in Flowing Water*. PhD, Loughborough University, 1974. URL. ↩

[40] F. Oviedo-Tolentino, F. Pérez-Gutiérrez, R. Romero-Méndez, and A. Hernández-Guerrero. Vortex-induced vibration of a bottom fixed flexible circular beam. *Ocean Engineering*, 88:463–471, September 2014. DOI. ↩

[41] F. Huera-Huarte and P. Bearman. Wake structures and vortex-induced vibrations of a long flexible cylinder—Part 1: Dynamic response. *Journal of Fluids and Structures*, 25(6):969–990, 2009. DOI. ↩

[42] J. K. Vandiver, V. Jaiswal, and V. Jhingran. Insights on vortex-induced, traveling waves on long risers. *Journal of Fluids and Structures*, 25(4):641–653, 2009. DOI. ↩

[43] J.-n. Song, L. Lu, B. Teng, H.-i. Park, G.-q. Tang, and H. Wu. Laboratory tests of vortex-induced vibrations of a long flexible riser pipe subjected to uniform flow. *Ocean Engineering*, 38(11-12):1308–1322, 2011. DOI. ↩

[44] Y. Gao, S. Fu, Y. Xiong, Y. Zhao, and L. Liu. Experimental study on response performance of vortex-induced vibration on a flexible cylinder. *Ships and Offshore Structures*, 12(1):116–134, 2016. DOI. ↩

[45] S. Kheirkhah, S. Yarusevych, and S. Narasimhan. Orbiting response in vortex-induced vibrations of a two-degree-of-freedom pivoted circular cylinder. *Journal of Fluids and Structures*, 28:343–358, January 2012. DOI. ↩

[46] C. Leong and T. Wei. Two-degree-of-freedom vortex-induced vibration of a pivoted cylinder below critical mass ratio. *Proceedings of the Royal Society A: Mathematical, Physical and Engineering Sciences*, 464(2099):2907–2927, 2008. DOI. ↩

[47] F. Flemming and C. Williamson. Vortex-induced vibrations of a pivoted cylinder. *Journal of Fluid Mechanics*, 522:215–252, January 2005. DOI. ↩

[48] N. Cagney and S. Balabani. Streamwise vortex-induced vibrations of cylinders with one and two degrees of freedom. *Journal of Fluid Mechanics*, 758:702–727, November 2014. DOI. ↩

[49] S. Kheirkhah, S. Yarusevych, and S. Narasimhan. Wake Topology of a Cylinder Undergoing Vortex-Induced Vibrations With Elliptic Trajectories. *Journal of Fluids Engineering*, 138(5):054501, 2016. DOI. ↩

[50] E. Marble, C. Morton, and S. Yarusevych. POD Analysis of the Wake Development of a Pivoted Circular Cylinder Undergoing Vortex Induced Vibrations. In *Volume 1B, Symposia: Fluid Measurement and Instrumentation; Fluid Dynamics of Wind Energy; Renewable and Sustainable Energy Conversion; Energy and Process Engineering; Microfluidics and Nanofluidics; Development and Applications in Computational Fluid Dyn*, volume 1B-2017, V01BT06A007. ASME, July 2017. DOI. ↩

[51] H. L. Burrough, A. P. Jeary, and J. M. Wilson. Structural dynamics of large multiflue chimneys. In *International Conferece on Wind Effects on Buildings and Structures*, pages 497–514, July 1975. URL. ↩

[52] H. Ishizaki. Effects of wind pressure fluctuations on structures. In *International Research Seminar on Wind Effects on Buildings and Structures*, Ottawa. National Research Council of Canada, Division of Building Research, University of Toronto Press, 1968. ↩

[53] F. X. Schneider and F. H. Wittmann. An investigation of wind excited transversal oscillations of slender structures. In *International Conference on Wind Effects on Buildings and Structures*, pages 381–388, 1975. ↩

[54] C. Williamson and A. Roshko. Vortex formation in the wake of an oscillating cylinder. *Journal of Fluids and Structures*, 2(4):355–381, 1988. DOI. ↩

[55] D. Jeon and M. Gharib. On the relationship between the vortex formation process and cylinder wake vortex patterns. *Journal of Fluid Mechanics*, 519:161–181, November 2004. DOI. ↩

[56] S.-C. Hsieh, Y. M. Low, and Y.-M. Chiew. Flow characteristics around a circular cylinder undergoing vortex-induced vibration in the initial branch. *Ocean Engineering*, 129:265–278, January 2017. DOI. ↩

[57] H. Choi, W.-P. Jeon, and J. Kim. Control of Flow Over a Bluff Body. *Annual Review of Fluid Mechanics*, 40(1):113–139, 2008. DOI. ↩

[58] M. Provansal, C. Mathis, and L. Boyer. Bénard-von Kármán instability: transient and forced regimes. *Journal of Fluid Mechanics*, 182:1–22, September 1987. DOI. ↩

[59] D. Gerich and H. Eckelmann. Influence of end plates and free ends on the shedding frequency of circular cylinders. *Journal of Fluid Mechanics*, 122(-1):109–121, 1982. DOI. ↩

[60] H. Eisenlohr and H. Eckelmann. Vortex splitting and its consequences in the vortex street wake of cylinders at low Reynolds number. *Physics of Fluids A: Fluid Dynamics*, 1(2):189–192, 1989. DOI. ↩

[61] C. H. K. Williamson. Three-dimensional wake transition. *Journal of Fluid Mechanics*, 328:345–407, December 1996. DOI. ↩

[62] M. S. Bloor. The transition to turbulence in the wake of a circular cylinder. *Journal of Fluid Mechanics*, 19(02), 1964. DOI. ↩

[63] M. Braza, P. Chassaing, and H. H. Minh. Numerical study and physical analysis of the pressure and velocity fields in the near wake of a circular cylinder. *Journal of Fluid Mechanics*, 165(-1):79, 1986. DOI. ↩

[64] C. Norberg. An experimental investigation of the flow around a circular cylinder: influence of aspect ratio. *Journal of Fluid Mechanics*, 258:287–316, January 1994. DOI. ↩

[65] M. P. Rockwood, K. Taira, and M. A. Green. Detecting Vortex Formation and Shedding in Cylinder Wakes Using Lagrangian Coherent Structures. *AIAA Journal*, 55(1):15–23, 2017. DOI. ↩

[66] B. R. Morton. The generation and decay of vorticity. *Geophysical & Astrophysical Fluid Dynamics*, 28(3-4):277–308, 1984. DOI. ↩

[67] F. H. Abernathy and R. E. Kronauer. The formation of vortex streets. *Journal of Fluid Mechanics*, 13(01), 1962. DOI. ↩

[68] M. M. Zdravkovich. Smoke observations of the formation of a Kármán vortex street. *Journal of Fluid Mechanics*, 37(03):491–496, 1969. DOI. ↩

[69] C. J. Wood. Visualization of an incompressible wake with base bleed. *Journal of Fluid Mechanics*, 29(02):259–272, 1967. DOI. ↩

[70] M. E. Davies. A comparison of the wake structure of a stationary and oscillating bluff body, using a conditional averaging technique. *Journal of Fluid Mechanics*, 75(02):209–231, 1976. DOI. ↩

[71] P. K. Kundu, I. M. Cohen, and D. R. Dowling. *Fluid Mechanics*. Elsevier Inc., 5th edition, 2012, page 891. ISBN. ↩

[72] C. H. K. Williamson. The natural and forced formation of spot-like 'vortex dislocations' in the transition of a wake. *Journal of Fluid Mechanics*, 243(-1):393–441, 1992. DOI. ↩

[73] W. Dunn and S. Tavoularis. Experimental studies of vortices shed from cylinders with a step-change in diameter. *Journal of Fluid Mechanics*, 555:409, May 2006. DOI. ↩

[74] J. A. Bourgeois, P. Sattari, and R. J. Martinuzzi. Alternating half-loop shedding in the turbulent wake of a finite surface-mounted square cylinder with a thin boundary layer. *Physics of Fluids*, 23(9):095101, 2011. DOI. ↩

[75] R. Skop and O. Griffin. On a theory for the vortex-excited oscillations of flexible cylindrical structures. *Journal of Sound and Vibration*, 41(3):263–274, 1975. DOI. ↩

[76] J. T. Klamo. *Effects of Damping and Reynolds Number on Vortex-Induced Vibrations*. PhD, California Institute of Technology, 2007. ↩

[77] A. Voorhees, P. Dong, P. Atsavapranee, H. Benaroya, and T. Wei. Beating of a circular cylinder mounted as an inverted pendulum. *Journal of Fluid Mechanics*, 610:217–247, September 2008. DOI. ↩

[78] F. S. Hover, A. H. Techet, and M. S. Triantafyllou. Forces on oscillating uniform and tapered cylinders in cross flow. *Journal of Fluid Mechanics*, 363:97–114, May 1998. DOI. ↩

[79] J. Lighthill. Fundamentals concerning wave loading on offshore structures. *Journal of Fluid Mechanics*, 173:667–681, December 1986. DOI. ↩

[80] R. D. Blevins. Flow-Induced Vibrations, 1990. ↩

[81] B. M. Sumer and J. Fredsøe. *Hydrodynamics Around Cylindrical Structures (Revised Edition)*, volume 26 of *Advanced Series on Ocean Engineering*. World Scientific Publishing Co. Pte. Ltd., 2006. DOI. ↩

[82] M. Gharib, E. Rambod, and K. Shariff. A universal time scale for vortex ring formation. *Journal of Fluid Mechanics*, 360:121–140, April 1998. DOI. ↩

[83] T. Sarpkaya. Fluid forces on oscillating cylinders. *NASA STI/Recon Technical Report A*, 78:275–290, 1978. URL. ↩

[84] N. M. Anand and A. Torum. Free span vibration of submerged pipelines in steady flow and waves. In *International Symposium Separated Flow Around Marine Structures*, pages 155–99, 1985. ↩

[85] N. Srinil and H. Zanganeh. Modelling of coupled cross-flow/in-line vortex-induced vibrations using double Duffing and van der Pol oscillators. *Ocean Engineering*, 53:83–97, October 2012. DOI. ↩

[86] A. Fujarra, C. Pesce, F. Flemming, and C. Williamson. Vortex-induced vibration of a flexible cantilever. *Journal of Fluids and Structures*, 15(3-4):651–658, 2001. DOI. ↩

[87] A. H. Techet, F. S. Hover, and M. S. Triantafyllou. Vortical patterns behind a tapered cylinder oscillating transversely to a uniform flow. *Journal of Fluid Mechanics*, 363:79–96, May 1998. DOI. ↩

[88] J. Vandiver, H. Marcollo, S. Swithenbank, and V. Jhingran. High Mode Number Vortex-Induced Vibration Field Experiments. In *Offshore Technology Conference*. Offshore Technology Conference, April 2005. DOI. ↩

[89] R. Wardlaw, K. Cooper, R. Ko, and J. Watts. Wind tunnel and analytical investigations into the aeroelastic behaviour of bundled conductors. *IEEE Transactions on Power Apparatus and Systems*, 94(2):642–654, 1975. DOI. ↩

[90] S. Kheirkhah. *Vortex-induced vibrations of a pivoted circular cylinder and their control using a tuned-mass damper*. PhD thesis, 2011. ↩

[91] N. Cagney and S. Balabani. Mode competition in streamwise-only vortex induced vibrations. *Journal of Fluids and Structures*, 41:156–165, 2013. DOI. ↩

[92] N. Cagney and S. Balabani. Fluid forces acting on a cylinder undergoing streamwise vortex-induced vibrations. *Journal of Fluids and Structures*, 62:147–155, April 2016. DOI. ↩

[93] J. G. Wong, J. Kriegseis, and D. E. Rival. An investigation into vortex growth and stabilization for two-dimensional plunging and flapping plates with varying sweep. *Journal of Fluids and Structures*, 43:231–243, November 2013. DOI. ↩

[94] D. E. Rival, J. Kriegseis, P. Schaub, A. Widmann, and C. Tropea. Characteristic length scales for vortex detachment on plunging profiles with varying leading-edge geometry. *Experiments in Fluids*, 55(1):1660, 2014. DOI. ↩

[95] J. Kriegseis and D. E. Rival. Vortex force decomposition in the tip region of impulsively-started flat plates. *Journal of Fluid Mechanics*, 756:758–770, October 2014. DOI. ↩

[96] J. N. Fernando and D. E. Rival. Characterizing the influence of upstream obstacles on very low head water-turbine performance. *Journal of Hydraulic Research*, 52(5):644–652, 2014. DOI. ↩

[97] S. Kheirkhah, R. Lourenco, S. Yarusevych, and S. Narasimhan. Mitigation of Vortex-Induced Vibrations of a Pivoted Circular Cylinder Using an Adaptive Pendulum Tuned-Mass Damper. *Journal of Fluids Engineering*, 135(11):111106, 2013. DOI. ↩

[98] C. E. Willert and M. Gharib. Digital particle image velocimetry. *Experiments in Fluids*, 10(4):181–193, 1991. DOI. ↩

[99] J. Westerweel. Fundamentals of digital particle image velocimetry. *Measurement Science and Technology*, 8(12):1379–1392, 1997. DOI. ↩

[100] F. Scarano and M. L. Riethmuller. Advances in iterative multigrid PIV image processing. *Experiments in Fluids*, 29(7):S051–S060, 2000. DOI. ↩

[101] M. Raffel, C. E. Willert, and J. Kompenhans. *Particle Image Velocimetry*. Experimental Fluid Mechanics. Springer Berlin Heidelberg, Berlin, Heidelberg, second edition, 2007. DOI. ↩

[102] J. Westerweel and F. Scarano. Universal outlier detection for PIV data. *Experiments in Fluids*, 39(6):1096–1100, 2005. DOI. ↩

[103] B. Wieneke. PIV uncertainty quantification from correlation statistics. *Measurement Science and Technology*, 26(7):074002, 2015. DOI. ↩

[104] W. C. Reynolds and A. K. M. F. Hussain. The mechanics of an organized wave in turbulent shear flow. Part 3. Theoretical models and comparisons with experiments. *Journal of Fluid Mechanics*, 54(02):263, 1972. DOI. ↩

[105] A. K. M. F. Hussain. Coherent structures and turbulence. *Journal of Fluid Mechanics*, 173(-1):303–356, 1986. DOI. ↩

[106] J. L. Lumley. *Stochastic tools in turbulence*. New York: Academic Press, 1972. ISBN. ↩

[107] B. W. van Oudheusden, F. Scarano, N. P. van Hinsberg, and D. W. Watt. Phase-resolved characterization of vortex shedding in the near wake of a square-section cylinder at incidence. *Experiments in Fluids*, 39(1):86–98, 2005. DOI. ↩

[108] R. Perrin, M. Braza, E. Cid, S. Cazin, A. Barthet, A. Sevrain, C. Mockett, and F. Thiele. Obtaining phase averaged turbulence properties in the near wake of a circular cylinder at high Reynolds number using POD. *Experiments in Fluids*, 43(2-3):341–355, 2007. DOI. ↩

[109] C. Morton and S. Yarusevych. On vortex shedding from low aspect ratio dual step cylinders. *Journal of Fluids and Structures*, 44:251–269, January 2014. DOI. ↩

[110] G. Berkooz, P. Holmes, and J. L. Lumley. The Proper Orthogonal Decomposition in the Analysis of Turbulent Flows. *Annual Review of Fluid Mechanics*, 25(1):539–575, 1993. DOI. ↩

[111] L. Sirovich. Turbulence and the dynamics of coherent structures. II. Symmetries and transformations. *Quarterly of Applied Mathematics*, 45(3):561–571, 1987. DOI. ↩

[112] X. Ma, G.-S. Katamanos, and G. E. Kaniadakis. Dynamics and low-dimensionality of a turbulent near wake. *Journal of Fluid Mechanics*, 410:S0022112099007934, May 2000. DOI. ↩

[113] P. Moin and J. Kim. The structure of the vorticity field in turbulent channel flow. Part 1. Analysis of instantaneous fields and statistical correlations. *Journal of Fluid Mechanics*, 155:441–464, June 1985. DOI. ↩

[114] J. Kim, P. Moin, and R. Moser. Turbulence statistics in fully developed channel flow at low Reynolds number. *Journal of Fluid Mechanics*, 177:133–166, April 1987. DOI. ↩

[115] a. E. Perry, M. S. Chong, and T. T. Lim. The vortex-shedding process behind two-dimensional bluff bodies. *Journal of Fluid Mechanics*, 116:77–90, March 1982. DOI. ↩

[116] J. Jeong and F. Hussain. On the identification of a vortex. *Journal of Fluid Mechanics*, 285:69–94, February 1995. DOI. ↩

[117] M. S. Chong, A. E. Perry, and B. J. Cantwell. A general classification of three dimensional flow fields. *Physics of Fluids A: Fluid Dynamics*, 2(5):765–777, 1990. DOI. ↩

[118] J. C. Hunt, A. A. Wray, and P. Moin. Eddies, streams, and convergence zones in turbulent flows. *Center for Turbulence Research, Proceedings of the Summer Program*:193–208, 1988. URL. ↩

[119] J. Zhou, R. J. Adrian, S. Balachandar, and T. M. Kendall. Mechanisms for generating coherent packets of hairpin vortices in channel flow. *Journal of Fluid Mechanics*, 387:353–396, May 1999. DOI. ↩

[120] L. Graftieaux, M. Michard, and N. Grosjean. Combining PIV, POD and vortex identification algorithms for the study of unsteady turbulent swirling flows. *Measurement Science and Technology*, 12(9):1422–1429, 2001. DOI. ↩

[121] M. A. Green, C. W. Rowley, and G. Haller. Detection of Lagrangian coherent structures in three-dimensional turbulence. *Journal of Fluid Mechanics*, 572:111–120, February 2007. DOI. ↩

[122] L. Xu and M. I. Jordan. On Convergence Properties of the EM Algorithm for Gaussian Mixtures. *Neural Computation*, 8(1):129–151, 1996. DOI. ↩

[123] J. A. Bilmes. A gentle tutorial of the EM algorithm and its application to parameter estimation for Gaussian mixture and hidden Markov models. *International Computer Science Institute*, 4(510):126, 1998. ISBN. ↩

[124] J. Jiménez, H. K. Moffatt, and C. Vasco. The structure of the vortices in freely decaying two-dimensional turbulence. *Journal of Fluid Mechanics*, 313:209–222, April 1996. DOI. ↩

[125] T. P. Bray. *A Parametric Study of Vane and Air-jet Vortex Generators*. Engineering Doctorate, Cranfield University, 1998. URL. ↩

[126] D. G. Akhmetov. *Vortex Rings*. Springer Berlin Heidelberg, Berlin, Heidelberg, 2009. DOI. ↩

[127] N. Cagney and S. Balabani. Wake modes of a cylinder undergoing free streamwise vortex-induced vibrations. *Journal of Fluids and Structures*, 38:127–145, April 2013. DOI. ↩

[128] Y. Wu and K. T. Christensen. Population trends of spanwise vortices in wall turbulence. *Journal of Fluid Mechanics*, 568:55–76, December 2006. DOI. ↩

[129] E. Konstantinidis, S. Balabani, and M. Yianneskis. The timing of vortex shedding in a cylinder wake imposed by periodic inflow perturbations. *Journal of Fluid Mechanics*, 543:45–55, November 2005. DOI. ↩

[130] P. Anagnostopoulos. Numerical study of the flow past a cylinder excited transversely to the incident stream. Part 2: timing of vortex shedding, aperiodic phenomena and wake parameters. *Journal of Fluids and Structures*, 14(6):853–882, 2000. DOI. ↩

[131] Y. Huang and M. A. Green. Detection and tracking of vortex phenomena using Lagrangian coherent structures. *Experiments in Fluids*, 56(7):147, 2015. DOI. ↩

[132] J. H. Gerrard. The mechanics of the formation region of vortices behind bluff bodies. *Journal of Fluid Mechanics*, 25:401–413, June 1966. DOI. ↩

[133] J. W. Schaefer and S. Eskinazi. An analysis of the vortex street generated in a viscous fluid. *Journal of Fluid Mechanics*, 6(02):241, 1959. DOI. ↩

[134] O. M. Griffin. A note on bluff body vortex formation. *Journal of Fluid Mechanics*, 284:217–224, February 1995. DOI. ↩

[135] P. W. Bearman. Investigation of the flow behind a two-dimensional model with a blunt trailing edge and fitted with splitter plates. *Journal of Fluid Mechanics*, 21(02):241, 1965. DOI. ↩

[136] A. K. M. F. Hussain and M. Hayakawa. Eduction of large-scale organized structures in a turbulent plane wake. *Journal of Fluid Mechanics*, 180:193, July 1987. DOI. ↩

[137] J. A. Ferré and F. Giralt. Pattern-recognition analysis of the velocity field in plane turbulent wakes. *Journal of Fluid Mechanics*, 198:27, January 1989. DOI. ↩

[138] T. Zhou, S. F. M. Razali, Y. Zhou, L. P. Chua, and L. Cheng. Dependence of the wake on inclination of a stationary cylinder. *Experiments in Fluids*, 46(6):1125–1138, 2009. DOI. ↩

[139] M. Bishop and S. Yarusevych. Mitigating Blockage Effects on Flow Over a Circular Cylinder in an Adaptive-Wall Wind Tunnel. *Journal of Fluids Engineering*, 133(8):081101, 2011. DOI. ↩

[140] T. Okamoto and M. Takeuchi. Effect of Side Walls of Wind-Tunnel on Flow around Two-Dimensional Circular Cylinder and Its Wake. *Bulletin of JSME*, 18(123):1011–1017, 1975. DOI. ↩

[141] C. Norberg. Flow around a circular cylinder: aspects of fluctuating lift. *Journal of Fluids and Structures*, 15(3-4):459–469, 2001. DOI. ↩

[142] K. Taira, S. L. Brunton, S. T. M. Dawson, C. W. Rowley, T. Colonius, B. J. McKeon, O. T. Schmidt, S. Gordeyev, V. Theofilis, and L. S. Ukeiley. Modal Analysis of Fluid Flows: An Overview. *AIAA Journal*, 55(12):4013–4041, 2017. arXiv: 1702.01453. DOI. ↩

[143] Z. Hosseini, R. J. Martinuzzi, and B. R. Noack. Sensor-based estimation of the velocity in the wake of a low-aspect-ratio pyramid. *Experiments in Fluids*, 56(1):13, 2015. DOI. ↩

[144] O. Lehmkuhl, I. Rodríguez, R. Borrell, and A. Oliva. Low-frequency unsteadiness in the vortex formation region of a circular cylinder. *Physics of Fluids*, 25(8):085109, 2013. DOI. ↩

[145] B. R. Noack, K. Afanasiev, M. Morzynski, G. Tadmor, and F. Thiele. A hierarchy of low-dimensional models for the transient and post-transient cylinder wake. *Journal of Fluid Mechanics*, 497(497):335–363, 2003. DOI. ↩

[146] J. Mcclure and S. Yarusevych. Surface and Wake Pressure Fluctuations of a Cylinder in Transitional Flow Regime. In *International Symposium on the Application of Laser and Imaging Techniques to Fluid Mechanics*, 2016. ↩

[147] D. E. Rival and B. van Oudheusden. Load-estimation techniques for unsteady incompressible flows. *Experiments in Fluids*, 58(3):1–11, 2017. DOI. ↩

[148] R. J. Moffat. Contributions to the Theory of Single-Sample Uncertainty Analysis. *Journal of Fluids Engineering*, 104(2):250, 1982. DOI. ↩

[149] R. J. Moffat. Using Uncertainty Analysis in the Planning of an Experiment. *Journal of Fluids Engineering*, 107(2):173, 1985. DOI. ↩

[150] R. J. Moffat. Describing the uncertainties in experimental results. *Experimental Thermal and Fluid Science*, 1(1):3–17, 1988. DOI. ↩

[151] P. Welch. The use of fast Fourier transform for the estimation of power spectra: A method based on time averaging over short, modified periodograms. *IEEE Transactions on Audio and Electroacoustics*, 15(2):70–73, 1967. DOI. ↩

[152] A. Sciacchitano, D. R. Neal, B. L. Smith, S. O. Warner, P. P. Vlachos, B. Wieneke, and F. Scarano. Collaborative framework for PIV uncertainty quantification: comparative assessment of methods. *Measurement Science and Technology*, 26(7):074004, 2015. DOI. ↩

[153] R. J. Adrian. Particle-Imaging Techniques for Experimental Fluid Mechanics. *Annual Review of Fluid Mechanics*, 23(1):261–304, 1991. DOI. ↩

[154] R. D. Keane and R. J. Adrian. Theory of cross-correlation analysis of PIV images. *Applied Scientific Research*, 49(3):191–215, 1992. DOI. ↩

[155] A. Sciacchitano, B. Wieneke, and F. Scarano. PIV uncertainty quantification by image matching. *Measurement Science and Technology*, 24(4):045302, 2013. DOI. ↩

Appendices

Appendix A

Displacement Sensor Calibration

The displacement sensors were calibrated using a Velmex BiSlide MN10-0500-M02-21 traverse with a displacement resolution of 5 µm. Figures A.1a and A.1b depict the output voltage for the streamwise and transverse sensors, respectively. The least squares method was used to fit a line ($V_0 = mx + b$) to the data and obtain the associated calibration coefficients. The linearity of the streamwise and transverse sensors was 180 µm and 200 µm, respectively, which corresponds to $\pm 0.0093D$ and $\pm 0.0103D$, respectively.

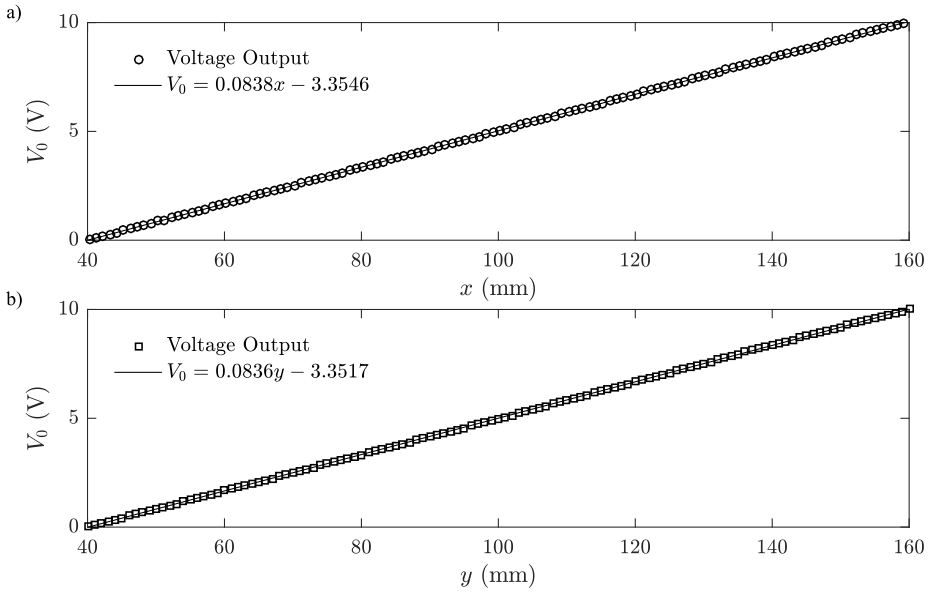

Figure A.1: Displacement sensor calibration.

Appendix B

Uncertainty Analysis

Uncertainty analysis is an essential component of any experimental investigation. This Appendix outlines the methods for calculating the uncertainty of measured and derived quantities presented throughout this thesis. Following the methodology of Moffat [148–150], the total uncertainty, ϵ_β, for a particular quantity β is estimated as the root-square-sum of the n sources of error, ϵ_i, over a 95% confidence interval:

$$\epsilon_\beta = \pm \left(\sum_{i=1}^{n} \epsilon_i^2 \right)^{1/2} \tag{B.1}$$

It is impossible to account for all n sources of error, therefore it is the investigator's responsibility to assess the major contributors to the total uncertainty in the analysis.

When a quantity cannot be measured directly, investigations often calculate the desired quantity from measured quantities. The uncertainty of a derived quantity, β, that is related to the independent measured quantities, α_i, through a known relationship $\beta = f(\alpha_1, \alpha_2, ..., \alpha_n)$, can be estimated using the root-sum-square approach:

$$\epsilon_\beta = \pm \left[\left(\frac{\delta\beta}{\delta\alpha_1} \epsilon_{\alpha_1} \right)^2 + \left(\frac{\delta\beta}{\delta\alpha_2} \epsilon_{\alpha_2} \right)^2 + ... + \left(\frac{\delta\beta}{\delta\alpha_n} \epsilon_{\alpha_n} \right)^2 \right]^{1/2} \tag{B.2}$$

where the partial derivatives are the sensitivity coefficients for the desired quantity with respect to the measured quantities. Application of Eq. B.2 is straightforward when the function f is known; however, some quantities are obtained from complex analytical processes that cannot be described by a single function. In the present study, the discrete nature of the data requires numerical approximations to derive some of the desired quanti-

ties. In such instances, a sequential perturbation method [150] is required to estimate the total uncertainty. In general, the uncertainty in measured quantities, α_i, is propagated to the derived quantity, β, according to the following procedure [149]:

1. Derive the quantity β_0 from the quantities α_i without accounting for uncertainty.
2. For $i = 1$ to n, sequentially perturb each input by increasing the value of α_i by its uncertainty interval, then calculate the derived quantity, β_i^+. Repeat by decreasing α_i by its uncertainty and calculating β_i^-. The n differences $\beta_i^+ - \beta_0$ and $\beta_i^- - \beta_0$ are the contribution to the total uncertainty of β for each α_i.
3. Calculate the uncertainty of β using Eq. B.1.

Table B.1 summarizes the experimental uncertainties with details of the calculations provided in the following sections.

B.1 Experimental Conditions

The experimental conditions consist of the Reynolds number, Re, and the cylinder aspect ratio, AR, mass ratio, m^*, and moment of inertia ratio, I^*.

The cylinder aspect ratio is calculated from its diameter, D, and length, L. The diameter was measured at two locations along the span using a digital caliper with a resolution of 0.01 mm, while the length was measured using a tape measure with a resolution of 1 mm. The associated relative uncertainty of the diameter and length are $\epsilon_D = \pm\ 0.1\%$ and $\epsilon_L = \pm\ 0.2\%$, respectively. Combining these estimates using Eq. B.2 results in $\epsilon_{AR} = \pm\ 0.2\%$ for the cylinder aspect ratio.

The mass ratio of the cylinder is calculated from the mass of the cylinder, m, and the mass of the displaced fluid, m_d. The mass of the cylinder is measured using a digital scale with a resolution of 0.001 kg, resulting in a relative uncertainty of $\epsilon_m = \pm\ 0.2\%$. In the calculation of the mass of the displaced fluid, it was assumed that the contribution due to the displaced air was negligible in comparison to that of the displaced water, i.e. $m_{d\ a} \ll m_{d\ w}$. The mass of the displaced water is calculated from the water density, ρ, cylinder diameter, D, and wetted length of the cylinder, L_0. The density was measured indirectly via measurement of the water temperature using a thermometer with a resolution of ± 1 °C, resulting in a small relative uncertainty of $\epsilon_\rho = \pm\ 0.0002\%$. The wetted length of the cylinder was measured using a tape measure with a resolution of 1 mm, resulting in a relative uncertainty of $\epsilon_{L_0} = \pm\ 0.5\%$. Using Eq. B.2, the total uncertainty of the mass of the displaced fluid is $\epsilon_{m_d} = \pm\ 0.5\%$ and the overall uncertainty for the mass ratio is $\epsilon_{m^*} = \pm\ 0.4\%$.

The moment of inertia ratio of the cylinder is calculated from the moment of inertia of

Table B.1: Measurement uncertainty estimates.

Parameter	Uncertainty*	Applies to
AR	$\pm 0.2\%$	
A_x^*	$\leq \pm 2.6\%$	Figs. 4.3 and 5.1
A_y^*	$\leq \pm 0.4\%$	Figs. 4.3, 4.4, 5.1, and 5.2
f_x^*, f_y^*	$\pm 1.7\%$	Fig. 4.2
I^*	$\pm 1.5\%$	
m^*	$\pm 0.4\%$	
Re	$\pm 4.9\%$	
U^*	$\leq \pm 8.3\%$	
D	$\pm 0.1\%$	
d_{wake}	$\pm 0.029D$	Figs. 5.9b, 5.10, and 5.11
f_n, f_x, f_y	$\pm 1.2\%$	
f_s, f_u, f_v	$\pm 3.9\%$	Figs. 5.13, 5.14, and 5.29
L	$\pm 0.2\%$	
L_f	$\pm 0.037D$	Fig. 5.9a
$\|\|\vec{U}\|\|/U_0$	$\leq \pm 14.2\%$	Figs. 5.3 and 5.4
u_{RMS}	$\leq \pm 9.8\%$ of max u_{RMS}	Figs. 5.5–7
u_d	$\pm 0.040U_0$	Fig. 5.9c
v_{RMS}	$\leq \pm 7.3\%$ of max v_{RMS}	Figs. 5.5–7
δ	$\leq \pm 0.4\%$	Fig. 4.1
ν	$\pm 2.5\%$	
vortex core position		
x	$\pm 0.04D$	Figs. 3.7b, 4.6, 4.7a, 4.8a, 4.8d, 5.23a, and 5.24a and **??**
y	$\pm 0.03D$	Figs. 3.7b and 4.6

* All uncertainty estimates are associated with a 95% confidence interval.

the cylinder, I, and the moment of inertia of the displaced fluid, I_d, about the pivot point. The moment of inertia of the cylinder is calculated from the cylinder mass, m, and length, L, while the moment of inertia of the displaced fluid is calculated from the water density, ρ, cylinder diameter, D, and wetted length of the cylinder, L_0. Their associated uncertainties, calculated using Eq. B.2, are $\epsilon_I = \pm 0.3\%$ and $\epsilon_{I_d} = \pm 1.4\%$. The total uncertainty of the moment of inertia ratio is calculated using Eq. B.2, resulting in $\epsilon_{I^*} = \pm 1.5\%$.

The diameter based Reynolds number is calculated from the free stream velocity, U_0, cylinder diameter, D, and fluid kinematic viscosity, ν. The kinematic viscosity was measured indirectly via measurement of the temperature using a thermometer with a resolution of ± 1 °C. As such, the relative uncertainty of the kinematic viscosity is $\epsilon_\nu = \pm\ 2.5\%$. The free stream velocity was determined from PIV measurements of the wake velocity as outlined in Appendix C. From the floor of the water tunnel to the surface, there is a gradual increase in the free stream velocity with z, thus there is a change in the local Reynolds number. Within the region of primary investigation the change in U_0 along the span is 1.18%. Additionally, the uncertainty estimate of the random error in PIV for measurement of the free stream velocity is less than 3%. Uncertainty from PIV measurements is discussed in Appendix B.3. Combining these estimates results in $\epsilon_{U_0} = \pm 4.2\%$. Finally, the uncertainty on the Reynolds number is calculated using Eq. B.2, with the uncertainty estimates for the free stream velocity, cylinder diameter, and kinematic viscosity as inputs, resulting in $\epsilon_{Re} = \pm 4.9\%$.

B.2 Displacement Sensor Measurements

The quantities obtained from displacement sensor measurements consist of the normalized amplitude, A_x^* and A_y^*, and normalized frequency, f_x^* and f_y^*, of structural vibrations in the streamwise and transverse directions, respectively, and the maximum deflection angle of the structure, δ.

The normalized amplitude of vibration is calculated from the cylinder diameter, D, and the amplitude of cylinder vibration. Streamwise and transverse cylinder position were measured using two Hoskin CP24MHT80 laser-based displacement sensors operating in "resolution mode" with a resolution of 20 µm and a linearity of 0.1%. The uncertainty of A_x^* and A_y^* is calculated using Eq. B.2, with the uncertainty estimates for the cylinder diameter and position as inputs, resulting in $\epsilon_{A_x^*} \leq \pm 2.6\%$ and $\epsilon_{A_y^*} \leq \pm 0.4\%$. The maximum deflection is calculated from the cylinder length, L, and the amplitude of cylinder vibration. Using Eq. B.2, the resultant relative uncertainty is $\epsilon_\delta \leq \pm 0.4\%$.

Spectral analysis of the cylinder displacement signal was employed to identify dom-

inant disturbance frequencies associated with the structure's natural frequency, f_n, and the normalized frequency of structural vibration in the streamwise, f_x^*, and transverse, f_y^*, directions. The one-dimensional spectra were computed using Welch's method [151]. The displacement signal was divided into equal windows of 2^{13} points with 50% overlap, resulting in a frequency resolution of 0.0122 Hz. Therefore, the uncertainty in determining a particular frequency is half the resolution, $\epsilon_{f_n} = \epsilon_{f_x} = \epsilon_{f_y} = \pm 1.2\%$. Using Eq. B.2, the relative uncertainty of the normalized frequency of vibration is $\epsilon_{f_x^*} = \epsilon_{f_y^*} = \pm 1.7\%$.

B.3 PIV Measurements

Uncertainty estimation in PIV measurements is challenging due to the multitude of error sources originating from calibration, image acquisition, and image processing [101]. Error associated with image acquisition includes the uncertainty in: particle seeding density, laser/camera alignment, and camera focus and aperture. Aspects contributing to error in image processing include: interrogation window selection, removal and replacement of erroneous data, and cross-correlation for displacement computation. Due to the numerous sources of error, there remains to be a consensus in the research community as to how PIV uncertainty should be quantified [99, 101, 152–154]. The present investigation uses the particle disparity method [152, 155] to estimate the uncertainty associated with random errors in PIV. This method is *a posteriori* in that the computed velocity field is input to determine the local random error. The particle disparity method is advantageous because it provides uncertainty in the instantaneous, mean and RMS velocity fields.

Figure B.1 presents the random errors in the mean (first column), streamwise RMS (second column), and transverse RMS (third column) velocity fields for the PIV configuration in the $x-y$ plane. The top, middle, and bottom row of Fig. B.1 correspond to the stationary cylinder and VIV at $U^* = 5.48$ and 7.08, respectively. The mean fields show that the highest error ($\epsilon_{||\vec{U}||/U_0} = \pm 14.2\%$) occurs near the formation length where vortices roll up at the end of the separated shear layers. The uncertainty is lower further downstream in the wake ($\epsilon_{||\vec{U}||/U_0} \leq \pm 8.1\%$) and much lower in the free stream at the transverse extent of measurement ($\epsilon_{||\vec{U}||/U_0} \leq \pm 3.3\%$) because there is less swirling motion in the fluid. Uncertainty is highest for $U^* = 5.48$ (Fig. B.1d) because vorticity is reoriented from the spanwise direction to the streamwise and transverse directions as the vortex tubes bend, see discussion in Section 5.5. This makes cross-correlation of the windowed seeding particles between images more difficult because of the increased out of plane motion. The random error in the RMS fields is normalized with their respective maximum values and is generally less than the random error in the mean fields. The error in the RMS fields

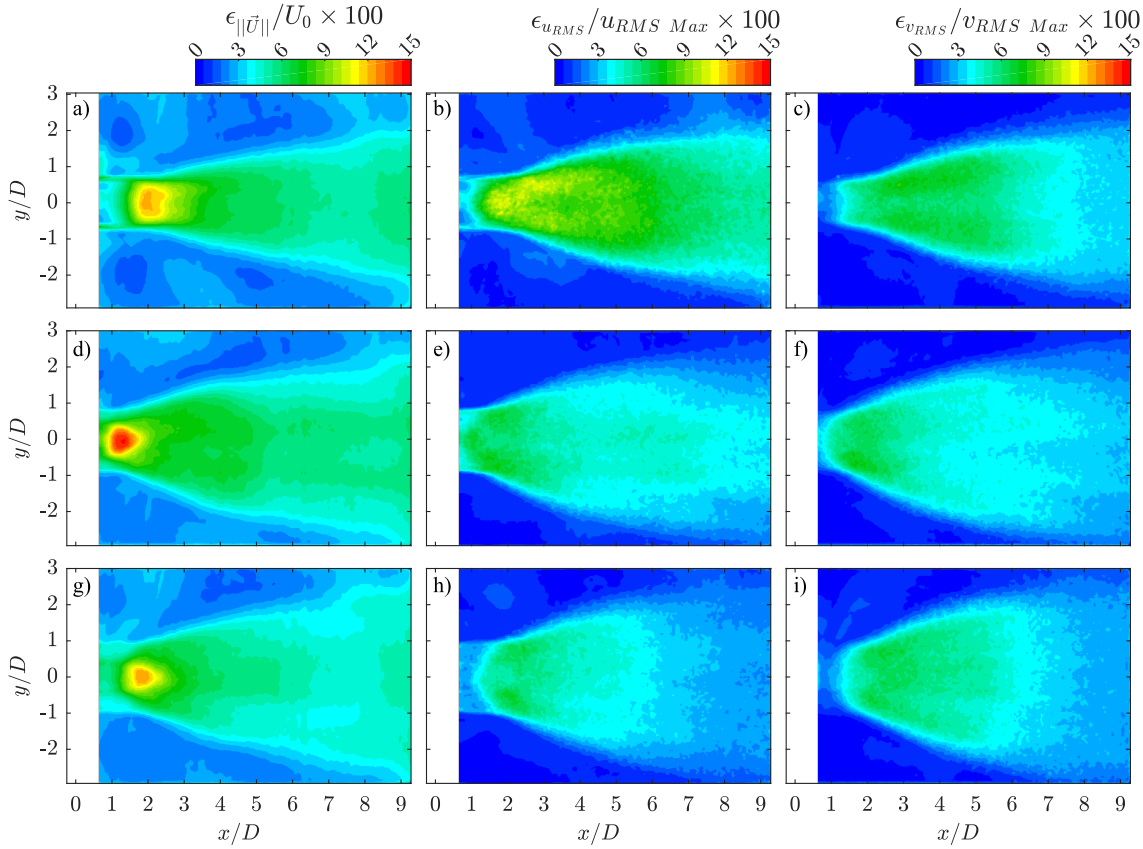

Figure B.1: PIV random error estimates in the $x-y$ plane for (a-c) stationary cylinder, (d-f) $U^* = 5.48$, and (g-i) $U^* = 7.08$. The first column shows the uncertainty in the velocity magnitude normalized by the free stream velocity, center column shows the uncertainty in the streamwise RMS velocity field, and right column shows the uncertainty in the transverse RMS velocity field. The RMS velocity uncertainties are normalized by the maximum RMS value of the corresponding component.

has a maximum of $\epsilon_{u_{RMS}} = \pm 9.8\%$ and $\epsilon_{v_{RMS}} = \pm 7.3\%$ with spatial distributions that are similar to their respective RMS fields (Figs. 5.5–7).

Figures B.2a–d present the random errors in the mean velocity field in the $x-z$ plane for the free stream, stationary cylinder, $U^* = 5.48$, and $U^* = 7.08$ cases, respectively. The maximum error in the free stream ($\epsilon_{||\vec{U}||/U_0} = \pm 3.0\%$) is lower than the other three cases ($\epsilon_{||\vec{U}||/U_0} = \pm 5.4\%$) because the absence of vortex formation and advection in the wake of the cylinder reduces the out of plane motion of the seeding particles. For the stationary

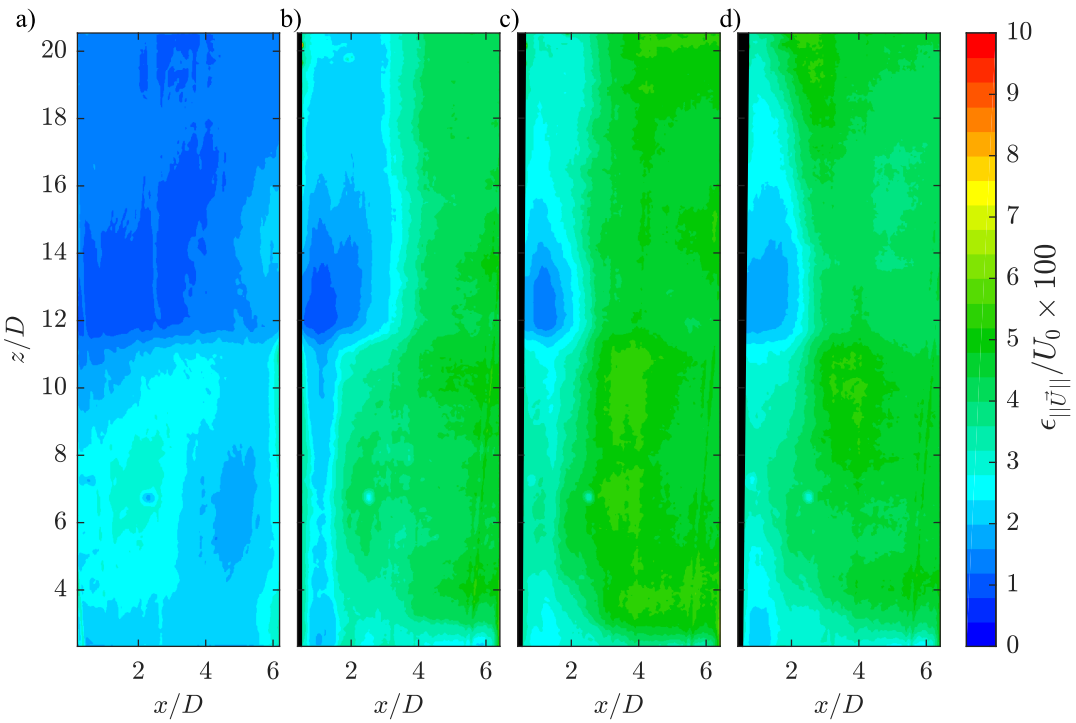

Figure B.2: PIV random error estimates in the $x - z$ plane for (a) free stream, (b) stationary cylinder, (c) $U^* = 5.48$, and (d) $U^* = 7.08$. Uncertainty in the velocity magnitude is normalized by the free stream velocity.

cylinder and VIV cases, the error is relatively low upstream of $x/D \approx 2$ because the measurement plane in this region is positioned far enough from the cylinder that it does not intersect the separated shear layer or the near wake. At $x/D \approx 2$ the error increases in the streamwise direction because this is approximately the streamwise location where spanwise structures in the wake initially intersect the measurement plane (Fig. 5.3). The effect of using two cameras is apparent in the error of the free stream as there is a notable spatial gradient in the spanwise direction at $z/D \approx 11$ where the two measured fields overlap. Factors such as laser illumination, camera/laser alignment, and camera focus contribute to the general difference in uncertainty above and below $z/D \approx 11$.

B.4 Derived Quantities

Quantities derived from PIV measurements consist of the vortex shedding frequency, wake half-width, d_{wake}, velocity deficit, u_d, and formation length, L_f. The reduced velocity, U^*, is derived from both PIV and displacement sensor measurements.

Spectral analysis of the velocity signal and POD temporal coefficients was employed to identify dominant disturbance frequencies associated with the shedding of coherent structures. The one-dimensional spectra were computed using Welch's method [151]. The displacement signal was divided into equal windows of 2^{10} points with 50% overlap, resulting in a frequency resolution of 0.0196 Hz. Therefore, the uncertainty in determining a particular frequency is half the resolution, $\epsilon_{f_s} = \epsilon_{f_u} = \epsilon_{f_v} = \pm 3.9\%$.

Figure 4.13 investigates and compares various definitions of the formation length, L_f, Uncertainty in the location of the maximum value in the RMS fields was assessed by applying the RMS uncertainties to their respective fields and then propagating it to the estimated parameters. Similarly, uncertainty in the streamwise extent of the recirculation region was assessed by applying the mean streamwise uncertainty to the mean streamwise velocity field and then propagating it through to the estimated parameter. The resultant uncertainties for the streamwise location of $v_{RMS\ Max}$, $u_{RMS\ Max}$, and $U/U_0 = 0$ are $\pm 0.037D$, $\pm 0.051D$, and $\pm 0.072D$, respectively. The results in Chapter 5 consider the formation length as the streamwise location of $v_{RMS\ Max}$, as such the uncertainty in the formation length is $\epsilon_{L_f} = \pm 0.037D$.

Uncertainties in the maximum velocity deficit, $u_{d\ Max}$, and the wake half-width, d_{wake}, were assessed by applying the uncertainty in the mean streamwise field to the respective field and then propagating it to the estimated parameters. In such a manner, the uncertainties were determined to be $\epsilon_{u_{d\ Max}} = \pm 0.040U_0$ and $\epsilon_{d_{wake}} = \pm 0.029D$.

The reduced velocity, U^*, is calculated from the cylinder diameter, D, natural frequency of the structure, f_n, and free stream velocity, U_0. As previously mentioned the error associated with each of these three parameters is $\epsilon_D = \pm 0.1\%$, $\epsilon_{f_n} = \pm 1.2\%$, and $\epsilon_{U_0} = \pm 4.2\%$. Using Eq. B.2, the total uncertainty of the reduced velocity is $\epsilon_{U^*} = \pm 8.3\%$.

B.5 GMM Vortex Identification

Uncertainty estimation in vortex identification is challenging because there remains to be an accepted definition of a vortex in turbulent flow [116]. The present investigation employs a novel vortex identification method using the statistical GMM and EM algorithms in combination with the Q-criterion. Figures B.3a and B.4a present the variation of the

streamwise and transverse vortex core position, respectively, with respect to the phase angle as per GMM based vortex identification using the Q-criterion for a stationary cylinder. Similarly, Figs. B.3b and B.4b present variation of the streamwise and transverse vortex core position, respectively, but use the λ_2-criterion as input to the algorithm. The absolute difference in vortex core locations computed using the Q and λ_2-criteria is depicted in Figs. B.3c and B.4c for the streamwise and transverse locations, respectively. Error in the vortex location is estimated as two standard deviations of the difference to provide a 95% confidence interval. The resultant uncertainties of the streamwise and transverse vortex core locations are estimated as $\epsilon_x = \pm 0.04D$ and $\epsilon_y = \pm 0.03D$, respectively.

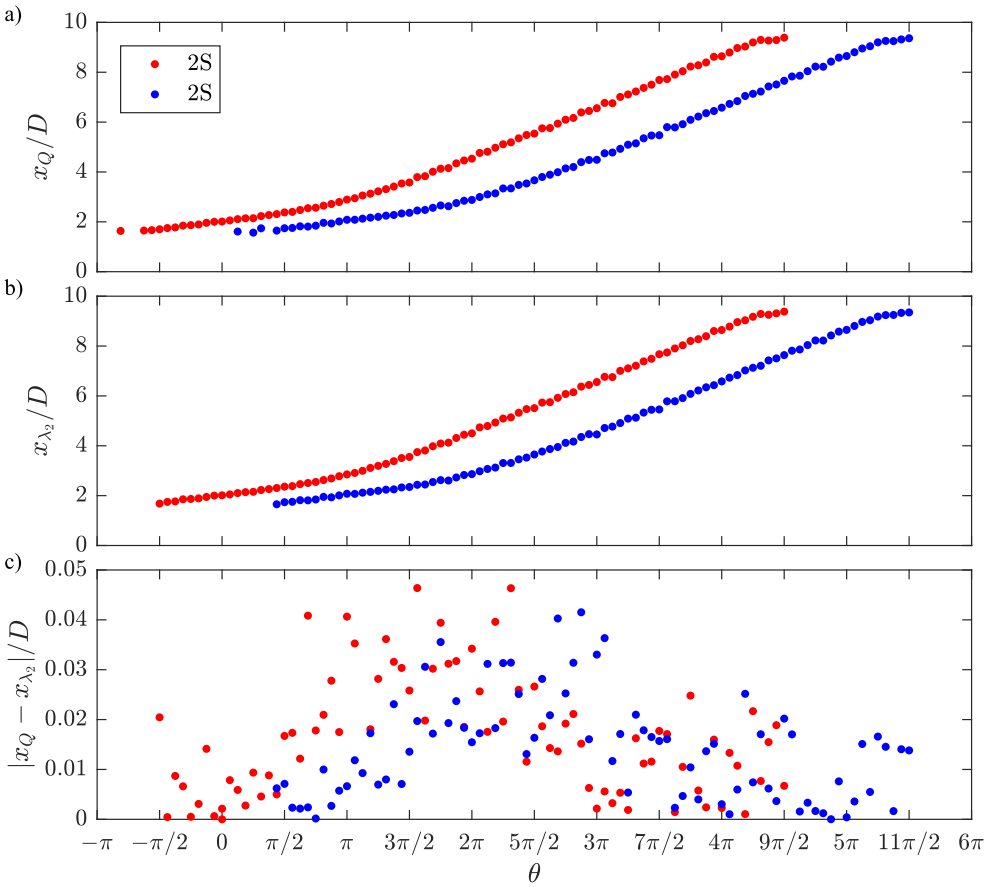

Figure B.3: Variation of streamwise vortex core position with respect to phase angle as per GMM based vortex identification using the (a) Q-criterion and (b) λ_2-criterion for a stationary cylinder. (c) Absolute difference between streamwise vortex core positions computed using the Q and λ_2-criteria.

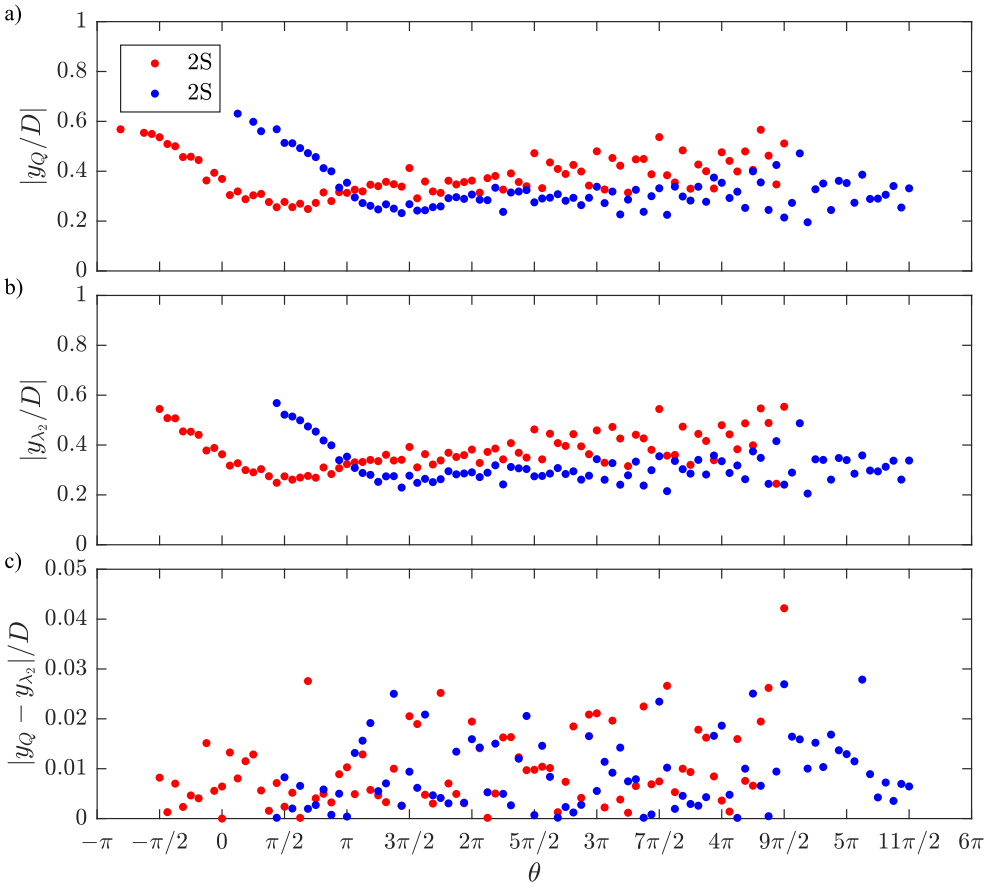

Figure B.4: Variation of transverse vortex core position with respect to phase angle as per GMM based vortex identification using the (a) Q-criterion and (b) λ_2-criterion for a stationary cylinder. (c) Absolute difference between transverse vortex core positions computed using the Q and λ_2-criteria.

Appendix C

Free Stream Characterization

The flow conditioning for the closed-loop water tunnel at the University of Calgary is shown in Fig. C.1. An axial pump, controlled with a variable frequency drive, supplies water to the plenum. A cylindrical conditioner mounted on the floor of the plenum prevents large recirculating flow from developing as the water enters the plenum. The flow passes through a honeycomb conditioning unit and three fine screens to reduce the turbulence intensity. A contraction with a six-to-one ratio accelerates the flow into the first test section.

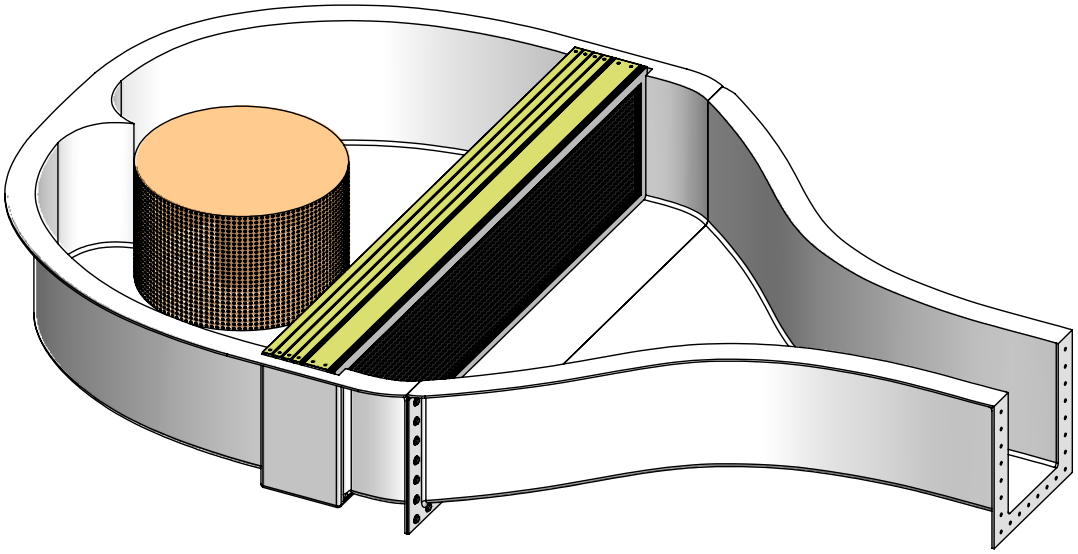

Figure C.1: Water tunnel conditioning elements.

The water tunnel free stream characteristics were extracted from planar PIV measurements in the xz plane at $y = 0$ with the model removed from the test section. Water depth in the test section under quiescent conditions was maintained at $L_0 = 429\text{mm}$. These measurements were taken at a water density, $\rho_{water} = 997.6\text{kg}\,\text{m}^{-3}$, and viscosity, $\mu_{water} = 0.9622 \times 10^{-3}\text{N}\,\text{s}\,\text{m}^{-2}$, for a measured water temperature of 22 °C. Careful monitoring and control of the water depth and cleanliness of the water tunnel throughout the experimental campaign minimized deviation from the characteristics reported in this section.

The mean streamwise and spanwise velocity fields obtained from time resolved PIV measurements are shown in Figs. C.2a and C.2b, respectively, with a field of view that extends from $2.32 \leq z/D \leq 20.54$ in the spanwise direction and from $0.19 \leq x/D \leq 6.19$ in the streamwise direction. The mean fields were calculated from 2044 velocity fields acquired at 20 Hz over the span of 102 s. The free stream velocity used in this study, $U_0 = 0.1606\text{m}\,\text{s}^{-1}$, is the spatial mean of the streamwise velocity in the xz plane. This is 2.4 % greater than the predicted free stream velocity, $U_{0_{predicted}} = 0.1568\text{m}\,\text{s}^{-1}$, obtained from ultrasonic measurements near the entrance of the first test section. The ultrasonic measurements at the center-line of the first test section were previously calibrated against LDV measurements, where the linear fit $U_{0_{predicted}} = 1.0966 U_{0_{ultrasonic}}$ provides the predicted free stream velocity for $R^2 = 0.99926$. It should be noted that, throughout the experimental campaigns, $U_{0_{ultrasonic}}$ was held constant to within $\pm 0.001\text{m}\,\text{s}^{-1}$ by maintaining the variable frequency drive at 24.7 Hz and the depth of the flowing water in the first test section at $L_0 = 428\text{mm}$.

Figure C.2c depicts contours of the turbulence intensity in the xz plane, with a mean value of 1.32 %. Within the spanwise region $5 < z/D < 19.5$, the turbulence intensity is low, the streamwise velocity is within 1 % of U_0 and the normalized spanwise velocity is within 1 % of zero. Below this region, $z/D < 5$, there is moderate turbulence and the flow has a notable spanwise component. Such an effect may be attributed to flow disruptions at the tunnel floor as the water exits the plenum and enters the first test section. This is not of concern in the present study because the primary investigation of the wake occurs within the range $5.2 \leq z/D \leq 19.1$.

Spanwise profiles of the mean velocity (Fig. C.3a) and turbulence intensity (Fig. C.3b) clearly distinguish these two regions. The overall min-max flow uniformity is 3.64 %, while that within the region of primary investigation is 1.18 %. At $z/D \approx 11.5$, a slight discontinuity in both profiles is a result of stitching the vector fields calculated from images acquired from the two high speed cameras mounted in spanwise succession.

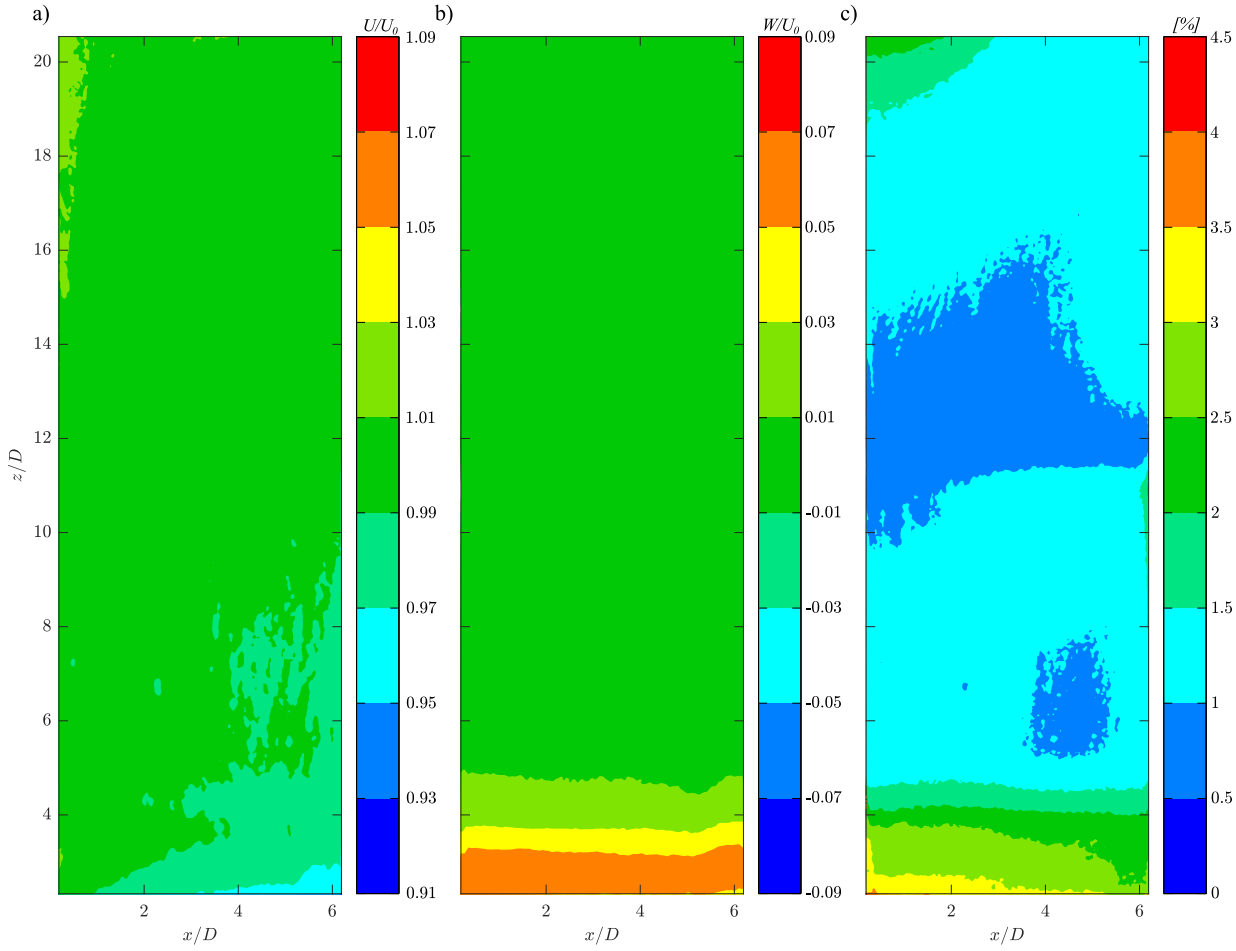

Figure C.2: Contours of the (a) streamwise mean velocity, (b) spanwise mean velocity, and (c) turbulence intensity in the xz plane acquired from PIV measurement.

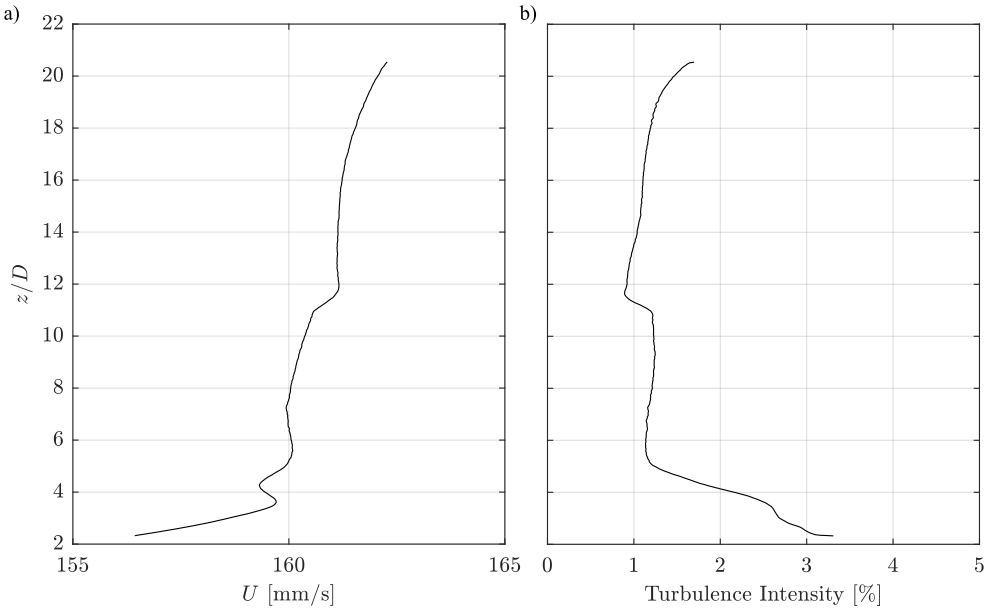

Figure C.3: Profiles of the (a) streamwise free-stream velocity and (b) turbulence intensity in the spanwise direction acquired from PIV measurement.

Appendix D

Assessment of Water Depth Effects

Vortex induced vibrations are caused by the periodic fluid induced loads along the span of the cylinder. The present study maintains a water depth of $L_0 = 428$mm between tests to ensure a consistent spanwise region of fluid structure interaction. Figure D.1 presents the amplitude of transverse and streamwise oscillations near the end of the lock-in region for various water depths. The results indicate that greater transverse and smaller streamwise responses occurs for deeper flows. Specifically, increasing the water depth by 20 mm from $L_0 = 425$ to 445mm generally causes A_y^* to increase by approximately $0.1D$ and A_x^* to decrease by approximately $0.02D$. Given that the uncertainty of measuring the water depth is ± 1mm in the present study, variability of the water depth is not expected to significantly impact the observed structural response.

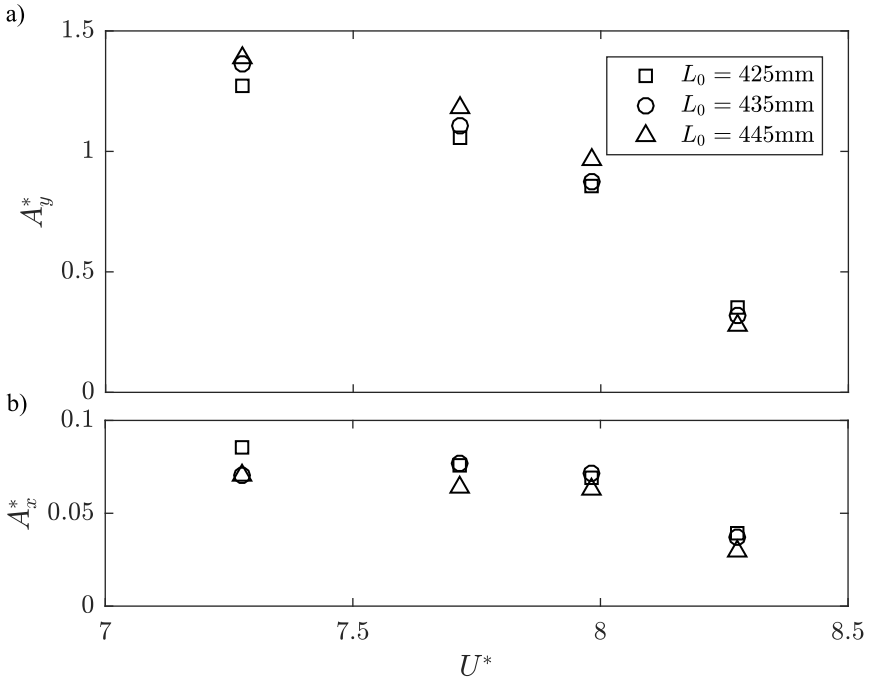

Figure D.1: Amplitude response in the (a) transverse and (b) streamwise directions for quiescent water depths $L_0 = 425,\ 435$, and 445mm. Free stream velocity is varied to obtain the reduced velocity range for a constant natural frequency of the structure, $f_n = 1.72$Hz.

Appendix E

Assessment of Initial Condition Effects

In the present study, all VIV tests were performed with identical initial conditions. The cylinder tip was released from rest at $(x/D, y/D) = (0, 0)$ and structural oscillations were permitted to develop for a period of 10 min before acquiring displacement and/or wake velocity measurements. This Appendix section investigates sensitivity of the structural response to the prescribed initial condition. Table E.1 outlines the five cases examined for VIV at $U^* = 6.70$. The first three cases release the cylinder tip from rest at $(x/D, y/D) = (0, 0)$, $(0, -1.5)$, and $(-1.5, 0)$, respectively. The fourth and fifth cases release the cylinder tip from $(x/D, y/D) = (0, -1.5)$ and provide an initial motion such that the cylinder trajectory is approximately circular with counter-clockwise and clockwise directions, respectively. The structural oscillations are permitted to develop for a period of 5 min before acquiring displacement measurements at 100 Hz for 15 min. Figures E.1a–e present the cylinder tip trajectory for the five cases, respectively. Examination of the

Table E.1: VIV initial conditions for $U^* = 6.70$.

Case	$x(t=0)/D$	$y(t=0)/D$	Motion at $t = 0$
1	0	0	rest
2	0	-1.5	rest
3	-1.5	0	rest
4	0	-1.5	CCW
5	0	-1.5	CW

trajectories reveals identical elliptic orientations, distinguished based on orbiting direction and tilt with respect to the cross-flow direction. Furthermore, spectra of the streamwise and transverse oscillations in Figs. E.2a and E.2b, respectively, reveal similar dominant peaks at the structure's natural frequency for all cases. Consequently, the prescribed initial condition does not impact the steady state structural response.

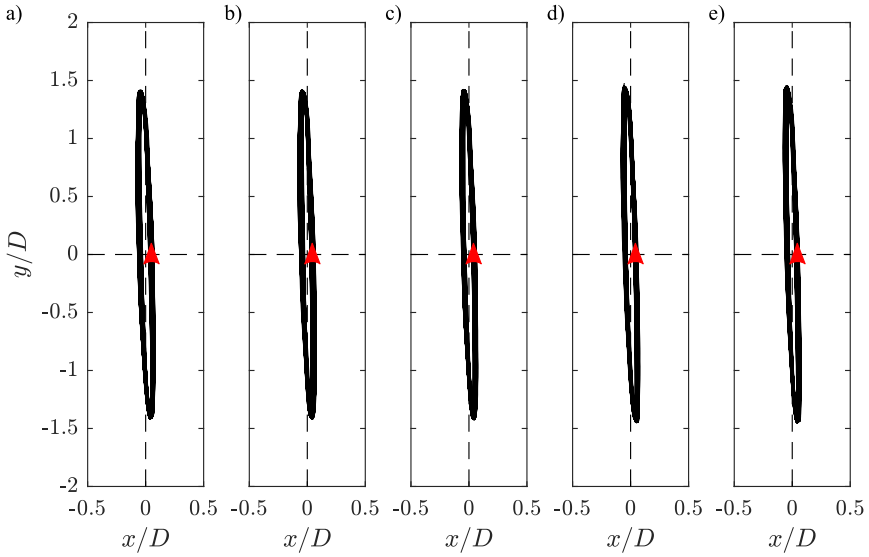

Figure E.1: Cylinder tip trajectories for the five cases listed in Table E.1; (a-e) cases 1-5, respectively. A red arrow in each image denotes the orbiting direction.

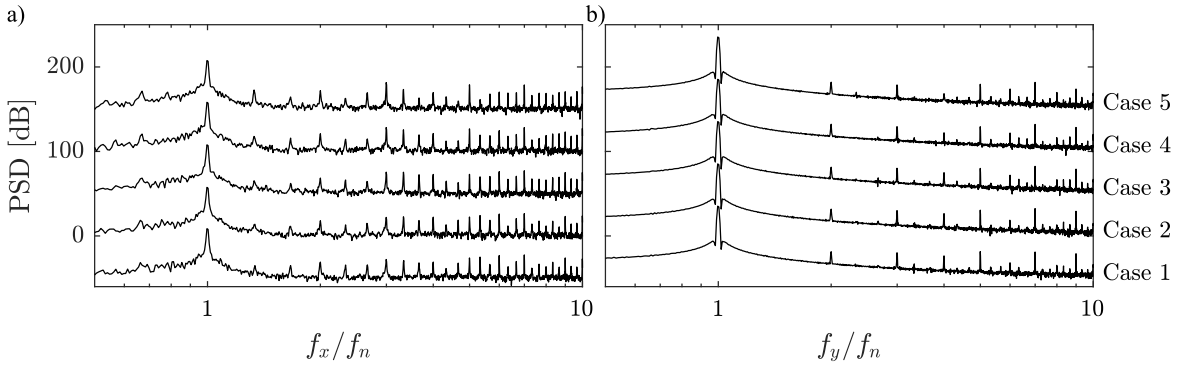

Figure E.2: Spectra of the (a) streamwise and (b) transverse vibrations for the five cases listed in Table E.1. Note, spectra are plotted with a consistent offset for clarity.

Appendix F

Supplementary Results - Proper Orthogonal Decomposition

The discussion of the Proper Orthogonal Decomposition results in Chapter 5 was limited to the horizontal planes and focused on the modal energy and spectra of the temporal coefficients. This Appendix presents results of the POD analysis on the PIV measurements in the vertical and horizontal planes. Appendices F.1–F.3 depict the temporal coefficients and spatial modes for the stationary, $U^* = 5.48$, and $U^* = 7.08$ cases, respectively. These results were omitted from the previous chapters for conciseness and are presented here for completeness of the data sets presented.

Figure F.1a presents the relative turbulent kinetic energy of each POD mode and Fig. F.1b presents the cumulative turbulent kinetic energy from the POD analysis in the vertical plane. All three cases exhibit three mode pairs with comparable energy content. Closer examination of the temporal coefficients and spatial modes in Figs. F.4, F.6, and F.10 reveals that mode pairs have similar temporal signals and wake topologies that are offset by a phase shift of approximately $\pi/2$. Figure F.2 presents the frequencies of the dominant peaks in the spectra of the temporal coefficients.

Examination of POD results from the vertical plane for the stationary case indicates there is cellular shedding near the base of the cylinder in agreement with observation of the sequential instantaneous streamwise velocity snapshots in the vertical plane in Section 5.2. The first mode pair captures the shedding of coherent structures at $fD/U_0 \approx 0.205$ in the region $z/D \gtrsim 8$. Similarly the third mode captures shedding at this frequency, except in the region $12 \lesssim z/D \lesssim 16$ where the first mode pair is dominant. The second mode pair captures shedding at a lower frequency, $fD/U_0 \approx 0.190$, near the base of the cylinder in the region $z/D \lesssim 8$. Structures near the base of the cylinder are shed at a lower frequency

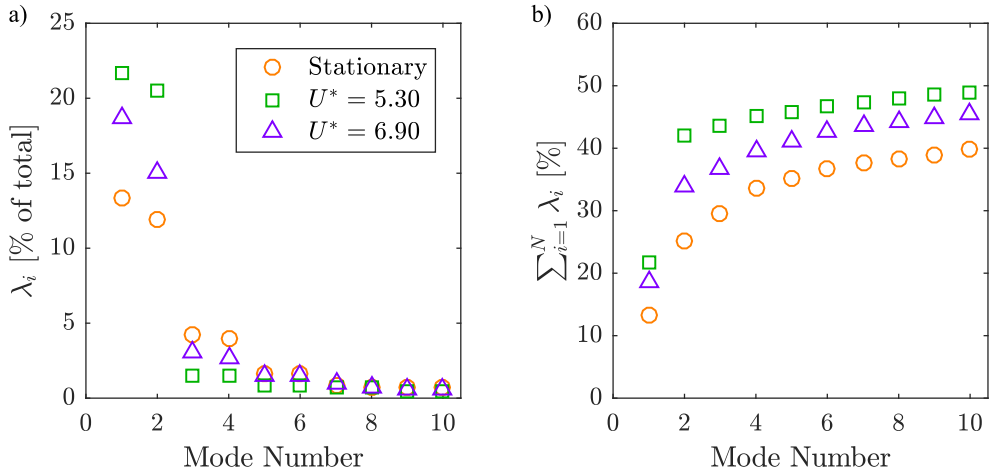

Figure F.1: Relative turbulent kinetic energy from POD analysis of the vertical, $x - z$, plane; (a) mode energy distribution (b) cumulative mode energy.

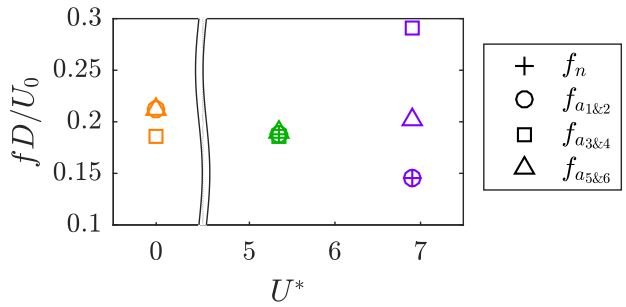

Figure F.2: Dominant peak in the power spectral density of the temporal coefficients from POD analysis of the vertical, $x - z$, plane.

because the free stream velocity is lower in this region as a result of the effects of the tunnel floor, Appendix C. It is important to note that the cellular shedding occurs below the spanwise investigation of the wake ($8.5 \lesssim z/D \lesssim 16$) and the results of the POD analysis are similar between horizontal planes.

For the VIV case at $U^* = 5.48$, Fig. F.2 reveals that spectra of the temporal coefficients for the six most energetic modes all exhibit dominant peaks at the structure's natural frequency. Examination of the spatial modes and temporal coefficients from the POD analysis in the vertical plane in Fig. F.6 reveals that the first mode pair captures coherent structures that exist along the entire span except near the hybrid wake transition from P+S to 2S at $z/D \approx 15$. The second mode pair captures the coherent structures near this

transition in the region $13.5 \lesssim z/D \lesssim 17.5$. The temporal coefficients of the second mode pair indicate there are significant cycle-to-cycle variations, which may be attributed to the variation of the spanwise location of dislocation between the P+S and 2S wake vortices. Similarly, the third mode pair captures coherent structures at the base of the cylinder near the hybrid transition between 2S and P+S shedding. The temporal coefficients of the third mode also indicate cycle-to-cycle variations that may be a result of variation of the spanwise location of vortex dislocation.

Results of the POD analysis in the vertical plane for the VIV case at $U^* = 7.08$ indicate the first and second mode pairs capture the shedding of coherent structures associated with the vortex pairs in P+S shedding. Spectral analysis of the temporal coefficients reveals dominant peaks at f_n and $2f_n$ for the first and second mode pairs, respectively, see Fig. F.2. Examination of the third and fourth spatial modes in Figs. F.10f and F.10g, respectively, reveals that the coherent structures captured by the second mode pair are more energetic higher along the span where there is greater contrast in the contours along the streamwise direction. This may be indicative of the 2P shedding pattern predicted based on the Morse and Williamson [1] shedding map, which was not observed in the wake reconstruction due to its limited spanwise range. Existence of the 2P shedding regime higher along the span would necessitate an additional wake transition between P+S and 2P shedding. Lower along the span, the third mode pair captures coherent structures shed at the frequency of vortex shedding from a stationary cylinder, f_s, in agreement with the spectral analysis of the wake velocity in Section 5.4 and the POD analysis in the horizontal plane in Section 5.6. Temporal coefficients of the third mode pair reveal cycle-to-cycle variations that are indicative of the intermittent shedding of vortices at f_n and f_s, as was found in Chapter 5.

The goal of the POD analysis was to extract the dynamics of the most energetic coherent structures for use in producing phase averaged reconstructions of the wake. The reference signal for POD based phase averaging was obtained from the cross plot of the first two temporal coefficients as outlined in Section 3.3.2. Figures F.3a and F.3b depict the cross plots obtained from POD analysis in the horizontal plane at $z/D \approx 6.5$ for the VIV cases $U^* = 5.48$ and $U^* = 7.08$, respectively. The data points in the cross plot for $U^* = 5.48$ fall closer to the ellipse given by

$$\frac{a_1^2}{2\lambda_1} + \frac{a_2^2}{2\lambda_2} = 1 \tag{F.1}$$

than the data points in the cross plot for $U^* = 7.08$. Physically, deviation from the ellipse means that the coherent structures captured by the first mode pair vary slightly from cycle-to-cycle. For the VIV case $U^* = 7.08$ at the plane $z/D \approx 6.5$, this coincides with the intermittent switching of vortex shedding at f_n and f_s. Figures F.3c–e show the

spanwise variation of data distribution about the ellipse for the stationary, $U^* = 5.48$, and $U^* = 7.08$ cases, respectively, with error bars indicating one standard deviation. The wider distribution is relatively consistent along the span for the stationary cylinder since the frequency of vortex shedding cannot lock onto the motion of the cylinder and varies slightly throughout time, see Section 5.4. For the VIV case at $U^* = 5.48$, the data points fall very close to the ellipse in the spanwise region of P+S shedding, while there is a slight increase in their distribution in the region of 2S shedding. Similarly, the spanwise region of P+S shedding for the VIV case at $U^* = 7.08$ exhibits a concentrated distribution. However, there is significant variability closer to the base where the intermittent switching in the frequency of vortex shedding is observed.

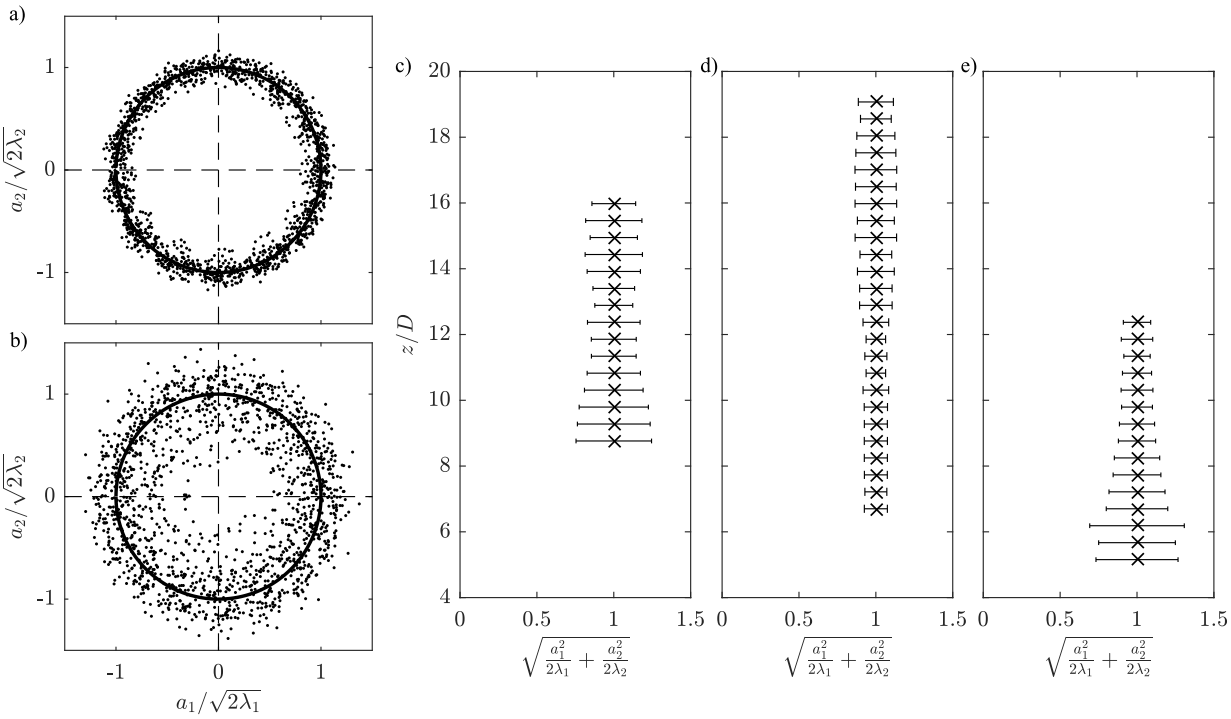

Figure F.3: Cross plots of temporal coefficients a_1 and a_2 for (a) $U^* = 5.48$ and (b) $U^* = 7.08$ at $z/D \approx 6.5$. Distribution of the cross plot for the investigated horizontal planes is shown for (c) stationary cylinder, (d) $U^* = 5.48$, and (e) $U^* = 7.08$ with error bars indicating one standard deviation.

F.1 Stationary Cylinder

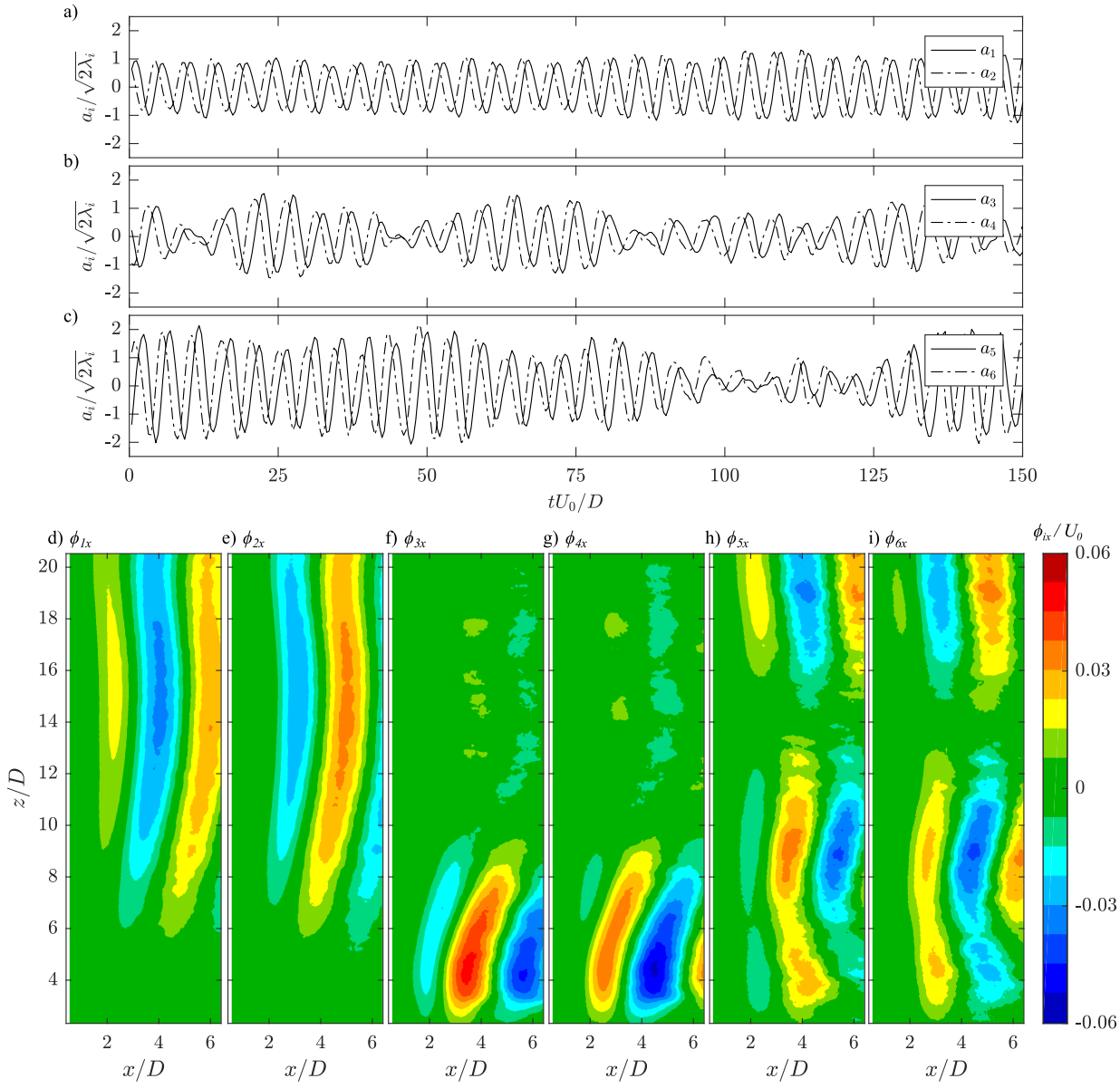

Figure F.4: POD analysis in the $x - z$ plane for a stationary cylinder. Temporal coefficients normalized with respective energy content for (a) modes 1 and 2, (b) modes 3 and 4, and (c) modes 5 and 6. Streamwise spatial modes for (d-i) POD modes 1 to 6.

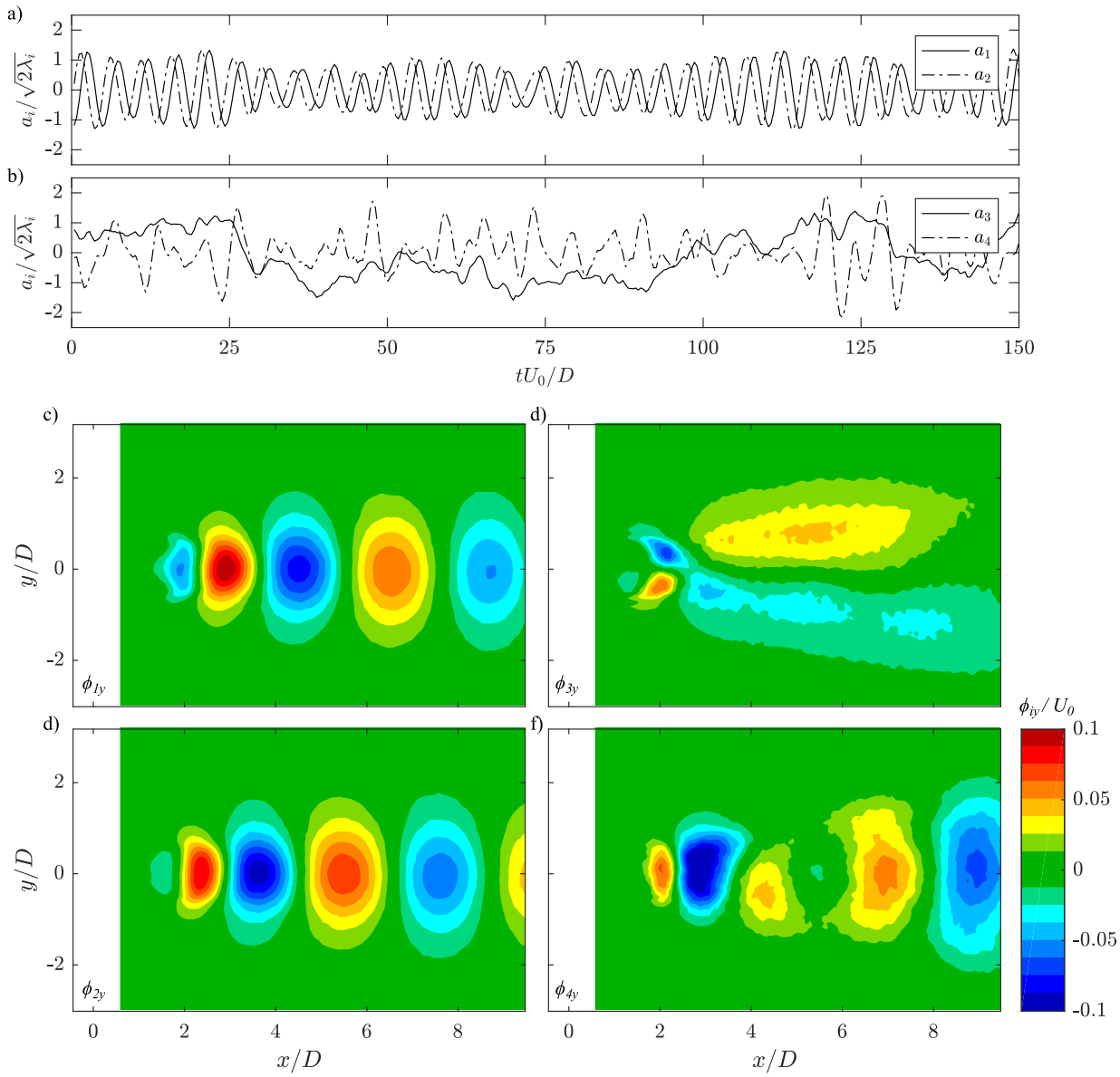

Figure F.5: POD analysis in the $x-y$ plane at $z/D \approx 10$ for a stationary cylinder. Temporal coefficients normalized with respective energy content for (a) modes 1 and 2, and (b) modes 3 and 4. Transverse spatial modes for (c-f) POD modes 1 to 4.

F.2 Reduced Velocity 5.48

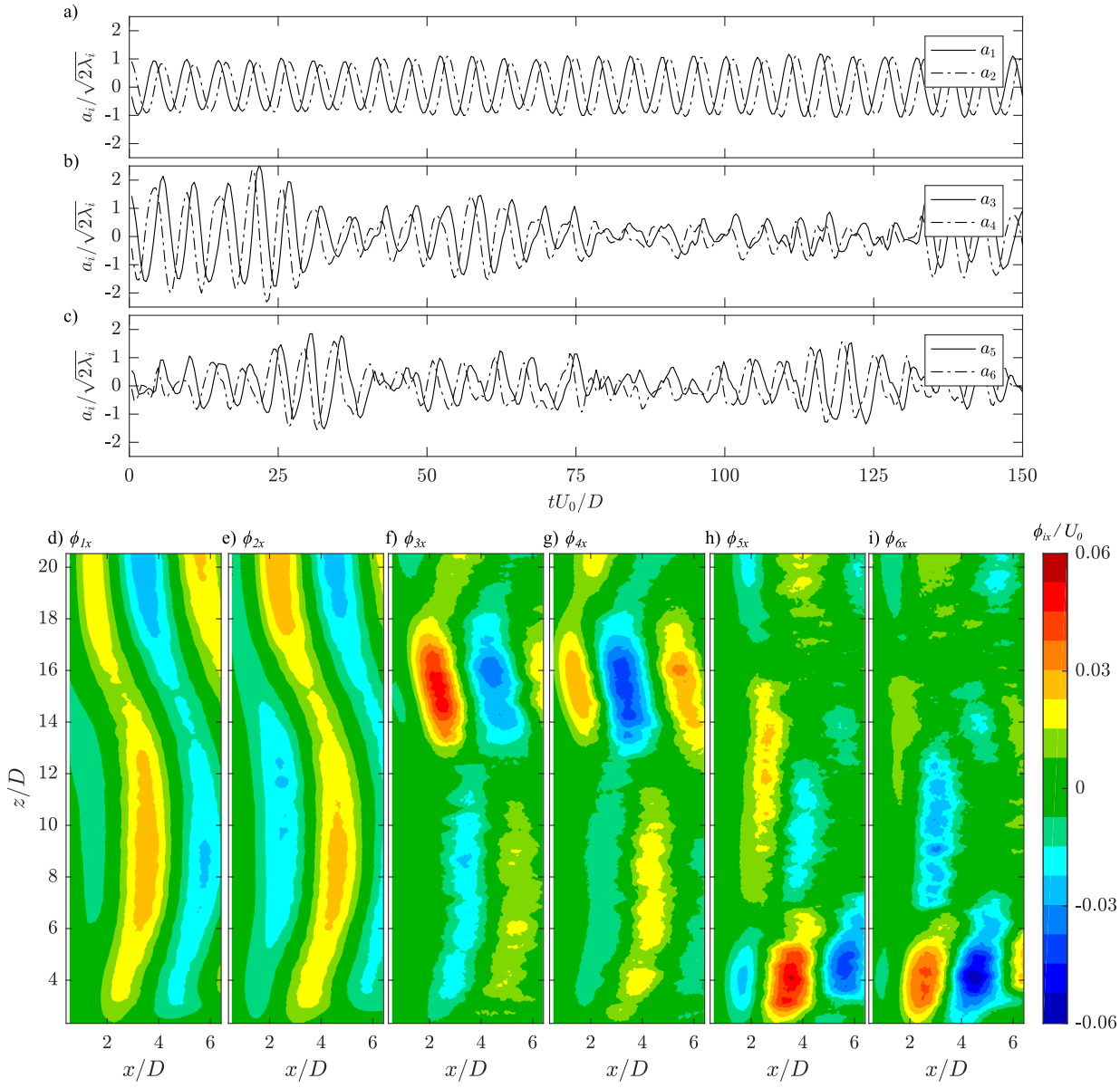

Figure F.6: POD analysis in the $x-z$ plane for the case $U^* = 5.48$. Temporal coefficients normalized with respective energy content for (a) modes 1 and 2, (b) modes 3 and 4, and (c) modes 5 and 6. Streamwise spatial modes for (d-i) POD modes 1 to 6.

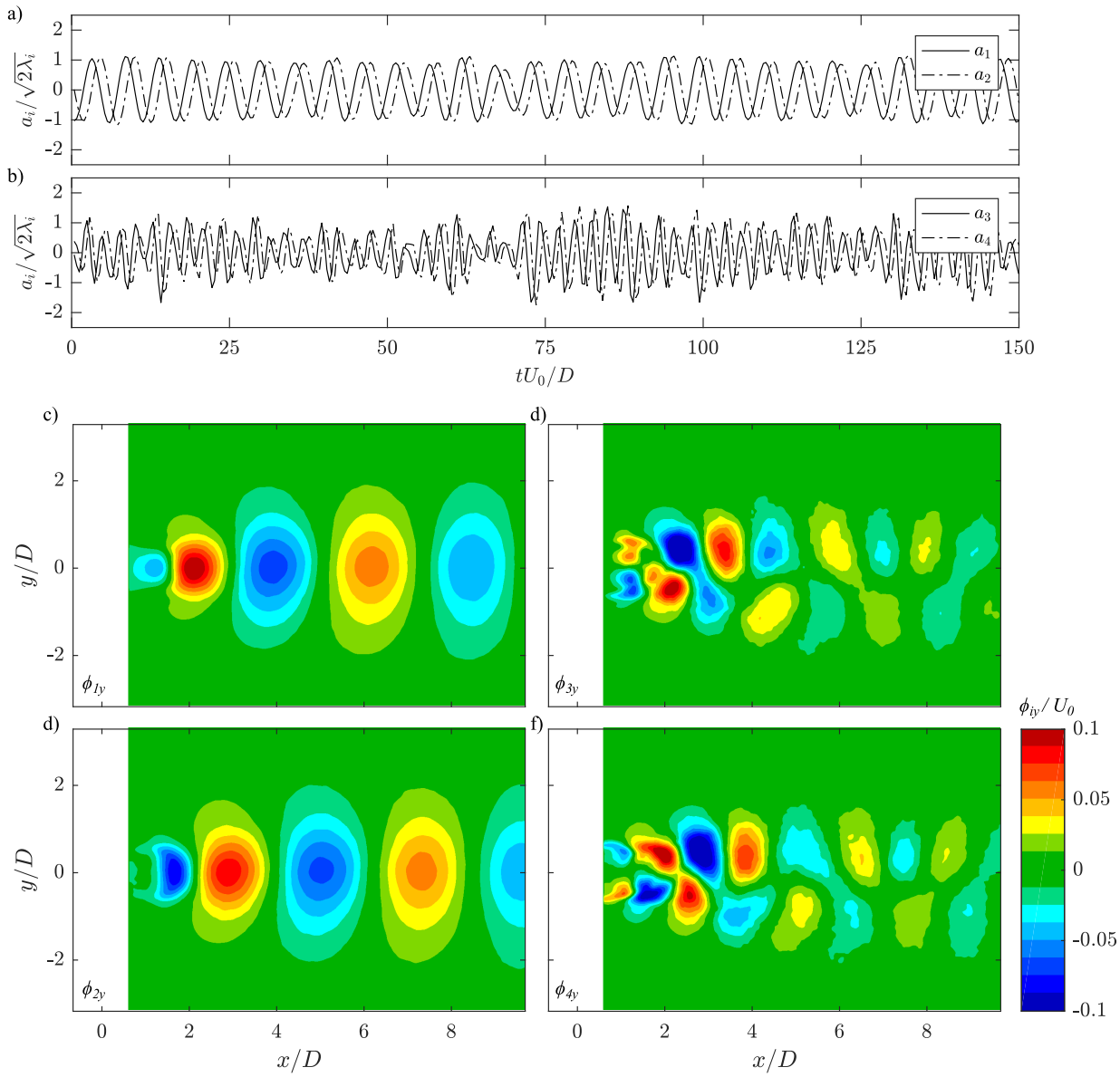

Figure F.7: POD analysis in the $x - y$ plane at $z/D \approx 6.5$ for the case $U^* = 5.48$. Temporal coefficients normalized with respective energy content for (a) modes 1 and 2, and (b) modes 3 and 4. Transverse spatial modes for (c-f) POD modes 1 to 4.

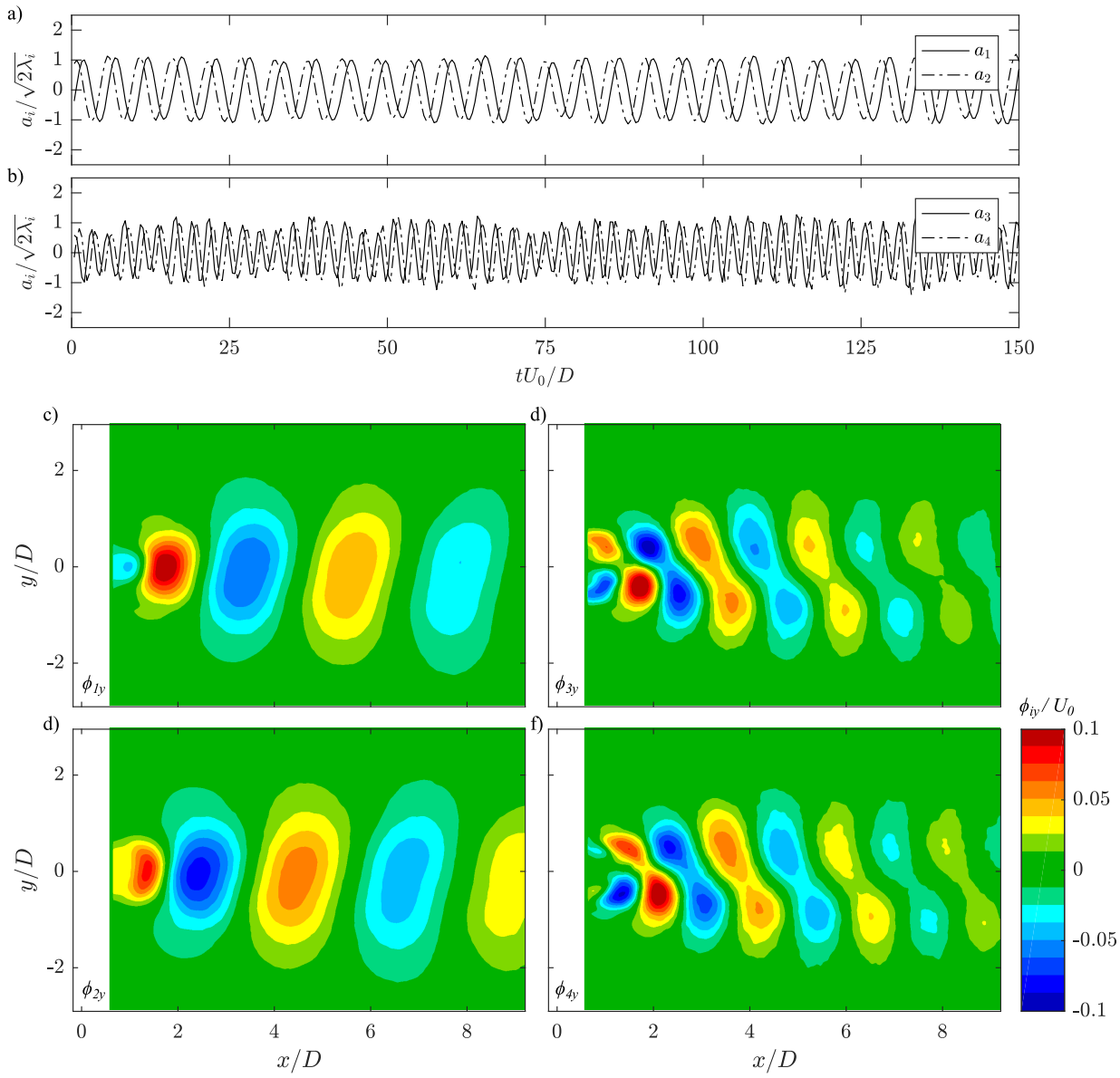

Figure F.8: POD analysis in the $x-y$ plane at $z/D \approx 13.5$ for the case $U^* = 5.48$. Temporal coefficients normalized with respective energy content for (a) modes 1 and 2, and (b) modes 3 and 4. Transverse spatial modes for (c-f) POD modes 1 to 4.

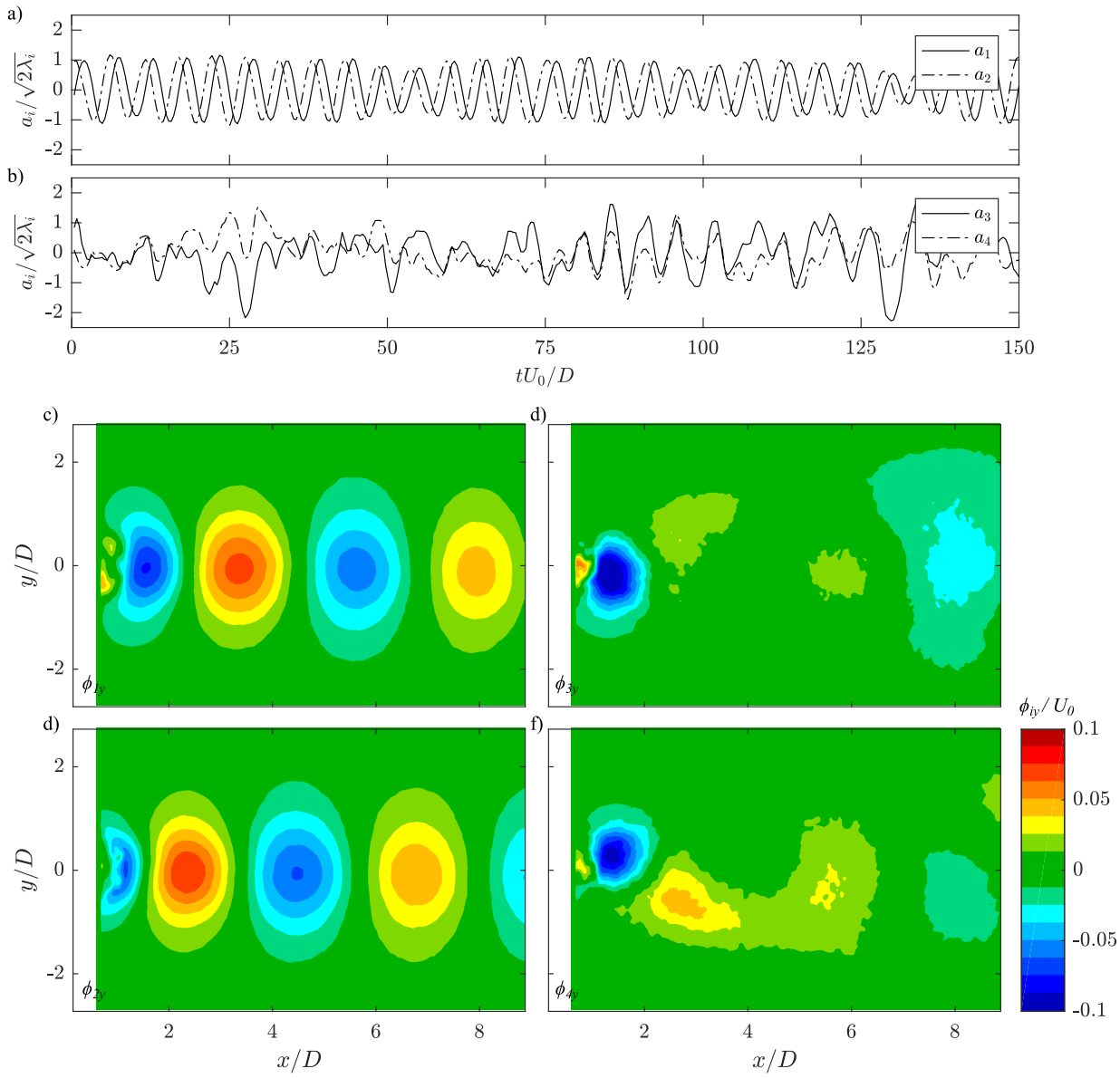

Figure F.9: POD analysis in the $x - y$ plane at $z/D \approx 18$ for the case $U^* = 5.48$. Temporal coefficients normalized with respective energy content for (a) modes 1 and 2, and (b) modes 3 and 4. Transverse spatial modes for (c-f) POD modes 1 to 4.

F.3 Reduced Velocity 7.08

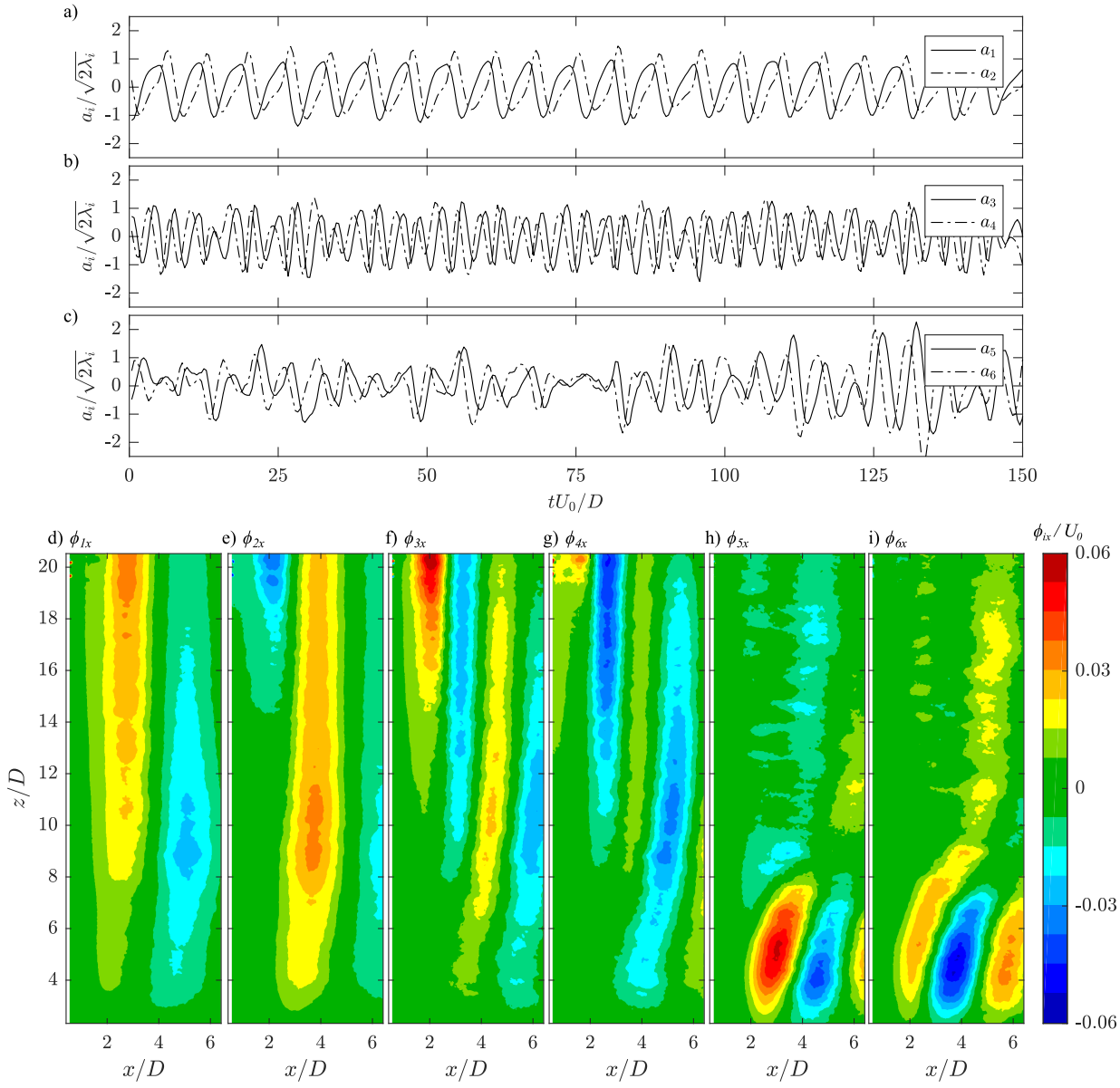

Figure F.10: POD analysis in the $x-z$ plane for the case $U^* = 7.08$. Temporal coefficients normalized with respective energy content for (a) modes 1 and 2, (b) modes 3 and 4, and (c) modes 5 and 6. Streamwise spatial modes for (d-i) POD modes 1 to 6.

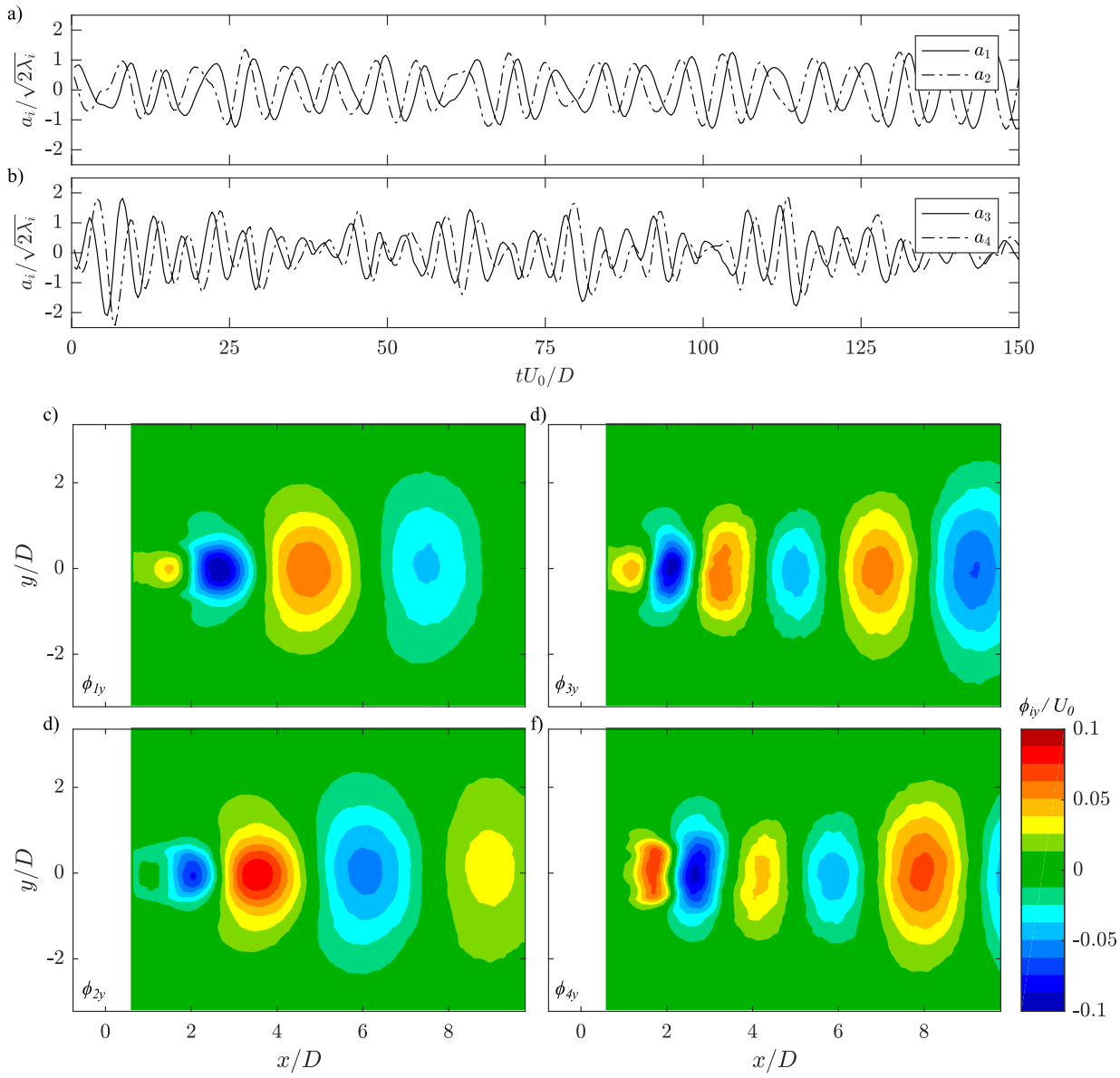

Figure F.11: POD analysis in the $x-y$ plane at $z/D \approx 5$ for the case $U^* = 7.08$. Temporal coefficients normalized with respective energy content for (a) modes 1 and 2, and (b) modes 3 and 4. Transverse spatial modes for (c-f) POD modes 1 to 4.

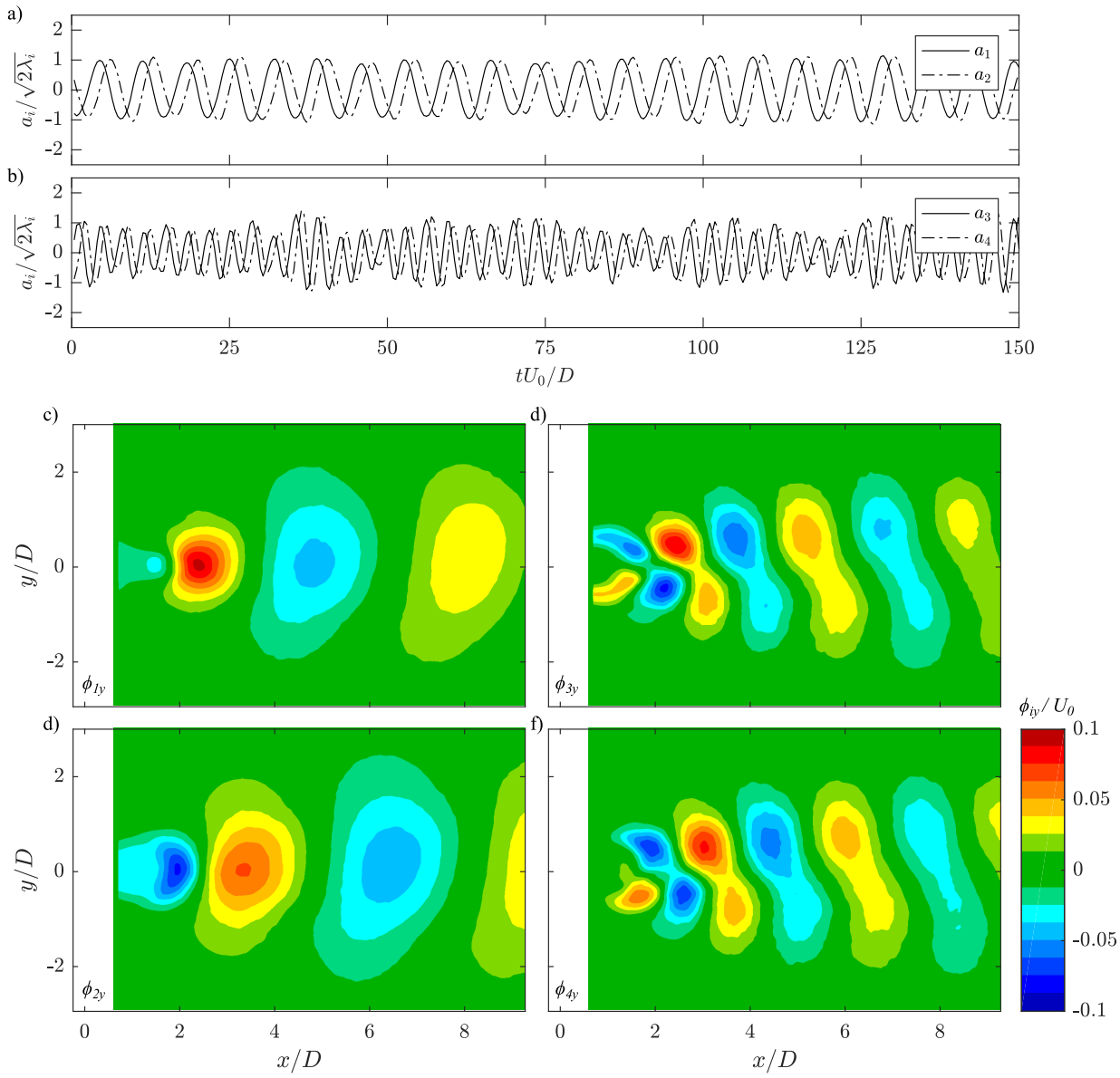

Figure F.12: POD analysis in the $x-y$ plane at $z/D \approx 12.5$ for the case $U^* = 7.08$. Temporal coefficients normalized with respective energy content for (a) modes 1 and 2, and (b) modes 3 and 4. Transverse spatial modes for (c-f) POD modes 1 to 4.

F.4 POD 2P Shedding

This Appendix section presents results of the POD analysis on the PIV measurements in the $x-y$ plane at $z/D \approx 18$ for 2P shedding at $U^* = 7.19$. Figure F.13a presents the relative turbulent kinetic energy of each POD mode and Fig. F.13b presents the cumulative turbulent kinetic energy. The first four modes form two mode pairs. Examination of the temporal coefficients and spatial modes in Fig. F.14 reveals that mode pairs have similar temporal signals and spatial mode topologies that are offset by a phase shift of approximately $\pi/2$.

Compared to the POD analysis on the PIV measurements in the $x-y$ plane for the P+S vortex shedding mode in Appendices F.2 and F.3. The energy associated with the second mode pair is greater, there are fewer transient fluctuations in a_3 and a_4, and the topology of the transverse spatial modes is spread out in the transverse direction. Such differences are attributed to both the larger amplitude of structural vibration, due to the measurement plane at a higher z/D, and the additional trailing vortex shed each cycle of cylinder oscillation. It should also be noted that the skewed topology of the spatial modes is dependent upon the elliptic orientation as observed in Chapter 4.

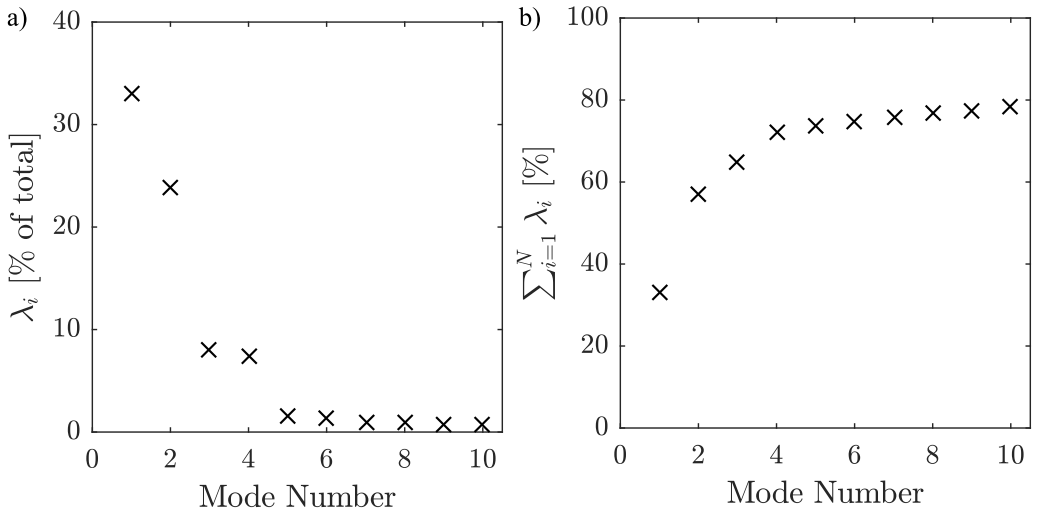

Figure F.13: Relative turbulent kinetic energy from POD analysis in the $x-y$ plane at $z/D \approx 18$ for 2P shedding at $U^* = 7.19$; (a) mode energy distribution (b) cumulative mode energy.

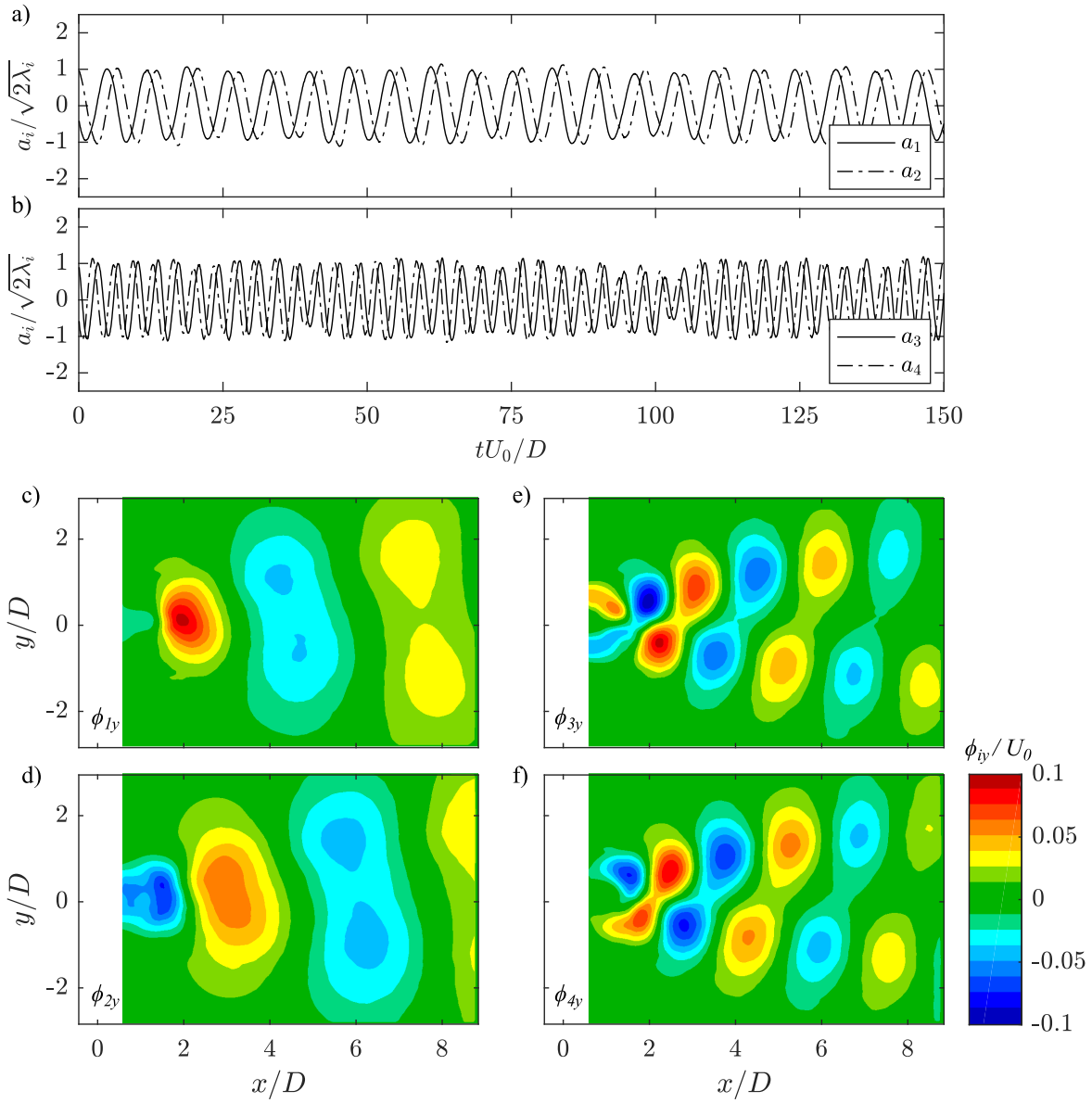

Figure F.14: POD analysis in the $x-y$ plane at $z/D \approx 18$ for 2P shedding at $U^* = 7.19$. Temporal coefficients normalized with respective energy content for (a) modes 1 and 2, and (b) modes 3 and 4. Transverse spatial modes for (c-f) POD modes 1 to 4.

Appendix G

GMM Vortex Identification Criterion Comparison

Numerous vortex identification methods have been developed with the goal of objectively defining a vortex to study the vortex dynamics in the formation and evolution of coherent structures in a fluid [116]. None of these methods have been universally accepted as optimal. The present study employs the Q-criterion for the statistical GMM vortex identification due to its relatively easy implementation and widespread use in vortex dominated flows [65, 118, 119]. Another method, the λ_2-criterion, has also been shown to accurately define vortex cores [116]. This Appendix compares results from the GMM algorithm and the circulation based estimated timing of vortex shedding for both the Q and λ_2-criteria.

Figures G.1a and G.1b show the Q-criterion and λ_2-criterion, respectively, computed from phase averaged velocity fields for a stationary cylinder. The Q-criterion is normalized by its maximum since a positive value indicates a vortex core, while the λ_2-criterion is normalized by its minimum since a negative value indicates a core. It can be seen that both criteria reveal a 2S shedding pattern evidenced by five vortices within the field of view, two of which are rolling up at the end of the shear layer. Examination of the separated shear layer regions reveals that the Q-criterion better distinguishes the rotational vorticity from the shear vorticity compared to the λ_2-criterion. Furthermore, the Q-criterion is more restrictive in identifying the regions pertaining to a vortex core in the wake.

Figures G.1c and G.1d depict the results of the GMM vortex identification algorithm using the Q-criterion and λ_2-criterion, respectively, on top of the vorticity contours. Vortex centroids, located by the spatial mean of each GMM subpopulation, are indicated by plus symbols and their area by the surrounding ellipse, which is computed by the region encompassed within three standard deviations around the centroid. The results illustrate

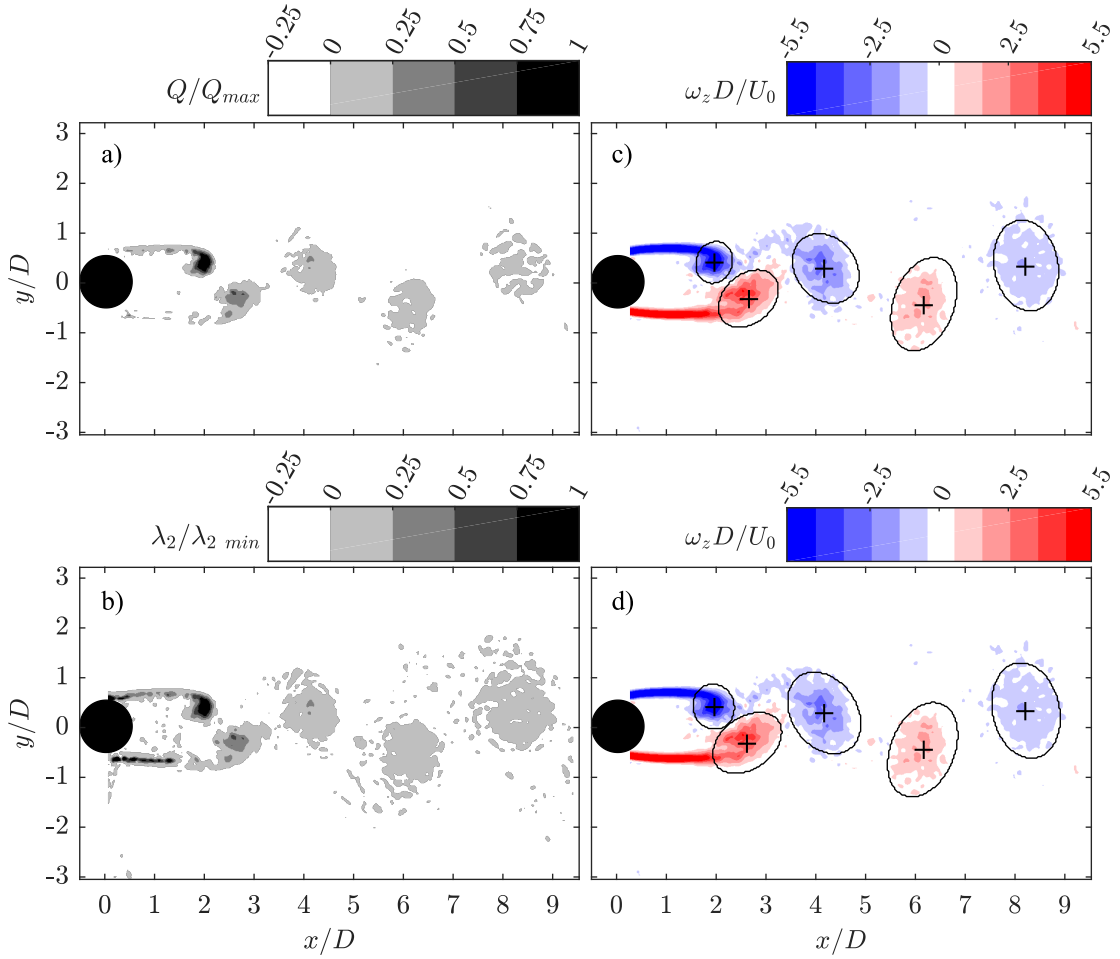

Figure G.1: Vortex shedding from a stationary cylinder. Vortex identification (a) Q-criterion and (b) λ_2-criterion computed from phase averaged velocity fields. Non-dimensionalized phase-averaged vorticity fields with vortex centroids and boundaries, indicated by plus symbols and surrounding ellipses, computed from GMM based vortex identification using the (c) Q-criterion and (d) λ_2-criterion. Note, flow is from left to right and the cylinder is represented by the black circle at $(x/D, y/D) = (0, 0)$.

that the algorithm correctly identifies the five vortices, distinguishing rotational from shear regions, and captures their skewed shape. The location of vortex centroids are similar for the two criteria, however their area is slightly different. In the near wake, $x/D \lesssim 5$, the vortex area computed from the Q-criterion is slightly smaller than that from the λ_2-criterion due to the vortex core identification being more restrictive. Beyond $x/D \approx 5$, the vortex area computed from the two criteria are nearly identical.

Variation of vortex circulation with phase angle is presented in Figs. G.2a and G.2b for the Q-criterion and λ_2-criterion, respectively, in order to elucidate the shedding process. The circulation is computed by integrating the vorticity within the area defined by GMM vortex identification, with error bars showing the methodological uncertainty associated with phase averaging based on a 99% confidence interval. The criteria and phase averaged velocity fields in Fig. G.1 depict the 2S shedding process at $\theta = 7\pi/8$. The dashed line, identifies the estimated phase angle of vortex shedding and is obtained from the intersection of two linear fits to the data before and after the expected instant of shedding. The line prior to shedding is automatically fit using the first five data points, then extended by iteratively adding points one by one as long as their deviation from the linear fit is less than two standard deviation of the error between each of the points and the corresponding fit. The line subsequent to shedding is similarly generated starting with the point excluded from the first linear fit based on the aforementioned procedure. The timing of vortex shedding is generally similar for both criteria, with methodological uncertainty limits identified by shaded regions. However, the λ_2-criterion estimates that shedding occurs approximately $\pi/32$ later than the Q-criterion. This may be a result of the uncertainty or the GMM algorithm computing a slightly larger vortex area for the λ_2-criterion.

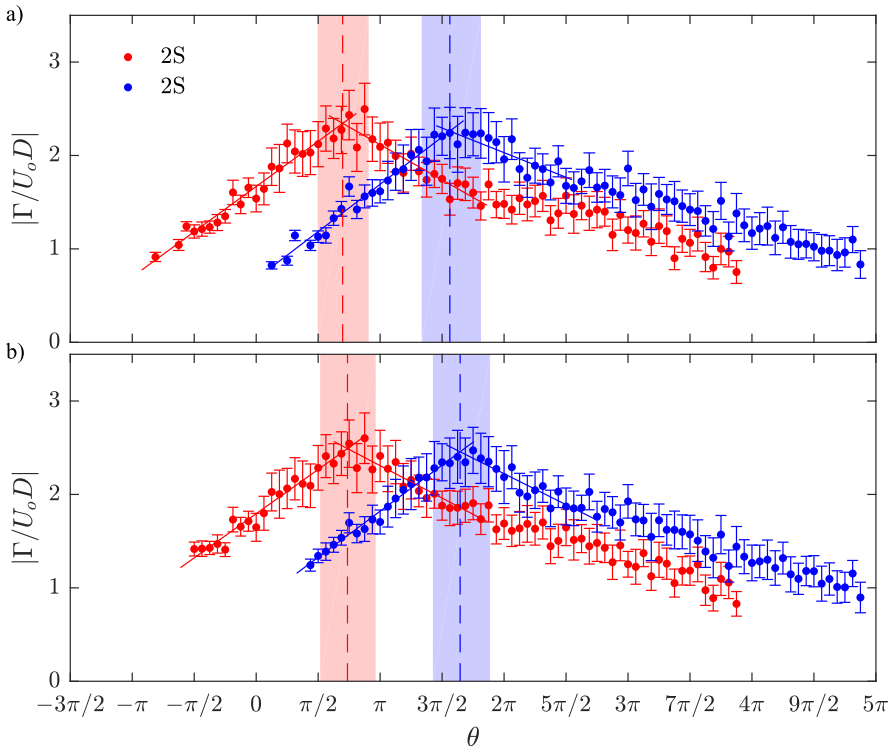

Figure G.2: Variation of vortex strength with respect to phase angle as per GMM based vortex identification computed using the (a) Q-criterion and (b) λ_2-criterion for a stationary cylinder. Dashed lines indicate the estimated timing of vortex shedding, with shaded regions representing methodological uncertainty.

Appendix H

Free Stream Variation

The present study adjusts f_n to manipulate U^* so as to maintain a constant Re throughout tests. Figure H.1 presents the peak deflection angle in the $y-z$ plane over a range of U^* obtained from variation of either f_n or U_0. Both cases generally exhibit a similar response; however, in the range $5.8 \leq U^* \leq 7.5$, the response obtained from variation of f_n is approximately $\delta_{yz} \approx 0.1°$ smaller than that from variation of U_0. This may be attributed to differences in the inertia ratio, damping coefficient, and/or Reynolds number. Examination of the response due to variation of U_0 reveals there is no hysteresis in the amplitude response. This finding should be verified with an additional test measuring the response for increasing and decreasing U_0 at the same U^* values with finer resolution.

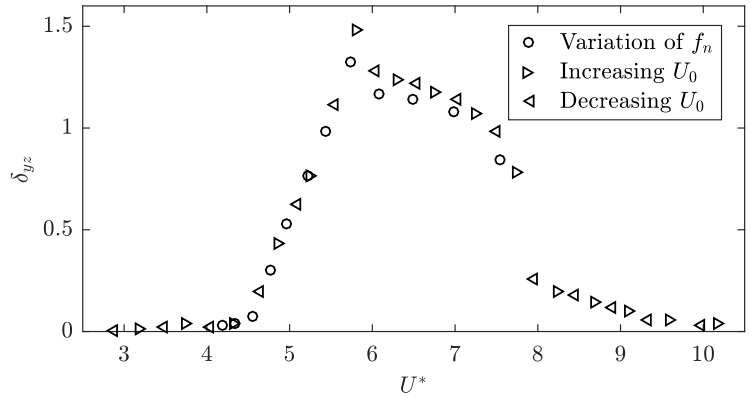

Figure H.1: Peak deflection angle in the $y-z$ plane measured in degrees. Variation of U^* with f_n: $89.0 \leq I^* \leq 115.9$, $0.0034 \leq \zeta \leq 0.0041$, and $\mathrm{Re} = 3100$. Variation of U^* with U_0: $I^* = 107.0$, $\zeta = 0.0039$, and $1840 \leq \mathrm{Re} \leq 6580$.